Skoltech

Skolkovo Institute of Science and Technology

NEW APPROACHES FOR NUMERICAL MODELING OF AIR-INJECTION BASED ENHANCED OIL RECOVERY

Doctoral Thesis

by

LYUDMILA KHAKIMOVA

DOCTORAL PROGRAM IN PETROLEUM ENGINEERING

Supervisor

Associate Professor of the Practice Alexey Cheremisin

Co-advisor

Dr. Artyom Myasnikov

Moscow – 2020

I hereby declare that the work presented in this thesis was carried out by myself at Skolkovo Institute of Science and Technology, Moscow, except where due acknowledgement is made, and has not been submitted for any other degree.

Candidate (Lyudmila Khakimova)

Supervisor (Prof. Alexey Cheremisin)

Abstract

Air injection-based Enhanced Oil Recovery (EOR) processes are receiving interest due to their high potential applicability to a wide range of reservoirs. Predicting the field performance of thermal EOR projects is based on laboratory and numerical modeling and very challenging. During numerical reservoir modeling, the following most essential difficulties are faced: the lack of a proper reaction kinetic model and the large number of pseudo-components, more precise determination of phase equilibria under critical conditions, porosity changes due to chemical reactions, the anisotropy of thermal properties, upscaling from laboratory to field scale and simulation time performance.

The first part of the presented work is dedicated to the construction and validation of 3D laboratory-scale numerical models of oxidation experiments, Ramped Temperature Oxidation (RTO), and Combustion Tube (CT) tests to provide a proper High-Pressure Air Injection (HPAI) and *In-Situ* Combustion (ISC) kinetic models for oxidation and combustion reactions for three different reservoir types (carbonate, bitumen, oil shales). Numerical models are constructed using the abilities of commercial thermal simulator CMG STARS with multilayer design and specific heater regimes to avoid constructional uncertainties and their further validation against the experimental data. Adaptation and history matching of ISC and HPAI performance laboratory experiments are provided for the carbonate oil field and Samara region oil sand bitumen. In order to describe the chemical behavior of hydrocarbons during the HPAI and ISC processes, we use modified and adapted reaction schemes, which include the polymerization of maltenes and asphaltenes in the low-temperature region (LTR), bond-scission reaction of hydrocarbon gas in LTR, thermal cracking and coke and vapor phase light oil combustion in the high-temperature oxidation region (HTR) for Samara region oil and bond-scission reaction of Maltenes in LTR for the carbonate oil field. The oxidation behavior of Bazhenov shales is studied by RTO and pressurized differential scanning calorimetry (PDSC). Based on the validation of the numerical model with the experimental results, it was revealed that kerogen or its derivatives undergo oxidation in several temperature regions. As a result, a

minimum set of kerogen pseudo-components in the solid phase necessary for describing oxidation reactions in LTR, HTR and pyrolysis reaction was determined.

In the second part of this work, we present an alternative approach to calculating phase behavior in multicomponent multiphase hydrocarbon systems. The method is based on using the Gibbs or Helmholtz system energy minimization technique. The problem of determining phase equilibrium is traced to the constrained minimization problem and solved numerically using the simplex method. The proposed algorithm is implemented in Matlab and does not require preliminary knowledge of the number of considered phases. It does not have any restrictions on the number of system components and phases. The results obtained are compared with experimental data and flash calculations for a set of binary, ternary, 5- and 11-component mixtures. The predictive and computational advantages of the proposed technique are demonstrated in comparison to flash calculations and existing k-values correlations for hydrocarbon mixtures, especially in the region close to the critical area.

Publications

Peer-Reviewed Articles Appearing in Technical/Scientific Journals:

1. **L. Khakimova**, A. Myasnikov, T. Bondarenko, E. Y. Popov, A. Cheremisin, I. Karpov, Validation of computational model of high-pressure air injection for Bazhenov formations by laboratory modelling results (Russian), Oil Industry Journal, pp. 85-89 (2017)
2. **L. Khakimova**, T. Bondarenko, A. Cheremisin, A. Myasnikov, and M. Varfolomeev, High pressure air injection kinetic model for Bazhenov Shale Formation based on a set of oxidation studies, Journal of Petroleum Science and Engineering, vol. 172, pp.1120-1132 (2019)
3. **L. Khakimova**, A. Askarova, E. Popov, R. G. Moore, A. Solovyev, Y. Simakov, I.Afanasiev, J. Belgrave, and A. Cheremisin, High-pressure air injection laboratory-scale numerical models of oxidation experiments for Kirsanovskoye oil field, Journal of Petroleum Science and Engineering, vol. 188, p. 106 796 (2020)
4. Isaeva, A., Dobrozhanskiy, V., **Khakimova, L.**, Podladchikov, Y. Numerical simulations of interphase mass transfer in multicomponent hydrocarbon systems using the direct energy minimization (Russian), Gas Industry Magazine, 2020, Accepted manuscript.
5. Yury Alkhimenkov, **Lyudmila Khakimova**, YuryPodladchikov, Stability of discrete schemes of Biot's poroelastic equations, Geophysical Journal International, Accepted 2020 November 29.
6. Yury Alkhimenkov, **Lyudmila Khakimova**, Ludovic Raess, Beatriz Quintal, YuryPodladchikov, Numerical modeling of the anisotropic elastodynamic Biot's equations on graphical processing units (GPUs), submitted to Journal of geophysical research: solid earth.
7. **L. Khakimova**, E. Popov, A. Cheremisin, J. Belgrave, Adaptation of ramped temperature oxidation test results on modeling of air injection enhanced oil recovery processes for bitumen reservoir, submitted to Journal of Petroleum Science and Engineering.

8. Elena D. Mukhina, PhD; Alexander N Cheremisin, PhD; **Lyudmila Khakimova**; Alsu Garipova, PhD; Ekaterina A Dvoretskaya; Maya V Vershinina; Daria Y Kalacheva; Konstantin Y Prochukhan; Anton A Kasyanenko; Alexey N Cheremisin, PhD, Enhanced Oil Recovery Technique Selection for Shale Oil Based on Numerical Simulation, submitted to Journal of Petroleum Science and Engineering.

Technical/Scientific Articles Appearing in Conference Proceedings:

1. **L. Khakimova**, A. Myasnikov, Y. Melnikova, and A. Zhabkina, Optimization Workflow for Modelling of Two Phase Thermal Multicomponent Filtration, 7th EAGE Saint Petersburg International Conference and Exhibition, cp-480-00145 (2016)
2. T. Bondarenko, **L. Khakimova**, A. Cheremisin, M. Spasennykh, High-Pressure Air Injection Laboratory and Numerical Modelling in Bazhenov Source Rocks, SPE Russian Petroleum Technology Conference, Society of Petroleum Engineers (2017)
3. **L. Khakimova**, Y. Podladchikov, and A. Myasnikov, Modelling of some nonlinear processes in deforming and reacting porous saturated rocks, Geophysical Research Abstracts, vol. 21 (2019)
4. **L. Khakimova**, Yu. Alkhimenkov, Yu. Podladchikov, A. Cheremisin. Modelling of nonlinear processes in deforming and reacting porous saturated rocks: different regimes for reaction front propagation, Geophysical Research Abstracts, vol. 21 (2020)

Acknowledgments

I express my gratitude to my supervisor, Prof. Alexey Cheremisin, and every member of Skoltech Center for Hydrocarbon Recovery, especially Prof. Mikhail Spasennykh and Prof. Dimitry Pissarenko for coordinating the Skoltech PhD program, Prof. Dmitry Eskin for his constructive advice relating to my PhD work, Dr. Denis Sabitov for the valuable scientific discussions, Dr. Evgeny Popov and Dr. Tatiana Bondarenko, who helped with experiments, and Alina Sabitova and Aliya Mukhametdinova for being nearby and for their moral support during the whole PhD program.

I thank Mikhail Varfolomeev, Anna Isaeva, Vladimir Dobrozhanskiy and all my co-authors for their help with the research work as well as with preparing publications and with the revision.

I acknowledge Dr. John Belgrave from Belgrave Oil and Gas Corporation, who, unfortunately, is no longer with us, Prof. Sudarshan (Raj) Mehta and Prof. Gordon Moore of the University of Calgary for sharing their expertise, giving constructive comments relating to my research and, finally, for the organizing the brilliant course of Enhanced Oil Recovery at Skoltech. The knowledge I acquired during this course helped me a lot in my PhD work.

I wish to thank Prof. Stefan Schmalholz, Prof. Evangelos Moulas, Dr. Ludovic Räss, Dr. Daniel Kiss, Yury Alkhimenkov and other members and students, past and present, of Scientific Computing Group at the Institute of Geosciences, University of Lausanne for introducing me to the world of computational geoscience and providing valuable discussions and inspiration for further research.

My special and endless gratitude is extended to my co-advisor, Dr. Artyom Myasnikov, who, although is no longer with us, continues to inspire by his example, and Prof. Yury Podladchikov of the University of Lausanne for sharing his expertise and professional attitude, for the numerous passionate scientific and near-scientific discussions, for the inspiration and the inestimable knowledge I have acquired during the time of our collaborative work. This thesis would hardly have been possible without their insight and support.

Finally, I cannot thank enough each member of my big family for their endless love, the opportunities and knowledge they provided me and for their constant support and faith in me.

Table of Contents

Abstract iii

Publications v

Acknowledgments vii

Table of Contents ix

Nomenclature xii

List of Figures xiii

List of Tables xix

Chapter 1. Introduction, literature review, and thesis outline 1

Chapter 2. Methodology for air injection EOR processes numerical model construction based on a set of laboratory studies 12

2.1 Laboratory methods 13

2.1.1 Ramped temperature oxidation (RTO) 13

2.1.2 Combustion tube test 15

2.2 3D digital models of experimental setups 16

2.2.1 Ramped temperature oxidation numerical model 16

2.2.2 Combustion tube numerical model 18

2.3 Conclusions to Chapter 2 23

Chapter 3. Adaptation and history matching of ISC and HPAI performance laboratory experimental results for numerical modeling of air injection-based EOR for different types of reservoirs 24

3.1 Adaptation of ramped temperature oxidation test results on modeling of air injection enhanced oil recovery processes for bitumen reservoir 24

3.1.1 Ramped temperature oxidation experimental results for bitumen 26

3.1.2 Numerical simulation of the RTO test for bitumen 30

3.2 High-pressure air injection laboratory-scale numerical models of oxidation experiments for carbonate oil field 40

3.2.1 High pressure ramped temperature oxidation experimental results for carbonate oil field 42

3.2.2 Medium pressure combustion tube experimental results for carbonate oil field 46

3.2.3 Fluid and kinetic model for carbonate oil field 49

3.2.4 HPRTO: history matching 57

3.2.5 MPCT: history matching 64

3.3 Insights on construction of HPAI reaction kinetic model for organic-rich source rock 73

3.3.1 Ramped temperature oxidation experimental results 74

3.3.2 Pressurized Differential Scanning Calorimetry experimental results 76

3.3.3 Construction and validation of numerical model 79

3.4 Conclusions to Chapter 3 90

Chapter 4. Simulations of phase behavior of multicomponent multiphase hydrocarbon systems using direct energy minimization technique 93

4.1 Methods 94

4.1.1 Flash calculations algorithm 95

4.1.2 Minimization of Helmholtz energy 98

4.1.3 Minimization of Gibbs energy 107

4.2 Results 112

4.3 Conclusions to chapter 4 128

Chapter 5. Summary, conclusions, and recommendations for future research 130

5.1 Summary 130

5.2 Conclusions 135

5.3 Recommendations for future research 136

Bibliography 139

Appendix A. Fugacity and fugacity coefficient 152

Appendix B. SRK and PR cases 155

Appendix C. The derivatives of the Helmholtz energy 160

Appendix D. Additional results for binary mixtures 162

Appendix E. Additional results for the methane—ethane—n-pentane ternary mixture. 165

Nomenclature

A – frequency factor

ARC – accelerating rate calorimetry

BF – Bazhenov Formation

BIC – binary interaction coefficient

CT – Combustion tube

E_a – activation energy

EOR – enhanced oil recovery

EOS – equation of states

GOC – generative organic carbon

GPU – graphical processing unit

HPAI – high-pressure air injection

HPRTO – high-pressure ramped temperature oxidation

H_r – reaction enthalpy

HTR – high-temperature region

ISC – *in-situ* combustion

LTR – low-temperature region

LTO – low-temperature oxidation

MPCT – medium pressure combustion tube

NGOC – non-generative organic carbon

NTGR – negative temperature gradient region

PDSC – pressurized differential scanning calorimetry

PR EOS – Peng-Robinson Equation of State

RTO – ramped temperature oxidation

SRK EOS – Soave-Redlich-Kwong Equation of State

List of Figures

Figure 2.1 Key aspects of construction HPAI/ISC numerical models 12
Figure 2.2 Schematic diagram of the RTO setup 14
Figure 2.3 Schematic diagram of the CT setup 16
Figure 2.4 High-Pressure Ramped Temperature Oxidation installation (left) and the digital model of the RTO setup in CMG STARS (right) 18
Figure 2.5 Demonstration of the grid sensitivity. The temperature profile in the first zone of the RTO digital setup during simulation 18
Figure 2.6 Medium Pressure Combustion Tube Installation (a) and the numerical model of the MPCT experiment in CMG STARS: model grid (b), initial porosity (c), initial permeability (d) 20
Figure 2.7 Schematic representation of the thermocouples and heaters installed in CT .. 22
Figure 3.1 Zoomed in temperature profiles by zones in the RTO test for bitumen 27
Figure 3.2 Temperature profiles by zones and mole concentrations of oxygen, nitrogen, helium, carbon monoxide, and carbon dioxide (above) and mole concentrations of ethylene, methane, propylene, ethane, hydrogen in RTO test for bitumen 29
Figure 3.3 Combustion front propagation in HTR through zones 4-7 in RTO test for bitumen 29
Figure 3.4 Numerical model of RTO test setup for bitumen 30
Figure 3.5 Numerical simulation results for RTO experiments for bitumen: temperature profiles by zones and molar concentration of nitrogen, carbon dioxide, and oxygen 35
Figure 3.6 Numerical simulation results at Zone 1 of the reactor for RTO test for bitumen: temperature profile, molar fraction of Maltenes, Asphaltenes, Light Oil and solid-phase concentration of Coke 36
Figure 3.7 Comparison of numerical and experimental results of RTO test for bitumen: temperature profiles for a) Zone 1; b) Zone 5; c) Zone 6 and d) Zones 7 of the reactor .. 38
Figure 3.8 Comparison of the results for experiment and simulation of RTO test for bitumen: mole fraction of Nitrogen, Oxygen and Carbon Dioxide 39
Figure 3.9 Zoomed in temperature profiles by zones in RTO test for carbonate oil field 43

Figure 3.10 Zoomed in temperature profiles for Zone 1 (above) and Zone 4 (below) in RTO test for carbonate oil field 44
Figure 3.11 Temperature profiles by zones and mole concentrations of oxygen, nitrogen, helium, carbon monoxide and carbon dioxide (above) and mole concentrations of ethylene, methane, propylene, ethane, hydrogen, propane, n-pentane, n-butane, i-butane (below) for carbonate oil field 45
Figure 3.12 Temperature profiles on the centerline (above) and wall-mounted (below) thermocouples by zones for carbonate oil field 47
Figure 3.13 Combustion front propagation (above) gas mole concentrations (below) for carbonate oil field 48
Figure 3.14 Zoomed in simulated temperature profiles for the traditional reaction model for carbonate oil field..... 52
Figure 3.15 Temperature dependence of heat flow for original oil sample as a result of PDSC test (black - 5°C/min, blue – 10°C/min, red – 15°C/min)..... 53
Figure 3.16 Temperature dependence of heat flow for maltenes fraction of original oil as a result of PDSC test (black - 5°C/min, blue – 10°C/min, red – 15°C/min) 53
Figure 3.17 Temperature dependence of heat flow for asphaltenes fraction of original oil as a result of PDSC test (black - 5°C/min, blue – 10°C/min, red – 15°C/min) 54
Figure 3.18 Zooed m in simulated temperature profiles for modified reaction model for carbonate oil field 56
Figure 3.19 Numerical simulation and experimental results for RTO test for carbonate oil sample: temperature profiles by zones and molar concentration of nitrogen, carbon dioxide, and oxygen (traditional reaction scheme) 58
Figure 3.20 Comparison of results for experiment and simulation for RTO test for carbonate oil example: a) cumulative oil mass; b) cumulative gas mass; c) cumulative water mass (traditional reaction scheme)..... 59
Figure 3.21 Numerical simulation and experimental results for RTO experiments for bitumen: temperature profiles by zones and molar concentration of nitrogen, carbon dioxide, and oxygen (modified reaction scheme) 60

Figure 3.22 Comparison of numerical and experimental results for RTO test for carbonate oil field: temperature profiles for Zones 4 (above) and 7(below) of the reactor (modified reaction scheme) 62
Figure 3.23 Comparison of results for experiment and simulation of RTO test for carbonate oil example: cumulative oil mass and cumulative water mass (modified reaction scheme) 63
Figure 3.24 Comparison of results for experiment and simulation of RTO test for carbonate oil example: cumulative gas mass (modified reaction scheme)..... 64
Figure 3.25 Comparison of the MPCT test results for experiment and simulation: temperature profiles for carbonate oil field (traditional reaction scheme) 65
Figure 3.26 Comparison of the MPCT test results for experiment and simulation: gas mole concentrations for carbonate oil field (traditional reaction scheme) 66
Figure 3.27 Comparison of the results for experiment and simulation: temperature profiles for carbonate oil field (modified reaction scheme)..... 66
Figure 3.28 Comparison of the MPCT test results for experiment and simulation: gas mole concentrations for carbonate oil field (modified reaction scheme) 67
Figure 3.29 Temperature profile for Zone 6 in MPCT test for carbonate oil field: in case of the traditional (above) and modified (below) reaction schemes 68
Figure 3.30 Cumulative oil (above) and water (below) production for experiment and simulation as a result of MPCT experiment for carbonate oil field (traditional reaction scheme) 71
Figure 3.31 Cumulative oil and water production for experiment and simulation as a result of MPCT experiment for carbonate oil field (modified reaction scheme)..... 72
Figure 3.32 Dependence of oxygen consumption rate on temperature at different heating rates (1.50, 1.75, 2.00 and 2.25°C/min) for oil shales 74
Figure 3.33 Change in the composition of the gas mixture when the sample is heated (1.50°C/min) for oil shales..... 75
Figure 3.34 Dependence of the activation energy E on the degree of conversion α for oil shales..... 76

Figure 3.35 DSC oxidation curves for oil shales, pressure 8 MPa. Upper right corner curve represents heating rate 1 K/min 77
Figure 3.36 Example of DSC curve separation into three individual peaks for oil shales, heating rate 10 K/min..... 77
Figure 3.37 Experimental and numerical oxygen consumption in RTO test for oil shales 81
Figure 3.38 Solid concentration of kerogen components with respect to the temperature 83
Figure 3.39 Global mole fraction of light oil component with respect to the temperature 83
Figure 3.40 Global mole fraction of heavy oil component with respect to the temperature 84
Figure 3.41 Solid concentration of coke component with respect to the temperature..... 84
Figure 3.42 Solid concentration of kerogen components and coke component, global mole fraction of light and heavy oil components with respect to the temperature for oil shales 85
Figure 3.43 PDSC simulation model schematic 86
Figure 3.44 Crucible representation in PDSC simulation model..... 86
Figure 3.45 Experimental and numerical results of PDSC test for oil shales..... 86
Figure 3.46 Schematic model of oxidation and thermal decomposition processes during HPAI 88
Figure 3.47 Relative permeability to water and oil with respect to water saturation for oil shales..... 89
Figure 3.48 Relative permeability to oil and gas with respect to liquid saturation for oil shales..... 89
Figure 4.1 Flowchart of flash calculations (vapor-liquid equilibrium case)..... 97
Figure 4.2. Flowchart of Helmholtz energy minimization algorithm (vapor-liquid equilibrium case)..... 102
Figure 4.3. Visualization of dimensionless system Helmholtz energy in discrete volume and compositional space for binary system Methane-Ethane under different initial conditions (blue star), and corresponding optimal solution (black circles). a) Initial

conditions correspond to the two-phase region: P = 4.8114 MPa, T = 250 K, Z1 = 0.4791; b) Initial conditions correspond to the critical region: P = 8.1060 MPa, T = 250 K, Z1 = 0.4791..... 106
Figure 4.4. Flowchart of Gibbs energy minimization algorithm (vapor-liquid equilibrium case) 109
Figure 4.5. Visualization of dimensionless system Gibbs energy in discrete compositional space for binary Methane-Ethane system under different initial conditions (blue star), and corresponding optimal solution (black circles). a,b) Initial conditions correspond to the two-phase region: P = 4.8114 MPa, T = 250 K, Z1 = 0.4791; c,d) Initial conditions correspond to the critical region: P = 8.1060 MPa, T = 250 K, Z1 = 0.4791. 111
Figure 4.6 Pressure-composition phase diagram for methane—ethane binary mixture at T = 250 K as a result of a) flash calculations and b) Gibbs minimization algorithm..... 114
Figure 4.7 Modulus of difference in molar fractions of vapor phase calculated by flash calculations and the proposed Gibbs energy minimization technique (methane—ethane binary mixture)..... 114
Figure 4.8 Zoomed in fragment of pressure-composition phase diagram for methane—ethane binary mixture at T = 250 K as a result of a) flash calculations and b) Gibbs minimization algorithm..... 115
Figure 4.9 Actual number of iterations used in flash calculations (methane—ethane binary mixture)..... 115
Figure 4.10 K-values at different pressures for methane—ethane binary mixture at T = 250 K for a) methane and b) ethane component 117
Figure 4.11 Phase compositions at different pressures for methane—ethane binary mixture at T = 250 K: a) liquid phase, b) vapor phase 117
Figure 4.12 K-values at different pressures for methane—n-heptane binary mixture at T = 344.3 K for a) methane and b) n-heptane 119
Figure 4.13 Phase compositions at different pressures for methane—n-heptane binary mixture at T = 344.3 K: a) liquid phase, b) vapor phase 119

Figure 4.14 Ternary phase diagram for the methane—ethane—n-pentane ternary mixture at at P = 2.53 MPa and T = 250 K obtained by a) flash calculations and b) Gibbs energy minimization algorithm. The transition from dark blue to dark red corresponds to an increase in the mole fraction of vapor from zero to one. White circles and white lines demonstrate the experimental and calculated boundaries of the two-phase region, respectively 122
Figure 4.15 K-values for the components of the quinary mixture 123
Figure 4.16 Phase compositions of the quinary mixture at P = 9.867 MPa and T = 311 K in a) liquid and b) vapor phases in case of flash calculations (blue), Gibbs energy minimization algorithm (red) and experiment (orange)..... 123
Figure 4.17 Compositions of the quinary mixture for vapor and liquid phases at T = 311 K and different pressures: 3.5646 MPa, 6.5224 MPa, 8.9425 MPa, 9.8664 MPa, 11.9693 MPa in case of flash calculations (blue frame), Gibbs energy minimization algorithm (red frame) and experiment (green frame)..... 125
Figure 4.18 Phase compositions of the 11-component mixture: concentration of nitrogen, carbon dioxide, methane, ethane, propane, i-butane, n-butane, i-pentane, n-pentane, hexane and heptane in liquid (above) and vapor phases in case of flash calculations (blue), Gibbs energy minimization algorithm (red) and experiment (orange) (below) 126
Figure 4.19 Computational time at different pressures for the methane—n-heptane binary mixture 127

List of Tables

Table 2.1 CT specifications 16
Table 2.2 Parameters of the RTO setup layers 17
Table 2.3 The porosity, permeability, and diameters of the CT layers 20
Table 3.1 Schedule of RTO experiment for Samara region oil sand bitumen 25
Table 3.2 Samara region oil sand bitumen properties 26
Table 3.3 Conditions to initialize RTO numerical model for bitumen 31
Table 3.4 Data for model components for bitumen sample 33
Table 3.5 Gas-liquid k-value correlations for bitumen pseudo-components 34
Table 3.6 Initial conditions for bitumen model pseudo-components 34
Table 3.7 Kinetic parameters obtained from history matching the RTO experiment for bitumen 37
Table 3.8 Mass of products for experiment and simulation of RTO test for bitumen 39
Table 3.9 Schedule of RTO experiment for carbonate oil field 41
Table 3.10 Schedule of CT experiment for carbonate oil field 42
Table 3.11 Traditional reaction scheme 49
Table 3.12 Data for Model Components for carbonate oil sample 50
Table 3.13 Gas-liquid k-value correlations for carbonate oil pseudo-components 50
Table 3.14 Conditions to initialize RTO numerical model for carbonate oil field sample 51
Table 3.15 Kinetic parameters estimated as a result of PDSC test for carbonate oil field 54
Table 3.16 Element composition of original oil and that produced in LTR, and original maltenes and asphaltenes and that produced in LTR for carbonate oil field 55
Table 3.17 Modified reaction scheme for carbonate oil field 55
Table 3.18 Adjusted kinetic parameters as a result of history matching of RTO experiment for carbonate oil field 57
Table 3.19 Mass of products for experiment and simulation of RTO experiment for carbonate oil field 60

Table 3.20 Mass of the products for the experiment and simulation for MPCT test for carbonate oil field 69
Table 3.21 Temperature parameters of LTR and HTR for oil shales 75
Table 3.22 Kinetic parameter at LTR and HTR for oil shales 76
Table 3.23 Results of PDSC individual peaks analysis for oil shales 78
Table 3.24 Kinetic characteristics of the sample oxidation at a pressure of 8 MPa for oil shales 79
Table 3.25 Pseudo-components of original oil for oil shales 80
Table 3.26 Pseudo-components of kerogen 82
Table 3.27 Kinetic data for oil shales 87
Table 3.28 Data for model components for oil shales 88
Table 3.29 Gas-Liquid K-Value Correlations for oil shales 89

Chapter 1. Introduction, literature review, and thesis outline

Air injection-based Enhanced Oil Recovery processes are receiving interest due to their high potential applicability to a wide range of reservoirs (Alfarge et al., 2017; Fassihi et al., 2016; Kokorev et al., 2014; Moore et al., 2012; Ursenbach et al., 2010). High-Pressure Air Injection (HPAI) and *In-Situ* Combustion (ISC) are examples of thermal production methods with the possibility of reducing the production cost since the process is without steam and water cycling, particularly in deep, high-pressure, low permeability fields, where other EOR methods are not profitable (Moore et al., 2012). HPAI and ISC have such advantages as a high recovery coefficient, less energy, and water consumption for oil production. Some of the oil in place is consumed to provide the heat (Yoshioka et al., 2017). HPAI and ISC have already been effectively applied for different types of reservoirs development and proven to be economically feasible (Ismail et al., 2016). However, a clear understanding of the process mechanism is still a challenge (Barzin et al., 2010; Bhattacharya et al., 2016; Bondarenko et al., 2017; Gutiérrez et al., 2012; Moore et al., 2012). The primary mechanism of the HPAI process is the thermal drive imposed by the combustion kinetics, oil swelling, and viscous drive caused by the flue gas, as well as steam distillation at elevated temperatures (Pu et al., 2020; Zhao et al., 2019a). During HPAI and ISC, compressed air is injected into a high gravity, high-pressure oil reservoir, where some portion of oil reacts with the oxygen at elevated temperatures. As a result, the flue gas mixture containing mainly CO_2 and nitrogen, mobilizes the oil and sweeps it towards the production end. Injected air spontaneously ignites the oil-in-place due to high-pressures and high-temperatures. If the oil is not reactive, the ignition is generally provided using a downhole heater or burner. Specifically designed compressors are used for air injection at desired pressure levels and volumes (Moore et al., 2007).

Predicting field performance of thermal EOR projects is based on laboratory and numerical modeling and very challenging (Bondarenko et al., 2017; Gutierrez et al., 2009). During numerical reservoir modeling, the following critical difficulties are faced: the lack of a proper reaction kinetic model and the large number of pseudo-components (Belgrave

et al., 1993; Freitag and Verkoczy, 2005; Jia and Sheng, 2016; Kok and Karacan, 1997), more precise determination of phase equilibria in the system with an account of parallel chemical reactions and under critical conditions (Barzin et al., 2010; Bhattacharya et al., 2016; Gutiérrez et al., 2012; Kristensen et al., 2008), porosity changes due to chemical reactions, anisotropy, upscaling from laboratory to field scale, and simulation time performance (Christensen et al., 2004; De Zwart et al., 2008; Druganova et al., 2010; Van Batenburg et al., 2011).

The first part of the presented work is dedicated to the construction and validation of 3D laboratory-scale numerical models of oxidation and HPAI and ISC performance experiments, Ramped Temperature Oxidation (RTO) (Burger, 1972; Fassihi et al., 1984; Moore et al., 1999), and Combustion Tube (CT) (Fadaei et al., 2011) tests (Chapter 2), to provide a proper HPAI and ISC kinetic models for oxidation and combustion reactions based on the abilities of thermal simulator CMG STARS widely used in industry. In Chapter 3, three different oil field examples are considered: carbonate oil field, Samara region oil sand bitumen and Bazhenov Shale Formation (organic-rich source rock). In each case, different oxidation behavior and recovery performance is expected, and specific details of correspondent investigations are presented below.

Air injection-based EOR methods, including *In-Situ* Combustion (ISC), are shown to be economically effective and have high potential also in the case of bitumen or heavy oil recovery (Adegbesan et al., 1987; Belgrave et al., 1993; Barzin et al., 2010; Sarathi, 1999; Moore et al., 2002; Moore et al., 2012). It involves initiating the oil combustion front in the reservoir associated with the thermal front propagation through the reservoir during air injection. ISC is considered to be one of the most energy-efficient thermal EOR methods since it eliminates energy losses for heat delivery from the surface to the reservoir and has a low natural gas and water requirement in comparison to steam-based EOR.

In Section 3.1, an investigation of the ISC process for bitumen oil sand was provided, which belongs to the South Tatar oil and gas area of the Volga-Ural oil and gas province are considered.

Predicting field performance of ISC projects is based on laboratory and numerical modeling and is very challenging (Guttierrez et al., 2009, Bondarenko et al., 2017). During numerical reservoir modeling, one faces the following most essential difficulties: proper reaction kinetic model construction with a chosen number of pseudo-components (Belgrave et al., 1993, Freitag et al., 2005, Kok et al., 1997, Li et al, 2006, Barzin et al.,2010, Gutierrez, 2012), more precise determination of phase equilibria in the system with an account of parallel chemical reactions and under critical conditions (Kristensen et al., 2009, Gutierrez, 2019, Barzin et al.,2010, Bhattacharya et al., 2016), porosity changes due to chemical reactions, anisotropy, upscaling from laboratory to field scale (Kapadia et al., 2012) and simulation time performance (Christensen et al., 2004, Zwart et al., 2008, Druganova et al., 2010, Van Batenburg et al., 2011). In Gutierrez et al., 2009, it was mentioned that "A good kinetic model is the heart and soul of a good combustion model." Within this work, the authors consider the aspect of a proper kinetic model validation. It can be defined as a combination of a set of chemical reactions and corresponding kinetic data, which is relevant for an adequate representation of the oxidation of the considered oil. There are two generally accepted oxidation mechanisms of oil species undergoing ISC process in the reservoir: low-temperature oxidation (LTO) or oxygen addition reactions, and high-temperature oxidation (HTO) or bond-scission reactions that produce water and carbon oxides (Fassihi et al., 1984). For bitumen and heavy oils, reactions undergoing the first oxidation mechanism take place in the so-called low-temperature region (LTR), while bond-scission reactions occur in the high-temperature region (HTR). It should be mentioned that the different oxygen uptake and heat-generation rate during the oxidation reaction corresponds to different temperature regions (Moore et al., 1992).

There are several qualitative and quantitative oxidation laboratory screening tests for ISC process evaluation. The combustion tube (CT) test is one of the most important experiments to evaluate ISC performance for a specific oil field. It provides a significant amount of input data for reservoir simulations and important combustion parameters. However, due to the organization of the experiment and associated physical processes inside the combustion tube, it is difficult to determine regions of different oxygen uptake

and match them with corresponding temperature regions, and, as a result, it is impossible to estimate the necessary kinetic parameters for the oxidation reaction scheme. In this case, ramped temperature oxidation (RTO) test could be more appropriate for evaluating oxidation behavior and obtaining relevant kinetic data (Mallory et al., 2018). Adaptation and history matching of RTO experimental results for laboratory-scale numerical modeling of the ISC process under experimental conditions make it possible to obtain kinetic parameters for adapted oxidation reaction schemes. In Section 3.1, the adaptation of RTO test results on modeling of air injection enhanced oil recovery processes for bitumen reservoir is presented. A bitumen sample from Samara region oil sand bitumen is used for experimental study in RTO test at the pressure of 0.7 MPa and air injection rate of 40 $st.m^3/(m^2hr)$ to verify reaction scheme for different temperature regions, adjust corresponding kinetic parameters and develop a laboratory-scale numerical model of ISC process for the specific oil field. During the research, it was shown that RTO test had an inalienable role in understanding the oxidation behavior of reported oil samples and fuel mechanism and in constructing an appropriate reaction kinetic scheme, which plays a significant part in feasible HPAI and ISC numerical models (Bhattacharya et al., 2016; Mallory et al., 2018). To describe the chemical behavior of hydrocarbons during the ISC process, a modified traditional (Belgrave et al., 1993; Chen et al., 2014) reaction scheme, which includes the polymerization of maltenes and asphaltenes in LTR, thermal cracking and coke combustion in the HTR, is used. Modification results in the incorporation of the vapor-phase combustion reaction of light oil in HTR, which appears in the system due to asphaltenes cracking and low-temperature oxidation (LTO) reactions.

In Section 3.2, a carbonate oil field is considered. The technology of HPAI injection is a complex of physicochemical process, and the success of applying the method in the field depends on the quality of its experimental and numerical study for the target object (Ursenbach et al., 2010). Before the stage of pilot testing of the technology, a thorough study of the physicochemical and thermodynamic characteristics of the corresponding processes is required, moreover, close to the natural conditions. The work presented in Section 3.2 is devoted to the construction and validation of laboratory-scale numerical

models of oxidation experiments to provide a proper HPAI kinetic model for oxidation and combustion reactions and estimate HPAI method feasibility for car oil field based on the results of oxidation studies. Two sets of oxidation tests were carried out, namely: high-pressure ramped temperature oxidation (HPRTO) and medium pressure combustion tube (MPCT) experiments (Gutiérrez et al., 2012; Mallory et al., 2018; Rodriguez et al., 2012). HPRTO allows a comprehensive understanding of the oxidation behavior (Yang and Chen, 2016). Also, the self-ignition temperature can be obtained from such experiments. MPCT test, in its turn, provides stoichiometry of the reactions and flied design parameter. The tests were done using rock and oil samples from carbonate oil field. An experiment on the HPRTO was carried out to understand the oxidation reactions, which take place in a range of relatively low temperatures, during which the first consumption of oxygen by oil occurs and, as a result, the first generation of energy. The temperature of the first section of the combustion tube is set to a high-temperature sufficient to reach the effective high-temperature oxidation model. 3D numerical models of HPRTO and MPCT experiments were constructed with an appropriate agreement with the design of experimental equipment to reduce constructional uncertainties (Sequera et al., 2010; Chen et al., 2014; Yang et al., 2016). Here its multilayer design, comprehensive thermal properties, and heating modes are considered. In order to describe the chemical behavior of hydrocarbons during the HPAI process, we used the reaction scheme, which includes polymerization of maltenes and asphaltenes in the low-temperature oxidation region, thermal cracking and coke combustion in the high-temperature oxidation region (Belgrave et al., 1993). The matched variables include fluid production masses and volumes, temperature profiles along the tubes at different times, and produced gas composition.

Section 3.3 is dedicated to the discussion of insights on the construction of the HPAI reaction kinetic model for organic-rich source rock. Oil shale is a low permeable sedimentary rock that contains a large amount of immature organic matter (kerogen). Bazhenov oil shale formation (BF) has high potential oil resources that can be unlocked through finding a suitable and efficient recovery technique (Jarvie, 2012; U.S. Department of Energy, 2013; Henderson, 2014; Popov, 2016). Therefore, it is crucial to find a suitable

recovery method for its development (Braduchan et al., 1986, Khalimov and Melik-Pashaev, 1980, Yakovleva-Ustinova, 2014). Thermal enhanced oil recovery methods should be considered for this task because generating hydrocarbons from insoluble organic matter like kerogen requires heating of the rock (Tiwari et al., 2013, Zhang et al., 2014; Deng and Li, 2011; Le-Doan et al., 2013; Kibodeaux, 2014). One of the potential techniques is air-injection-based enhanced oil recovery – high-pressure air injection (HPAI). A pilot test of HPAI was initiated in a permeable layer of BF by RITEK and showed promising results (Kokorev V.I. et al., 2014). However, to test this technique, specialized oxidation studies are required (Moore et al., 2002). These studies help to assess the feasibility of air-injection-based enhanced oil recovery methods for oil shale and BF in particular, which represents a complex physical-chemical process with unpredictable behavior. One of the most significant and difficult steps in the numerical simulation of oxidation and pyrolysis processes in shales is to build a chemical reaction model that includes kinetics, which must represent the oxidation behavior and chemical changes of both the oil and kerogen (Fan et al., 2010; Zheng et al., 2017). Accessing the suitability of air-injection-based EOR is not a straightforward procedure in general (Clara et al., 1999; Yannimaras et al., 1995; Bhattacharya et al., 2015), but accessing this method for such a complex system as oil shales is even more complicated (Khamidulin et al., 2010; Balushkina et al., 2014; Vasiliev et al., 2015; Chugunov et al., 2015). It has been proved that the development of a chemical reaction model and its kinetics is crucial for the success of air-injection-based processes (Barzin et al., 2010). The classical heavy oil kinetic models consist of pyrolysis, oxygen addition reactions, and bond scission reactions (Sarathi, 1999; Belgrave, 1990). In the case of oil shale, kerogen has additional reaction steps, which should be taken into account in the overall chemical reaction model. High molecular weight kerogen has a very complex and not fully determined chemical structure (Kelemen et al., 2007). Therefore, the thermal decomposition and oxidation behavior of kerogen is not well understood nowadays yet. In our previous work (Bondarenko et al., 2017b) experimental studies on oil shale were performed in order to understand the mechanisms of kerogen thermal decomposition. As a result, fracturing occurred through the voids formed by

kerogen oxidation at 450°C, while intensive reactions began to appear at 120°C. In another work of the authors Bondarenko et al., 2017a, as a result of high pressure ramped temperature oxidation test (HPRTO) on a BF sample, the exothermic reaction of kerogen oxidation started at approximately 140°C. In addition, an experimental scheme for evaluation of HPAI in oil shale was proposed, where laboratory oxidation studies were pointed out as a very important step. The reasons for these studies are to determine temperature ranges over which oxygen uptake rates are high, to determine Arrhenius kinetic parameters for low and high-temperature oxidation ranges, to establish whether the dominant oxidation mode corresponds to the low or the high-temperature range, to determine if oxidation reactions can be ignited spontaneously or if artificial ignition is required and to estimate the auto-ignition temperatures corresponding to the onset of elevated oxygen uptake rates in both the low and high-temperature ranges. In the case of kerogen-bearing rocks, the identification of what fractions of oil and kerogen correspond to what reactions were not fully determined previously.

In the second part of this work, Chapter 4, an alternative approach to calculating phase behavior in multicomponent multiphase hydrocarbon systems is presented. Compositional simulation studies are widely used to examine the applicability of different recovery methods in two-phase reservoirs (oil reservoirs with gas caps, gas reservoirs with oil rims), gas condensate reservoirs, etc. Although non-equilibrium thermodynamic processes in reservoirs are of certain interest (Bogachev et al. 2019), as a rule, reservoir fluids (phases) are considered to be in local thermodynamic equilibrium. Compositional reservoir simulators (e.g. CMG STARS, CMG GEM, ECLIPSE 300) use flash calculations to estimate compositions and properties of the equilibrated phases. These algorithms are iterative and based on the equality of the fugacity of each component throughout all phases (Brusilovsky 2002; Danesh 1998; Orr 2005). Performing flash calculations in reservoir simulations may result in expensive computations and unreliable values for the physical properties of phases. These problems arise, for example, when the considered temperatures and pressures are close to their critical values (Danesh 1998). The iterative procedure of flash calculations requires large numbers of successive substitutions to converge in the

critical region. Thus, if the maximum number of iterations is limited, the phase parameters can be determined with an appreciable error. The limitations on the maximum number of iterations are reasonable since the equilibrium parameters of multicomponent reservoir fluids must be determined in each cell at each time step in reservoir simulations. For example, the keyword FCCRIT in ECLIPSE 300 sets the maximum number of iterations in flash calculations (ECLIPSE 2014). For a large reservoir, the total number of flash calculations may be significant. Hence, reducing computational time and ensuring a sufficient level of model accuracy are important considerations in compositional reservoir simulation. Various techniques have been proposed to accelerate flash calculations. For example, options of the above-mentioned keyword FCCRIT in ECLIPSE 300 allow the user to modify the flash calculation error target for cells. The keyword SKIPSTAB invokes the fast flash option (ECLIPSE 2014). In this case, the simulator does not perform the Michelsen stability test for cells in the middle of single-phase regions. The Michelsen stability test is a commonly used technique that precedes flash calculations and gives information if there are one or two hydrocarbon phases (Brusilovsky 2002; Danesh 1998; ECLIPSE 2014). More sophisticated techniques to improve the computational performance of flash calculations have been reported in the literature (Kissinger, 1957; Taylor and Fryer, 1992). Above all, the Michelsen (1982a, 1982b, 1986) method should be noted. This method helps to increase the speed of flash calculations when binary interaction coefficients (BIC) between components are equal to zero. Hendriks and van Bergen (1992) presented the procedure, increasing the speed of flash calculations for sets of nonzero BIC. They proposed to approximate the BIC matrix by spectral decomposition. Alternatively, Li and Johns (2006) approximated BIC by the two-parameter formula to obtain the reduced parameters and speed up flash calculations. Gorucu and Johns (2015) compared eight reduced and conventional methods of flash calculations. They revealed the advantages of the two-parameter BIC approximation technique over the spectral decomposition method. Petitfrere and Nichita (2015) also compared reduced and conventional methods of flash calculations in a series of numerical simulations. They reported that reduced methods are more efficient than conventional methods only for mixtures with many components (more

than 20) and several non-zero BIC. Gaganis (2018) proposed a non-iterative procedure to test the phase stability. This procedure involves the use of two discriminating functions that act as classifiers: a positive value of one of the two functions determines the stability state of the mixture. The application of this technique can significantly reduce the CPU time required for phase stability calculations. Koldoba (2018) proposed to approximate the equation of state and the Gibbs energy by simple expressions. This approach made it possible to obtain explicit analytical formulas for the equilibrium ratios (known as K-values). Koldoba (2018) demonstrated the applicability of this approach in a practically important range of pressures and temperatures. The use of machine learning is becoming popular for speeding up flash calculations (Gaganis et al. 2012; Kashinath et al. 2018; Wang et al. 2019). For example, Wang et al. (2019) proposed to use artificial neural networks to accelerate flash calculations in compositional simulations. Artificial neural networks are applied for both phase stability tests and flash calculations. The authors state that in some cases, computational costs can be reduced by up to 90%.

It should be noted that all the approaches mentioned assume the consideration of various consequences of thermodynamic equilibrium. System energy parameters, such as the Helmholtz or the Gibbs energy, are not considered directly. Hence, it is not even necessary to obtain the precise expression for the system energy, since, for example, at a given pressure and temperature, instead of the Gibbs energy direct minimization, the corresponding constraints on the derivatives of the Gibbs energy are considered. In Chapter 4 of this work, an explicit expression for the Helmholtz and Gibbs energies of a multicomponent mixture is obtained. It is then demonstrated that the Helmholtz and Gibbs energies minimization problem can be formulated as a linear programming problem. This fact suggests a simple algorithm for determining the values of phase mole fractions, phase compositions, and molar volumes. Thus, simulation parameters of phases can be calculated sufficient for the compositional reservoir using this algorithm. This particular energy minimization technique is already used in metamorphic petrology to describe phase transformations of multiphase and multicomponent rocks (Connolly 2005; Conolly 2017; Connolly and Galvez 2018; Vrijmoed and Podladchikov 2015) in equilibrium with porous

fluids and melts. More generally, as early as 1958, White et al. suggested to use the nonlinear optimization theory to solve the equilibrium problem by "minimizing the free energy directly" instead of the iterative solution of a nonlinear system of equations obtained by setting the partial derivatives of the energy to zero that is equivalent to conditions for all reactions to be in equilibrium. The "reactions" method has a significant disadvantage due to the information required prior to the start of calculations on the precise set of chemical reactions constraining equilibrium. In a recent book on geochemical modeling, Bethke (2007) stated in the introduction: “The balanced reactions of the equilibrium constant method are counterparts to the species compositions required by the minimization technique; in fact, given the same choice of components, the reactions, and expressions of species compositions take the same form.” The free-energy minimization can be split into two major substeps: the minimization technique and the discretization of the compositional space strategy. Numerous workers have developed non-linear minimization techniques for the calculation of petrological phase equilibria without involving of the discretization of the global compositional space (Shvarov 1978, Saxena 1983, Wood 1984, Ghiorso and Carmichael 1985, DeCapitani 1987, Karpov 1997, Bina 1998). One weakness of non-linear techniques is that the algorithm can be trapped in local minima. An alternative to non-linear techniques is to approximate the continuous compositional variation of solution phases by sets of discrete compositions (White 1958, Connolly 1987). With these approximations, the optimization algorithm guarantees the convergence to a global minimum given that the compositions are sufficiently resolved (Ignizio, 1981). Nonetheless, a more accurate representation of the composition of complex mixtures is needed and a larger number of discrete compositions is required. It results in computation memory problems during calculations, which imposes restrictions on this method (Gaganis, 2018). This paper presents a new phase stability method that is applicable when repeated phase behavior calculations are needed, as is the case with multiphase fluid flow compositional simulation in upstream petroleum engineering. Two discriminating functions act as classifiers in such a way that a positive value of one of the two functions determines the stability state of the mixture. The two functions are generated offline prior to the simulation, and their

expressions are straightforward so that they can be evaluated rapidly in a non-iterative way for every discretization block and at each timestep during the simulation. The CPU time required for phase stability calculations is dramatically reduced while still obtaining correct classification results corresponding to the global minimum of the system Gibbs energy function. The method can be applied to any chemical engineering problem where the class of several objects needs to be determined repeatedly and quickly (Van Zeggeren 1970).

The goal and objectives of this thesis are formulated below.

Goal:

Development of a set of tools and approaches to increase the predictive power of air-injection based enhanced oil recovery numerical modeling.

Objectives:

1. To provide an adaptation and history matching of ISC and HPAI performance laboratory experimental results for numerical modeling of air-injection based EOR for different types of reservoirs:

- to construct 3D digital models of oxidation experiments using thermal hydrodynamic simulator CMG STARS;
- to adapted the reaction and kinetic model to take into account kerogen oxidation behavior during HPAI in the organic-rich source rock;
- to provide an adapted reaction scheme and kinetic parameters, describing HPAI process for medium oil carbonate reservoir and ISC for bitumen.

2. To develop an alternative approach to calculating phase behavior in multicomponent multiphase hydrocarbon systems:

- to implement direct free-energy (Gibbs and Helmholtz energy) minimization technique for multiphase multicomponent hydrocarbon mixtures;
- to provide a validation of the implemented free-energy minimization algorithm on experimental data and iterative flash calculations.

Chapter 2. Methodology for air injection EOR processes numerical model construction based on a set of laboratory studies

The strategy of HPAI and ISC combustion numerical model construction used in this dissertation is presented in Figure 2.1 and consists of a selection of pseudo-components based on the phase and oxidation behavior of considered hydrocarbons, the development of a hydrodynamic model, which includes a reaction kinetic model, its validation against laboratory-scale representations of HPAI or ISC processes and incorporation of matched hydrodynamic model into a full-field one, providing the necessary upscaling. Each part is developed based on a comprehensive set of experimental studies.

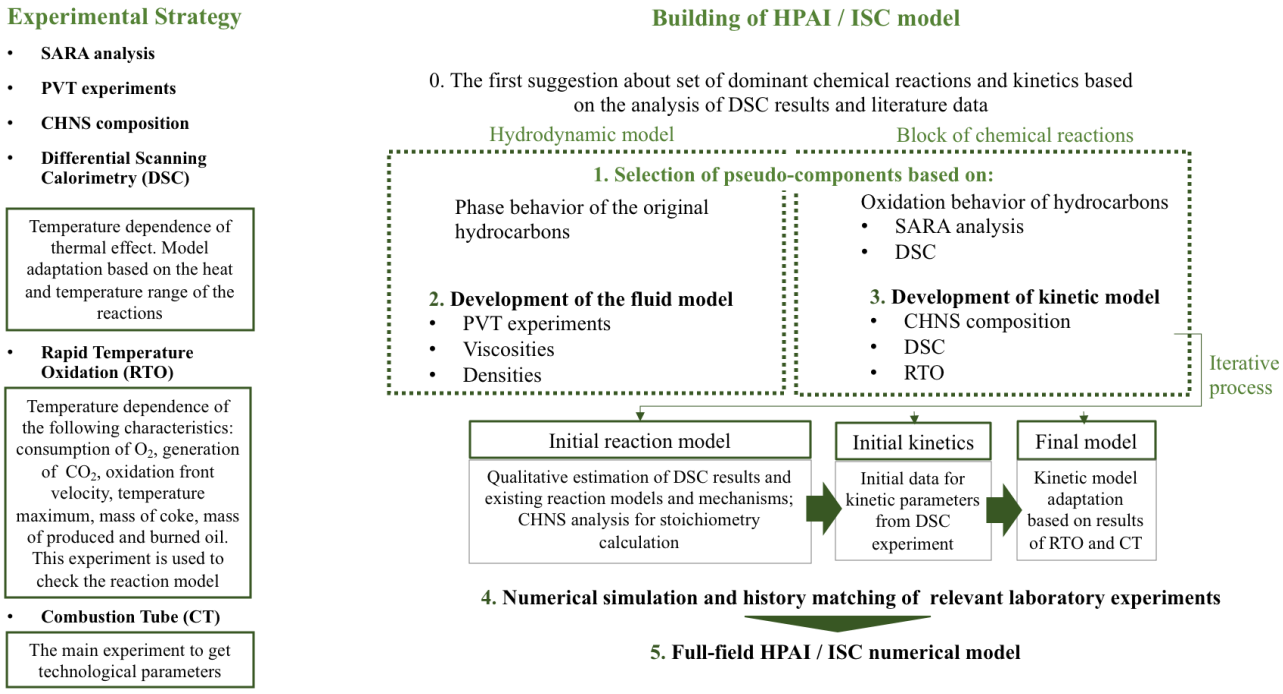

Figure 2.1 Key aspects of construction HPAI/ISC numerical models

In order to construct a hydrodynamic ISC or HAPI process that includes an adequate model of the oxidation/combustion reaction and its kinetics it is necessary to provide experiments and laboratory analyses in the following directions:

- composition and element analysis of target hydrocarbons to lump correct pseudo-components and provide correct quantification of further suggested reactions;

- static qualitative oxidation experiments to make the first suggestion about oxidation/combustion behavior and kinetics (differential scanning calorimetry);
- dynamic quantitative oxidation /combustion tests under conditions close to the reservoir supported with numerical studies to make a decision of reaction scheme and adjust kinetic parameters (ramped temperature oxidation test);
- dynamic quantitative combustion performance tests to evaluate physics and recovery performance, which could be observed in the field, and generate experimental data for history matching with numerical results (combustion tube test).

In this work, we suggest the necessity of the ramped temperature oxidation (RTO) test numerical simulations before the numerical modeling of combustion tube (CT) test:

- RTO test – history matching for reaction model adaptation and kinetic parameters adjustment;
- CT test – history matching for finalizing kinetic parameters, relative permeability curves, and specific PVT parameter of the system fluids adjustment.

2.1 Laboratory methods

2.1.1 Ramped temperature oxidation (RTO)

The RTO experiment is carried out on equipment consisting of a one-dimensional reactor that was filled with a mixture of crushed rock, oil, and water in predetermined proportions corresponding to real oil saturation. During the experiment, the air is injected into the reactor, and the temperature rises linearly along the entire length of the reactor with control over the temperature in the core holder. In experiments, the RTO reactor operates in differential mode until the moment the exothermic reaction starts in the first zone. A detailed description of the RTO system was presented by (Yang and Chen, 2016).

A schematic diagram of the RTO setup of the experiment on the oxidation of oil with a linear increase in temperature is given in Figure 2.2. The RTO Rector is a thin-walled reactor with an outer diameter of 25.4 mm, a wall thickness of 1.65 mm and a reactor length of 483 mm made of steel grade Inconel. The copper of the reactor is used to evenly distribute heat from the heaters along the entire length of the reactor, mounted on top of

the copper shell. The reactor is divided into seven intervals of 57 mm, the temperature in which is recorded by internal thermocouples inserted into the center of the bulk model.

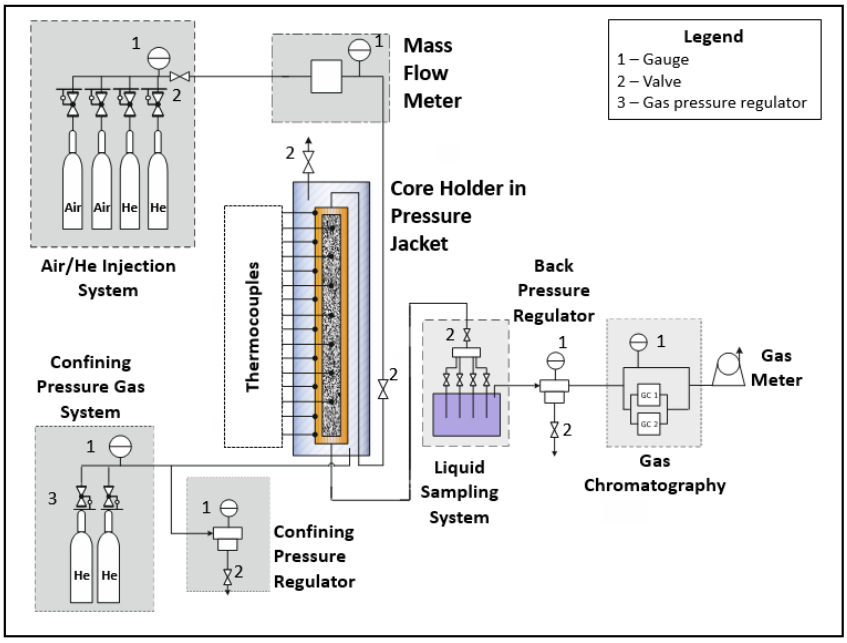

Figure 2.2 Schematic diagram of the RTO setup

The construction of the experimental setup makes it possible to conduct the experiment under field pressure and measure real-time temperature response, amount and composition of produced gases, fluids. Specifically, operating pressures up to 41MPa can be reached and maintained in the reactor. Gas chromatographs are directly connected to the outlet of the reactor, which makes it possible to analyze all produced gases, including hydrocarbon gases, without any limitations connected with the organic content in the bulk model (such limitations often exist on similar equipment due to the relatively low range determination of the content of carbon oxides in gas analyzers). The liquid fluids produced are taken into a sampling system equipped with four traps to analyze the composition and assign it the corresponding oxidation temperature range. The ability to control the temperature and heating rate within the range of 25-800°C allows to carry out experiments in an isothermal and non-isothermal mode with a minimum heating rate that simulates the actual heating rate during ISC. After the determination of the negative temperature gradient region (NTGR) during the experiment, the reactor is set to the desired heat, which will contribute

to the stability of the combustion front and effective mobilization of oil. In addition, the low heating rate allows evaluating the compositional data associated with oxygen addition reactions in LTR, while too rapid of a heating rate causes the minimization of its effect during the experiment.

2.1.2 Combustion tube test

This experiment is a combustion performance test and used for planning the air injection-based EOR in the field. The results obtained from the combustion tube (CT) test allow the displacement efficiency of the target EOR method under reservoir conditions to be estimated. It also gives a significant amount of data to validate HPAI or ISC numerical models, except the detailed kinetics of the undergoing reactions due to the constructional feature of the CT setup and experimental procedure. The combustion performance test is carried out on medium pressure combustion tube (MPCT) laboratory installation. A detailed description of the experimental setup is given in (Fadaei et al., 2011). The schematic diagram of the installation is shown in Figure 2.3. Technical characteristics are given in Table 2.1. The MPCT core holder is divided into 12 zones, each of which is equipped with a centerline thermocouple that measures the temperature in the center of the zone, an external heater, and a thermocouple mounted on the outer wall of the core holder. The length of each zone is 15 cm.

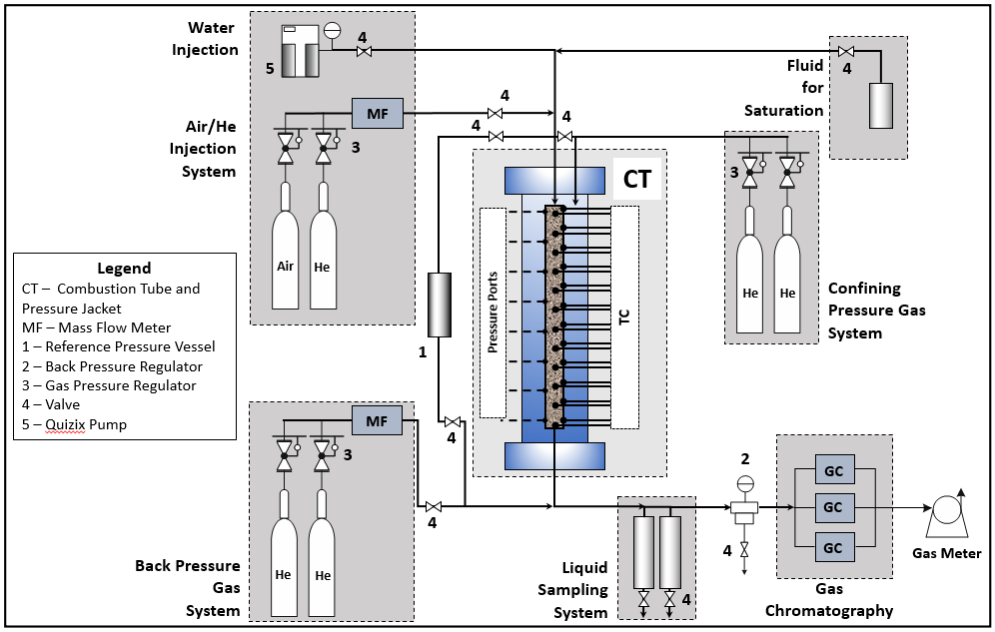

Figure 2.3 Schematic diagram of the CT setup

Table 2.1 CT specifications

Internal diameter x Length, mm	99.6 x 1837
Reactor volume, l	14.3
Reactor material	Inconel steel
Maximum pressure, MPa	21
Maximum operating temperature, °C	1200
A number of wall thermocouples, pcs.	12
A number of internal thermocouples, pcs.	12
The number of pressure ports in the reactor, pcs.	8

2.2 3D digital models of experimental setups

2.2.1 Ramped temperature oxidation numerical model

The 3D radial model of the RTO experimental setup was constructed (Figure 2.4) in the CMG STARS commercial simulator to provide validation of the suggested air-based EOR

process against the experimental results and to adjust mostly kinetic parameters in the oxidation reaction scheme used during history matching procedure.

The characteristics of the layers are specified considering the design of the experimental setup, which consists of a reactor, a steel wall, microfiber insulation, a copper part, and ceramic heaters (Table 2.2). The thermo-physical parameters were calibrated so that the actual temperature on the wall of the HPRTO coincided with the temperature of the corresponding layer in the numerical model. Figure 2.5 shows the grid sensitivity of the RTO numerical model, namely, temperature profiles in the first zone of the RTO digital setup during the simulation for a different number of grid blocks in vertical directions. The optimal number of grid blocks (49) in the vertical direction was specified based on grid sensitivity studies (Figure 2.5).

Table 2.2 Parameters of the RTO setup layers

Layer	**Porosity**	**Permeability, mD**	**Thermal heat capacity, 10^3 kJ/m^3/°C**	**Thermal conductivity, kJ/m/hr/°C**
Reactor	0.307	3000	2.09	27.67
Steel wall	0	0	3.59	39
Microfiber insulation	0	0	0.1086	0.452
Cooper	0	0	2.8	14.52
Ceramic heaters	0	0	4.95	738.072

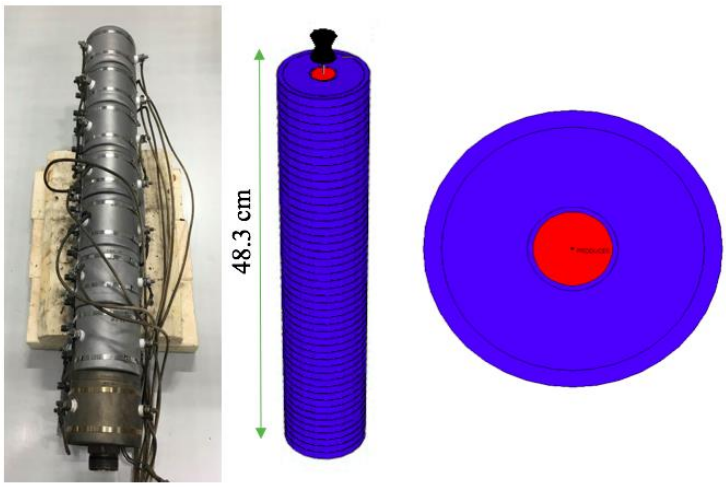

Figure 2.4 High-Pressure Ramped Temperature Oxidation installation (left) and the digital model of the RTO setup in CMG STARS (right)

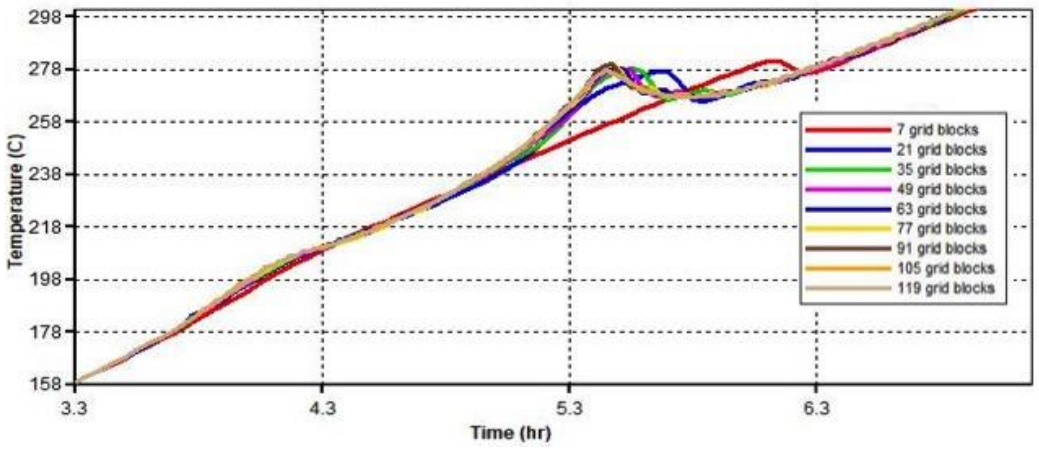

Figure 2.5 Demonstration of the grid sensitivity. The temperature profile in the first zone of the RTO digital setup during simulation

2.2.2 Combustion tube numerical model

The 3D radial model of the CT experimental setup was constructed (Figure 2.6) in the CMG STARS commercial simulator to provide further validation of a preliminary history matched hydrodynamic model with the results of the RTO experiment and to finalize kinetic parameters, relative permeability curves, and specific PVT parameters of suggested pseudo components.

A few key points that should be considered during the construction of a digital 3D model of CT equipment are:

• Conducting a preliminary analysis of the sensitivity of the model to the system parameters;

• Consideration of the multilayer design of the combustion tube;

• Accurate simulation of heater regimes;

• “History matching” of the stages preceding air injection: inert gas injection and heating of the first zone to initiate the source.

A 3D radial model of the MPCT experimental setup was built to adapt the model of chemical reactions and kinetics of oxidative processes. It consists of 11 grid blocks in the radial direction, one block in the azimuthal direction, and 45 blocks in the vertical direction (Figure 2.6). Each of the 12 temperature zones is divided into three cells, the size of which is sufficient to represent the combustion process in the tube.

Numerical simulation studies were reported in the literature (Fadaei et al., 2011), and it was determined that a full reconstruction of the geometry of the combustion tube installation allows not only for the correct reproduction of chemical transformations but also for such physical phenomena, as heat transfer and heat loss. In this regard, cells were added between the large steel flange filled with insulation (63 mm) and the flange covering the core holder (19 mm), and the corresponding cells at the end of the core holder. The distance from the steel flange at the end of the core holder to the steel casing is 1 cm. An additional cell of a much smaller size was added to the core sample model to avoid injection to the center of the first tube cell and incorrect displacement. The space around the core holder is filled with helium and pyrite, and it is filled with helium between the steel casing and pressure casing. It should be noted that the first and last zones of the core-holder are filled with sand, which is also reflected in the model.

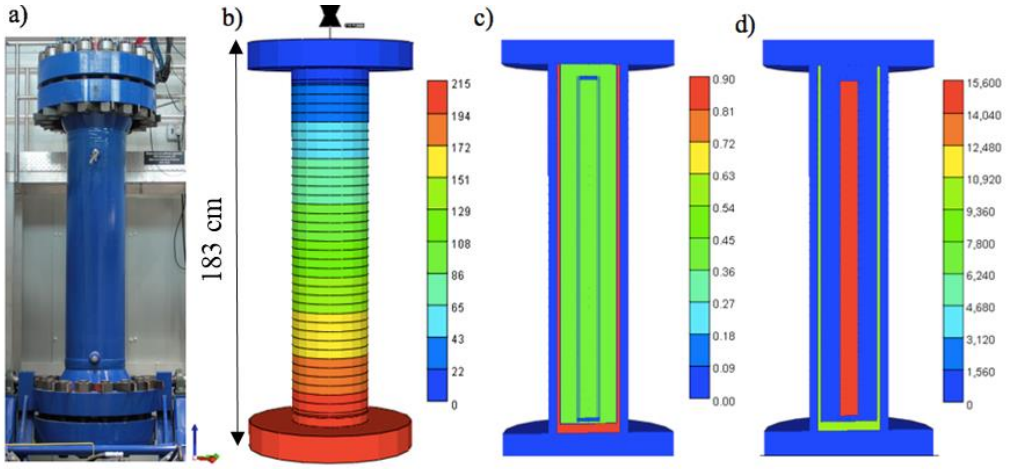

Figure 2.6 Medium Pressure Combustion Tube Installation (a) and the numerical model of the MPCT experiment in CMG STARS: model grid (b), initial porosity (c), initial permeability (d)

All layers of the combustion tube installation, including heaters, were reproduced in a numerical model of the experiment. The central cells represent the rock sample, then a steel tube wall, insulation, which consists of mineral wool, heating elements, insulation, consisting of pyrite and helium, a steel wall, an annular space filled with helium, and a pressure casing made of steel. The porosity and permeability characteristics of the layers and their sizes were set, taking into account the design of the experimental setup (Table 2.3).

Table 2.3 The porosity, permeability, and diameters of the CT layers

Layer	Diameter, mm	Material	Porosity, %	Permeability, mD
1.	100	Rock	40	15600
2.	102	Steel	0	0
3.	120	Mineral wool	45	100
4.	164	Steel	0	0
5.	254	Porous thermal insulation + He	45	1000
6.	260	He	99	10000
7.	406	Steel	0	0
8.	620	Steel flanges/air	100	0

The average porosity of core samples is 40 %, the insulation porosity is assumed to be 45%, sand zones are taken to be 35% since the porosity of these zones was not determined. It should be noted that the first and last (45) cells correspond to large steel flanges, 2 and 42 - inside the core holder are filled with He, 3, and 41 cells represent steel flanges that cover the core holder. The porosity of the annulus between the steel casing and the pressure shell is assumed to be equal to 99% in the model.

Permeability is reproduced similarly to porosity. The permeability of the annular space filled with helium is assumed to be 10,000 mD, the insulation region with pyrite and helium is 1000 mD, and for mineral wool, it is 100 mD. This data corresponds to the time before air injection, which was transferred to the numerical model.

The next important aspect of the model adaptation is the initialization of the model and reproduction of the injection conditions. It includes establishing the initial temperatures in the cells, accounting for the heat loss, the gradual increase of the pressure in the system by the preliminary pumping of helium into the system, initiation of combustion and maintaining the necessary temperatures in accordance with the work of heaters during the experiment, switching to helium and the gradual release of pressure in the system. This procedure is a key step before starting the model adaptation.

The 1.83 m long combustion tube consists of 12 heating zones each 15.24 cm long (see Figure 2.7) and heaters physically located on the heater support column at j =4. Each heating zone, as shown in the accompanying diagram on Figure 2.7, consists of:

1. A thermocouple inserted into the tube center (TC_{nn})
2. A thermocouple mounted on the exterior tube wall (TW_{nn})
3. A 1 kW wire-type heating element (HR_{nn}) wrapped around the heating zone.

The heater is not wrapped directly on the combustion tube. There is a 1.8 cm layer of mineral wool insulation wrapped around the tube and held in place by thin metal cladding. The heater is wrapped around the metal cladding. This heating arrangement diffuses the

heat input to the model and prevents hot-spots on the tube wall. The center and wall thermocouples are located at the axial midpoint of each heating zone which is reflected in the numerical model.

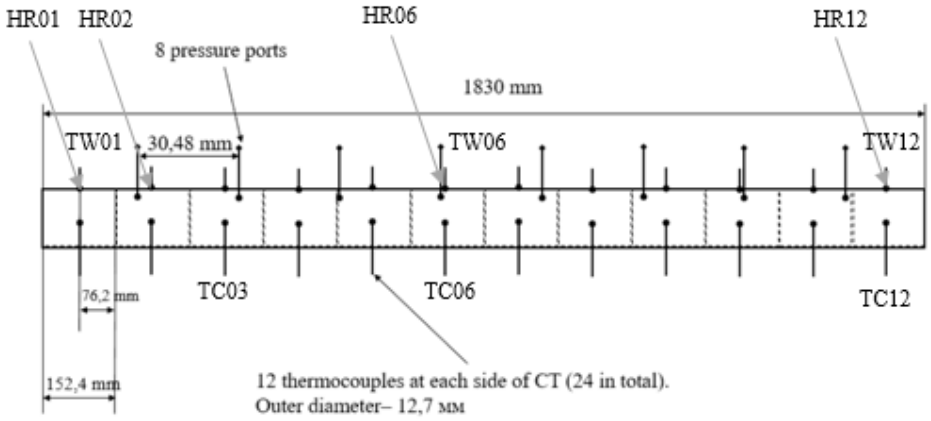

Figure 2.7 Schematic representation of the thermocouples and heaters installed in CT

Heat loss coefficients for surroundings are introduced along with the ambient temperature of each cell, including initial heater temperature set as 26ºC. The heaters distribute 1,000 W heat over three grid blocks per heaters, and they are set to adiabatic control, maintaining the temperature on the core holder wall 20 °C lower than the indicators of the central thermocouple. That allows the angle of inclination of the temperature profile during the cooling of the zone to be reproduced.

2.3 Conclusions to Chapter 2

In this chapter, we proposed a general methodology for modeling air-injection based EOR methods evaluation using the abilities of the commercial thermal simulator CMG STARS. This approach, including comprehensive experimental (Section 2.1) and numerical studies, made it possible to adapt reaction kinetic models for different types of reservoirs.

As a part of the above-mentioned methodological approach, 3D digital models of oxidation and ISC performance laboratory experiments were constructed using the thermal hydrodynamic simulator CMG STARS. (Section 2.2) Each of them has a multilayer design and proper heater regimes, which help to avoid constructional uncertainties during an adaptation of experimental results and validation of laboratory-scale numerical models. The presence of insulation layers in both experimental setups and annular space in CT influences radial heat transfers and can consequently control the temperature levels observed.

Chapter 3. Adaptation and history matching of ISC and HPAI performance laboratory experimental results for numerical modeling of air injection-based EOR for different types of reservoirs

3.1 Adaptation of ramped temperature oxidation test results on modeling of air injection enhanced oil recovery processes for bitumen reservoir

In order to investigate the oxidation behavior and ISC performance for bitumen, the RTO test was conducted using an oil sand bitumen sample from Samara oil region and was analyzed. 3D numerical simulations of this experiment were provided using the thermal hydrodynamic simulator CMG STARS to verify the reaction scheme for bitumen and predict experimentally observed oxidation temperature regions, adjust corresponding kinetic parameters and develop a laboratory-scale numerical model of the ISC process for the specific oil field.

Samara region oil sand bitumen belongs to the South Tatar oil and gas area of the Volga-Ural oil and gas province. The characteristics of the reservoir are summarized as the following: the depth of the formation - 150 -190 m, the total thickness of the reservoir and the oil-saturated part - 17.6 m and 10.2 m, respectively, the average porosity - 29 %, permeability - 736 mD, the average oil saturation - 94 %, which is quite favorable from an economic perspective. The bitumen has a gravity of 15.9 ^{o}API and oil viscosity, on average, of 9400 mPa.s at reservoir temperature. The current level of reservoir pressure is 0.72 MPa. The tendency for the burning zone to override is determined not only by vertical permeability, oil gravity, and pay thickness but also the prevailing reservoir pressure. The reservoir temperature of the studied reservoir is 8 ^{o}C, which is relatively low and affects the selection of the ignition method and the ability to establish down-hole combustion. Preliminary calculations of the combustion temperature predict high values due to high porosity and oil viscosity.

In this case, the RTO test was conducted using the experimental setup, whose specification and schedule were presented in Section 2.1. The reactor was vertically installed, and the air was injected from top to bottom. The working pressure in the reactor was 0.7 MPa created by air from a high-pressure cylinder, while helium was injected into the annular space between the pressure jacket and the reactor to create a confining pressure. The start of the pressurization and helium injection, air injection, preset temperature rise, and other operational events are given in Table 3.1. Experimental conditions were close to reservoir conditions for a specific oil field: pressure was 0.7 MPa, and operating parameters were the following: air injection rate of 40 st.m3/m2/hr, heating rate of 40°C/hr. Table 3.2 presents the initial properties of the oil sand bitumen used. During the experiment, the air was injected into the reactor, and the temperature rose linearly along the entire length of the reactor with the control over the temperature in the core holder. The heating schedule was preset. In the experiment, the RTO reactor operates in differential mode until the moment when the exothermic reaction started in the first zone. A detailed description of the RTO experimental setup was presented by (Burger, 1972; Fassihi et al., 1984; Moore et al., 1999).

Table 3.1 Schedule of RTO experiment for Samara region oil sand bitumen

Time	**Stage of the experiment**
0	Start of the air injection with a rate 15.34 st.l/h
0.19	Start of the temperature rise with a speed of 40°C/h.
6.65	Switch to trap 2 (280°C)
8.24	Switch to trap 3 (350°C)
10.71	Switch to trap 4 (450°C)
23.36	End of air injection; Start of He injection with a rate 15.34 st.l/h
27.93	End of He injection; the start of the pressure drop
28.47	End of the pressure drop

Table 3.2 Samara region oil sand bitumen properties

Property	Bitumen sample
Molecular weight, g/gmol	373
Density at 20°C, kg/m^3	956
Viscosity at 25°C, cp	1387
Asphaltenes, wt%	16.96
Carbon, wt%	66.9
Hydrogen, wt%	8.77
Nitrogen, wt%	0.26
Sulfur, wt%	3.85

3.1.1 Ramped temperature oxidation experimental results for bitumen

Exothermic and endothermic fronts traversing the core pack in the reactor during RTO test were detected by internal thermocouples. The resulting temperature profiles recorded by these thermocouples located on the corresponding seven zones of the reactor are shown in Figure 3.1. The transition of the exothermic fronts observed is associated with oxygen-addition and bond-scission reactions of bitumen accompanied by the oxygen uptake. The existence of endothermic peaks is due to the evaporation of water and volatile hydrocarbons. The start of the exothermic oxidation reaction in the first zone of the reactor is observed at around 180°C. Figure 3.1 shows the existence of two temperature regions, LTR (below 310°C) and HTR (above 370°C), which visually differ in the shapes of temperature peaks. The NTGR reflecting the transition between different oxidation regimes is visible in the range from 310°C to 370°C. It could be noticed that the temperature profiles for zones 1, 2 and 3 have two local maximums, which means that two different exothermic fronts traverse the core pack in the reactor during the experiment. For these three zones, the first temperature peaks are located in the range of 180°C to 310°C, which corresponds to LTR. The specific shape and magnitude of temperature peaks make

it possible to suggest that the rate of oxygen consumption is relatively slow. Thus, these exothermic fronts are likely a consequence of the dominance of oxygen-addition reactions in LTR. In addition, along with exothermic waves, endothermic fronts attributed to the water and hydrocarbon vaporization are to occur during the ISC process. In this particular experiment, a low initial water content results in a relatively low effect of water vaporization; therefore, the exothermic fronts are hardly detected by internal thermocouples.

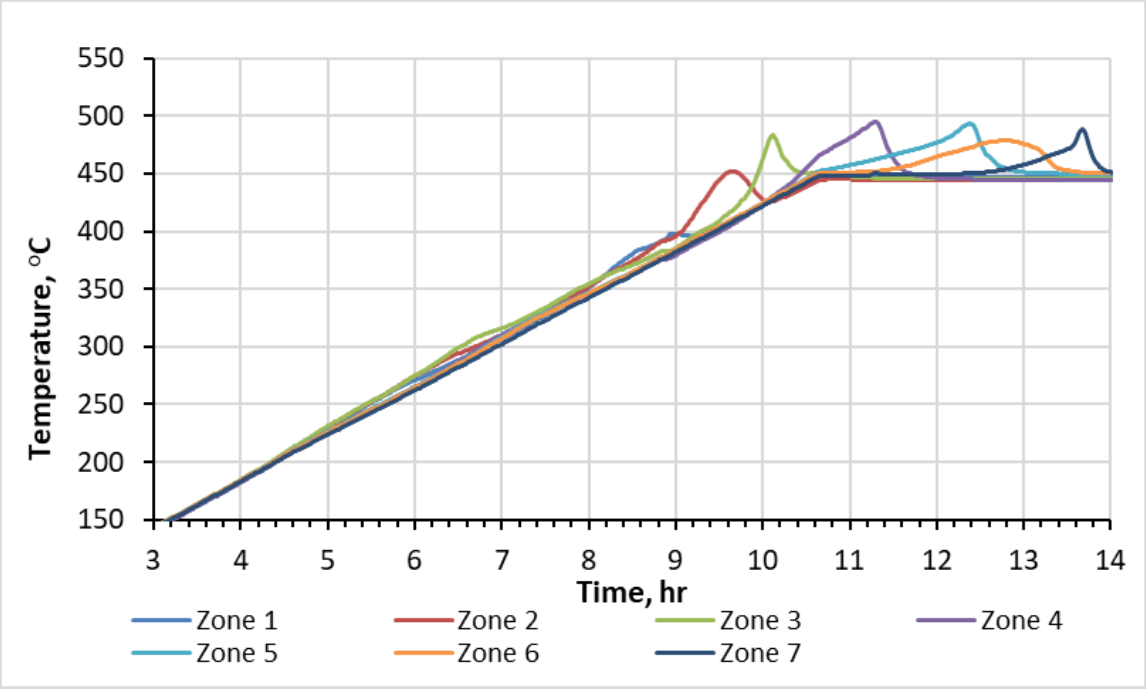

Figure 3.1 Zoomed in temperature profiles by zones in the RTO test for bitumen

The molar concentrations of oxygen, nitrogen, carbon monoxide, carbon dioxide and helium produced that were matched with the recorded temperature profiles in time are presented in Figure 3.2. An increase in the nitrogen molar fraction produced occurs after the start of exothermic reactions. The maximum value of the molar fraction of detected nitrogen is reached in LTR. In addition, Figure 3.2 shows the incomplete consumption of oxygen in LTR. This indicates the dominance of oxygen-addition reactions in this region where the air is consumed, and the generation of carbon dioxide and other combustion gases does not compensate for this consumption. The displayed location of the first

temperature peaks in zones 1, 2 and 3 show that the exothermic processes in the first three zones of the reactor occur in parallel. It could be a consequence of the partial consumption of oxygen in zone 1, which allows it to move through the core pack and simultaneously react in the first three zones of the tube. Intensive hydrocarbon gas generation is observed at around 370°C due to thermal cracking, followed by bond-scission reactions in HTR, which corresponds to the region with sharp and more well-defined temperature peaks. The maximum molar fraction value of carbon dioxide produced is reached at about the same temperature level. Figure 3.2 shows the restoration of the initial molar concentration of nitrogen at around the same temperature. All these observations indicate the start of the HTO process at around 370°C.

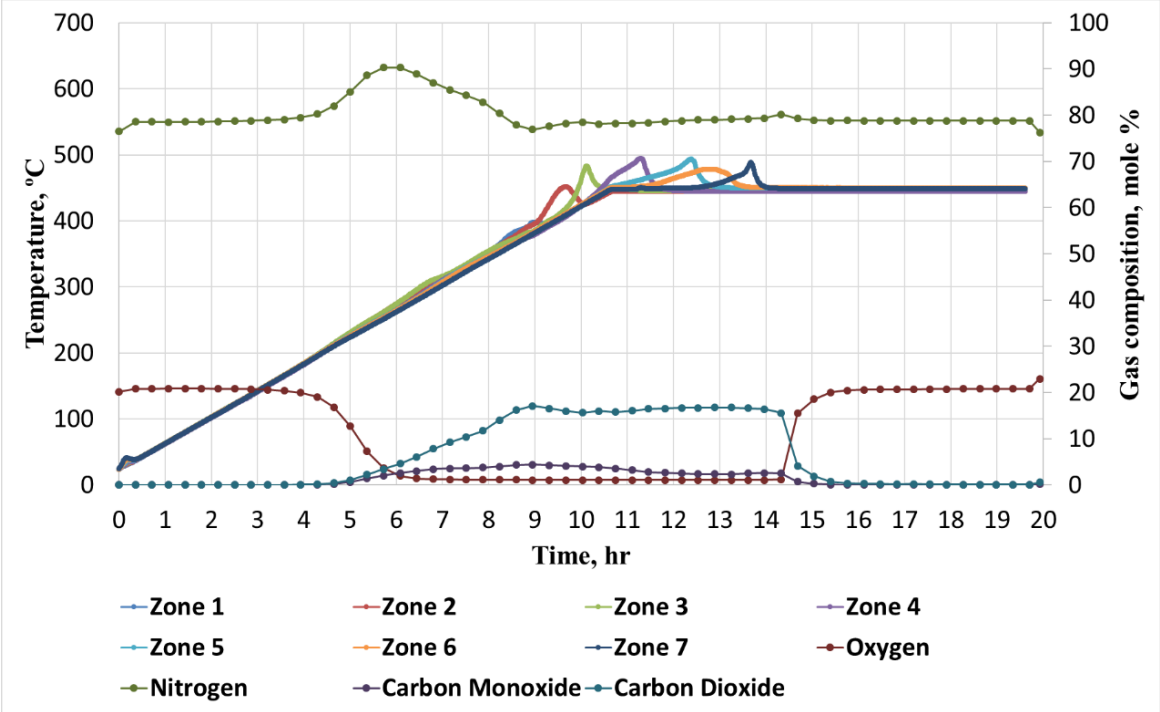

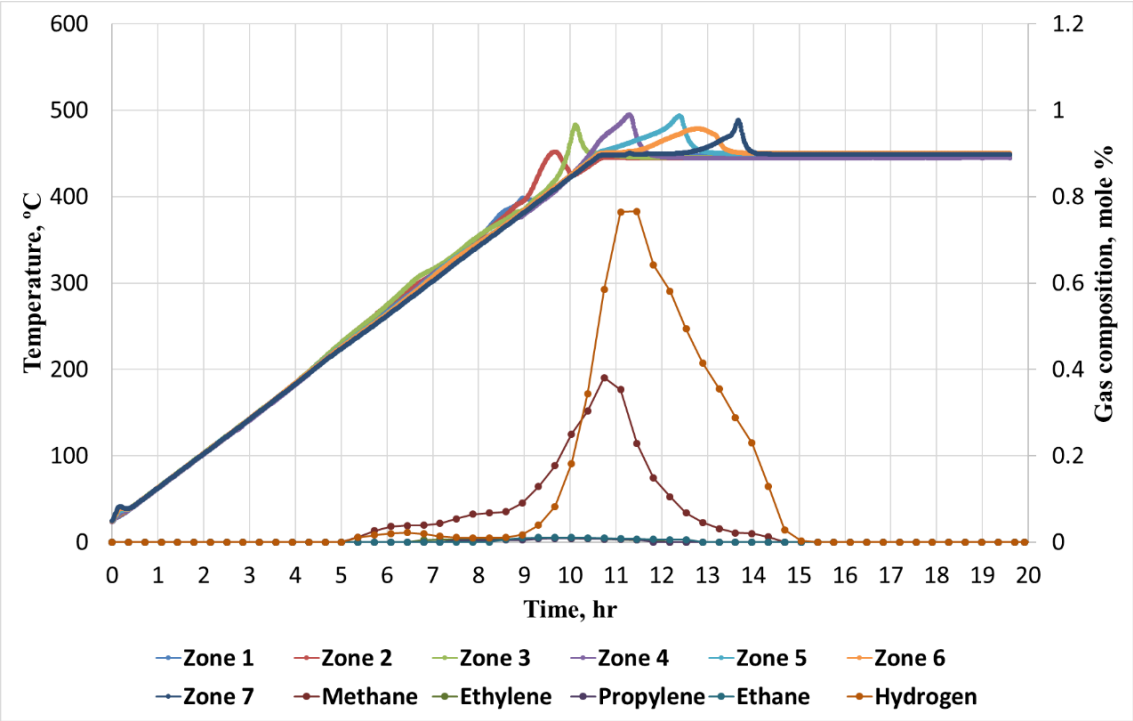

Figure 3.2 Temperature profiles by zones and mole concentrations of oxygen, nitrogen, helium, carbon monoxide, and carbon dioxide (above) and mole concentrations of ethylene, methane, propylene, ethane, hydrogen in RTO test for bitumen

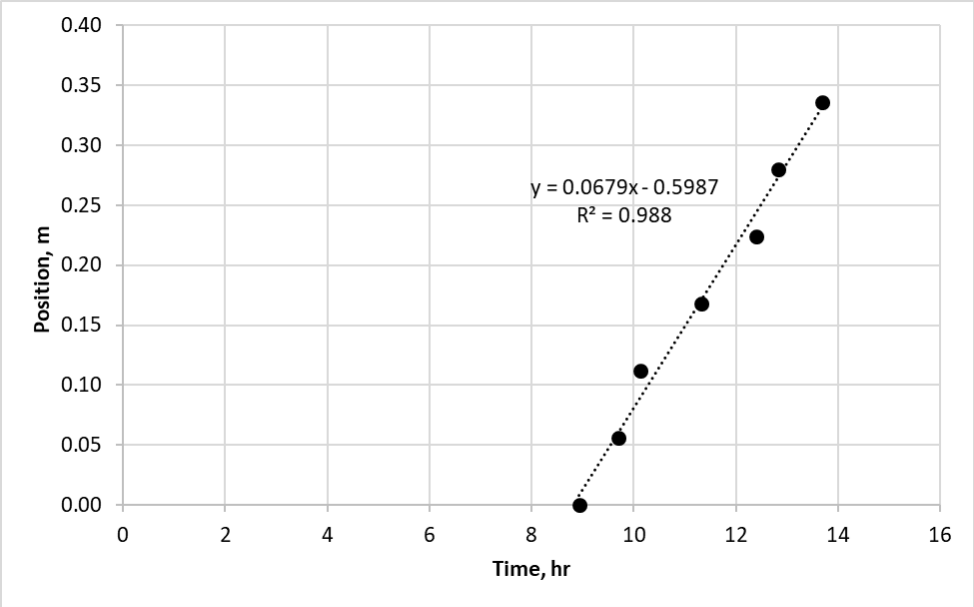

Figure 3.3 Combustion front propagation in HTR through zones 4-7 in RTO test for bitumen

3.1.2 Numerical simulation of the RTO test for bitumen

In order to simulate the RTO reactor, the thermal hydrodynamic simulator CMG STARS was used. Numerical simulation of the RTO experiment was performed using the radial model with 49 grid blocks in the flow path and four grid blocks in radial directions (Figure 3.4). The number of grid blocks was chosen based on the grid size sensitivity analysis to achieve a stable model (Section 2.2.1). The radial blocks repeat layers of an experimental setup such as a reactor, steel wall, insulation, and heaters. 3D design of the RTO reactor and characteristics of the layers are presented in Section 2.2.1.

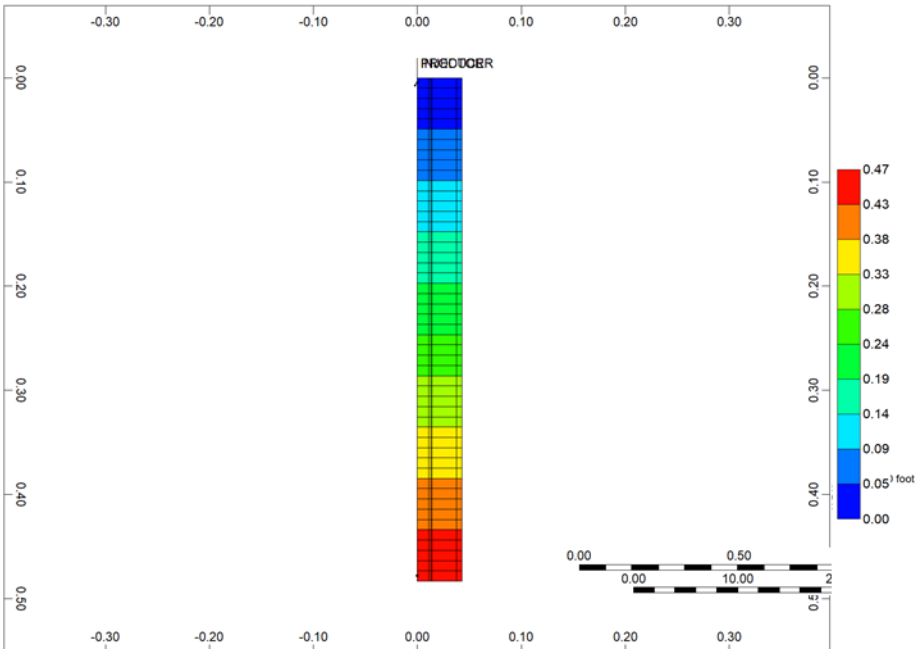

Figure 3.4 Numerical model of RTO test setup for bitumen

Conditions to initialize the model are summarized in Table 3.3 and include bitumen temperature dependences of density and viscosity. This data was used as reference conditions for matching in test simulations. The determination of the temperature-dependent viscosities of the oil pseudo components was based on the mixing rule in the form:

$$\mu_{oil} = \prod_{i=1}^{N_c} \mu_i^{x_i}$$

Where N_c is the number of oil pseudo components; x_i is the mole fraction of the i^{th} pseudo component in the oil phase; μ_{oil} and μ_i are the viscosity of the whole oil and i^{th} oil pseudo component, cp, respectively. The measured viscosity-temperature data was extrapolated based on Walther's correlation:

$$\log_{10}(\log_{10}(\mu_{oil} + 0.7)) = A - B\log_{10}(T),$$

where μ_{oil} is the viscosity of the whole oil or known pseudo component viscosity, cp; and T is the absolute temperature, K. The widely used Andrade's equation given by

$$\mu_{oil} = Ae^{\frac{B}{T}},$$

where μ_{oil} is the viscosity of the whole oil or known pseudo component viscosity, cp; and T – absolute temperature, K, was avoided since the resulting viscosities after extrapolation to combustion temperatures were unrealistically low.

Table 3.3 Conditions to initialize RTO numerical model for bitumen

Pressure, MPa	0.7
Temperature, °C	25
Porosity, %	48
Initial mole fraction of Maltenes, wt%	0.942
Rock thermal capacity, kJ/m^3/K	2100
Rock thermal conductivity, W/m/K	1.71
Viscosity at different temperatures	
Viscosity at 25°C, cp	1387
Viscosity at 40°C, cp	342.2
Viscosity at 50°C, cp	159.7
Density at different temperatures	
Density at 20°C, kg/m^3	956
Density at 40°C, kg/m^3	941
Density at 60°C, kg/m^3	927

In order to represent the oxygen consumption, carbon dioxide, water, and heat generation as a result of bitumen oxidation and compositional changes during RTO test, a traditional reaction kinetic model (Belgrave et al., 1993) is used as a basis, which is specified for Athabasca Bitumen. This model includes the LTO of maltenes and asphaltenes (Adegbesan et al., 1987), thermal cracking of asphaltenes, and the HTO of coke (Thomas et al., 1983). The model presented in this work includes modifications to take into account the effect of vapor-phase combustion reaction of volatile oil fractions. The significance of the vapor-phase combustion during the ISC process is suggested and studied by Mallory et al., 2018 and Bhattacharya et al., 2016. In this particular model, a bond-scission vapor-combustion reaction of Light oil pseudo-component is incorporated. Light oil fraction appears in the model as a result of thermal cracking and LTO of Maltenes and Asphaltenes and has high volatility. The starting kinetic parameters and flammable limits for this reaction, which are necessary to control the transfer of vaporized components to gas phase, are taken from Bhattacharya et al., 2016.

The reaction model used in this research is summarized as follows:

Thermal Cracking:

1) 1.0 Asp = 0.66383 Maltenes + 12.40909 CO_2 + 17.264822 Coke +0.515094 Light Oil,

first order;

Low temperature oxidation:

2) *1.0 Maltenes + 2.77594 O_2 = 0.38185 Asphaltenes + 0.004 Light Oil*,

first order with respect to hydrocarbon mass fraction, 0.4246 orders with respect to oxygen partial pressure;

3) *1.0 Asphaltenes + 7.5075 O_2 = 106.37116 Coke + 0.01327Light Oil*,

first order with respect to hydrocarbon mass fraction, 4.7627 orders with respect to oxygen partial pressure;

High-temperature oxidation:

4) *1.0 Coke + 1.1245 O_2 =1.0 CO_2 + 0.249 H_2O,*

first order with respect to both reactants, where the H/C ratio is 0.498

5) *1.0 Light Oil + 20.347 O_2 =13.269 CO_2 + 15.51 H_2O,*

first order with respect to both reactants.

Hence, to incorporate this reaction scheme into the numerical model, target oil is characterized by using three pseudo components: Maltenes, Asphaltenes, and Coke. In addition, the fluid model includes Light oil pseudo-component to reproduce the vapor phase combustion reaction. The fluid model description includes PVT properties of components in a mixture, k-value correlations, summarized in Table 3.4 - Table 3.5.

Table 3.4 Data for model components for bitumen sample

Component	**Molar Mass, g/mol**	**Tcrit, °C**	**P crit, kPa**
CH_4	16	-82.55	4600.15
Light Oil	212	433.85	1520
Maltenes	329	612	1480
Asphaltenes	1092	1399.23	162.48
O_2	32	-118.55	5045.99
N_2	28	-146.95	3394.39
CO_2	44	31.05	7376.46
Water	18	374	22100
Coke	12.498	-	-

Table 3.5 Gas-liquid k-value correlations for bitumen pseudo-components

Component	KV1	KV4	KV5
CH4	$5.45*10^5$	-879.84	-265.99
Light Oil	$2.43*10^6$	-1600.00	-283.55
Maltenes	$1.32*10^8$	-8600.00	-273.15
Asphaltenes	0	-11987.70	-273.15
CO2	$8.62*10^8$	-3103.39	-247.09

Table 3.6 lists the initial physical model conditions at the time when enriched oxygen injection started. These parameters are calculated based on the mass balance data and molar mass of oil and its fractions.

Table 3.6 Initial conditions for bitumen model pseudo-components

Property	Value
Oil saturation	0.423
Water saturation	0.013
Gas saturation	0.564
Mole fraction of Maltenes	0.942
Mole fraction of Asphaltenes	0.058

The simulated molar concentrations of produced oxygen, nitrogen, carbon dioxide in time, and temperature profiles associated with each zones of the reactor are presented in Figure 3.5. To illustrate the mechanism of bitumen oxidation underlying the model, it is advised to consider the processes occurring in the first zone of the reactor during simulation of RTO test. Figure 3.6 shows the distribution of modeled pseudo components in time in zone 1 of the reactor and how its' changes correspond to the temperature changes in the same part of the reactor. The oxidation of Maltenes occurs in the LTR resulting in the first local temperature maximum shown in Figure 3.6. This is the representation of the first

exothermic wave traversing through the core pack associated with LTO. Light oil pseudo component appears in the system as a result of LTO and thermal cracking. The second heat release in HTR, or the second exothermic front moving through the reactor, results from HTO of Coke and vapor-combustion of Light oil pseudo component.

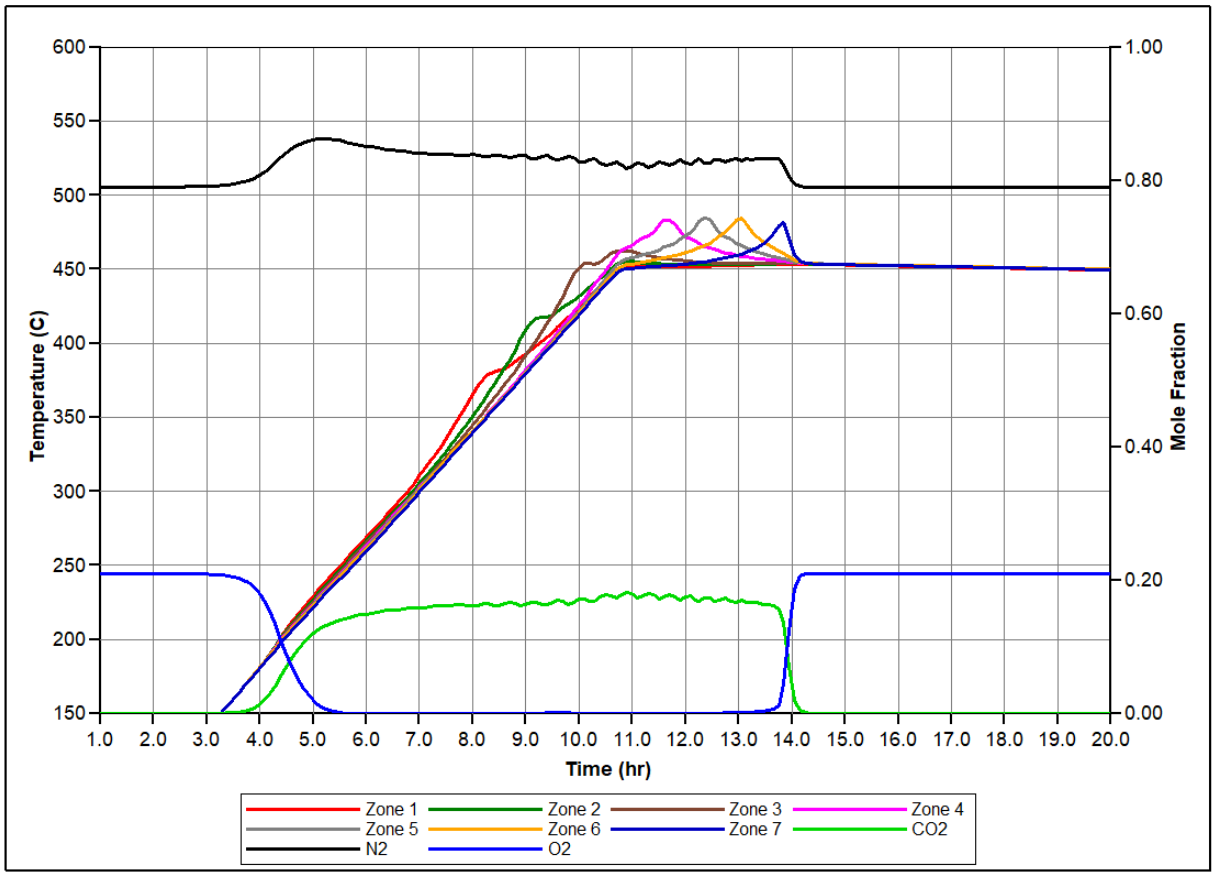

Figure 3.5 Numerical simulation results for RTO experiments for bitumen: temperature profiles by zones and molar concentration of nitrogen, carbon dioxide, and oxygen

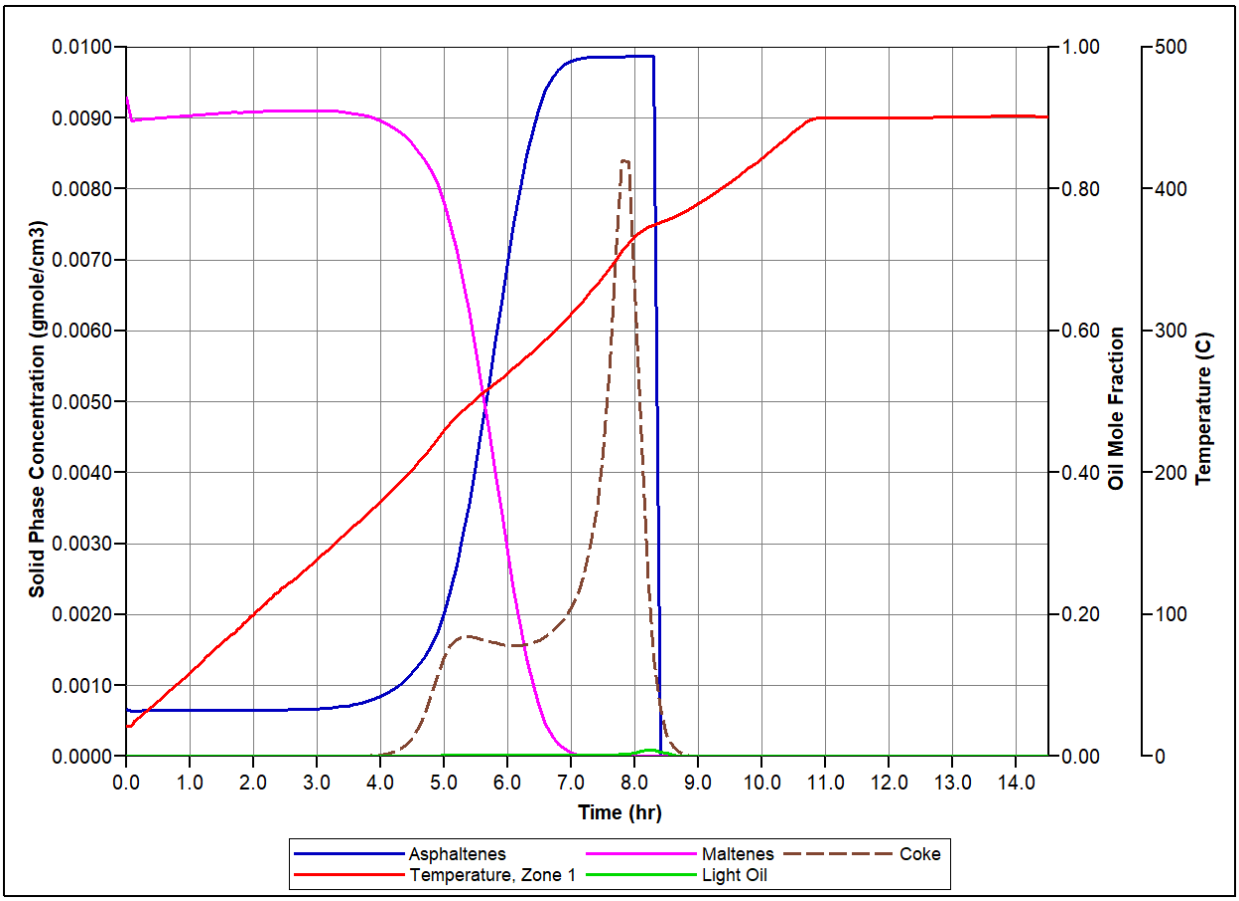

Figure 3.6 Numerical simulation results at Zone 1 of the reactor for RTO test for bitumen: temperature profile, molar fraction of Maltenes, Asphaltenes, Light Oil and solid-phase concentration of Coke

The goal of the history matching procedure is to match oil, water, nitrogen, oxygen, and combustion gases production masses and replicate the experimentally observed temperature regions of heat release peaks during the experiment, especially the temperature which corresponds to the initiation of oxidation processes. These functions are assumed to be the objective functions for which the error in experimental and simulated values is minimizing during the history matching procedure. The construction of the experimental setup makes it possible to decrease the number of parameters that could significantly influence the changes in the characteristics mentioned above. If the fluid and chemical reaction model is specified, the number of variables can be ideally reduced to the kinetic parameters. In this work, the frequency factor, activation energies, and heat of reactions

were manually adjusted. The obtained Arrhenius kinetic parameters are summarized in Table 3.7.

Table 3.7 Kinetic parameters obtained from history matching the RTO experiment for bitumen

Reaction	A	E_a, kJ/mol	H_r, kJ/mol
1	$2.10*10^{12}$ hr^{-1}	181.041	0
2	$1.05*10^{8}$ hr^{-1} $kPa^{-0.4246}$	86.730	$5.474*10^{3}$
3	$1.21*10^{8}$ hr^{-1} $kPa^{-4.7627}$	185.600	$5.564*10^{3}$
4	$1.02*10^{2}$ hr^{-1} kPa^{-1}	34.763	$5.537*10^{2}$
5	$1.00*10^{2}$ hr^{-1} kPa^{-1}	100.0	$5.230*10^{2}$

Figure 3.7 presents the simulated temperature profiles in zones 1, 5, 6 and 7 as a result of the history matching procedure with reference to the experimental temperature profiles recorded by thermocouples located on the corresponding zones of the reactor. The simulation shows good correspondence with experimental results and captures the exothermic behavior observed in LTR and HTR. One of the objective functions in the history matching procedure is the temperature at which the first exothermic front starts. The simulation repeats two different exothermic fronts are traversing the core pack in the reactor, which is demonstrated in Figure 3.7 (a) by occurrence of two local maxima of the temperature profile in the first zone. Figure 3.8 shows the simulated and experimentally measured molar concentrations of produced oxygen, nitrogen, and carbon dioxide. The model repeats the increase in the molar concentration of nitrogen in LTR, the maximum and minimum concentration values of the considered gases. The incomplete consumption at the beginning of the oxidation process is captured but not for the whole temperature region (LTR and NTGR), as is observed in the experiment. In addition, discrepancies in the NTGR modeled are detected. The simulation captures the fact of NTGR appearance or stopping of the oxidation processes between LTR and HTR (Figure 3.5). However, modeled exothermic behavior does not align with the experimental results in the region close to the upper temperature limit of the NTGR. The mechanism undergoing the NTGR existence is assumed to be connected with the vaporization of volatile oil fractions for

further combustion (Mallory et al., 2018), which should be taken into account when developing the model. This emphasizes the need to further investigate the basic oxidation reaction model in common with a phase behavior description for multicomponent hydrocarbon systems.

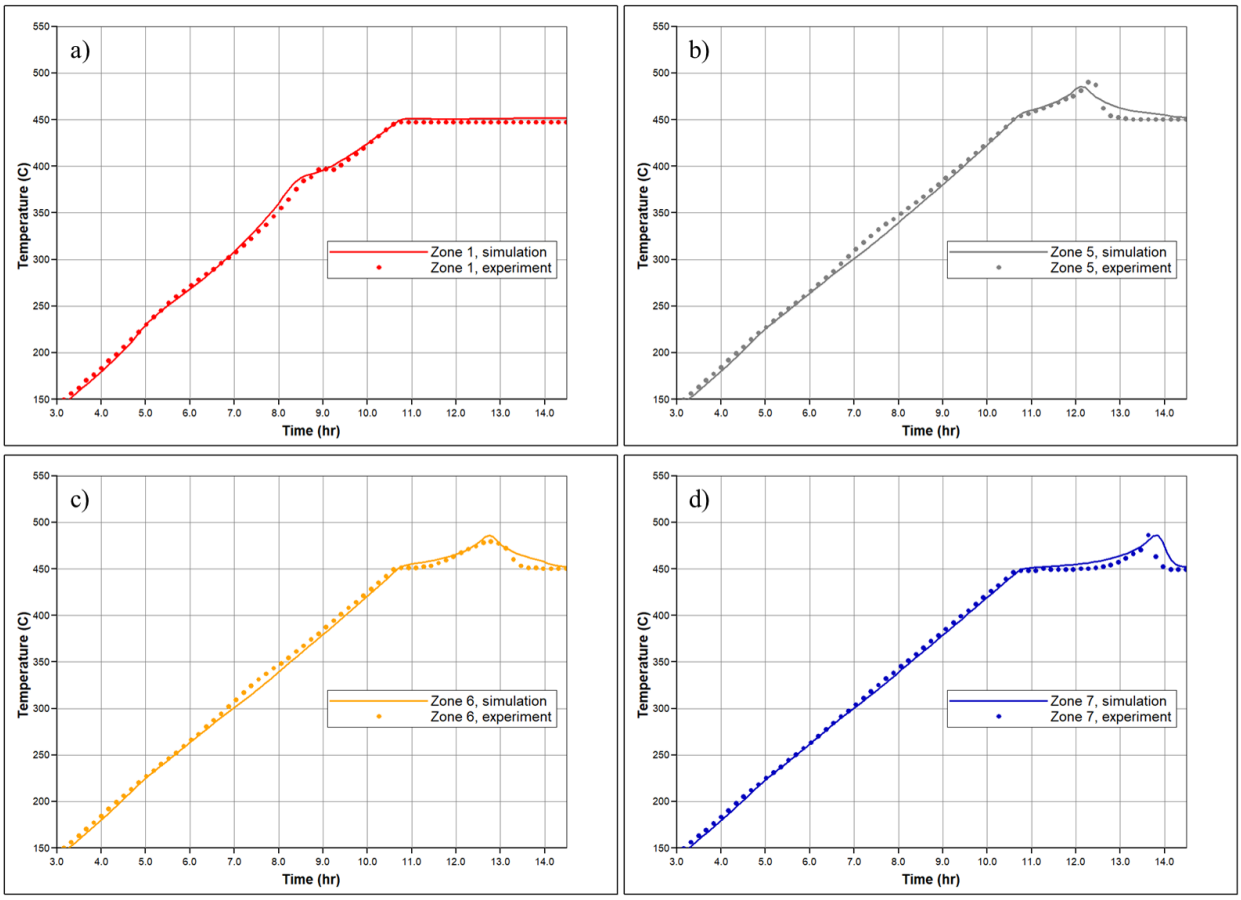

Figure 3.7 Comparison of numerical and experimental results of RTO test for bitumen: temperature profiles for a) Zone 1; b) Zone 5; c) Zone 6 and d) Zones 7 of the reactor

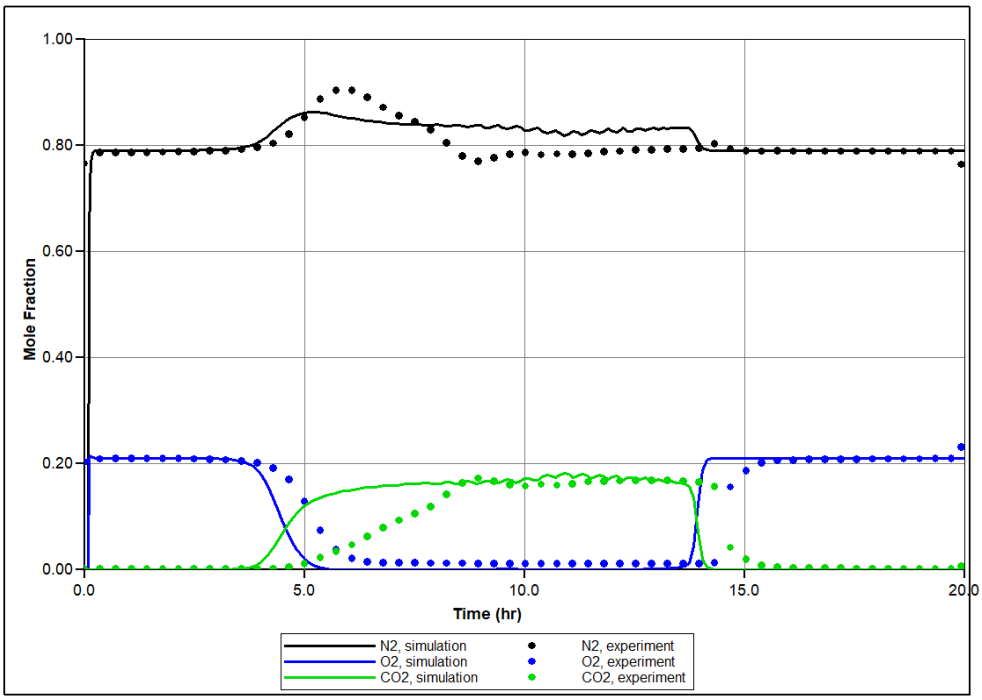

Figure 3.8 Comparison of the results for experiment and simulation of RTO test for bitumen: mole fraction of Nitrogen, Oxygen and Carbon Dioxide

Table 3.8 presents the values of cumulative oil, water, and CO_2 obtained during the experiment and simulation. The maximum discrepancy in experimental and simulated data does not exceed 16%. The predicted value of produced oil shows an oil recovery factor of 0.35, while the experimentally obtained value equals 0.33.

Table 3.8 Mass of products for experiment and simulation of RTO test for bitumen

	Experiment	**Simulation**
Mass of obtained oil, g	11.26	11.71
Mass of CO_2, g	18.7	21.83
Mass of obtained water, g	12.38	11.97

3.2 High-pressure air injection laboratory-scale numerical models of oxidation experiments for carbonate oil field

The studied field belongs to the North Kinelsky oil and gas region of the South Tatar oil and gas area of the Volga-Ural oil and gas province. All identified oil deposits are confined to the roofing of the Tournaisian stage. The average depth of the formation, according to borehole data, is 1339 m. At depths below 1000 m, the fracture gradient tends to be 15.83 kPa/m, which limits downhole injection pressure to 21.4 MPa. The total thickness of the reservoir varies from 2.4 to 16.5 m. The thickness of the oil-saturated part is 1.2-13.8 m. The average porosity is in the range of 11-12 %, and permeability is in the range of 55 to 95 mD. The average oil saturation is 75 %, which is quite favorable from an economic perspective. The crude oil has a gravity of 33.2 ^{o}API and dead oil viscosity, on average, of 13 mPa.s. The current levels of reservoir pressure are in the range of 4.5-11 MPa, depending on the location. The tendency for the burning zone to override is determined not only by vertical permeability, oil gravity, and pay thickness but also by the prevailing reservoir pressure. The reservoir pressure of the studied reservoir is 27 ^{o}C, which is relatively low. This might affect the selection of the ignition method and the ability to establish down-hole combustion. Rock permeability impacts the air injectivity, areal and vertical sweep, and maximum pattern size that can be accommodated. According to experimental data lowering the porosity results in a lower fuel load. Low porosities result in relatively low quantities of oil burned per unit bulk volume of reservoir rock, which directly impacts combustion temperature. Preliminary calculations of the combustion temperature predict low values due to low porosity, relatively high oil viscosity, and low reservoir temperature. Generally, feasible conditions can be achieved assuming high oxygen utilization combustion, and they are subject of further investigations.

To investigate oxidation behavior and high-pressure air injection (HPAI) performance for a carbonate oil field, two sets of oxidation tests were carried out, namely: high pressure ramped temperature oxidation (HPRTO) and medium pressure combustion tube (MPCT). Both experiments were conducted using experimental setups, whose specification and schedule were presented in Section 2.1. The RTO reactor was vertically installed in a

pressure jacket, and the air was injected from top to bottom. Experimental conditions were close to reservoir conditions for a specific oil field: pressure was 12 MPa, created by air from a high-pressure cylinder, while helium was injected into the annular space between the pressure jacket and the reactor to create a confining pressure. Operating parameters were the following: air injection rate of 40 st.m3/m2/hr, heating rate of 40°C/hr. The start of the pressurization, air injection, temperature rise, and other process events are given in Table 3.9.

Table 3.9 Schedule of RTO experiment for carbonate oil field

Time	**Stage of the experiment**
0	Start of the air injection with a rate 15.34 st.l/h
0.15	Start of the temperature rise with a speed of 40°C/h.
7.44	Switch to trap 2 (325°C)
11.01	Switch to trap 3 (450°C)
20.44	End of air injection; Start of He injection with a rate 15.34 st.l/h; Switch to trap 4
29.34	Start of He injection; the start of the pressure drop
31.23	End of the pressure drop

The working pressure in the CT reactor was 12 MPa (Section 3.2); the initial temperature was 27 ºC. The start of the pressurization, air injection, temperature rise, and other process events are given in Table 3.10.

Table 3.10 Schedule of CT experiment for carbonate oil field

Time, h	Event
0	Start of the pressure rise in the system
3.48	Start of the He injection
3.77	Start of the first zones heating
5.18	Start of the air injection with a rate 314 st.l/h
5.36	Beginning of the combustion in Zone 1
13.58	Combustion front propagation in Zone 10, switch to He injection
18.48	End of He injection, the start of the pressure drop
23.98	End of the pressure drop, end of the experiment

3.2.1 High pressure ramped temperature oxidation experimental results for carbonate oil field

The temperature profiles recorded by axial thermocouples located on the corresponding 7 zones of RTO setup (Figure 2.2) are shown in Figure 3.9. The NTGR is visible in the range from 290°C to 350°C. As the figure shows, there is a distinct LTR (160°C – 290°C), in which LTO reactions dominate, and a HTR (350°C – 400°C), in which HTO reactions dominate (sharp temperature profiles). The start of the exothermic oxidation reaction in the first zone of the reactor begins at 160°C. It should be noted that the thermocouple in section 6 at high heating rates (exothermic reaction) showed an incorrect value (the height of the peak should have been higher), which was demonstrated by testing it after the experiment.

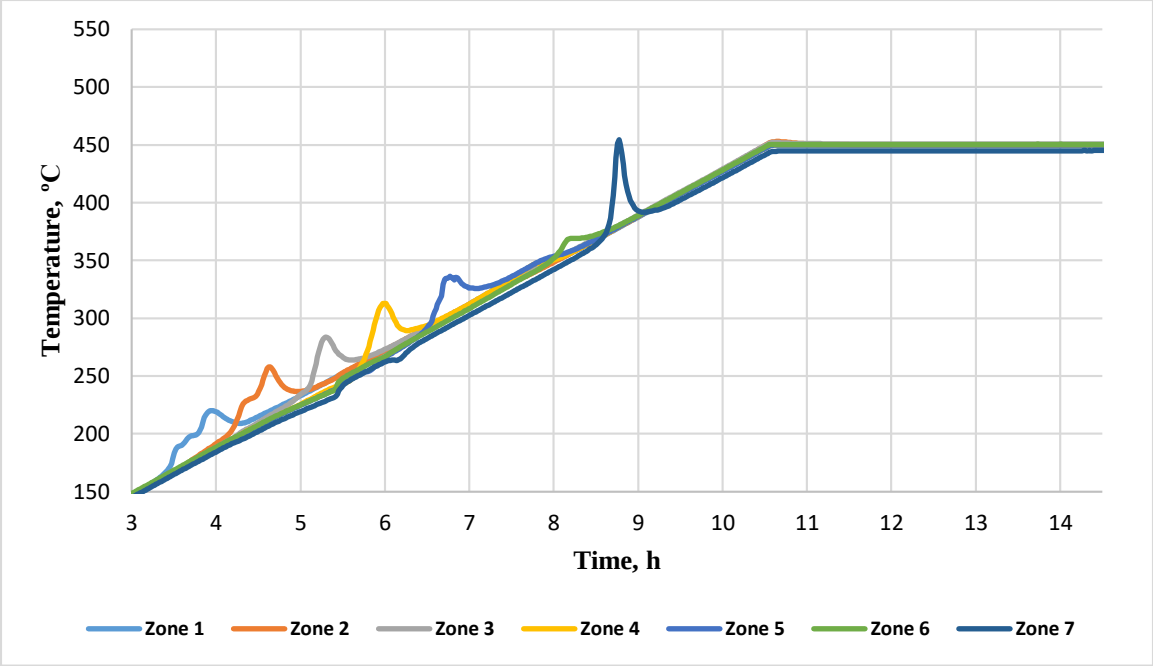

Figure 3.9 Zoomed in temperature profiles by zones in RTO test for carbonate oil field

The exothermic wave in the LTR is registered for the first five zones of the reactor. The magnitude of the first temperature peak for Zone 1 (or for Zone 2-5) is compatible with the magnitude of the first temperature peak for Zone 7 (in the HTR). Thus, the oxygen consumption in these five zones in the LTR is not as slow as was observed for bitumen (Figure 3.1). It could be concluded that along with oxygen addition reactions, bond-scission reactions proceed in the LTR. In Figure 3.10, it could be seen that temperature profiles for the first five zones have two exothermic peaks. In this case, the second temperature peak located in the HTR is poorly resolved but still exists, which means that two different exothermic fronts traverse the core pack in the reactor during the experiment. In addition, the endothermic front is detected during the experiment, which results in temperature uptakes in Figure 3.9. This process is attributed to the water and hydrocarbons vaporization during HPAI.

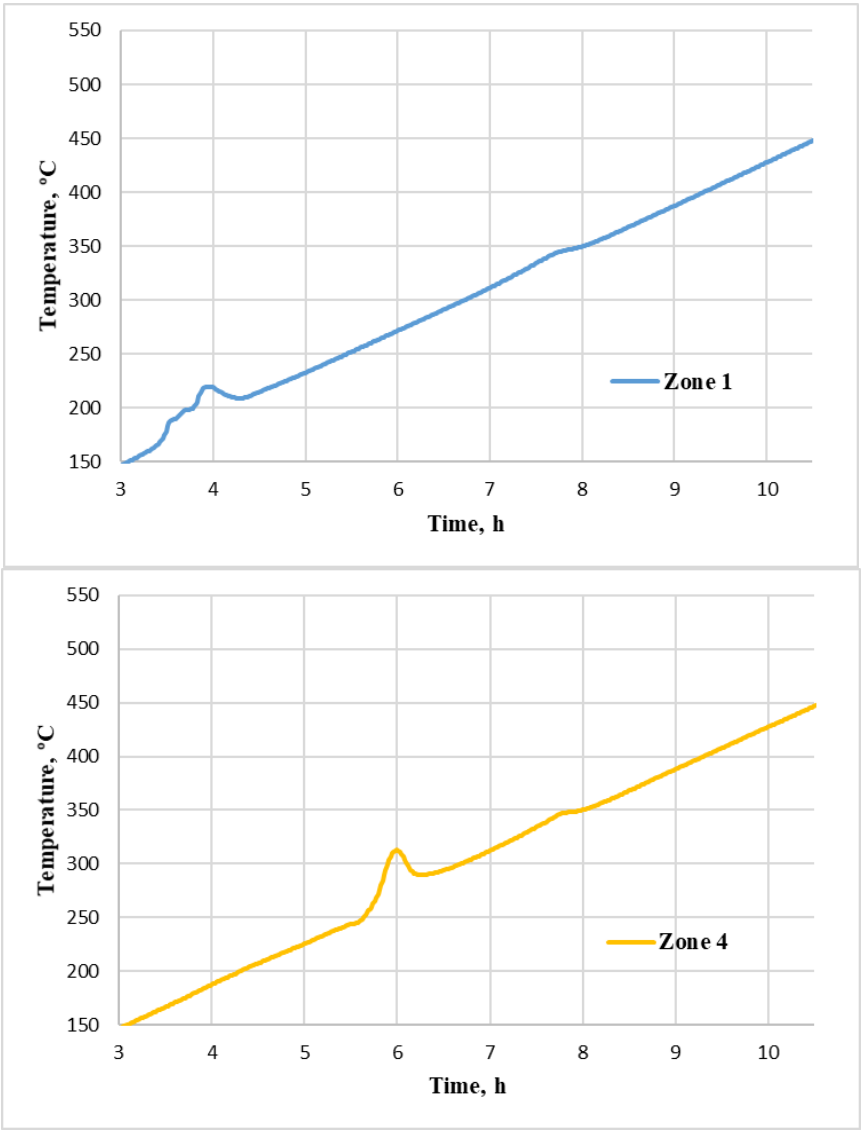

Figure 3.10 Zoomed in temperature profiles for Zone 1 (above) and Zone 4 (below) in RTO test for carbonate oil field

The molar concentrations of oxygen, nitrogen, helium, carbon monoxide, and carbon dioxide are presented in Figure 3.11. The start of hydrocarbon gas generation begins at about 300°C due to oil cracking, followed by HTO, and displayed sharp temperature peaks, which may indicate the burning of the formed hydrocarbon gases. The proportion of methane in the exhaust gases is higher than all other hydrocarbon gases. An increase in the nitrogen concentration at the production end of the reactor occurs after the start of exothermic reactions. This indicates the occurrence of LTO reactions where the air is not

completely consumed, and the generation of combustion gases does not compensate for this consumption. According to the nitrogen concentration curve, the low-temperature and high-temperature oxidation reactions proceed simultaneously along the length of the reactor from the beginning to the end of the oxidation. The decrease in the nitrogen concentration at the outlet corresponds to the start of the HTO, which indicates a reduction in the proportion of LTO reactions or, in other words, oxygen-addition reactions.

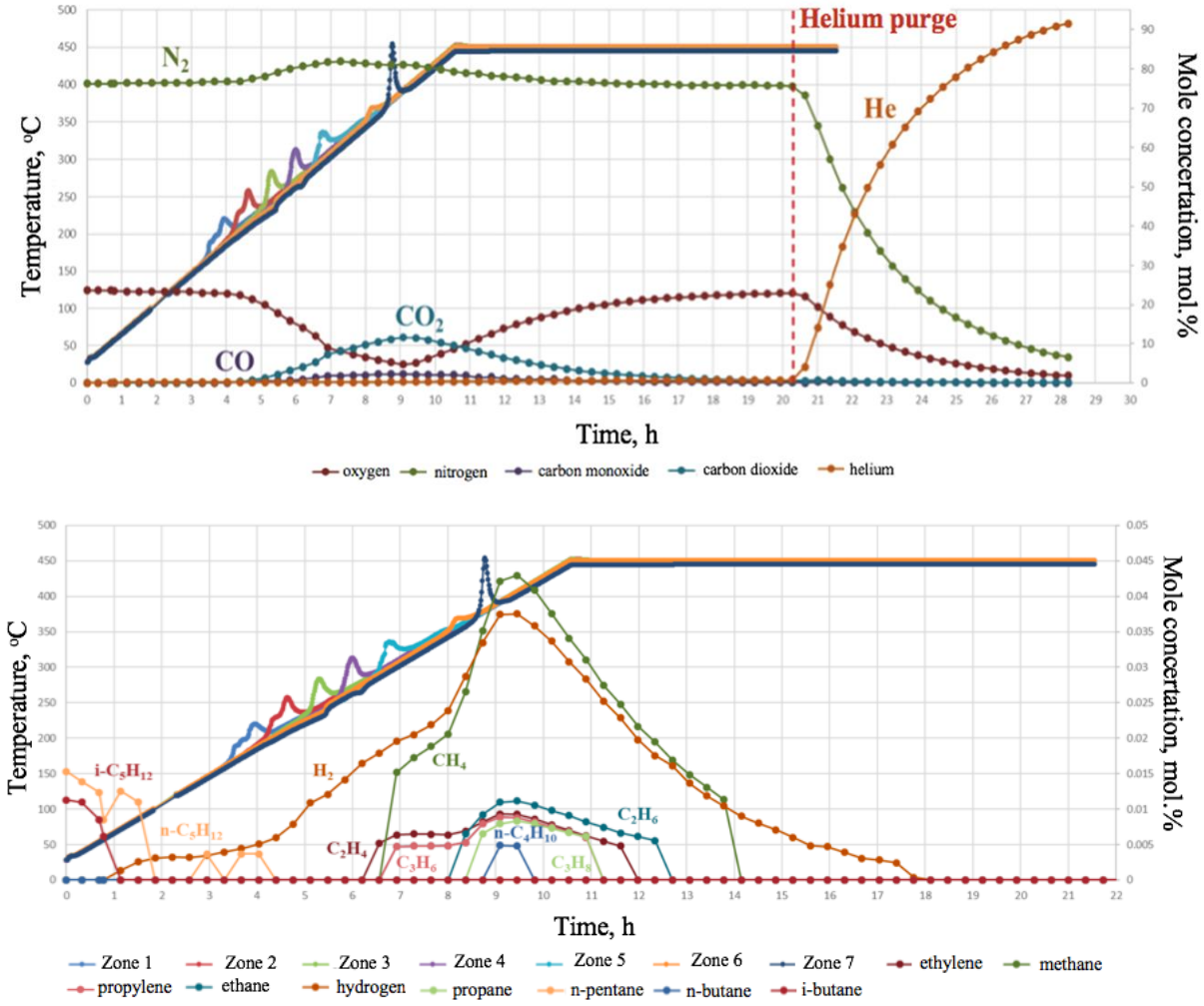

Figure 3.11 Temperature profiles by zones and mole concentrations of oxygen, nitrogen, helium, carbon monoxide and carbon dioxide (above) and mole concentrations of ethylene, methane, propylene, ethane, hydrogen, propane, n-pentane, n-butane, i-butane (below) for carbonate oil field

3.2.2 Medium pressure combustion tube experimental results for carbonate oil field

The temperature values for centerline thermocouples (left) and thermocouples located on the core holder wall (right) for 12 zones (Figure 2.7) are shown in Figure 3.12. The maximum temperatures achieved as a result of combustion reactions for each of the zones are presented in Figure 3.13 (above). The maximum temperature of Zone 1 was 526°C. The first 2-4 zones are usually transition zones. By the time the air supply stopped, the combustion front did not reach the 11^{th} and 12^{th} zones. In Zones 11 and 12, the temperatures were 435°C and 278°C, respectively, which indicates that residual combustion occurred in these zones. There was still oxygen remaining in the model after air was pumped (Figure 3.13 (below)). When helium injection began, the heaters were not turned off. This allowed the combustion process to continue due to the use of air, which remained in the model. According to Figure 3.12, the temperatures of the 8th and 9th zones reached a maximum of around 450°C, and the temperature of zone 12 began to rise. With the pressure that was created in the experiment, the amount of oxygen (air) remaining in the system at the time of the transition to helium injection was sufficient for residual combustion to occur in the later zones. This process is visible in Figure 3.12 in the period between 8 and 15 hours from the start of air injection.

After the temperature in the center of the zone reached its maximum, the heater of this zone was set to adiabatic control mode, maintaining the temperature on the core holder wall 20 ° C lower than the readings of the axial thermocouple. This is the reason for the change in the slope of the temperature profile during the cooling zone.

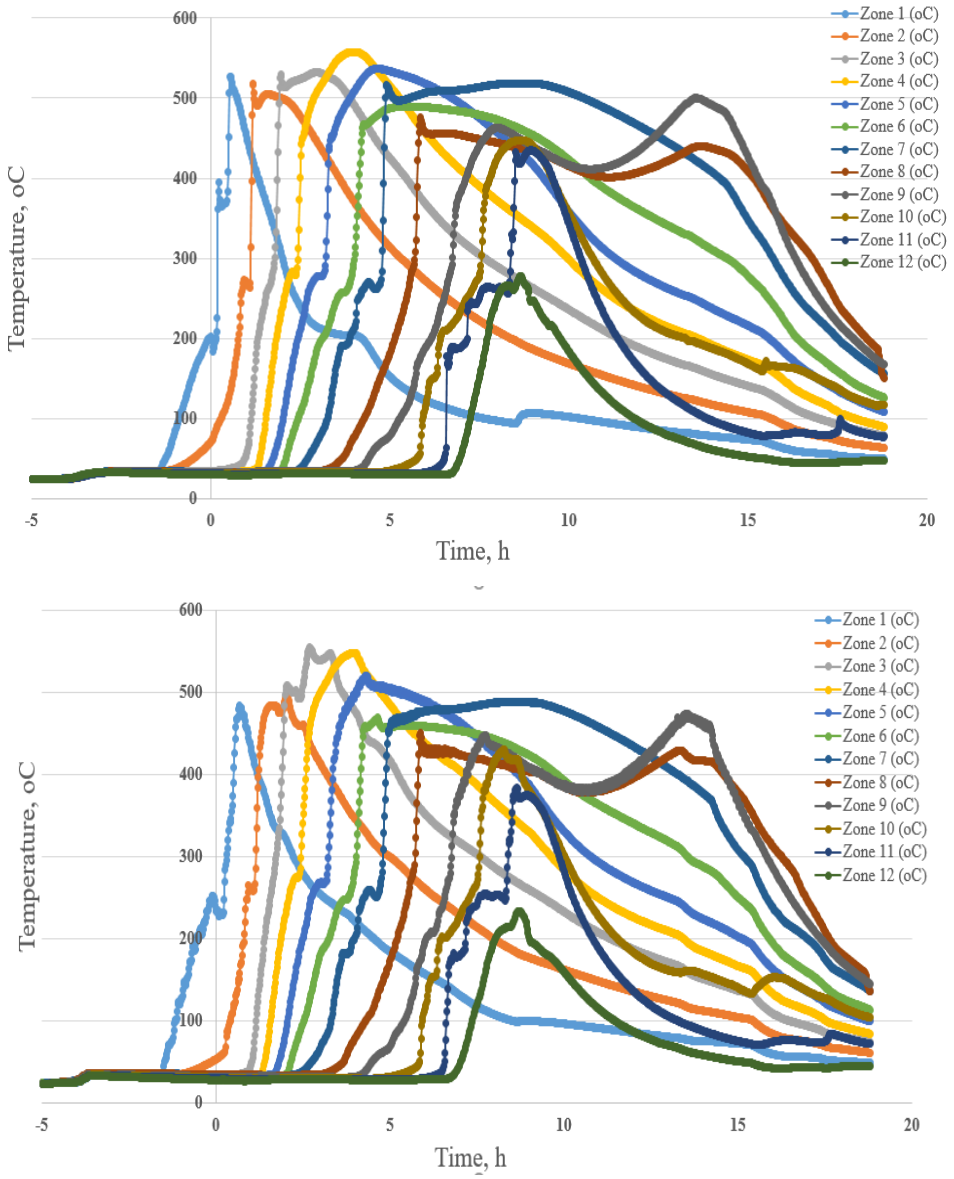

Figure 3.12 Temperature profiles on the centerline (above) and wall-mounted (below) thermocouples by zones for carbonate oil field

The velocities for the combustion front were calculated based on the rate of achievement in the zones of the bulk model with a temperature of 350°C (a horizontal dotted line in Figure 3.13 (above)). Figure 3.13 (below) shows the progress through the combustion tube of the high-temperature combustion front (at a temperature of 350°C). The front velocity was calculated from these data. The combustion front velocity with a temperature of 350°C through Zones 3-10 was 18.1 cm / h. The first two zones were not taken into account since

the front velocity had not yet stabilized, and there was a delay in the propagation of the front from Zone 1 to Zone 2 due to the so-called “Plugs” of mobilized oil.

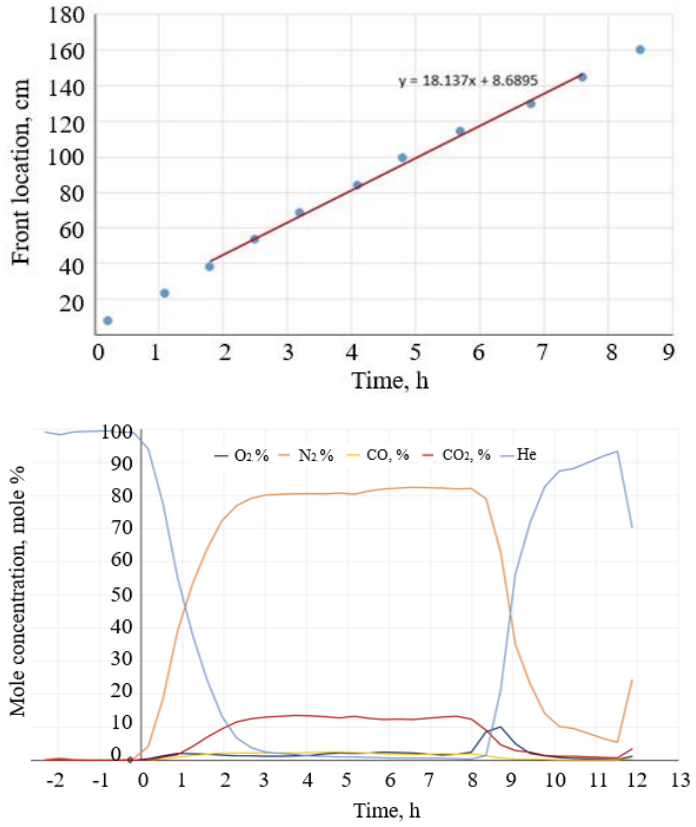

Figure 3.13 Combustion front propagation (above) gas mole concentrations (below) for carbonate oil field

Figure 3.13 (below) shows the molar concentration of oxygen, nitrogen, helium, carbon monoxide, and carbon dioxide. An increase in the yield of propane, n-butane and other hydrocarbon gases occurs at the time of initiation of combustion which corresponds to the zone of low-temperature oxidation. Another explanation of this effect is that at the initial stage of the combustion front, it does not capture the entire zone, but only some part of it. Accordingly, hydrocarbon gases are removed from these uncovered parts of the zone by the high-temperature oxidation process. The increase in nitrogen concentration at the reactor output occurs after the start of the combustion process. According to the composition change in Figure 3.13 (above) in the interval from 2.5 to 8 hours, the

stabilization of the component composition of gases leaving the MPCT is observed, which corresponds to the steady-state combustion mode.

3.2.3 Fluid and kinetic model for carbonate oil field

There have been several reaction combustion schemes published in the literature (Belgrave *et al.*, 1993; Sarathi et al., 1999; Barzin et al., 2010; Yang et al., 2016). All of these schemes are similar in terms of reaction types in that they have low-temperature oxidation, thermal cracking, and high-temperature oxidation contributions. However, the schemes differ due to their definitions of pseudo-components. In this research, the following reaction scheme by (Belgrave et al., 1993) is chosen. The initial kinetic parameters are taken from Belgrave et al., 1993.

Table 3.11 Traditional reaction scheme

Traditional reaction scheme
Thermal Cracking:
1) 1.0 Asp = CH_4 + 1.2631343 Maltenes + 8.686364 CO_2 + 4.496471 H_2S + 17.474796 Coke
Low temperature oxidation:
2) *1.0 Maltenes + 2.26125 O_2 = 0.311685 Asphaltenes,* first order with respect to hydrocarbon mass fraction, 0.4246 orders with respect to oxygen partial pressure 3) *1.0 Asphaltenes + 7.5075 O_2 = 106.59626 Coke*, first order with respect to hydrocarbon mass fraction, 4.7627 orders with respect to oxygen partial pressure
High-temperature oxidation:
4) *1.0 Coke + 1.1245 O_2 =1.0 CO_2 + 0.249 H_2O,* first order with respect to both reactants, where the H/C ratio - 0.498

Based on this reaction scheme, target oil was characterized by using three pseudo components: maltenes, asphaltenes, and coke. The description of the fluid model includes PVT properties of components in a mixture, k-value correlations, summarized in Table 3.12 and Table 3.13.

Table 3.12 Data for Model Components for carbonate oil sample

Component	Molar Mass, g/mol	Tcrit, °C	P crit, kPa
CH_4	16	-82.55	4600.15
Maltenes	268	714.44	709.64
Asphaltenes	1092	1399.23	162.48
O_2	32	-118.55	5045.99
N_2	28	-146.95	3394.39
CO_2	44	31.05	7376.46
Water	18	374	22100
Coke	12.498	-	-

Table 3.13 Gas-liquid k-value correlations for carbonate oil pseudo-components

Component	KV1	KV4	KV5
CH4	$5.45*10^5$	-879.84	-265.99
Maltenes	$1.32*10^8$	-8600.00	-273.15
Asphaltenes	0	-11987.70	-273.15
CO2	$8.62*10^8$	-3103.39	-247.09

Table 3.14 lists the initial physical model conditions at the time when enriched oxygen injection started. These parameters are calculated based on the mass balance data and molar mass of oil and its fractions.

Table 3.14 Conditions to initialize RTO numerical model for carbonate oil field sample

Property	Value
Oil saturation	0.739
Water saturation	0.111
Gas saturation	0.150
Mole fraction of Maltenes	0.995
Mole fraction of Asphaltenes	0.005

In order to verify the model, the preliminary simulations of the RTO test were provided using the thermal simulator CMG STARS. The results, which were able to be obtained by varying initially suggested kinetic parameters in the traditional reaction model (Table 3.11), are presented in Figure 3.14. The model captures the temperature of oxidation process initiation, the temperature region of the oxidation, and endothermic behavior, but it does not repeat the NTGR and other features of the exothermic behavior observed. The model prepared can be used to simulate the HPAI process in the target oil field, and looking ahead, shows satisfying correspondence with experimental results obtained during the combustion performance test (see Section 3.2.5). In this work, additional investigations were provided to improve the predictive power of the model. For these purposes, the pressurized differential scanning calorimetry (PDSC) test was conducted for the original oil and its fractions under 10 MPa and different heating rates (5°C/min, 10°C/min, 15°C/min).

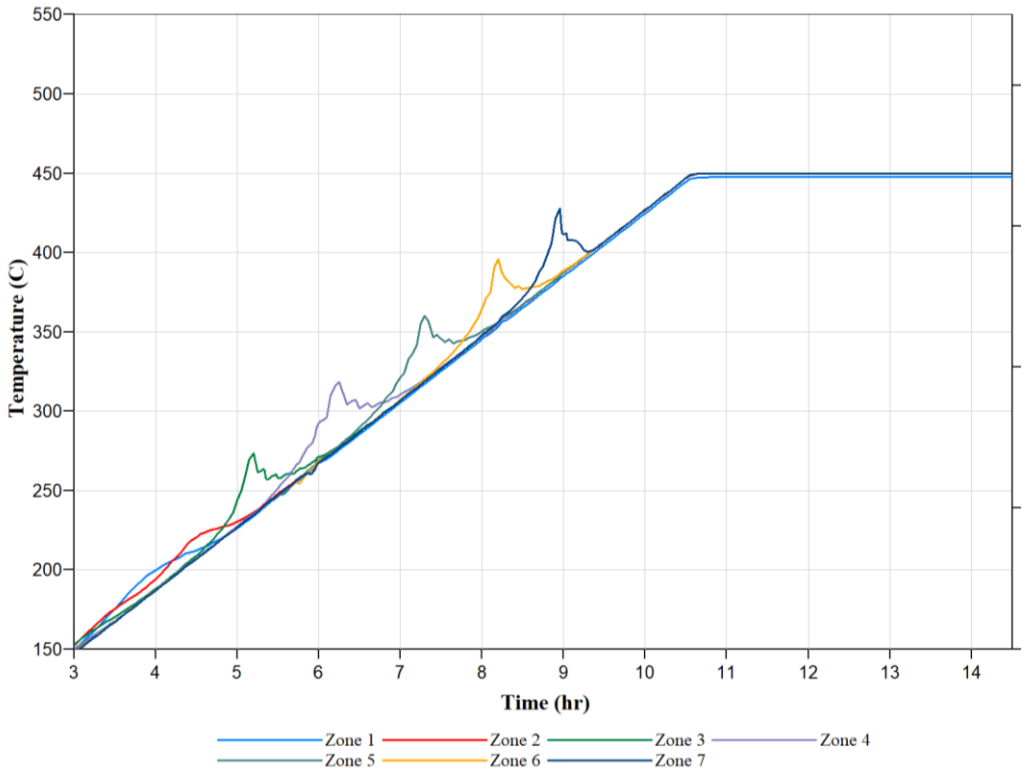

Figure 3.14 Zoomed in simulated temperature profiles for the traditional reaction model for carbonate oil field

The results of PDSC tests are presented in Figure 3.15 - Figure 3.16. The shape of the registered heat flow for the original oil sample (Figure 3.15) in the LTR repeats the form of the exothermic peaks in LTR detected during the HPRTO experiment (Figure 3.9), along with the location of NTGR and HTR. In order to identify the impact of each pseudo component (Maltenes and Asphaltenes) considered in the oxidation processes, the PDSC test was provided for maltenes and asphaltenes fractions produced from the original oil sample (Figure 3.17, Figure 3.16). It could be concluded that the reason for the first exothermic wave in the HPRTO experiment is mostly the oxidation of a maltenes fraction, including not only oxygen-addition but also a bond-scission process. Thus, the bond-scission reaction of a maltenes fraction in the original oil should be taken into account in the model.

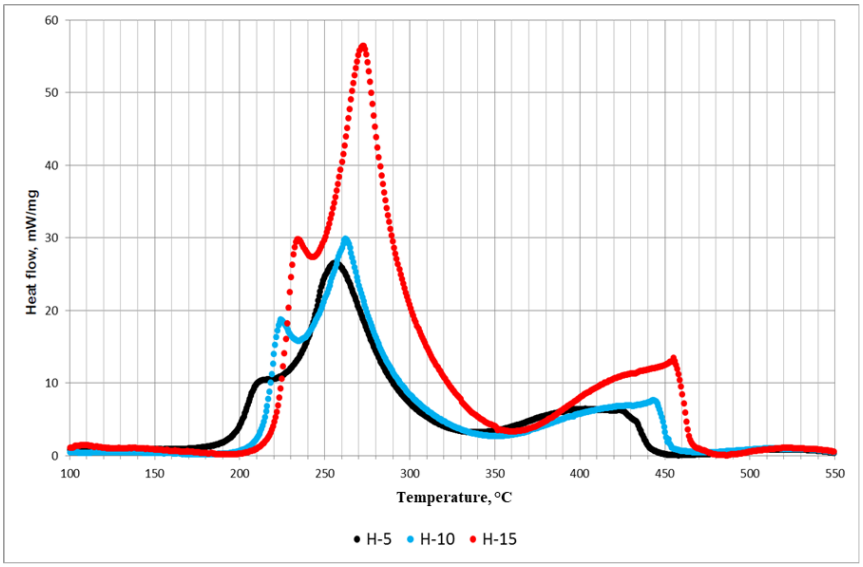

Figure 3.15 Temperature dependence of heat flow for original oil sample as a result of PDSC test (black - 5°C/min, blue – 10°C/min, red – 15°C/min)

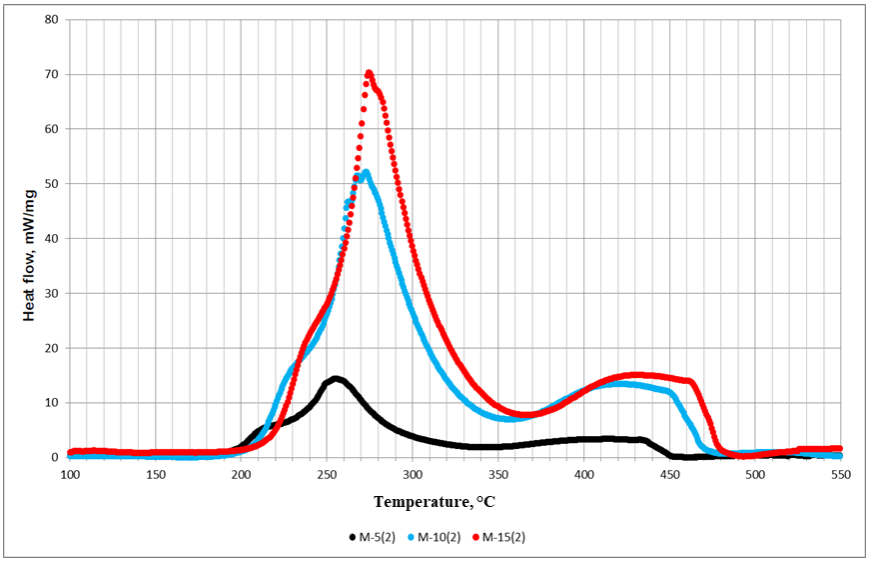

Figure 3.16 Temperature dependence of heat flow for maltenes fraction of original oil as a result of PDSC test (black - 5°C/min, blue – 10°C/min, red – 15°C/min)

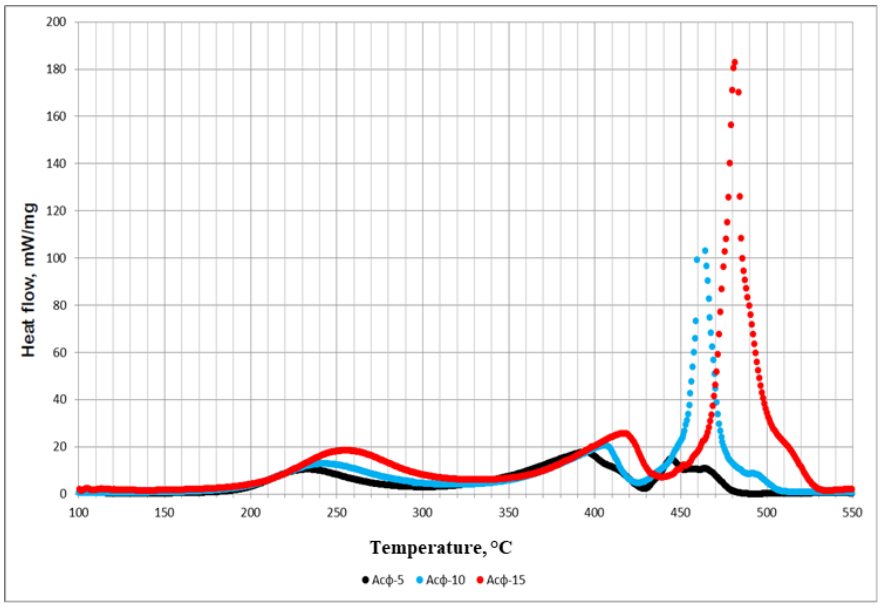

Figure 3.17 Temperature dependence of heat flow for asphaltenes fraction of original oil as a result of PDSC test (black - 5°C/min, blue – 10°C/min, red – 15°C/min)

Based on the PDSC results, the oxidation kinetic parameters for the original oil, maltenes, and asphaltenes fraction are calculated using the Kissinger method (Kissinger, 1957; Taylor and Fryer, 1992) and presented in Table 3.15, where LTO is the low-temperature oxidation; HTO is the high-temperature oxidation; H is the heat of the reaction; E_a is the activation energy; A is the frequency factor.

Table 3.15 Kinetic parameters estimated as a result of PDSC test for carbonate oil field

Sample		**Original oil**	**Asphaltenes**	**Maltenes**
H, J/g	LTO	5,158.96	3,199.76	7,577.82
	HTO	6,812.07	14,717.29	4,802.17
E_a, J/mole	LTO	15,881.03	111,878.11	112,851.41
	HTO	70,613.27	35,466.78	213,518.68
A, 1/s	LTO	6.63E-04	8.49E+06	2.47E+06
	HTO	3.25E+00	6.83E-03	2.03E+11

In addition, the element analysis of the original oil fractions and the fractions produced in the temperature range corresponding to LTR (collected in trap one during HPRTO experiment) was conducted. The results are summarized in Table 3.16 and demonstrate the significant differences in the amount of carbon and hydrogen in the initial maltenes fraction and asphaltenes produced. It could be concluded that asphaltenes with an observed content of C and H cannot be generated by the polymerization reaction of maltenes in the LTR.

The production of carbon dioxide and water as a result of a bond-scission reaction could be added to solve the problem of element content discrepancy. Thus, the traditional reaction scheme (Table 3.11) was modified by the addition of the bond-scission reaction of Maltenes pseudo component in the LTR where the stoichiometry was calculated based on the CHNS analysis of original maltenes and asphaltenes fractions (Table 3.16) produced to keep the equality in element masses. The initial kinetic parameters for this reaction are in correspondence to the parameters calculated based on the PDSC test for maltenes fraction. The modified reaction scheme is presented in Table 3.17.

Table 3.16 Element composition of original oil and that produced in LTR, and original maltenes and asphaltenes and that produced in LTR for carbonate oil field

Sample	N	C	H	S
	%	%	%	%
Original oil	0,270	81,647	11,426	3,353
Oil from trap1	0,222	81,252	11,828	2,858
Maltenes from original oil	0,202	84,636	11,854	3,362
Maltenes from trap 1	0,145	84,076	12,035	2,945
Asphaltenes from original oil	1,766	82,673	7,667	6,211
Asphaltenes from trap1	1,588	80,116	7,778	5,881

Table 3.17 Modified reaction scheme for carbonate oil field

Modified reaction scheme
Thermal Cracking:
1 Asphaltenes + 20.785 O2 → 70 Coke + 10 CO2 + 24.57 H2O, first order
Oxygen-addition and bond-scission reactions in LTR:
2) *Maltenes + 7.1 O2 → 0.2 Asphaltenes + 4 CO2 + 5.6 H2O,* first order with respect to hydrocarbon mass fraction, 3 order with respect to oxygen partial pressure 3) *1.0 Asphaltenes + 7.5075 O_2 = 106.59626 Coke,*

first order with respect to hydrocarbon mass fraction, 4.7627 order with respect to oxygen partial pressure
High-temperature oxidation:
4) *1.0 Coke + 1.1245 O_2 =1.0 CO_2 + 0.249 H_2O,* first order with respect to both reactants, where the H/C ratio - 0.498

The incorporation of the modified reaction scheme (Table 3.17) in the before developed hydrodynamic model gives the preliminary results shown in Figure 3.18.

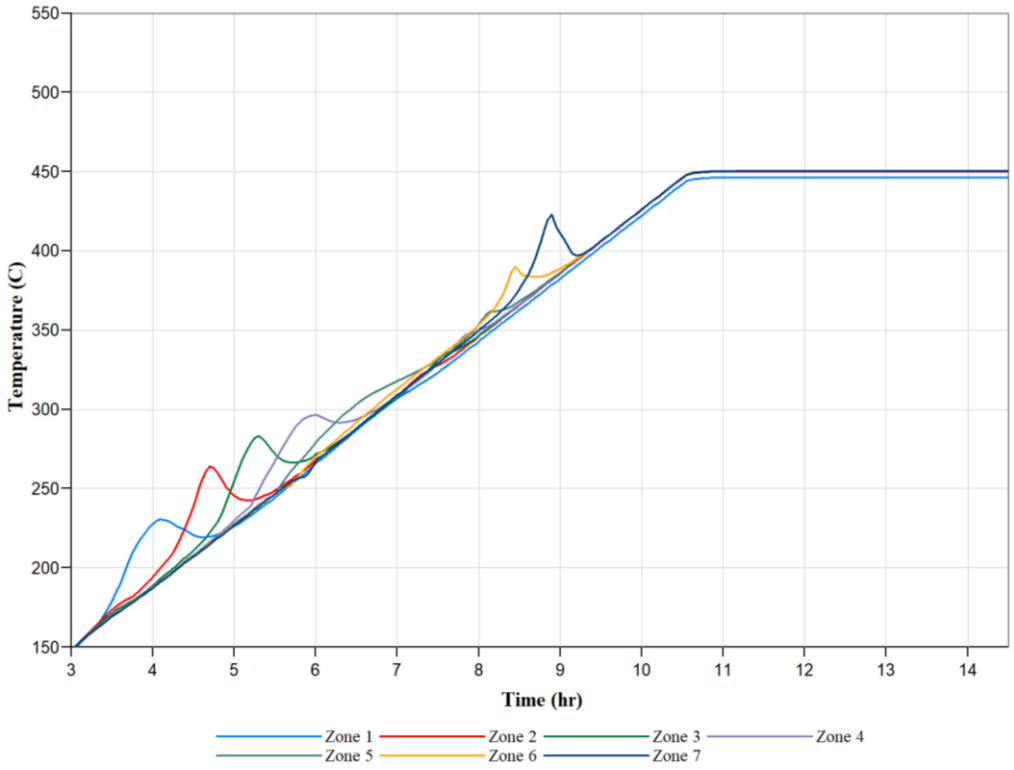

Figure 3.18 Zooed m in simulated temperature profiles for modified reaction model for carbonate oil field

3.2.4 HPRTO: history matching

The frequency factor, activation energies, and heat of reactions were manually adjusted for the case of traditional (Table 3.11) and modified (Table 3.17) reaction models using the history matching procedure. The history-matched Arrhenius kinetic parameters for traditional and modified reaction schemes are summarized in Table 3.18. It is the initial guess of kinetic parameters for the previously chosen chemical reaction model, which should be used in the MPCT simulation. The results of the history matching procedure are presented in Figure 3.19 and Figure 3.21. The cumulative masses of produced oil, water, and gas and the temperature of oxidation initiation were specified as an objective function for error minimization.

Table 3.18 Adjusted kinetic parameters as a result of history matching of RTO experiment for carbonate oil field

Traditional reaction scheme			
Reaction	**A, 10^9**	**E_a, kJ/mol**	**H_r, kJ/mol**
1	2,760 hr^{-1}	181.041	0
2	0.4 hr^{-1} $kPa^{-0.4246}$	86.73	$5.874*10^2$
3	9.01 hr^{-1} $kPa^{-4.7627}$	185.6	$3.14*10^3$
4	7.00 hr^{-1} kPa^{-1}	34.763	$4.71*10^2$
Modified reaction scheme			
1	2.76*1014 hr^{-1}	181.041	0
2	5.05*102 hr-1 kPa-$^{0.4246}$	112.000	$9.27*10^3$
3	$1.12*10^6$ hr^{-1} $kPa^{-4.7627}$	185.600	$3.14*10^3$
4	$2.79*10^0$ hr^{-1} kPa^{-1}	34.763	$5.71*10^2$

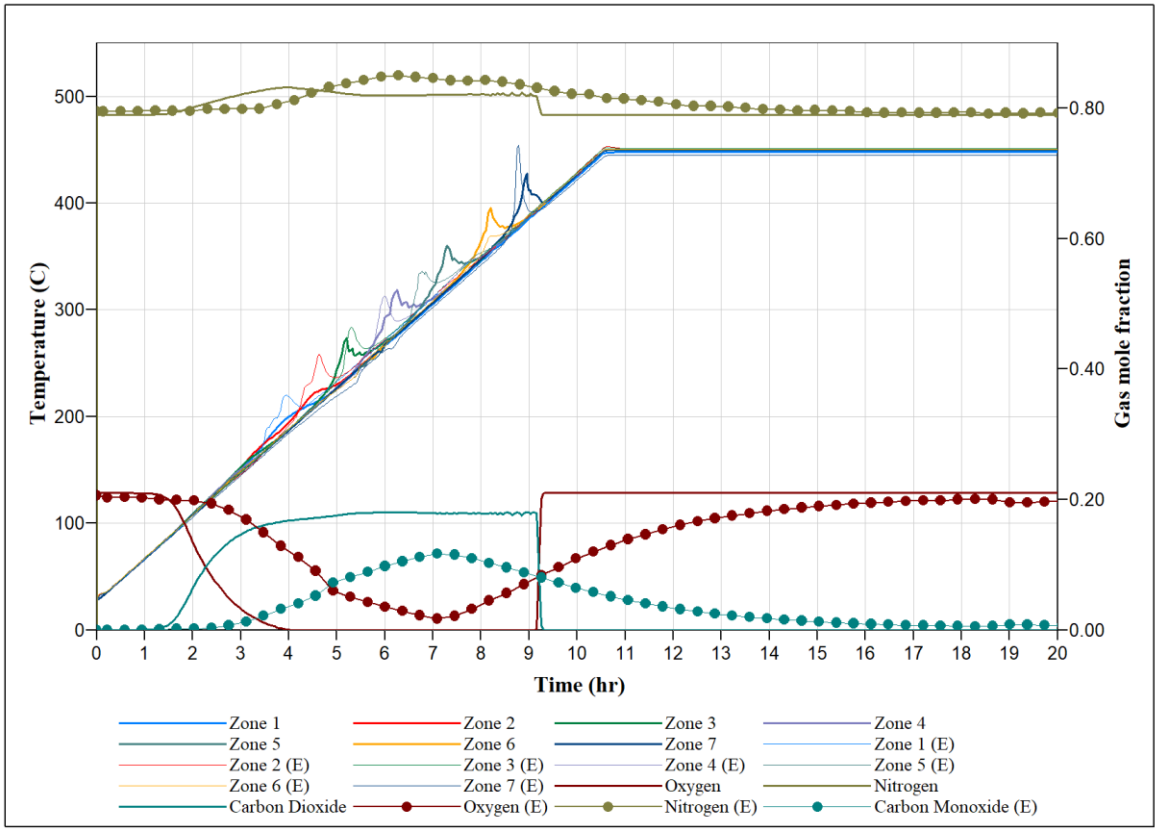

Figure 3.19 Numerical simulation and experimental results for RTO test for carbonate oil sample: temperature profiles by zones and molar concentration of nitrogen, carbon dioxide, and oxygen (traditional reaction scheme)

The experimental and simulated results based on the model with the traditional reaction scheme incorporated are presented in Figure 3.19. The numerical calculations were conducted with the adjusted kinetic parameters (Table 3.18). A comparison of the history-matched cumulative oil, water, and gas cumulative production masses and experimental data are plotted in Figure 3.20 and show satisfactory agreement between experimental data and simulation results. While satisfactory matches of both the whole temperature region and location of the first temperature peak are achieved, the calculated temperature profiles have different shapes in the low 350°C temperature region, and the NTGR cannot be resolved. This discrepancy could be explained by the possible inconsistency of the chemical reaction model and the specific PVT and oxidation behavior of target oil. This also could be a consequence of specific undefined phase transitions of oil fractions during

the oxidation processes and requires additional study. Table 3.19 presents the values of cumulative oil, water, and CO_2 obtained during the experiment and simulation for the case of traditional and modified reaction models. The error in integral values of the combustion gases produced and oxygen consumption is more than 30% in the case of the traditional reaction scheme. It should be noted that the simulated heat release in the LTR is a result of Coke combustion and artificially high values of frequency factors (adjusted during the history matching procedure), which does not have an apparent experimental basis. This results in the fact that oxygen-addition reactions in the form presented in the traditional reaction model cannot produce experimentally observed heat release.

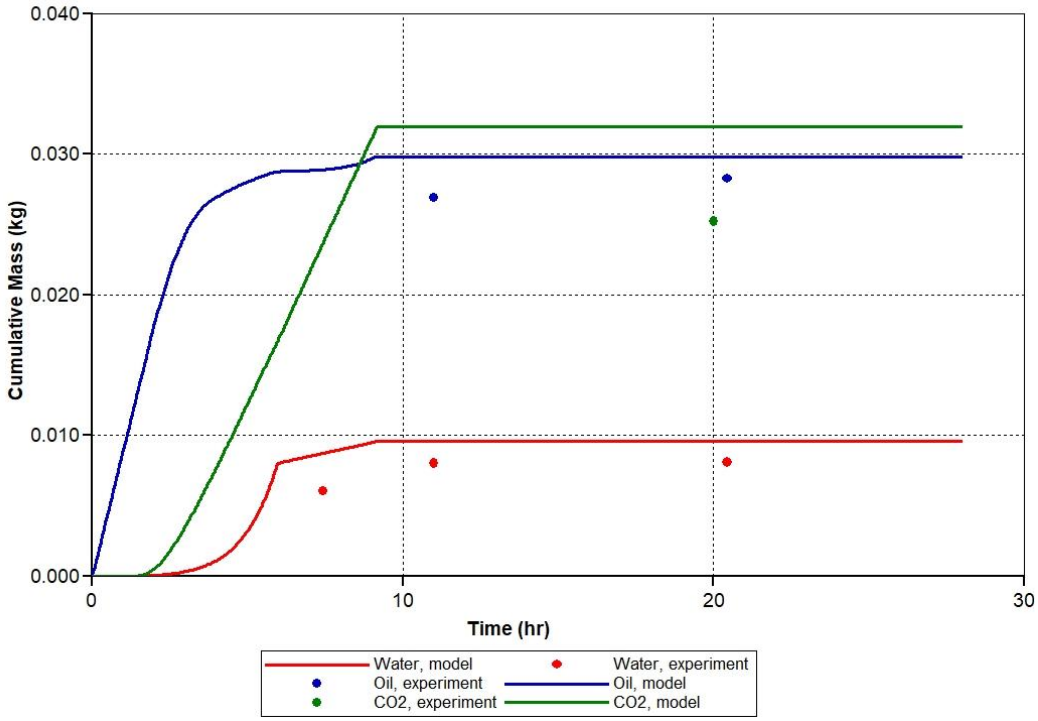

Figure 3.20 Comparison of results for experiment and simulation for RTO test for carbonate oil example: a) cumulative oil mass; b) cumulative gas mass; c) cumulative water mass (traditional reaction scheme)

Table 3.19 Mass of products for experiment and simulation of RTO experiment for carbonate oil field

	Experiment	Traditional reaction scheme *(Belgrave et al 1993)*	Modified reaction scheme
Mass of obtained oil, g	26.40	28.61	28.60
Mass of CO_2, g	21.23	30.98	21.98
Mass of obtained water, g	8.02	9.58	9.57

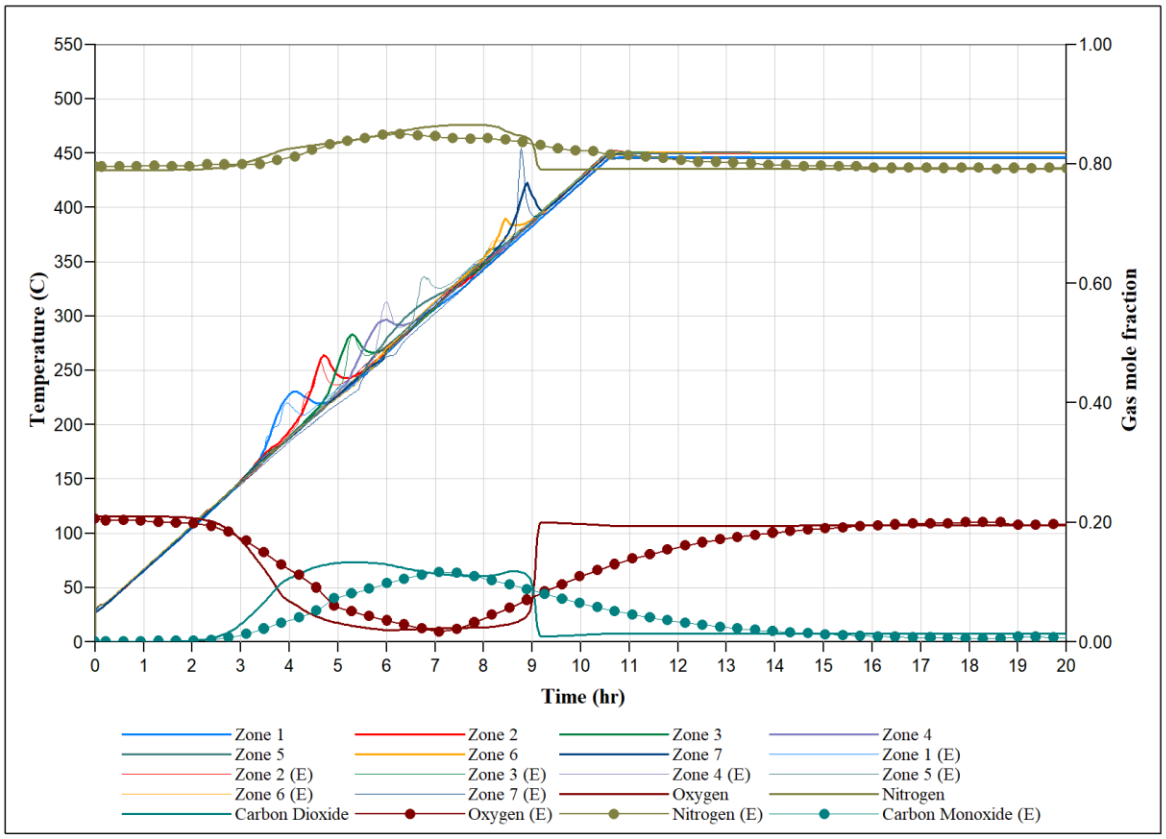

Figure 3.21 Numerical simulation and experimental results for RTO experiments for bitumen: temperature profiles by zones and molar concentration of nitrogen, carbon dioxide, and oxygen (modified reaction scheme)

The same simulation of the HPRTO experiment was provided based on the numerical model in which the modified reaction scheme was incorporated. The adjusted kinetic parameters as a result of the history matching procedure are summarized in Table 3.18.

The temperature profiles of the HPRTO experiment achieved from the history-matched simulation at seven different zones of the experimental setup and molar fraction of gases are presented in Figure 3.21. The model represents the existence of experimentally observed NTGR (290°C - 350°C), the location of the first temperature peak. In this case, during numerical simulation of the HPRTO test, the exothermic (Figure 3.22 (a)) and endothermic (Figure 3.22 (b)) fronts traversing the core pack are reproduced and satisfactory match the fronts observed experimentally. Figure 3.22 (a) shows the comparison of temperature profiles associated with Zone 4 of the reactor for numerical simulation and experiment. The heat release peaks in the LTR and HTR are captured. A comparison of the history-matched cumulative oil, water, and carbon dioxide cumulative production masses and experimentally measured corresponding values are plotted in Figure 3.23 and Figure 3.24 and summarized in Table 3.19. The maximum discrepancy in simulated and experimental cumulative masses of produced fluids and gasses does not exceed 1%. In this case, the adjusted frequency factor used in Coke combustion reaction is relatively low, which corresponds to the experimental observations of Coke combustion rate. While excellent matches of cumulative masses of produced gases are reached, the real-time detected mole fraction of oxygen, carbon dioxide, and nitrogen during numerical simulation of HPRTO does not ideally align with the experimental curves (see Figure 3.21). In addition, the simulated exothermic behavior does not fully align with the experimental result in the transition zones between different temperature regions. The reason could be the same as discussed above, and further investigation of the basic oxidation reaction model and phase behavior description for multicomponent hydrocarbon systems is required.

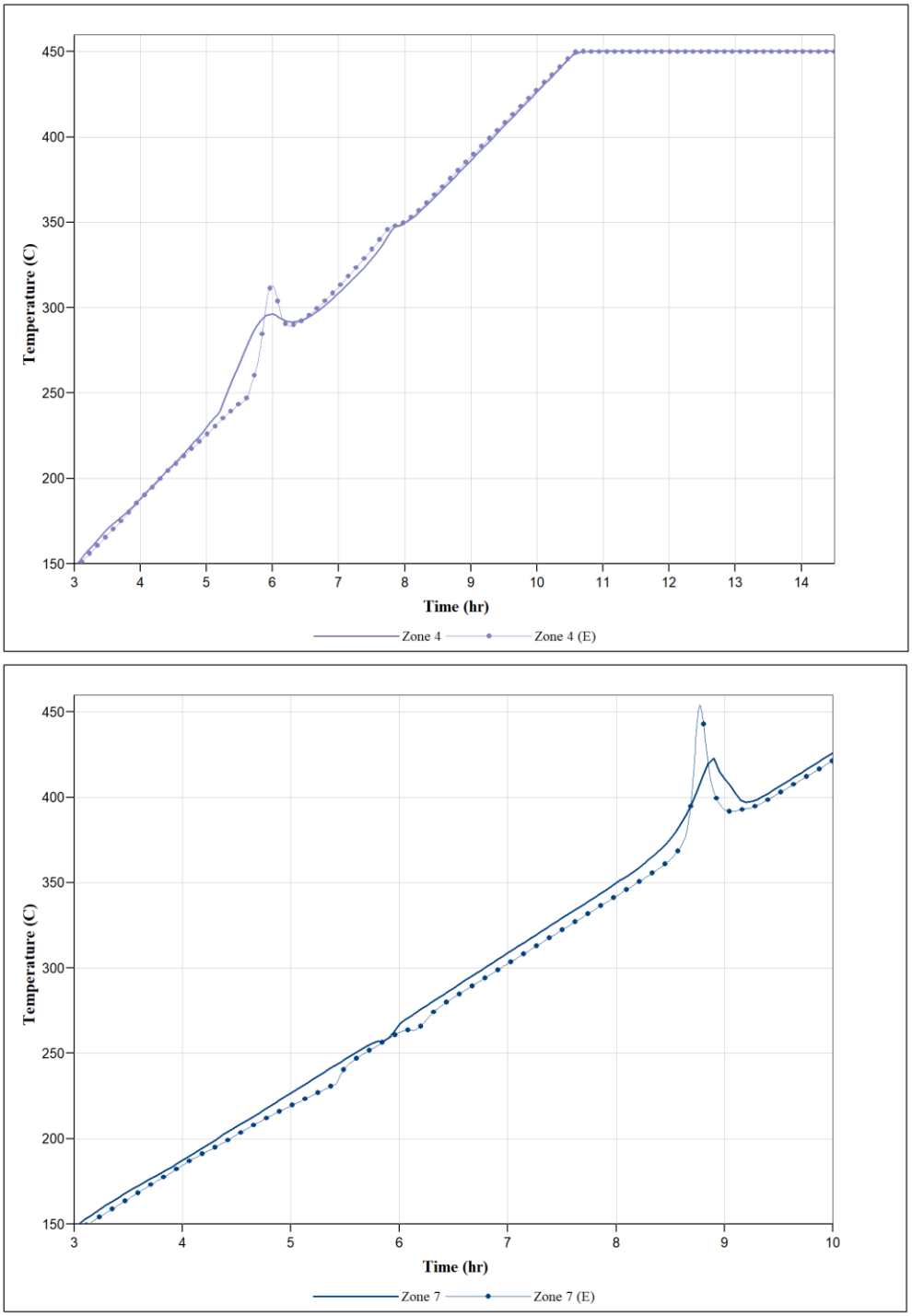

Figure 3.22 Comparison of numerical and experimental results for RTO test for carbonate oil field: temperature profiles for Zones 4 (above) and 7(below) of the reactor (modified reaction scheme)

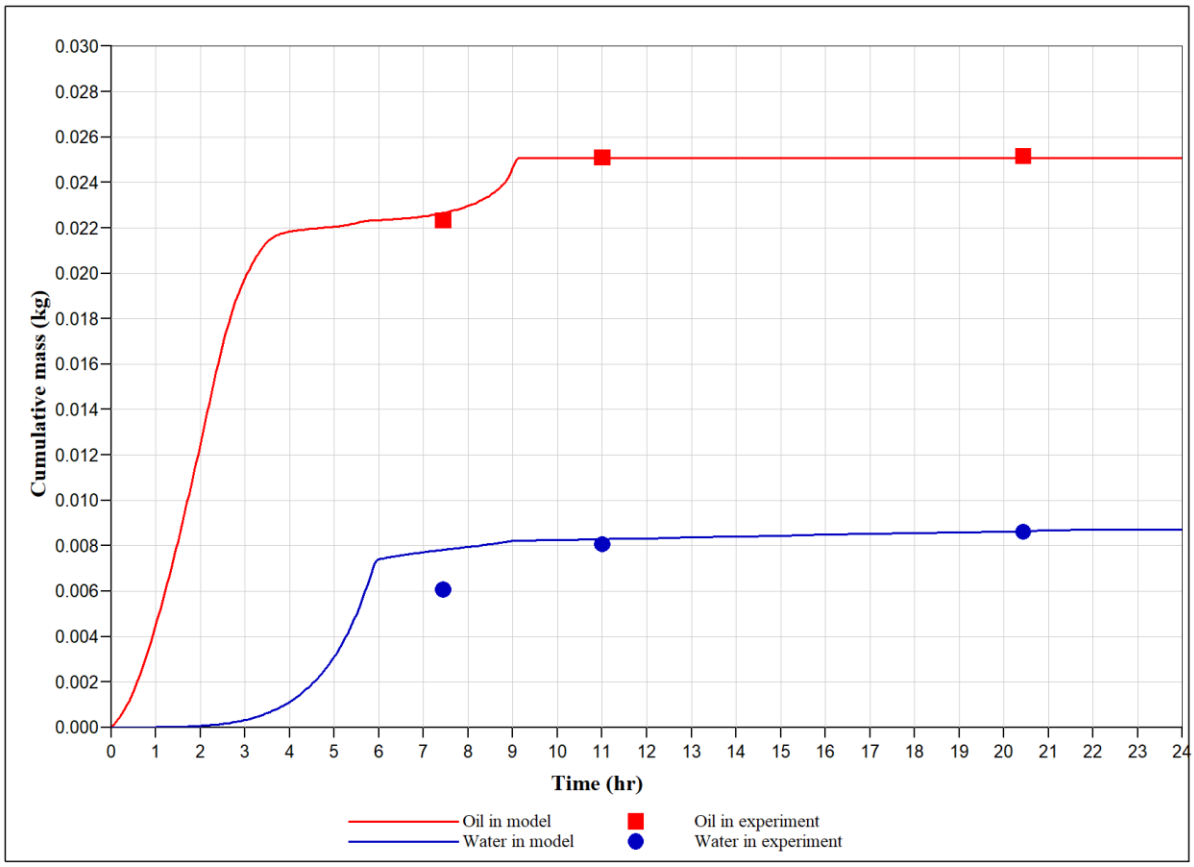

Figure 3.23 Comparison of results for experiment and simulation of RTO test for carbonate oil example: cumulative oil mass and cumulative water mass (modified reaction scheme)

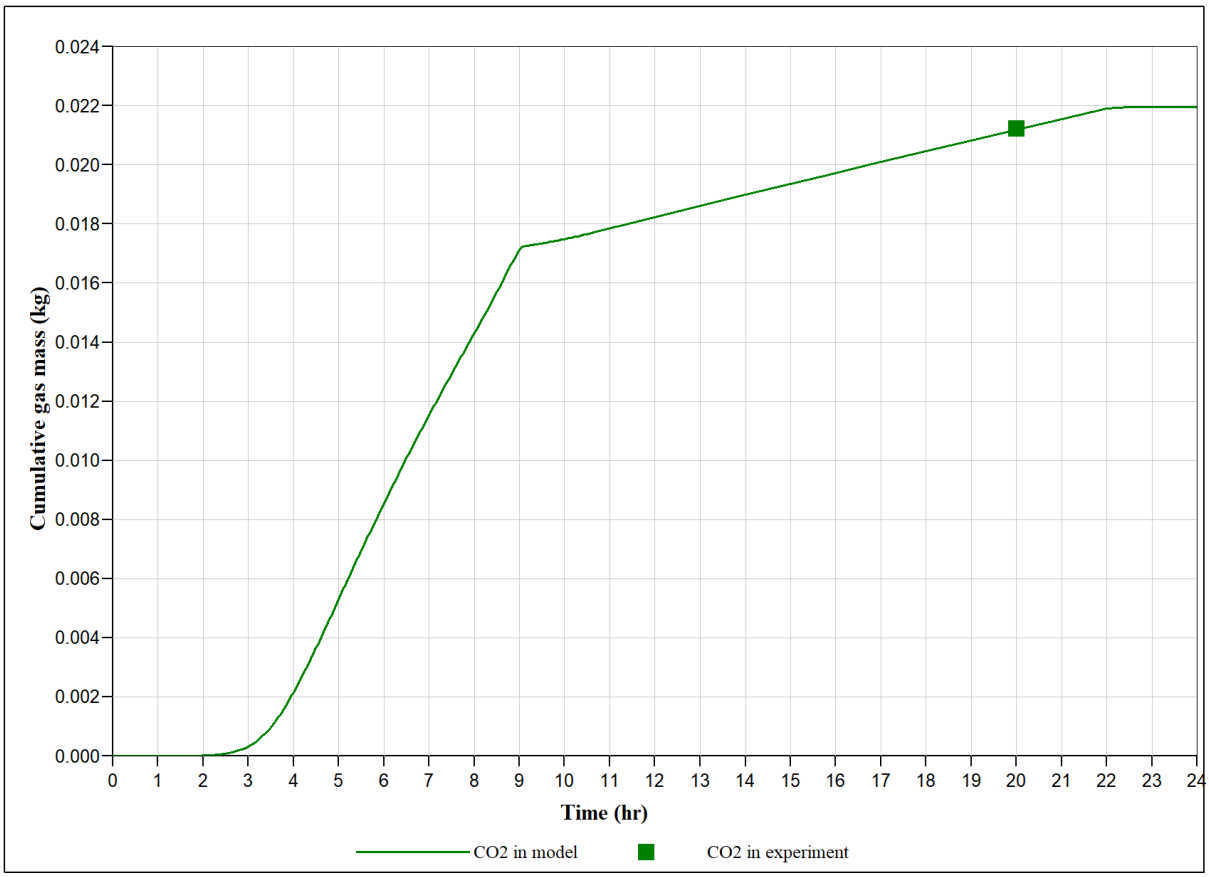

Figure 3.24 Comparison of results for experiment and simulation of RTO test for carbonate oil example: cumulative gas mass (modified reaction scheme)

3.2.5 MPCT: history matching

The numerical modeling of MPCT experiment and optimization process was carried out in the thermal hydrodynamic simulator CMG STARS. A hydrodynamic model exactly repeats the one used in HPRTO numerical simulation. The model of chemical reactions and kinetics is also taken from the HPRTO model for the initial run. The history matching was carried out by varying the kinetic parameter (in particular, the pre-exponential factor in the first reaction), and the operation regimes of the heaters. Heat losses and thermal properties of specific layers were adjusted during this process to achieve the best match. Relative permeability curves have a significant impact on the results of the combustion tube simulation and are the essence of the adaptation of the model according to the results

of the experiment. The adapted relative permeability curves obtained during history matching are allowed to match the cumulative production of water and oil (Table 3.20).

As a result, a good match of the temperature peaks obtained in the experiment and the numerical model was achieved as well as the cumulative production of water and oil, and the inconsistency of gas yield was minimized. Below are the results of the adaptation of the numerical models in which the classical and modified reaction schemes were incorporated with respect to the experimental data (Figure 3.25-Figure 3.26 and Figure 3.27-Figure 3.28, respectively). Figure 3.25 shows a comparison of temperature fronts in each zone, and Figure 3.26 demonstrates the gas mole concentrations (in case of the classical reaction scheme is incorporated in the numerical model) in the experiment and simulation. Figure 3.27 and Figure 3.28 represents the same results but for the case of the modified reaction model used while the rest of the hydrodynamic model is the same as in the previous case.

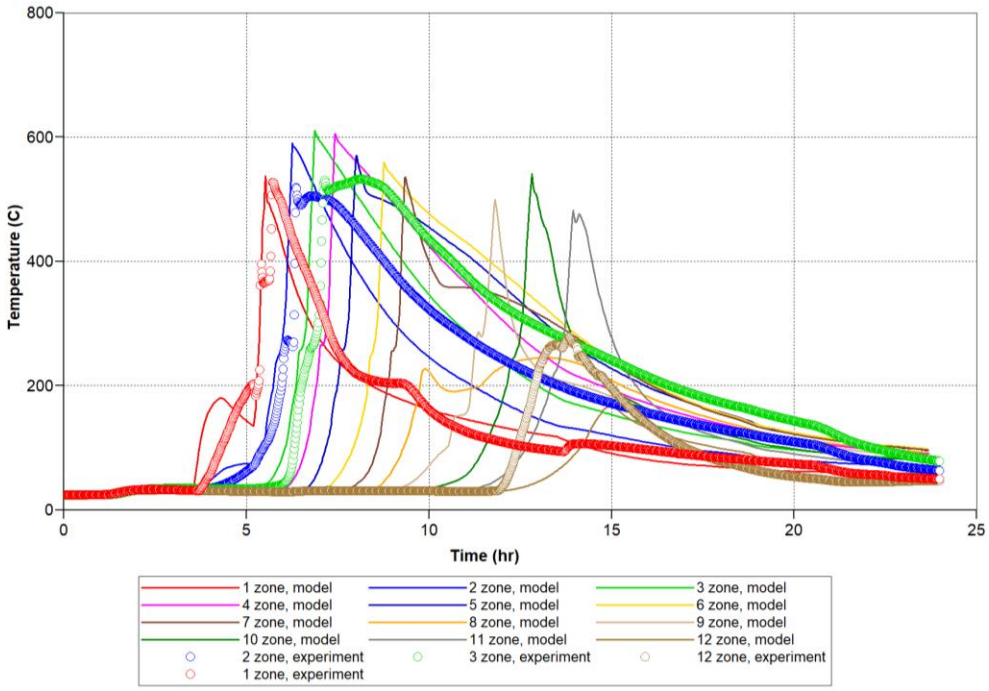

Figure 3.25 Comparison of the MPCT test results for experiment and simulation: temperature profiles for carbonate oil field (traditional reaction scheme)

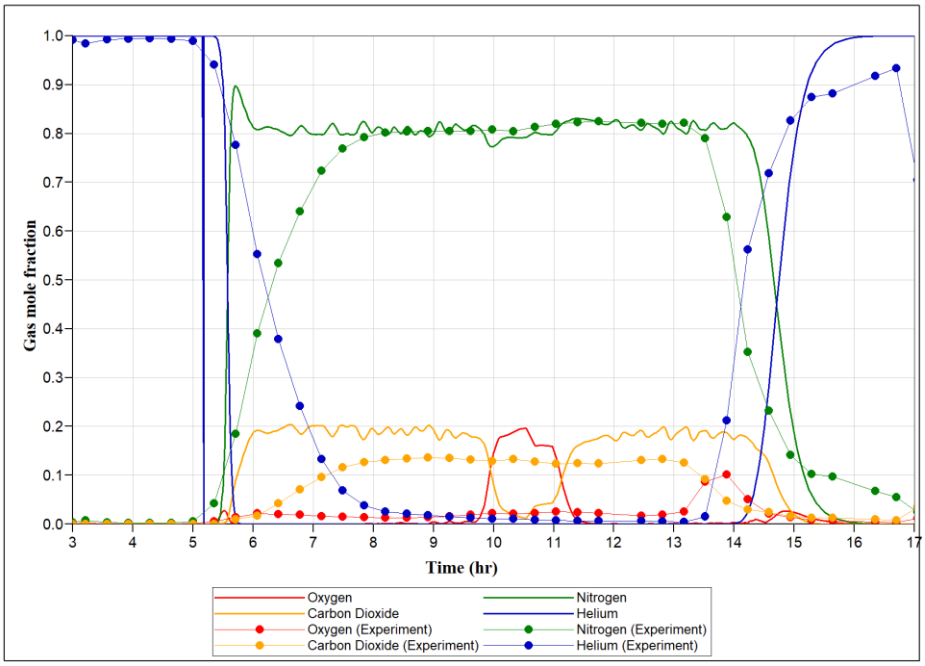

Figure 3.26 Comparison of the MPCT test results for experiment and simulation: gas mole concentrations for carbonate oil field (traditional reaction scheme)

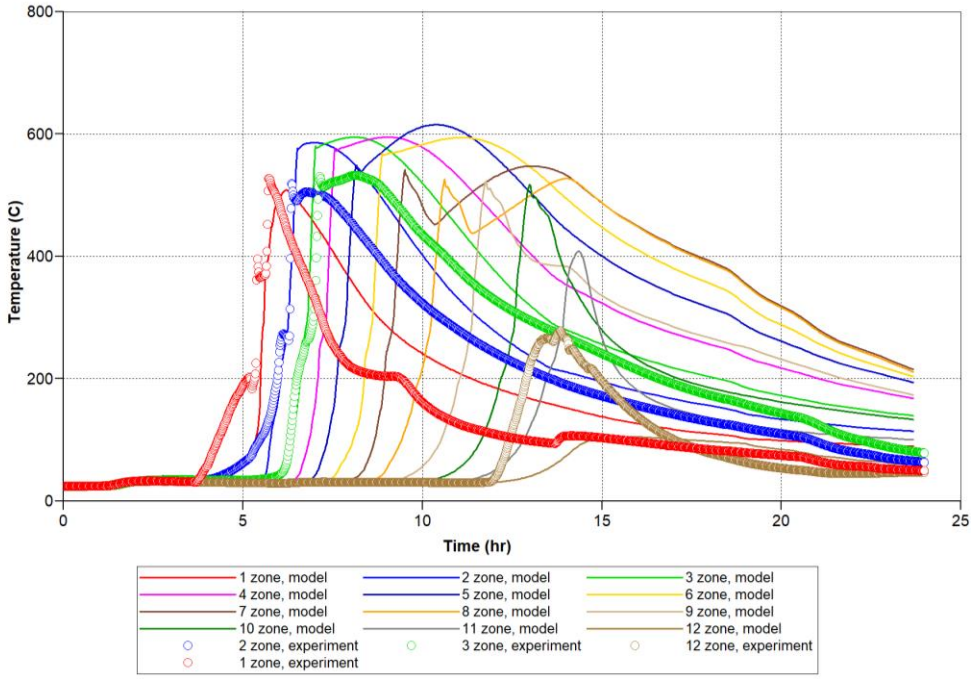

Figure 3.27 Comparison of the results for experiment and simulation: temperature profiles for carbonate oil field (modified reaction scheme)

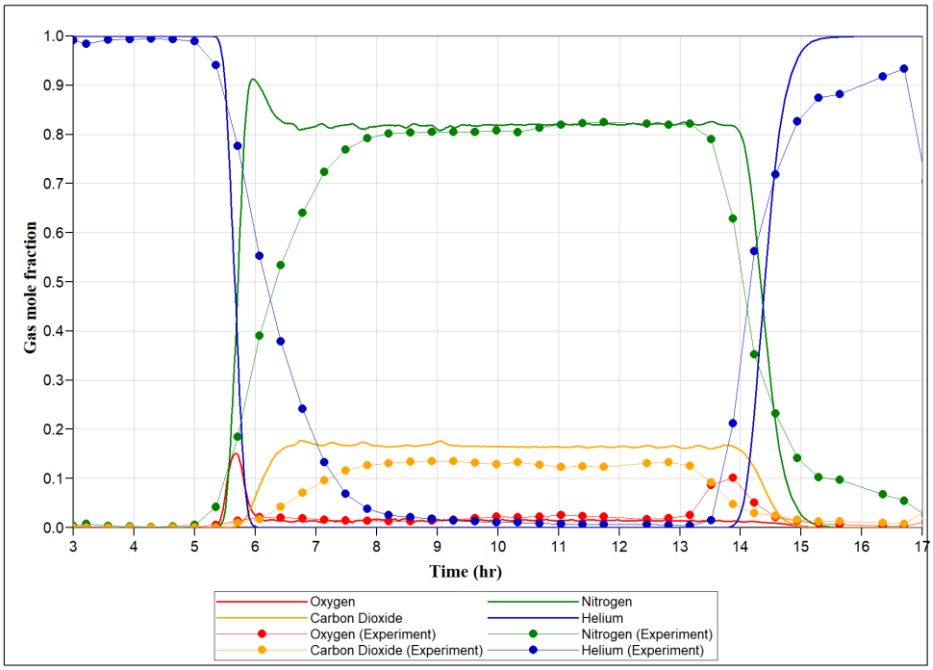

Figure 3.28 Comparison of the MPCT test results for experiment and simulation: gas mole concentrations for carbonate oil field (modified reaction scheme)

In both cases, the first five zones demonstrate good agreement between the experimental curves and temperature profiles obtained in the simulation. The shape of 6–9 zones for modeling differs from the experimental curves, but the beginning of the combustion front coincides. This may be due to the combustion front "slip" and delay of the burning process. In Zone 7 and 8, a similar process is observed, in which a sharp drop in temperature turns into a smoother curve. In zones 10 and 11, it was possible to repeat the shape of the curves and the peak temperature in zone 11. In Zone 12, the curve obtained by numerical simulation lags behind the experimental values, indicating a higher heat loss in the model. But, it should be mentioned that the numerical model in which the modified reaction scheme is incorporated captures the shape of temperature profiles in the zones after the fifth one better. It is demonstrated in Figure 3.29, where the temperature profiles corresponding to Zone 6 of the CT were presented with respect to the experimentally detected one. This is a consequence of the fact the numerical model of HPRTO experiment with the modified reaction scheme showed a better agreement of exothermic behavior with the experiment than the model with the traditional reaction scheme used (see Section 3.2.4).

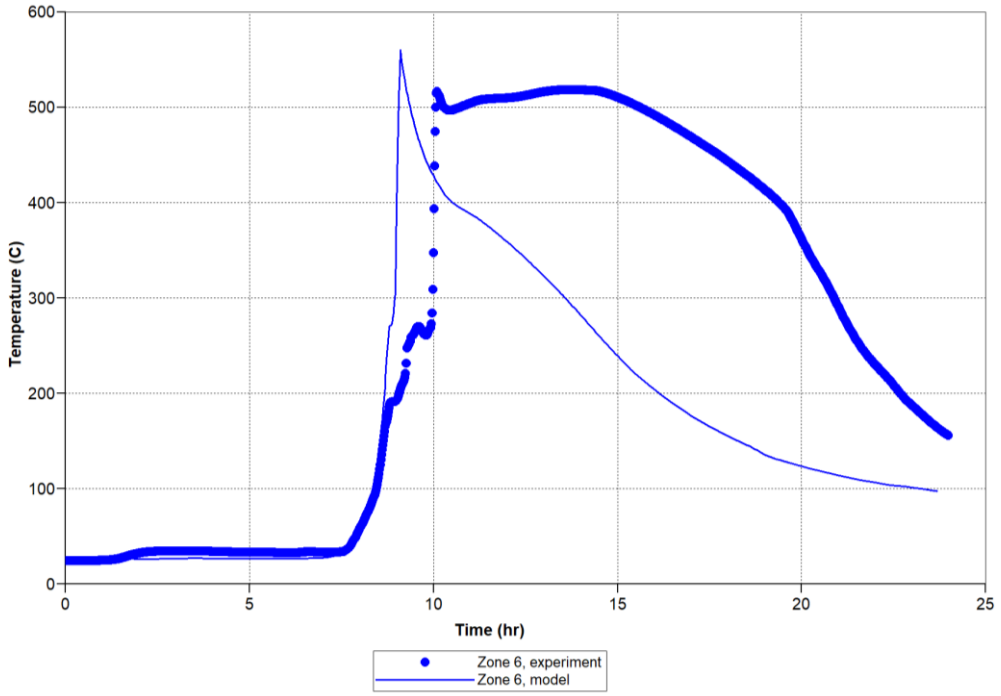

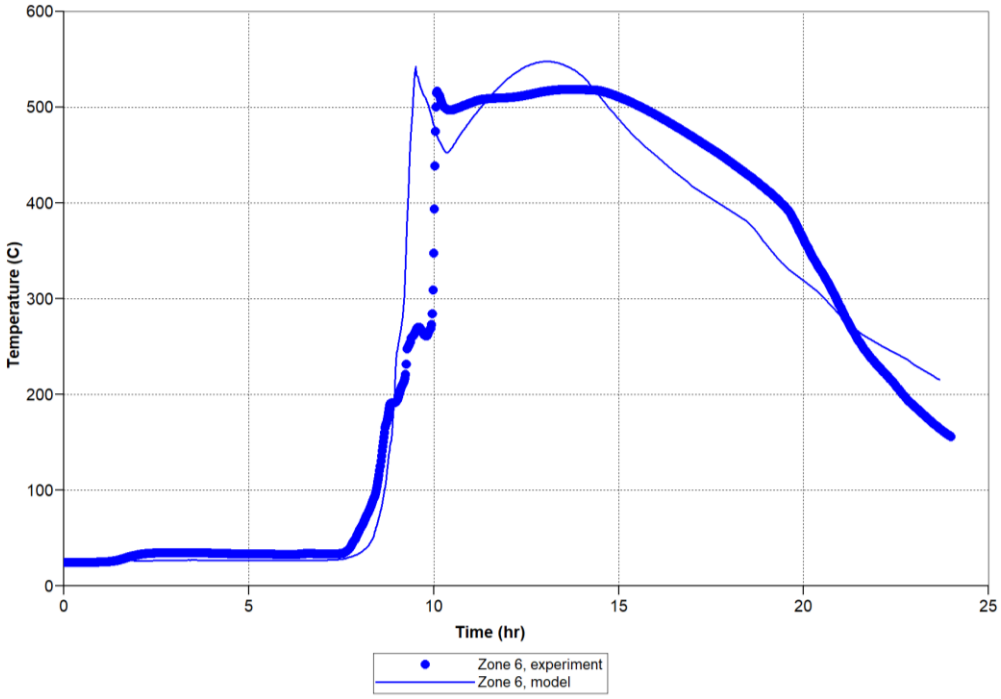

Figure 3.29 Temperature profile for Zone 6 in MPCT test for carbonate oil field: in case of the traditional (above) and modified (below) reaction schemes

Below is the material balance of oil and water for the experiment and numerical simulation. In Table 3.20 the absolute values of the produced oil, water and gases obtained in the case of modeling and experiment are presented.

Table 3.20 Mass of the products for the experiment and simulation for MPCT test for carbonate oil field

	Experiment	Traditional reaction scheme *(Belgrave et al 1993)*		Modified reaction scheme	
		Absolute value	Normalized difference, %	Absolute value	Normalized difference, %
Mass of obtained oil, g	2564.26	2485.64	3.06	2485.64	3.06
Oil burned, g	220	224.62	2.1	219.6	0.186
Mass of CO_2, g	544.59	820	50.57	622	14.21
Mass of consumed O_2, g	114.4	130.7	14.25	114.0	0.35
Mass of obtained water, g	2220.9	2250.9	1.35	2247.1	1.18
Air injected, g	799.81	794.5	0.66	799.81	0
Air consumed, g	688.8	681.5	1.06	686.1	0.39
Coke, g	3.3	0	>100	10.5	>100

Figure 3.30 (above) shows the dynamics of oil yield and the comparison of cumulative oil production for the experiment and numerical simulation. Figure 3.30 (below) shows the dynamics of water production and a comparison of the accumulated water production for the experiment and numerical simulation for the case of the traditional reaction model. The same experimental and numerical results agreement is observed for the case of the modified reaction model (Figure 3.31).

There are few issues that should be addressed, such as propagation of the combustion front and the mechanisms of the oil recovery (Fadaei et al., 2011). Both resulting models give a good agreement of the temperature profiles in all zones, an excellent agreement with the experimental values of the accumulated water and oil, which is mostly a consequence of well-adjusted relative permeability curves and thermal properties of the layers. There is a discrepancy in the mole concentrations of O_2 and CO_2, and in the total oxygen. This discrepancy significantly reduces the numerical model in which the modified reaction scheme is implemented. These differences in results repeat the results of HPRTO test

numerical modeling. Nevertheless, the necessity of further investigation of the phase transition behavior of target oil and basic chemical reaction model is required. However, these models repeat general features of the MPCT experiment (temperature peaks, front velocity, cumulative oil, and water), which are the most important characteristics of the oil recovery process by high-pressure air injection and could be tested in the full-field model.

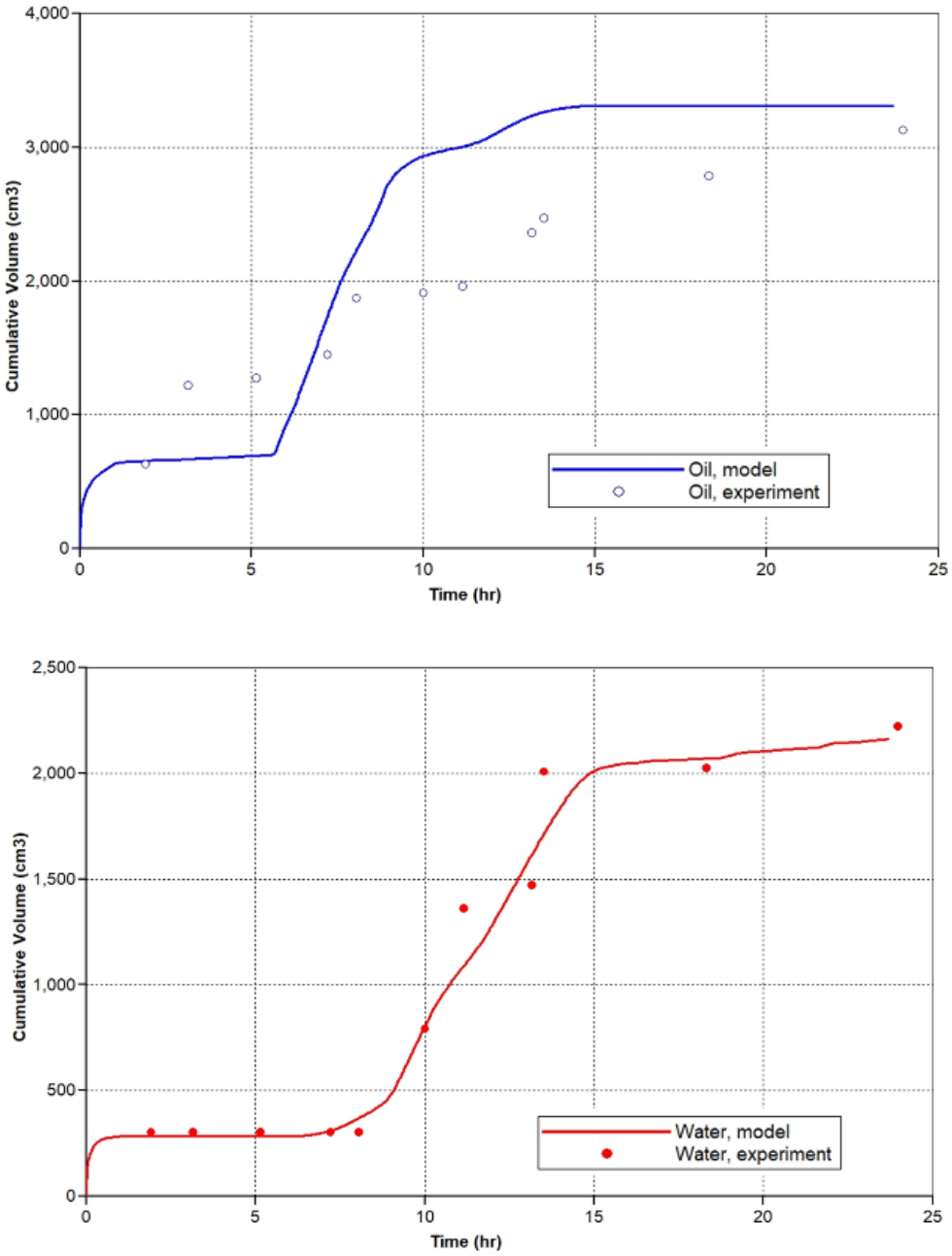

Figure 3.30 Cumulative oil (above) and water (below) production for experiment and simulation as a result of MPCT experiment for carbonate oil field (traditional reaction scheme)

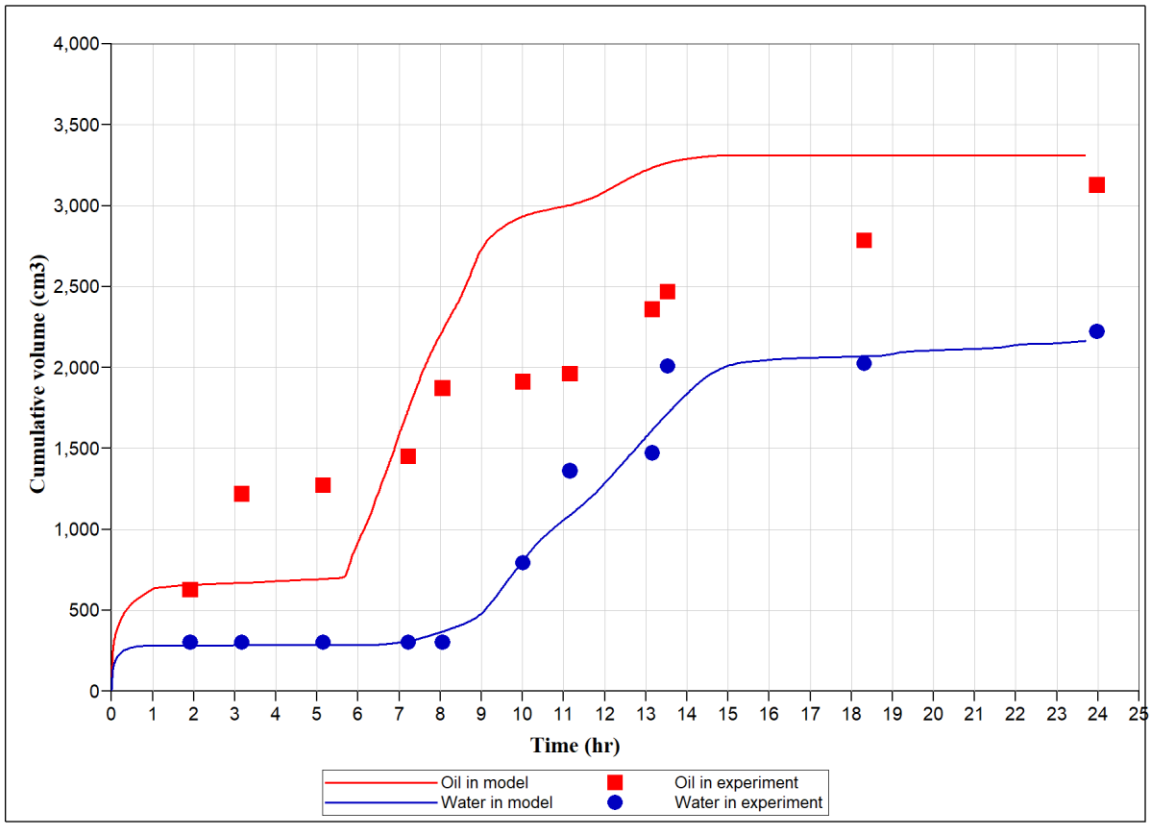

Figure 3.31 Cumulative oil and water production for experiment and simulation as a result of MPCT experiment for carbonate oil field (modified reaction scheme)

3.3 Insights on construction of HPAI reaction kinetic model for organic-rich source rock

The purpose of this study was to develop a complex approach, including experimental studies and numerical simulation for the investigation of oxidation processes induced by HPAI in oil shales. Application of this approach implies the following steps: estimation of HPAI method feasibility for oil shales based on the results of oxidation studies; revealing main oxidation processes based on the experimental results and computer modeling; choice of pseudo components, reflecting oxidation properties and phase behavior of oil and kerogen; developing of a minimal set of relevant chemical reactions; validation of kinetic model.

In this study, a set of experiments was conducted prior to the combustion tube test described in the article Bondarenko et. al., 2017c and Khakimova et al., 2017. Information obtained was also needed for setting a combustion tube ignition zone heater to a sufficient temperature to ignite the oil readily after the start of air injection. The temperature should be not high enough due to the economic and technological constraints in the field and not to be too low to cause low-temperature oxidation reactions. Three sets of oxidation study tests were carried out, namely: pressurized differential scanning calorimetry (PDSC), accelerating rate calorimetry (ARC), and ramped-temperature oxidation (RTO) experiments. All of the tests were done using rock samples of BF that contains immature kerogen (Type I). PDSC and ARC tests were performed on the mixture of oil and core (1:9 wt:wt) to mimic conditions that were simulated in the combustion tube test. Using PDSC, temperature ranges where heat generation rates are significant were established, and activation energies corresponding to the different heat generation steps were calculated. During the ARC test, “heat-wait-search-adiabatically follow runaway” method was implemented, and temperature corresponding to maximum self-heating rate was determined. RTO experiment was performed on native rock sample without additional oil saturation to establish absorbed oil and kerogen reactivity with air in the porous medium and to determine the ignition temperature in porous media conditions. As a result, temperature ranges over which oxygen uptake rates are high were established, and

Arrhenius parameters for low and high temperature ranges were determined. It was revealed that dominant oxidation mode corresponds to the low temperature range, which indicated that oil and kerogen can be ignited spontaneously under reservoir temperature. In addition, experiment highlighted negative temperature gradient region and the auto-ignition temperature corresponding to the onset of elevated oxygen uptake rates was estimated.

3.3.1 Ramped temperature oxidation experimental results

The dependence of the rate of oxygen consumption by the sample from the temperature of the sample for all the heating rates is shown in Figure 3.32. The obtained shape of the curves allows us to describe the process within the framework of the classical model of hydrocarbon oxidation, including the processes at the low-temperature region (LTR) and high-temperature region (HTR). In addition, the third peak appears in the temperature range 550-650 ºC, similar to DSC curves. However, due to very low intensity, it was not possible to analyze this peak quantitatively. The change in the composition of the gas mixture at a heating rate of 1.50°C/min is shown in Figure 3.33.

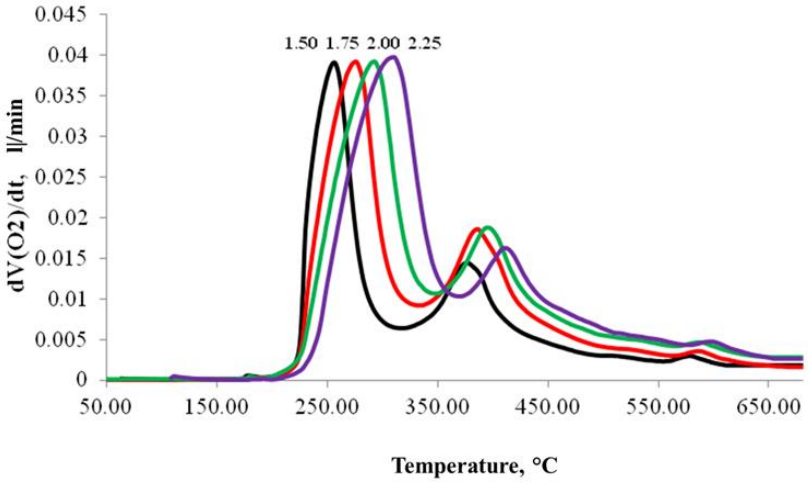

Figure 3.32 Dependence of oxygen consumption rate on temperature at different heating rates (1.50, 1.75, 2.00 and 2.25°C/min) for oil shales

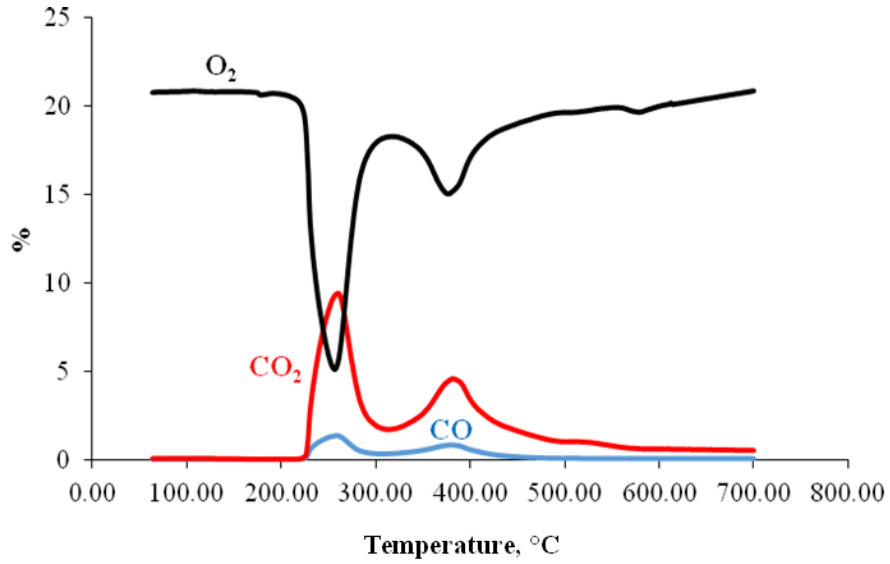

Figure 3.33 Change in the composition of the gas mixture when the sample is heated (1.50°C/min) for oil shales

Data on temperature intervals of oxidation reactions are given in Table 3.21.

Table 3.21 Temperature parameters of LTR and HTR for oil shales

Heating Rate, K/min	LTR		HTR	
	Temperature interval, °C	Peak temperature, °C	Temperature interval, °C	Peak temperature, °C
1.50	225-289	255.6	322-423	377.1
1.75	224-311	276.8	318-446	387.0
2.00	224-332	293.3	325-455	395.3
2.25	234-356	308.9	331-478	410.1

Calculation of kinetic parameters was carried out by three methods: ASTM E 698-11 (I), ASTM E 698-11 (II) and Ozawa-Flynn-Wall method.

Graphical representation of the dependence of the activation energy on the degree of conversion is presented in Figure 3.34. From the data obtained conclusion about high efficiency of air injection method can be drawn according to screening procedures described in work of Cinar et al. (2011).

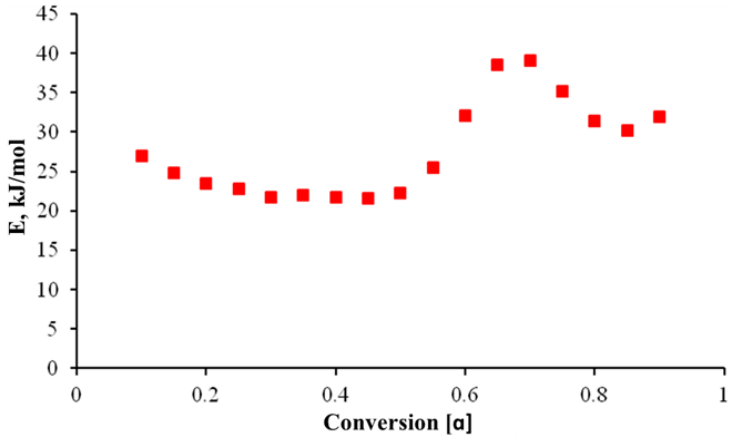

Figure 3.34 Dependence of the activation energy E on the degree of conversion α for oil shales

The kinetic parameters of the oxidation process are listed in Table 3.22.

Table 3.22 Kinetic parameter at LTR and HTR for oil shales

Heating rate, K/min	LTR		HTR	
	E_a, kJ/mol	A	E_a, kJ/mol	A
ASTM E 698 (I)	10.3±0.5	$6.94*10^{-2}$	34.5±5.3	8.87
ASTM E 698 (II)	13.9±0.4	$20.19*10^{-2}$	34.2±4.0	8.58
Ozawa-Flynn-Wall	21.7±1.5	$1.78*10^{-4}$	39.0±2.8	$3.82*10^{-3}$

To calculate the organic matter content, the total amount of carbon oxides and absorbed oxygen was used. Amount of carbon and hydrogen that was combined with oxygen were estimated. The initial content of organic matter in the obtained samples was 4.5%.

3.3.2 Pressurized Differential Scanning Calorimetry experimental results

From DSC results, we can see three exothermic peaks, which is different from typical DSC curves for crude oils oxidation (Figure 3.35). The reason for this behavior is the oxidation processes of kerogen. Comparing with two peaks corresponding to crude oil oxidation (Yuan et al., 2018), we observed three peaks in DSC curve of oil shales that could

correspond to oxidation of different components. In the numerical part, we will discuss it in more detail.

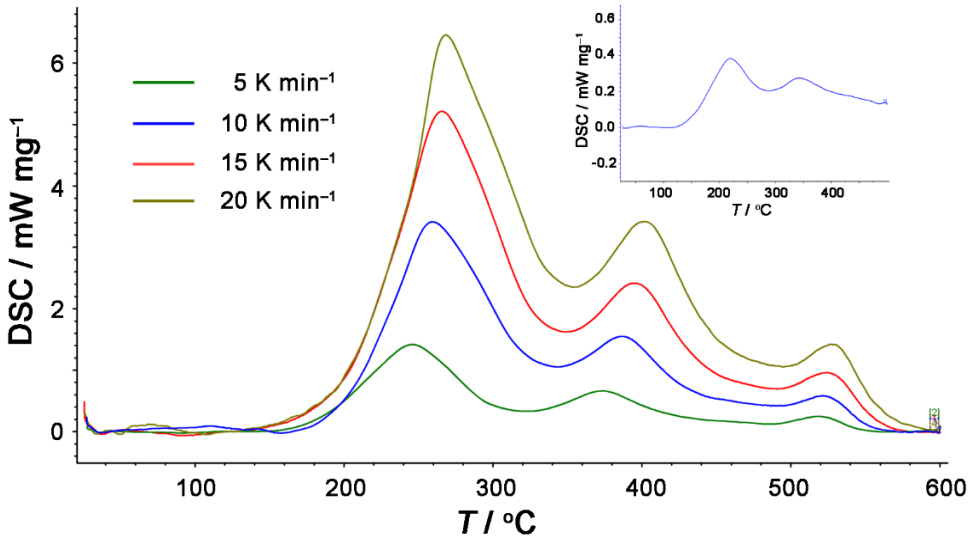

Figure 3.35 DSC oxidation curves for oil shales, pressure 8 MPa. Upper right corner curve represents heating rate 1 K/min

Pre-smoothed using the NETZSCH Proteus 6.0 tool, DSC curves were separated into individual peaks using the NETZSCH Peak Separation 3 program (Figure 3.36).

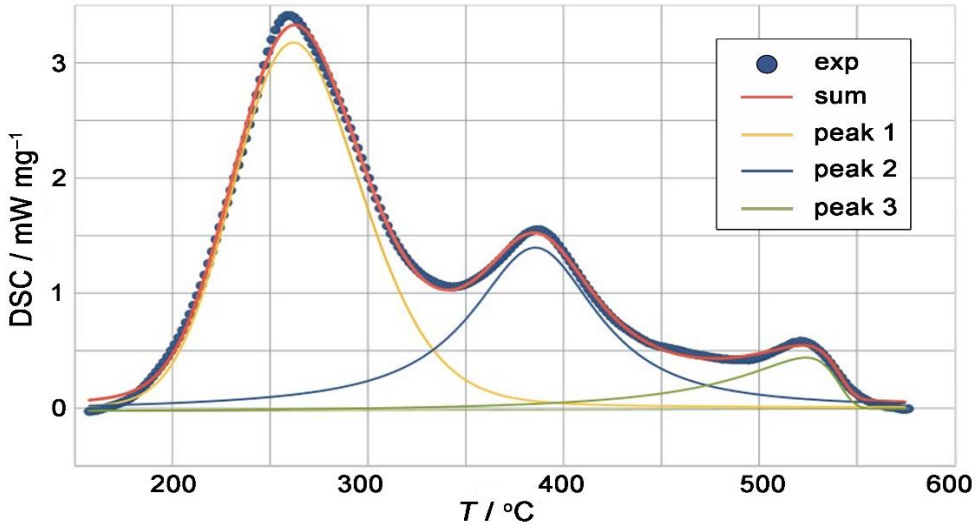

Figure 3.36 Example of DSC curve separation into three individual peaks for oil shales, heating rate 10 K/min

In Table 3.23 results of PDSC individual peaks analysis, namely onset temperature of the processes, $T_{on,\,i}$, maximum temperature of the peaks, $T_{peak,\,i}$, individual peaks thermal

effects, ΔH_i , and thermal effects of reaction in general, ΔH, sample mass losses, Δm, with heating rates β and under pressure P are presented.

Table 3.23 Results of PDSC individual peaks analysis for oil shales

β, K/min	$T_{on,\,1}$, °C	$T_{peak,\,1}$	ΔH_1**, J/g	$T_{on,\,2}$, °C	$T_{peak,\,2}$, °C	ΔH2**, J/g	$T_{on,\,3}$, °C	$T_{peak,\,3}$, °C	ΔH_3**, J/g	ΔH**, J/g	*Δm, %*
P = 8 MPa											
1	143.8	217.6			335.2			-		3126	7.0
5	179.6	246.1			373.6			518.5		2183	10.8
10	200.4	259.2			387.6			521.3		2754	11.2
15	204.5	265.7			395.1			524.2		2954	11.3
20	223.0	268.2			402.1			526.6		2955	10.3
1	150.0*	217.6*	1658*	256.2*	340.8*	1328*	469.5*	-	-	3126	7.0
5	184.4*	245.4*	1214*	308.5*	372.9*	697*	469.5*	523.1*	117*	2183	10.8
10	203.0*	262.3*	1568*	321.6*	386.1*	721*	447.3*	523.0*	189*	2754	11.2
15	201.7*	267.8*	1710*	329.7*	395.4*	752*	442.2*	524.8*	229*	2954	11.3
20	209.7*	273.4*	1630*	339.2*	402.9*	698*	449.7*	528.3*	229*	2955	10.3
P = 14 MPa											
10	191.7	259.8			385.9			540.1		2519	11.7
20	220.3	253.7			378.4			534.6		3649	11.3

* − Calculated for individual components of DSC curves.

** thermal effect of the reaction is calculated based on the initial mass of the sample; the linear function was chosen as the baseline.

The kinetic characteristics of individual oxidation processes were calculated by Friedman and Ozawa-Flynn-Wall methods for oxidation processes at a pressure of 8 MPa. The corresponding activation energies, E_a, and the logarithms of the pre-exponential factors, log A, are given in Table 3.24.

Based on the results obtained, the ignition temperature for CT test was set on 250°C (Bondarenko et. al., 2017c). After setting this temperature, oil ignited readily, and combustion front propagated steadily. Kinetic parameters were used in building the chemical model, and temperature profiles were used in matching experimental and numerical data.

Table 3.24 Kinetic characteristics of the sample oxidation at a pressure of 8 MPa for oil shales

Peak number	Friedman*		Ozawa-Flynn-Wall*	
	E_A / kJmol^{-1}	lg A	E_A / kJmol^{-1}	lg A
1	77 ± 7	5.0	87 ± 9	6.1
2	193 ± 9	12.9	171 ± 9	11.3
3**	438 ± 66	27.2	383 ± 71	24.0

* − The values given correspond to a conversion of 0.5;

** − When processing data for the third peak, the heating rate of 5 K min^{-1} was not used.

3.3.3 Construction and validation of numerical model

As was stated before, one of the most significant and difficult steps in the numerical simulation of HPAI process in kerogen-bearing rocks is to develop a chemical reactions model including kinetics, which can represent the oxidation behavior and chemical changes both of the oil and kerogen. In this work, numerical simulation consisted of multistage validation represented effects, which were observed during oxidation experiments. As a result, the hydrodynamic model including basic block of chemical reactions and primary kinetic model, were proposed. The process of consequent construction and multistage validation of hydrodynamic model included several main steps:

1) selection of pseudo-components to represent Bazhenov oil from the phase and oxidation behavior;
2) determination of minimal set of pseudo-components of kerogen and relevant chemical reactions, which is mostly based on the data obtained during RTO test;
3) building a kinetic model for previously proposed chemical reactions by comparison with experimental results.

The first step was to propose a minimal set of pseudo-components to represent Bazhenov oil from the phase and oxidation behavior experiments. The Bazhenov oil composition was taken from the work Bondarenko et al (2017c). One of the features of Bazhenov oil is high content of light fractions. Nevertheless, heavy fractions of oil were also presented but in small amount and had a significant impact on phase behavior in the system. Therefore,

heavy oil component should be also taken into account (Gutierrez et al., 2011). Another reason to use at least two pseudo-components to represent oil is that different oil fractions have different oxidation behavior, in other words for part of the fractions bond-scission reactions are dominant in LTR and for another part – in HTR, which is proved by numerous studies (Li et al., 2006; Gutierrez et al., 2011.). Experimental results of PDSC test described above were not an exception.

To provide numerical simulations described in this work, the CMG STARS commercial simulator was used. It is worth mentioning that the approximation of composition-independent k-values is used to solve the problem of phase equilibrium. Such an approach does not sufficiently take into account the influence of oxidation processes on the phase equilibria. This contribution can be significant when studying the process of HPAI (Kristensen et al., 2008). However, the simplified approach was used in this work. An equation of state (EOS)-based CMG WinProp was used for phase behavior predictions. By lumping oil components from original oil composition in WinProp we ended up with pseudo-components, described in Table 3.25.

Table 3.25 Pseudo-components of original oil for oil shales

Pseudo-component	**LO**	**HO**
Description	Light Oil	Heavy Oil
Composition	C_5-C_{11}	C_{12+}
Molecular weight, g/mol	132	500
Mole fraction	0.98	0.02

In order to model oxidation reactions of light and heavy oils, we used slightly modified chemical reactions described in Smith et al (1973). In this model, another pseudo-component was used, namely IG, which consists of CO and CO_2 in proportion 20/80.

Bond-scission reaction for Light Oil in LTR:

$1LO + 11.7O_2 \rightarrow 399.6IG + 138.1\ H_20$

Bond-scission reaction for Heavy Oil in HTR:

$1HO + 44.4O_2 \rightarrow 34.3IG + 519.3\ H_20$

The thermal cracking reaction of heavy oil was not added to proposed block of chemical reactions, which is acceptable due to the small number of heavy fractions in initial

oil composition. In addition, oxygen-addition reactions, which occurs in early stages of air injection, are not included in the proposed block of chemical reactions. Nevertheless, oxygen-addition reactions should be taken into account, since their existence was shown in the results of high-pressure ramped temperature oxidation test (HPRTO), conducted previously, but it's implementation in the model requires additional investigations. Further experimental work must be conducted to analyze in more details LTO reactions and develop correct procedure to take them into account in numerical simulation (Jia et al., 2014) (Jia and Sheng, 2016).

The next step was to modify the reactions proposed above by adding kerogen pseudo-components. A minimal set of kerogen components was determined based on the RTO test results. As described above, the RTO test was conducted on non-extracted kerogen-bearing rock without additional saturation with oil. Therefore, the results of this experiment are appropriate for making assumptions about kerogen representation in the model. For this purpose, the numerical simulation was carried out on the basis of multistage validation of consequently modified numerical model. Because of absence of temperature profiles data, oxygen consumption over temperature data was used to validate numerical model against experiment. The result of final stage validation is presented in Figure 3.37.

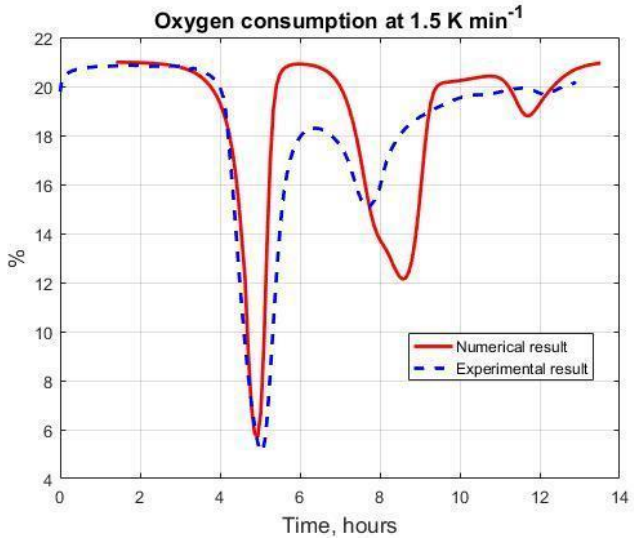

Figure 3.37 Experimental and numerical oxygen consumption in RTO test for oil shales

First of all, we faced the problem of kerogen description from the phase behavior point of view and its contribution to drainage processes. The following approach, which could be implemented only with capability of CMG STARS commercial simulator, was done. In this case, kerogen in the model was represented as a complex of solid components that reflects its heterogeneous structure. Under this approach kerogen does not participate in drainage processes, but undergoes chemical transformations.

Secondly, there was a problem of kerogen pseudo-components determination that should reflect its oxidation and pyrolysis mechanisms. In this work kerogen was represented as a complex of non-permeable components in solid phase, which consists of non-generative organic carbon (NGOC) part (KER_COKE) and part that can be thermal decomposed (Kerogen_solid1 and Kerogen_solid2) (Table 3.26). This minimal set of kerogen reflected chemical properties is in accordance with the literature. In work of Bogdanovich et al (2017), pyrograms of extracted and non-extracted samples of BF showed the delay in NGOC oxidation in non-extracted sample, which means that NGOC in kerogen, which is Kerogen_COKE burns after the GOC. In other words, we can make an assumption that third peak corresponds to Kerogen_COKE burning. Based on the data and observations obtained from the RTO experiment the following transformations of kerogen were determined and described in the model: oxidation of GOC part in LTR, which correspond to the 1st oxygen uptake, thermal decomposition of GOC part and oxidation of NGOC part in HTR, which correspond to the 3^{d} oxygen uptake. The 2^{d} peak corresponds to the oxidation of synthetic oil, generated from kerogen during pyrolysis of Kerogen_solid2.

Table 3.26 Pseudo-components of kerogen

Pseudo-component	**Kerogen_COKE**	**Kerogen_solid1**	**Kerogen_solid2**
Description	Non-generative organic carbon	Generative organic carbon	
Molecular weight, g/mol	13	1090	1090
Mass fraction	0.05	0.45	0.4

Kerogen_solid1 and Kerogen_solid2 reflect GOC part of kerogen and can be approximated by the asphaltene-like component, which oxidation and thermal decomposition behavior is described in literature (Belgrave et al., 1993; Barzin et al., 2010). In this work, the modified

LTO reaction and thermal cracking scheme proposed by Belgrave et al. (1993) for Athabasca bitumen were adapted (see Figure 3.38). It should be highlighted that composition of the synthetic oil that was generated by kerogen thermal decomposition was assumed the same as the original oil. In other words, the same pseudo-components representation was used. Distribution of light oil and heavy oil generated during the pyrolysis of kerogen (Kerogen_sold2) is shown in Figure 3.39, Figure 3.40. Kerogen_COKE, which represents NGOC part of kerogen, was approximated by a coke-like component (Yang et al., 2009). Thus, two types of coke appear during the simulation, namely kerogen_COKE and COKE. The distribution of coke component generated as a result of chemical processes is represented in Figure 3.41.

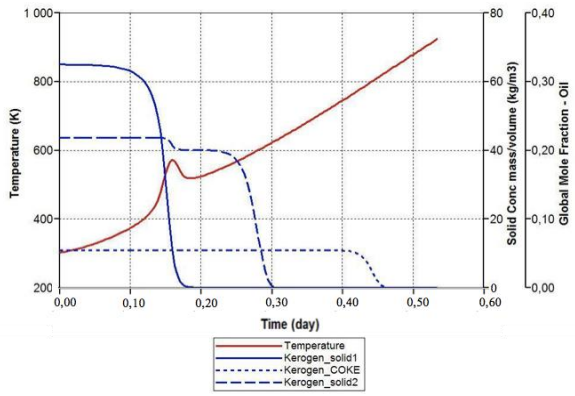

Figure 3.38 Solid concentration of kerogen components with respect to the temperature

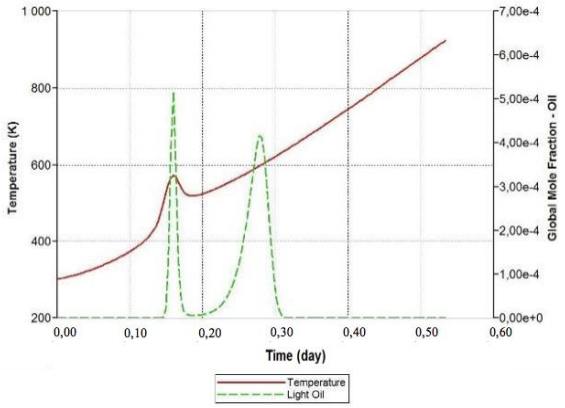

Figure 3.39 Global mole fraction of light oil component with respect to the temperature

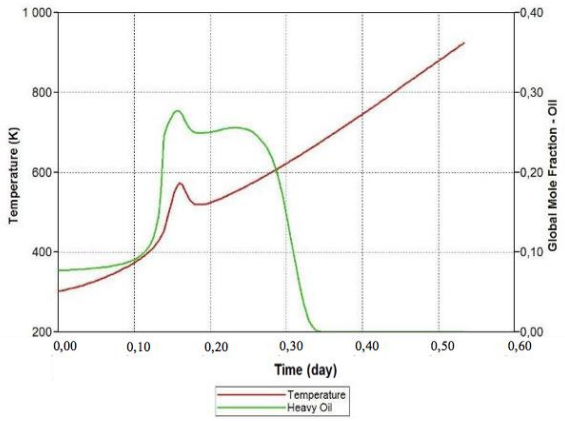

Figure 3.40 Global mole fraction of heavy oil component with respect to the temperature

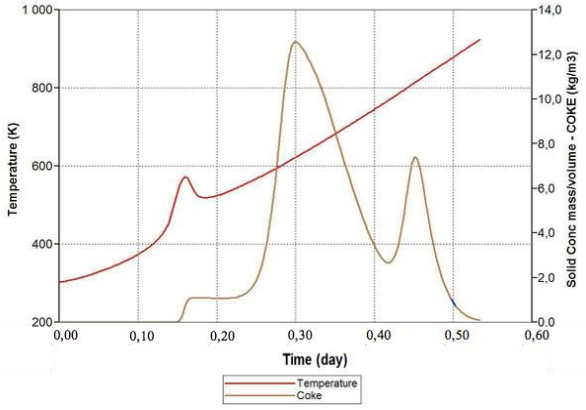

Figure 3.41 Solid concentration of coke component with respect to the temperature

As a result, we ended up with the following block of chemical reactions which approximates oxidation and pyrolysis of kerogen:

Oxidation of generative organic part of Kerogen in LTR:

Kerogen_solid1 + 7.5O_2 -> 101.5COKE

Pyrolysis of generative organic part of Kerogen:

Kerogen_solid2 -> 83.8COKE

Kerogen_solid2 -> 8.2LO

Kerogen_solid2 -> 2.2HO

Oxidation of non-generative organic part of Kerogen in HTR:

1Kerogen_COKE+ 1.2O_2 ->0.5$H_2$0 + 1IG

Oxidation of Coke:

1COKE + 1.2O_2 ->0.5$H_2$0 + 1IG

In total, eight reactions (in combination with oxidation of light oil and heavy oil) took place in the system during the numerical experiment. The distribution of all pseudo-components is represented on Figure 3.42.

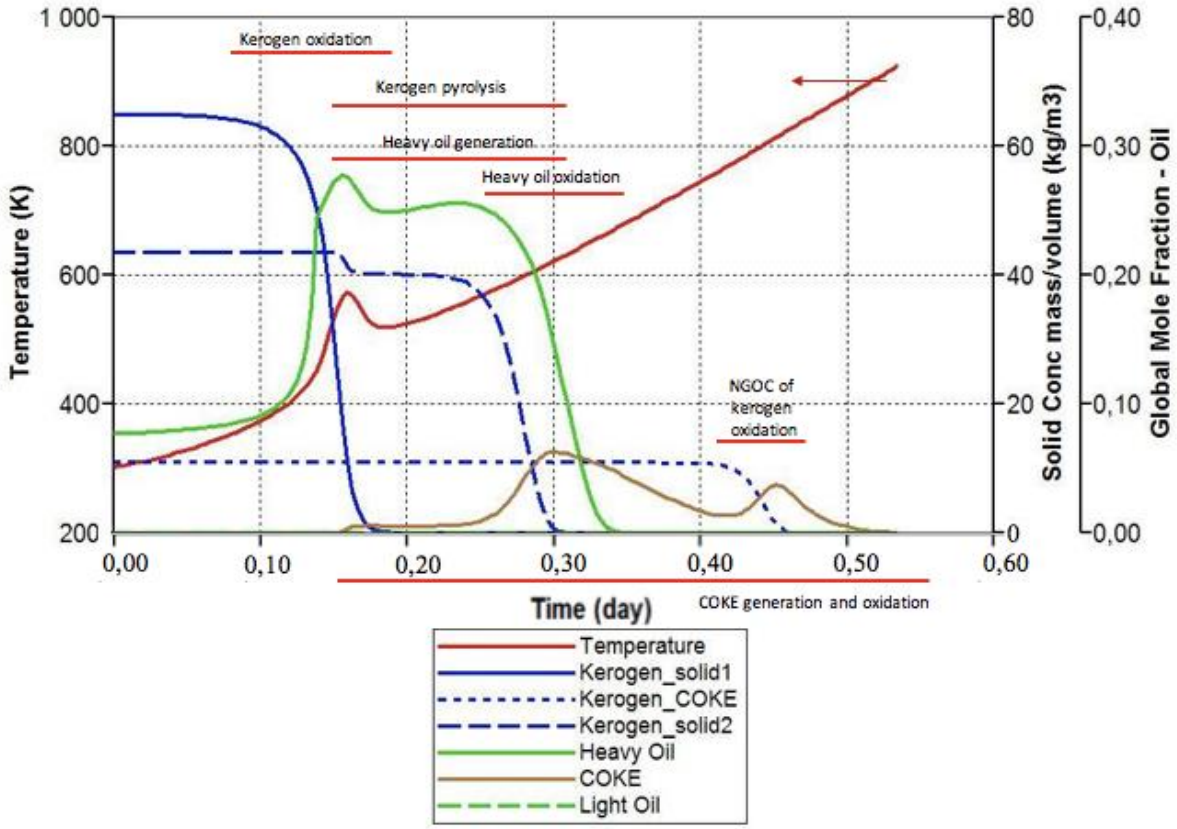

Figure 3.42 Solid concentration of kerogen components and coke component, global mole fraction of light and heavy oil components with respect to the temperature for oil shales

Additionally, the determination of kinetic model for the proposed block of chemical reactions was based on the results of PDSC test. To model the experiment CMG STARS commercial simulator was used. To construct the numerical model of DSC experiment we mainly focused on the physical concepts of this device without detailed reproduction of its geometry, using a radial grid. Nevertheless, the used liner size is close to original one. Experimental material, as described above, was a mixture of non-extracted kerogen-bearing rock and oil (1:9). Because of small amount of material and the absence of possibility to measure temperature at different parts of crucible, the experimental material was placed into one grid block (see Figure 3.43, Figure 3.44). Adjusted grid blocks except upper one to that grid block have no porosity and permeability in order to represent crucible walls. Other grid blocks represent free space around the crucible. Injector and producer are located in the upper layer of grids in order to simulate synthetic air (21% O_2 and 79% N_2)

circulation. Intensive air circulation in the upper layer provides air supply into the crucible to react with material. Evolved gases are produced from the producer. Heating was provided by placing a heater in center lower grid block to increase the temperature linearly with 10°C/min.

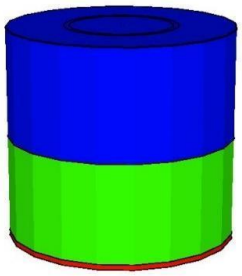

Figure 3.43 PDSC simulation model schematic

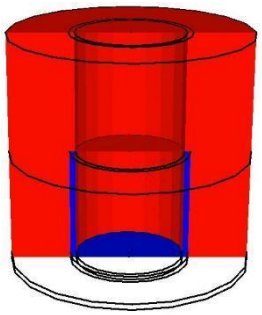

Figure 3.44 Crucible representation in PDSC simulation model

Result of final stage validation is presented on the Figure 3.45 and corresponding kinetic parameters for proposed block of chemical reactions are summarized in Table 3.27.

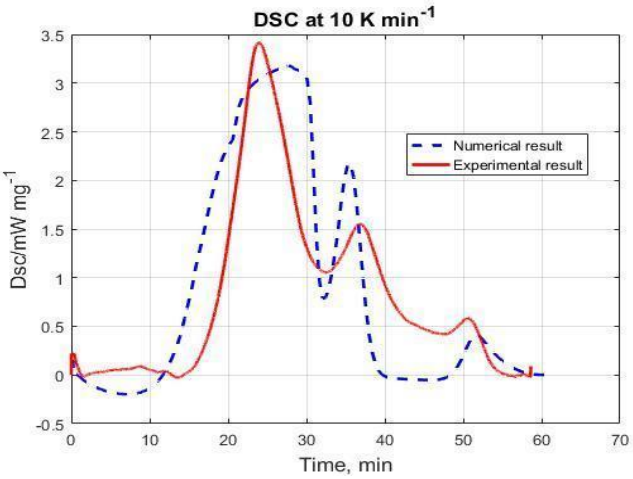

Figure 3.45 Experimental and numerical results of PDSC test for oil shales

Table 3.27 Kinetic data for oil shales

Reaction	A	E_a (J/mol)	H_r (J/mol)
Bond-scission reaction for Light Oil in LTR	$8.1*10^7$	$7.7*10^4$	$3*10^6$
Bond-scission reaction for Heavy Oil in HTR	$5*10^{-14}$	$1.8*10^4$	$3*10^7$
Oxidation of generative organic part of Kerogen in LTR	$8.1*10^4$	$5*10^4$	$4.3*10^5$
Pyrolysis of generative organic part of Kerogen	$9*10^{21}$	$2.3*10^5$	0
Pyrolysis of generative organic part of Kerogen	$9*10^{21}$	$2.3*10^5$	0
Pyrolysis of generative organic part of Kerogen	$9*10^{21}$	$2.3*10^5$	0
Oxidation of non-generative organic part of Kerogen in HTR	$1*10^{27}$	$4.2*10^5$	$8.3*10^6$

Full description of consequent-parallel oxidation processes is demonstrated in Figure 3.46. The initial reactants consist of light oil (LO) and heavy oil (HO); kerogen pseudo-components, non-generative organic part (Kerogen_COKE), and generative organic (Kerogen_solid1 and Kerogen_solid2). During the air injection, two chemical processes occur, namely oxidation and pyrolysis. In addition, oxidation mode depends on temperature interval and reactants nature. Low-temperature region (approximately 100-300°C) starts from oxygen addition reactions and generative organic part of kerogen followed by bond-scission reactions of light oil (LO) and oxidation of generative part of kerogen (Kerogen_solid1). High-temperature region divided in two temperature regions (HTR1 and HTR2) in terms of reactions occurred. At the HTR1 heavy oil cracking occurs and generative organic part of kerogen (Kerogen_Solid2) at about 300°C started to undergo thermal decomposition with generation of light oil (LO), heavy oil (HO) and coke (COKE) components. These reactions overlapped with bond-scission reactions of original heavy oil (HO) and synthetic oil (LO and HO) that is continuously generated from kerogen pyrolysis. At the HTR2, that started from approximately 450-500°C, oxidation of non-organic part of kerogen (Kerogen_COKE) occurred. In addition, bond-scission reactions of coke (COKE),

generated during kerogen and synthetic oil pyrolysis, occurred as well. It should be mentioned that oxygen addition reactions and heavy oil cracking were not part of the final chemical reactions model used in the simulation. It might be the reason of mismatch in temperature region of 250-300°C.

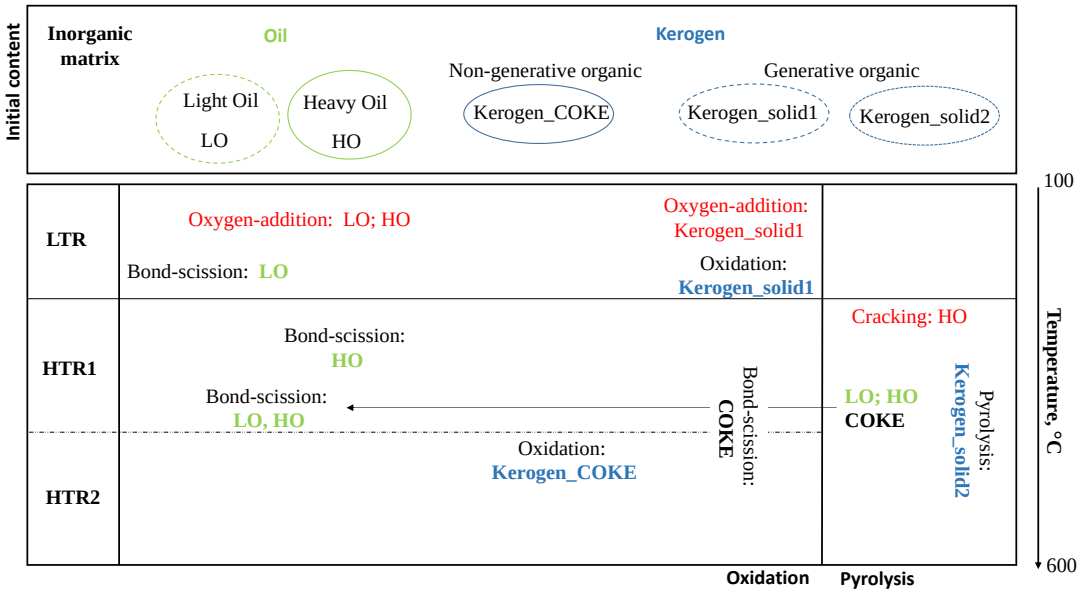

Figure 3.46 Schematic model of oxidation and thermal decomposition processes during HPAI

Data for model components, K-values correlations and relative permeability curves presented in Table 3.28 and

Table 3.29, Figure 3.47 and Figure 3.48.

Table 3.28 Data for model components for oil shales

Component	**Molar weight, g/mol**	T_c, ℃	P_c, *kPa*
LO	132	319.8	2320.8
HO	500	614.8	1480
H2O	18	374	22100
IG	40.8	-79	5171
Ker_Coke	13.13	-	-
Ker_Solid1,2	1090	904	792
O2	32	-119	5050

Gas-Liquid K-Value Correlations are assumed to be independent of composition:

$$K - Value = \frac{K_{v1}}{P} \exp \frac{k_{v4}}{T - K_{v5}}$$

Table 3.29 Gas-Liquid K-Value Correlations for oil shales

Component	K_{v1}	K_{v4}	K_{v5}
LO	$7.5*10^7$	-4628	-137.41
HO	$1.9*10^7$	-6560	-80.1
H2O	$1.2*10^7$	-3820	-227
IG	$8.6*10^8$	-3100	-272
Ker_Coke	0	0	0
Ker_Solid1,2	0	0	0

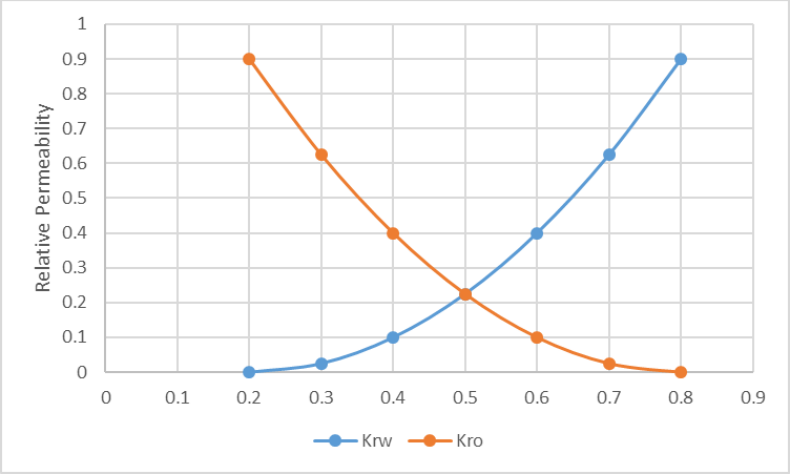

Figure 3.47 Relative permeability to water and oil with respect to water saturation for oil shales

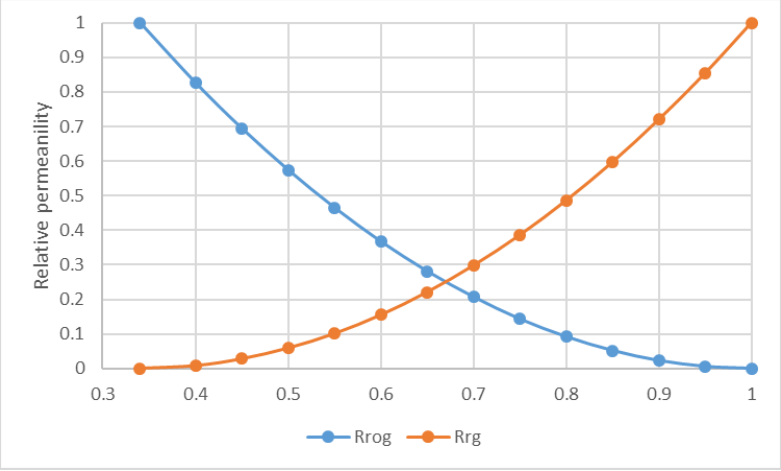

Figure 3.48 Relative permeability to oil and gas with respect to liquid saturation for oil shales

3.4 Conclusions to Chapter 3

In this chapter, we focused on a general methodology (Chapter 2) application for modeling both HPAI and ISC as a basis for thermal EOR methods evaluation using the abilities of the commercial thermal simulator CMG STARS. The methodology which can combine laboratory and numerical modeling of the HPAI process as a possible EOR technique for the carbonate oil field at reservoir conditions was developed and applied (Section 3.2). This approach helped to provide a proper kinetic model for one of the existing oil combustion reaction schemes and for a modified one, taking into account the bond-scission reaction of maltenes in the LTR, which could be used as a starting model in full-field simulations. Indeed, numerical simulations gave a satisfactory correlation with experimental results: oil recovery factor of 0.89, oxidation front velocity of 18.1 cm/h, and optimal airflow rate of 220 $st.m^3/m^3$ in the MPCT experiment. However, modeling the HPRTO experiment did not give as good of a correlation to experimental results for both of the reaction schemes considered. This was due to the fact that during the HPRTO experiment, displacement of oil and filtration effects are negligible in comparison to the oil phase transition and oxidative behavior. On the one hand, this makes it possible to significantly reduce the number of factors influencing the results of the experiment to kinetic parameters of the chosen chemical reaction model, PVT properties of the chosen oil pseudo-components, and thermal properties of the experimental tube layers, but on the other hand, it increases the importance of these factors, and its accounting requires further oxidation studies.

During the research, it was shown that the RTO test had an inalienable role in the understanding of the oxidation behavior of the reported oil samples and fuel mechanism and construction of the appropriate reaction kinetic scheme, which plays a significant part in feasible HPAI and ISC numerical models. This was also demonstrated using the example of a bitumen reservoir (Section 3.1). The laboratory-scale numerical model of the RTO experiment was constructed and validated against laboratory measurements for oil sand bitumen. Numerical simulations showed a good agreement with experimental results such

as O2 uptake, CO2 generation, obtained amount of oil and water, peak temperatures, oil recovery factor of 0.33, oxidation front velocity of 6.79 cm/hr.

Adaptation and history matching of the RTO experimental results for laboratory-scale numerical modeling were allowed to obtain kinetic parameters for the adapted reaction scheme, describing the ISC process for bitumen, which could be used as a starting model in full-field simulations. In order to describe the chemical behavior of hydrocarbons during the ISC process, a modified traditional reaction scheme was used, which includes the polymerization of Malthenes and Asphaltenes in the LTR, thermal cracking, and coke combustion in the HTR. Modification results in the incorporation of the vapor-phase combustion reaction of light oil in the HTR, which appears in the system due to asphaltenes cracking and LTO reactions. Due to this, thermal energy generation in HTR was induced not only by coke burning but also by vapor-phase combustion. The incorporation of this mechanism allowed us to get non-zero residual coke, which was observed during the experiment. The proposed model qualitatively replicate temperature peaks in the LTR (180 to 310°C), HTR (350 to 470°C), and NTGR (310 to 350°C).

In addition, a complex approach for the investigation of oxidation processes during HPAI in oil shales was demonstrated (Section 3.3). The corresponding workflow, including oxidation experiments and numerical simulation, was demonstrated by the example of Bazhenov Shale Formation. A set of oxidation study tests were carried out, namely: PDSC and RTO. As a result of experimental work, temperature ranges beyond which oxygen uptake rates are high were established, and Arrhenius parameters for low and high-temperature oxidation ranges were determined. It was revealed that the dominant oxidation mode corresponds to the low-temperature range, which indicates that oil and kerogen can be ignited spontaneously under reservoir temperature. In addition, the experiment highlighted a negative temperature gradient region, and the auto-ignition temperature corresponding to the onset of elevated oxygen uptake rates was estimated. During the validation of the numerical model with the experimental results, it was revealed that kerogen or its derivatives undergo oxidation in several temperature regions; therefore, it should be represented by separate pseudo-components, which reflect different physical-

chemical properties. As a result, the minimum set of kerogen pseudo-components in solid-phase are necessary for describing bond-scission oxidation reactions in LTR, which begin near 140°C, and HTR, which occur up to 600°C, and pyrolysis reaction, which occurs between 300°C and 650°C, was determined. The oxidation behavior of Bazhenov oil, which mostly contains light fractions, was represented by the bond-scission oxidation reaction of light oil in LTR and bond-scission oxidation reaction of heavy oil in HTR. Initial oxygen-addition reactions are not included in the proposed block of chemical reaction, despite the possibility of concluding their existence based on the results of RTO test. The chemical reactions and their kinetics proposed in this chapter, which are supported by extensive experimental data, can be used as a starting model for oil shale oxidation kinetic model development for other shale oil formation under the conditions associated with high-pressure air injection tests.

Chapter 4. Simulations of phase behavior of multicomponent multiphase hydrocarbon systems using direct energy minimization technique

Correctly determining phase behavior is important for the numerical simulation and evaluation of the recovery performance of thermal EOR methods in two-(or more)-phase reservoirs. Commercial reservoir simulators (e.g. CMG STARS, CMG GEM, ECLIPSE 300) use the following techniques to calculate the composition and properties of resulting phases in hydrocarbon mixtures: k-value correlations (Wilson), tabulated k-values, which does not depend on mixture composition, and flash calculations. The most precise one is considered to be the iterative flash calculation algorithm (Brusilovsky 2002; Danesh 1998; Orr 2005), which is computationally ineffective in the zone close to the critical due to the absence of convergence. In order to accelerate phase behavior calculations and reveal possible instabilities rapidly, ab initio flash calculation is used. This approach is incorporated in the commercial reservoir simulator Intersect and involves the initial application of successive substitutions, eigenvalues and eigenvectors of the BICs matrix. However, in case that the calculations do not converge, the traditional iterative algorithm is used (Firoozabadi and Pan, 2000). In this chapter, we consider an alternative to the flash calculations approach based on the direct minimization of the Helmholtz and Gibbs energy of a multicomponent mixture. The core of the algorithm is the non-linear free-energy constrained minimization problem, which is formulated in the form of a linear problem by discretization in compositional space and, as a result, could be solved by linear programming methods. With this approximation of compositional space, the convergence to a global minimum is guaranteed by the optimization algorithm. The Helmholtz and Gibbs energy minimization algorithms consist of the following major parts (see Figure 4.2 and Figure 4.4): the discretization of compositional space, whose dimension is in 1 less than a number of components (and one additional volume space dimension in case of the Helmholtz energy minimization), optimization problem solving, an optional iterative block of compositional grid refinement around the current optimal solution to solve the possible computation memory filling and post-processing for interpretation of the results.

The objective of this study is to demonstrate the applicability of this technique to hydrocarbon systems. To do this, flash calculations and the Gibbs energy minimization technique are compared in a series of numerical simulations. First, the agreement between these two approaches are shown for a set of binary mixtures. The mixtures of a particular composition are analyzed. The experimental parameters of these mixtures are known. Thus, the calculated and experimental values of phase properties are also compared. It is revealed that the proposed energy minimization technique may even reproduce experimental values better than flash calculations in the region close to the critical region. A certain computational advantage of the proposed technique is also shown. Second, the simulations are extended to multicomponent mixtures with three, five, and eleven components. Overall, the results make it possible to suggest that the proposed Helmholtz and Gibbs energy minimization techniques are applicable to describe the phase behavior of multicomponent fluids in a reservoir simulation.

4.1 Methods

In this study, we consider the Helmholtz energy minimization technique and compare it to flash calculations. Both of these approaches use equations of state (EOS) of multicomponent mixtures. Cubic EOS are commonly used to describe reservoir fluids. The two most popular EOS of this class are the Soave—Redlich—Kwong (SRK) and the Peng—Robinson (PR) equations (Brusilovsky 2002; Danesh 1998; Isaeva et al. 2018). These equations can be written for pressure p in the following general form

$$p = \frac{nRT}{V - nB_{\mathrm{M}}} - \frac{n^2 A_{\mathrm{M}}}{\left(V + \xi_1 nB_{\mathrm{M}}\right)\left(V + \xi_2 nB_{\mathrm{M}}\right)}, \qquad (1)$$

where n is the total number of moles of the phase (mixture) considered, T denotes the temperature, V denotes the phase volume, R is the universal gas constant, A_{M} and B_{M} - the phase parameters. The numerical coefficients ξ_1 and ξ_2 define a specific equation: $\xi_1 = 1$, and $\xi_2 = 0$ in SRK; $\xi_1 = \left(1 + \sqrt{2}\right)$, and $\xi_2 = \left(1 - \sqrt{2}\right)$ in PR. The parameters A_{M} and B_{M} can be interpreted as the molecule attraction and repulsion parameters (Orr, 2005).

Their values are constant if the phase consists of one component. For a mixture, A_{M} and B_{M} depend on the phase composition and the corresponding parameters of its individual components.

When EOS (1) is applied to a mixture, the specific expressions for A_{M} and B_{M} are given by the mixing rules. Random mixing rules are used:

$$A_{\mathrm{M}} = \sum_{i=1}^{N_c}\sum_{j=1}^{N_c} x_i x_j A_{ij}\,, \quad A_{ij} = \left(1-\delta_{ij}\right)\left(A_i A_j\right)^{\frac{1}{2}}, \tag{2}$$

$$B_{\mathrm{M}} = \sum_{i=1}^{N_c} x_i B_i\,,$$

where δ_{ij} are BIC between components i and j, x_i is the mole fraction of component i, N_c is the total number of components, A_i and B_i describe properties of individual components. If n_i denotes the number of moles of each component in the phase, $i = 1,2,\ldots,N_c$, then

$$n = \sum_{j=1}^{N_c} n_j\,, \qquad x_j = \frac{n_j}{n}. \tag{3}$$

EOS (1) is used in flash calculations the Helmholtz and Gibbs energy minimization cases. In the following part we begin with describing the flash calculations algorithm and we proceed to the free energy minimization techniques.

4.1.1 Flash calculations algorithm

The majority of phase equilibrium calculations for hydrocarbons are limited only to two phases: the vapor-liquid equilibrium is considered between liquid oil and gas. This assumption is popular because the effect of water on the hydrocarbon phase behavior can be neglected in a wide class of practical tasks (Danesh 1998). Thus, for simplicity, the vapor-liquid equilibrium is to be considered for illustrating the flash calculations procedure.

Figure 4.1 demonstrates the flowchart of flash calculations. The corresponding step-by-step algorithm can be found in (Brusilovsky 2002; Isaeva et al. 2018; Orr 2005). Flash

calculations start with initial (approximate) values of the equilibrium ratios (known as K-values). The K-value of component i is defined as

$$K_i = \frac{x_{i,V}}{x_{i,L}},$$

where $x_{i,V}$ is the mole fraction of component i in vapor, $x_{i,L}$ is the mole fraction of component i in liquid. K-values in multicomponent hydrocarbon systems depends on temperature, pressure, and composition. These parameters are provided to the input of the algorithm in Figure 4.1.

Flash calculations assume iterative refinement of the K-values set: from initial "guess" (typically the Wilson equation is used) to the values corresponding to vapor-liquid equilibrium. This iterative process relies on the equality of component fugacities in equilibrated vapor and liquid phases. As shown in Figure 4.1, the current K-value of component i is modified by multiplying it by the calculated ratio of component fugacities $\frac{f_{i,L}}{f_{i,V}}$, where $f_{i,L}$ is the fugacity of a component j in liquid, $f_{i,V}$ is the fugacity of a component i in vapor. Hence, when this ratio becomes close to one, the K-value almost stops changing. The same procedure is carried out with all components. The criterion to stop the iterative procedure is shown in Figure 4.1. The result of this procedure is interpreted as reaching the thermodynamic equilibrium between vapor and liquid phases. Thus, the corresponding K-values, fugacities, phase fractions, Z-factors, compositions are considered to describe the system (mixture) in vapor-liquid equilibrium.

The number of phases at equilibrium may not be known a priori (single-phase or two-phase state). However, this problem can be solved by combining flash calculations with the Michelsen stability test (Brusilovsky 2002; Danesh 1998; ECLIPSE 2014). Another limitation is related to calculations in the critical region, where the compositions of equilibrated phases are very close (Danesh 1998). This may result in large numbers of iterations in the procedure described above.

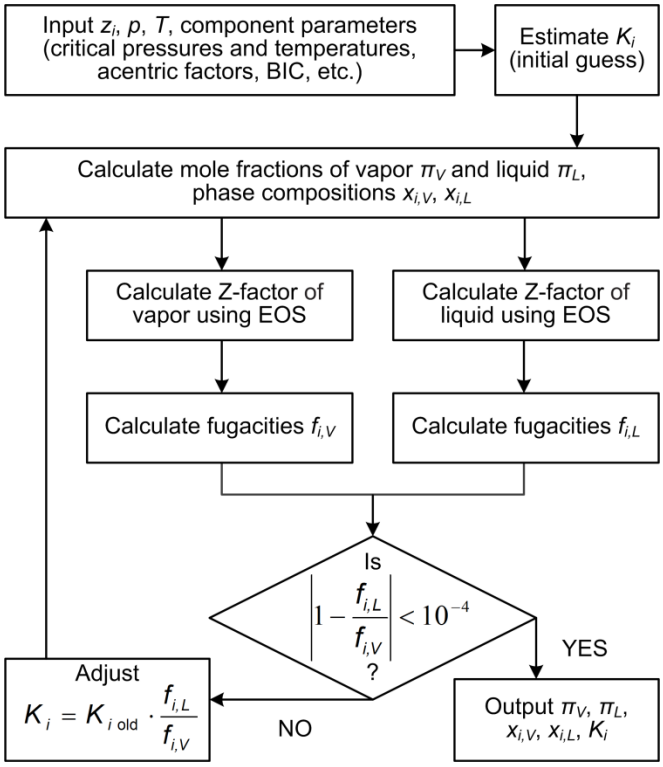

Figure 4.1 Flowchart of flash calculations (vapor-liquid equilibrium case)

Thus, flash calculations are based on the equality of fugacity of each component in vapor and liquid phases. This requirement is equivalent to the equality of component chemical potentials, which in turn is a consequence of the general criterion of thermodynamic equilibrium at a given pressure and temperature – the minimum Gibbs energy (Brusilovsky 2002; Danesh 1998). As shown in Appendix A, when EOS is known, it is possible to calculate the fugacity of a component i using the following expression

$$\ln(f_i) = \int_{V_0}^{\infty} \left(\frac{1}{RT} \left(\frac{\partial p}{\partial n_i} \right) \Bigg|_{T,V,n_{j\neq i}} - \left(\frac{1}{V} \right) \right) dV + \ln\left(\frac{n_i RT}{V_0} \right),$$

where V_0 is the phase volume at the considered temperature and pressure, all other parameters coincide with (1) and (3). For example, if we consider SRK or PR EOS (1) and mixing rules (2), the corresponding fugacity can be expressed as

$$\ln\left(\frac{f_i}{x_i p}\right) = -\ln\left(Z\left(1-\frac{\tilde{B}_{\mathrm{M}}}{Z}\right)\right) + \frac{\tilde{B}_i}{\tilde{B}_{\mathrm{M}}}(Z-1) + \left(\frac{\left(2\sum_{j=1}^{N_c} x_j \tilde{A}_{ij}\right) - \frac{\tilde{A}_{\mathrm{M}}\tilde{B}_i}{\tilde{B}_{\mathrm{M}}}}{\tilde{B}_{\mathrm{M}}(\xi_1-\xi_2)}\right)\ln\left(\frac{Z+\xi_2\tilde{B}_{\mathrm{M}}}{Z+\xi_1\tilde{B}_{\mathrm{M}}}\right), \quad (4)$$

where $Z = pV_0/RT$ is the compressibility factor, parameters $\tilde{A}_i$ and $\tilde{B}_i$ of individual components and, consequently, mixture parameters $\tilde{A}_{ij}$, $\tilde{A}_{\mathrm{M}}$, $\tilde{B}_{\mathrm{M}}$ are considered in the dimensionless form: $\tilde{A}_i = \frac{pA_i}{R^2T^2}$, $\tilde{B}_i = \frac{pB_i}{RT}$. The working expressions (4) are derived in Appendix B.

Hence, for flash calculations, it is not necessary to obtain the precise expression for the system energy (Gibbs or Helmholtz energy). Indeed, our reasoning in Appendices A and B involves only derivatives of the thermodynamic state functions.

In this study, an alternative approach is proposed. An explicit expression for the Helmholtz and Gibbs energy of a multi-component mixture is obtained, and its minimum is sought after.

4.1.2 Minimization of Helmholtz energy

Let us consider the Helmholtz energy F of a multi-component system (phase) with N_c components. With independent variables of temperature T and volume V, it can be formally written as

$$F = F\left(T, V, n_1, \ldots n_{N_c}\right),$$

where n_i, as above, is the number of moles of each component, $i = 1, \ldots, N_c$.

We can restore the expression for the Helmholtz energy using the information on its derivatives. As shown in Appendix A, the first derivatives of the Helmholtz energy are related to the component chemical potential μ_i and the system pressure p

$$\left(\frac{\partial F}{\partial n_i}\right)\Bigg|_{T,V,n_{j\neq i}} = \mu_i, \qquad \left(\frac{\partial F}{\partial V}\right)\Bigg|_{T,n_i} = -p.$$

Hence, it can give, for example, the Helmholtz energy change of a phase at constant temperature T and composition n_i due to the volume change from V_1 to V_2

$$F(T,n_i,V_2)-F(T,n_i,V_1)=-\int_{V_1}^{V_2} pdV\,.$$

Since EOS (1) is being considered, by integration, we have

$$F(T,n_i,V_2)-F(T,n_i,V_1)=-\left(nRT\ln(V-nB_{\mathrm{M}})-\frac{nA_{\mathrm{M}}}{B_{\mathrm{M}}(\xi_1-\xi_2)}\ln\left(\frac{V+\xi_2 nB_{\mathrm{M}}}{V+\xi_1 nB_{\mathrm{M}}}\right)\right)\Bigg|_{V_1}^{V_2}.$$

Thus, for the Helmholtz energy of a multicomponent phase, it can be written

$$F(T,n_i,V)=E(T,n_i)-\left(nRT\ln(V-nB_{\mathrm{M}})-\frac{nA_{\mathrm{M}}}{B_{\mathrm{M}}(\xi_1-\xi_2)}\ln\left(\frac{V+\xi_2 nB_{\mathrm{M}}}{V+\xi_1 nB_{\mathrm{M}}}\right)\right), \quad (5)$$

Where the term $E(T,n_i)$ denotes the part of the Helmholtz energy that is independent of the system volume V. In order to describe isothermal processes with mass exchange between the phases, the dependence of $E(T,n_i)$ on n_i must be revealed. This dependence can be restored using the fugacities discussed above. Fugacities are related to the component chemical potentials and defined by the expression

$$\mu_i''-\mu_i'=RT\ln\left(\frac{f_i''}{f_i'}\right)=RT\left(\ln(f_i'')-\ln(f_i')\right),$$

where μ_i'' and μ_i' are the chemical potentials of a component i corresponding to two different states of the system (phase), f_i'' and f_i' are the fugacities of a component i in these system states. Hence, expression (4) or its equivalent in the dimensional form given in Appendix B can be used and is written

$$RT\ln(f_i)=RT\ln(n_iRT)-RT\ln(V-nB_{\mathrm{M}})+\left(\frac{n\,RTB_i}{V-nB_{\mathrm{M}}}\right)+$$
$$+\left(\frac{\left(2\sum_{j=1}^{N_c}x_jA_{ij}\right)-\frac{A_{\mathrm{M}}B_i}{B_{\mathrm{M}}}}{B_{\mathrm{M}}(\xi_1-\xi_2)}\right)\ln\left(\frac{V+\xi_2 nB_{\mathrm{M}}}{V+\xi_1 nB_{\mathrm{M}}}\right)-\left(\frac{nA_{\mathrm{M}}B_i}{B_{\mathrm{M}}}\right)\frac{V}{(V+\xi_1 nB_{\mathrm{M}})(V+\xi_2 nB_{\mathrm{M}})}, \quad (6)$$

where parameters A_i, B_i, A_{ij}, A_{M}, B_{M} are non-reduced. Thus, we have information on component chemical potentials from (6).

At this point, one of two ways can be selected. First, by analogy with the derivation of formula (5), the increment of chemical potential from (6) can be expressed and integrated with respect to n_i obtaining the corresponding Helmholtz energy change. This procedure may give additional information on the term $E(T,n_i)$ in (5). In the second approach, the last term in (5) can be differentiated with respect to n_i – this gives terms included in the chemical potential. Comparing these terms with (6) reveals the additions that must be included in the Helmholtz energy (5). The second way seems to be easier, since it only requires differentiation. Thus, differentiating (5) dives

$$\frac{\partial}{\partial n_i}\left(F(T,n_i,V)-E(T,n_i)\right)=-RT\ln\left(V-nB_{\mathrm{M}}\right)+\left(\frac{n\,RTB_i}{V-nB_{\mathrm{M}}}\right)+$$
$$+\left(\frac{\left(2\sum_{j=1}^{N_c}x_jA_{ij}\right)-\dfrac{A_{\mathrm{M}}B_i}{B_{\mathrm{M}}}}{B_{\mathrm{M}}\left(\xi_1-\xi_2\right)}\right)\ln\left(\frac{V+\xi_2nB_{\mathrm{M}}}{V+\xi_1nB_{\mathrm{M}}}\right)-\left(\frac{nA_{\mathrm{M}}B_i}{B_{\mathrm{M}}}\right)\frac{V}{\left(V+\xi_1nB_{\mathrm{M}}\right)\left(V+\xi_2nB_{\mathrm{M}}\right)}. \tag{7}$$

The derivation of (7) is discussed in detail in Appendix C.

Comparing (6) and (7) shows that (6) includes the additional term $RT\ln(n_iRT)$. Hence, in order to make the Helmholtz energy (5) consistent with (6) it can be considered in the following form

$$F(T,n_i,V)=C(T)+\sum_{i=1}^{N_c}RTn_i\left(\ln\left(RTn_i\right)-1\right)-$$
$$-nRT\ln\left(V-nB_{\mathrm{M}}\right)+\frac{nA_{\mathrm{M}}}{B_{\mathrm{M}}\left(\xi_1-\xi_2\right)}\ln\left(\frac{V+\xi_2nB_{\mathrm{M}}}{V+\xi_1nB_{\mathrm{M}}}\right), \tag{8}$$

where the additional term $C(T)$ may depend on temperature. Note that this term stays the same for any state of a multi-component system in isothermal processes; therefore, we are not interested here in its specific form.

Now having the explicit expression for the Helmholtz energy of a multicomponent phase (8), we can proceed with the minimization problem. The rigorous method for determining the equilibrium at a given temperature and volume is to find the conditions at which the Helmholtz energy of a system is at its global minimum for all possible combinations of phases and component distribution (Brusilovsky 2002; Danesh 1998; Orr 2005). When we consider a multiphase system in the thermodynamic equilibrium, its total Helmholtz energy can be written in the simple form

$$F = \sum_{\alpha=1}^{N_P} F_\alpha \pi_\alpha , \qquad (9)$$

where F_α is the Helmholtz energy of phase α per mole, π_α is the number of moles of phase α, N_P denotes the number of phases (Gmehling et al. 2012). For simplicity, let us consider one mole of a multi-component multiphase system; hence, we can write

$$\sum_{\alpha=1}^{N_P} \pi_\alpha = 1 . \qquad (10)$$

For example, in the case of a vapor-liquid system, we have the Helmholtz energy (9) in the form $F = F_V \pi_V + F_L \pi_L$ where π_V and π_L are the mole fractions of vapor and liquid phases, respectively $\pi_V + \pi_L = 1$.

The Helmholtz energy of the individual phase F_α in (9) depends on the temperature T, phase composition, and molar volumes V_α: $F_\alpha = F_\alpha\left(T, x_{i,\alpha}, V_\alpha\right)$, where $x_{i,\alpha}$ denotes the mole fraction of component i in phase α. EOS (1) is assumed to describe the behavior of each phase in the multicomponent multiphase system. Hence, for $F_\alpha\left(T, x_{i,\alpha}, V_\alpha\right)$, the expression (8) can be used.

Let us formalize the requirement of minimum Helmholtz energy at the thermodynamic equilibrium conditions. One mole of a mixture is considered, in which the overall mole fraction of component i is z_i, $i = 1,2,\ldots,N_c$. At a given volume V and temperature T, the global minimum value of (9) is sought after for all possible combinations of phases π_α and

component distribution $x_{i,\alpha}$. The mole fractions of phases π_α and component fractions in phases $x_{i,\alpha}$ must satisfy (10) and the following additional conditions

$$\sum_{\alpha=1}^{N_P} V_\alpha \pi_\alpha = V, \qquad \sum_{\alpha=1}^{N_P} x_{i,\alpha}\pi_\alpha = z_i, \qquad i = 1,2,\ldots,N_c. \tag{11}$$

Overall, it gives the minimization problem that can be considered as a linear programming problem. Indeed, the total Helmholtz energy (9) has the form of the dot product if we interpret the sets $(\pi_1, \pi_2, \ldots, \pi_{N_P})$ and $(F_1, F_2, \ldots, F_{N_P})$ as vectors. Hence, the thermodynamic equilibrium conditions can be rewritten as the following linear programming problem:

$$x_{i,\alpha}, V_\alpha, \pi_\alpha = \arg\left(\min_{\tilde{x}_{i,\alpha}, \tilde{V}_\alpha, \tilde{\pi}_\alpha} \left(\sum_{\alpha=1}^{N_P} F_\alpha \tilde{\pi}_\alpha \right) \right), \tag{12}$$

where $x_{i,\alpha}$, V_α and π_α must satisfy the constraints (10) and (11); the values $F_\alpha = F_\alpha(T, x_{i,\alpha}, V_\alpha)$ in (12) are calculated in accordance with (8).

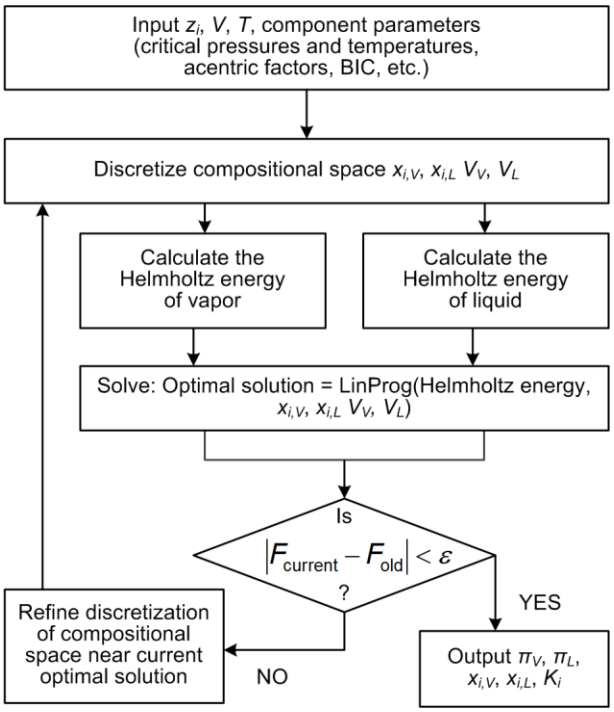

Figure 4.2. Flowchart of Helmholtz energy minimization algorithm (vapor-liquid equilibrium case)

The Helmholtz energy minimization algorithm for solving the minimization problem specified by (12) with the constraints (10) and (11) is implemented in Matlab and presented in Figure 4.2. It consists of two main parts: the discretization of independent variable space and the minimization technique – linear programming solver using the simplex method. In the case of Helmholtz energy $F_\alpha = F_\alpha\left(T, x_{i,\alpha}, V_\alpha\right)$ minimization at given P-T-C conditions, since the independent variables are temperature, system composition, and system volume, both volume and compositional space should be discretized. To illustrate the result of the Helmholtz energy minimization algorithm, let us consider a binary system Methane-Ethane at a temperature of 250 K, the initial composition of Methane – 0.4791, and different pressures – 4.8114 MPa and 8.1060 MPa, which correspond to initial system volumes - $6.0376*10^{-5}$ m^3/mol (dimensionless value: 0.1754) and $1.5386*10^{-4}$ m^3/mol (dimensionless value: 0.4470). In this case, the discretized space of independent variables is two-dimensional (2D) - volume-composition of Methane space. The discrete values of Helmholtz energy at each point of the 2D volume-composition space obtained for the binary system Methane-Ethane under different initial conditions (blue star), and the corresponding optimal solution (black circles), as a result of Helmholtz energy minimization, are visualized in Figure 4.3. In Figure 4.3 (a), it is shown that the initial point in 2D dimensionless volume-composition of Methane space $\left(V, x_1\right)$ has coordinates of (0.4470, 0.4791), which is represented by a blue star. Likewise, Figure 4.3 (a) demonstrates that the optimal solution consists of two points with different coordinates in volume-compositional space (see black circles in Figure 4.3(a)). This means that under these initial conditions, two values of Helmholtz energy $F_V = F_V\left(V_V, x_{1,V}\right)$ and $F_L = F_L\left(V_L, x_{1,L}\right)$ with specific fractions π_V and π_L, satisfy the minimization problem specified by (12) with the constraints (10) and (11), or, in other words, this result corresponds to a case of two coexisting phases with mole fractions of π_V and π_L for vapor and liquid phases, respectively, $\pi_V + \pi_L = 1$. It should be mentioned, that the optimal values of Helmholtz energy obtained for each phase and mole fractions satisfy (9).

The result of the second case with a higher initial pressure of 8.1060 MPa is presented in Figure 4.3(b). Here we can see that the points corresponding to the optimal solution (black circles) are located very close (~ length of minimal discretization interval) to the point corresponding to the initial system value (blue star) in the dimensionless volume-composition-space. This means that under these initial conditions, two values of Helmholtz energy and satisfying the minimization problem specified by (12) with the constraints (10) and (11) represent the same value, or, in other words, this result corresponds to the case of a critical region where the difference between phases is imperceptible.

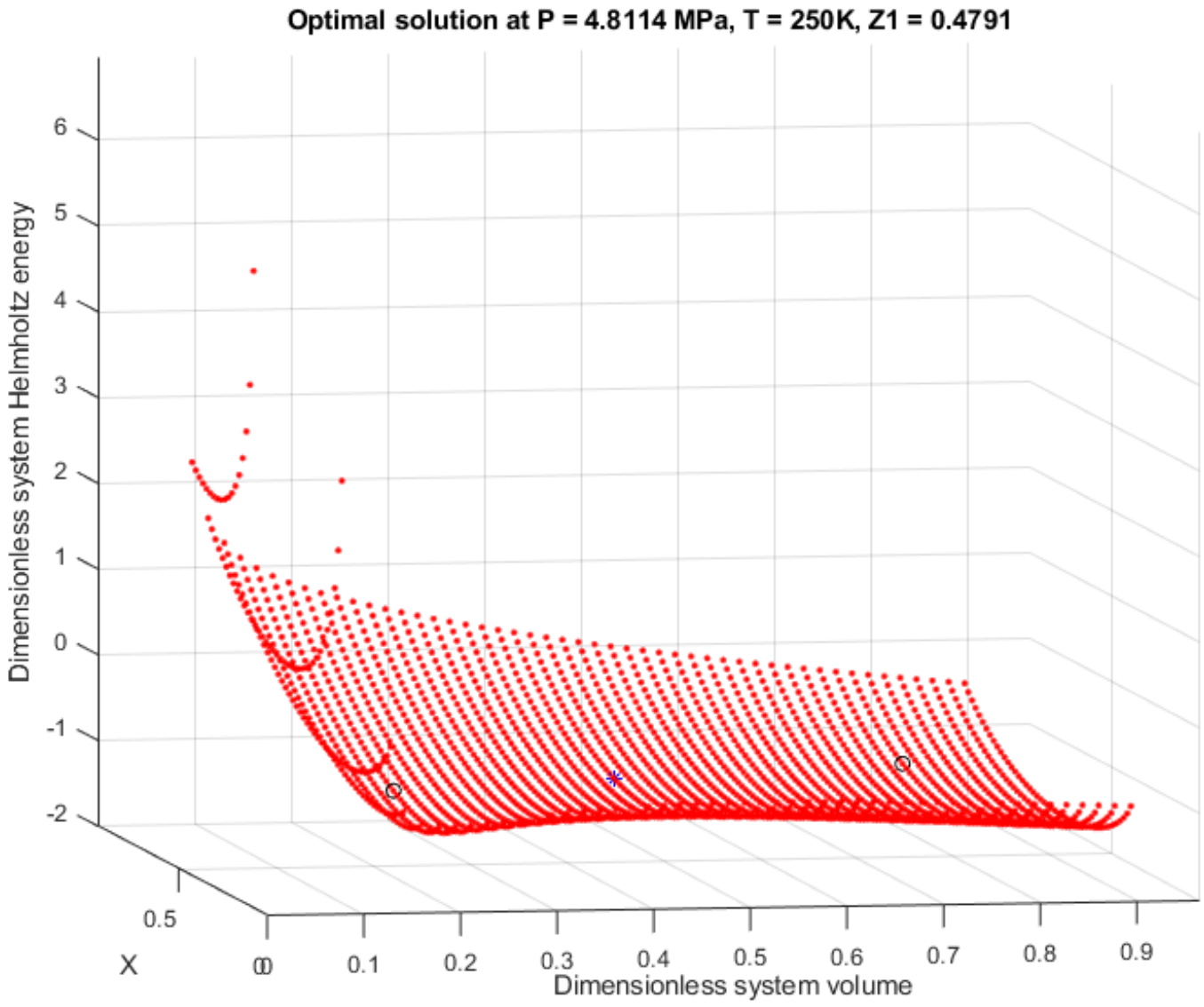
Optimal solution at P = 4.8114 MPa, T = 250K, Z1 = 0.4791
Dimensionless system Helmholtz energy
6
5
4
3
2
1
0
-1
-2
X
0.5
0
0.1
0.2
0.3
0.4
0.5
0.6
0.7
0.8
0.9
Dimensionless system volume

(a)

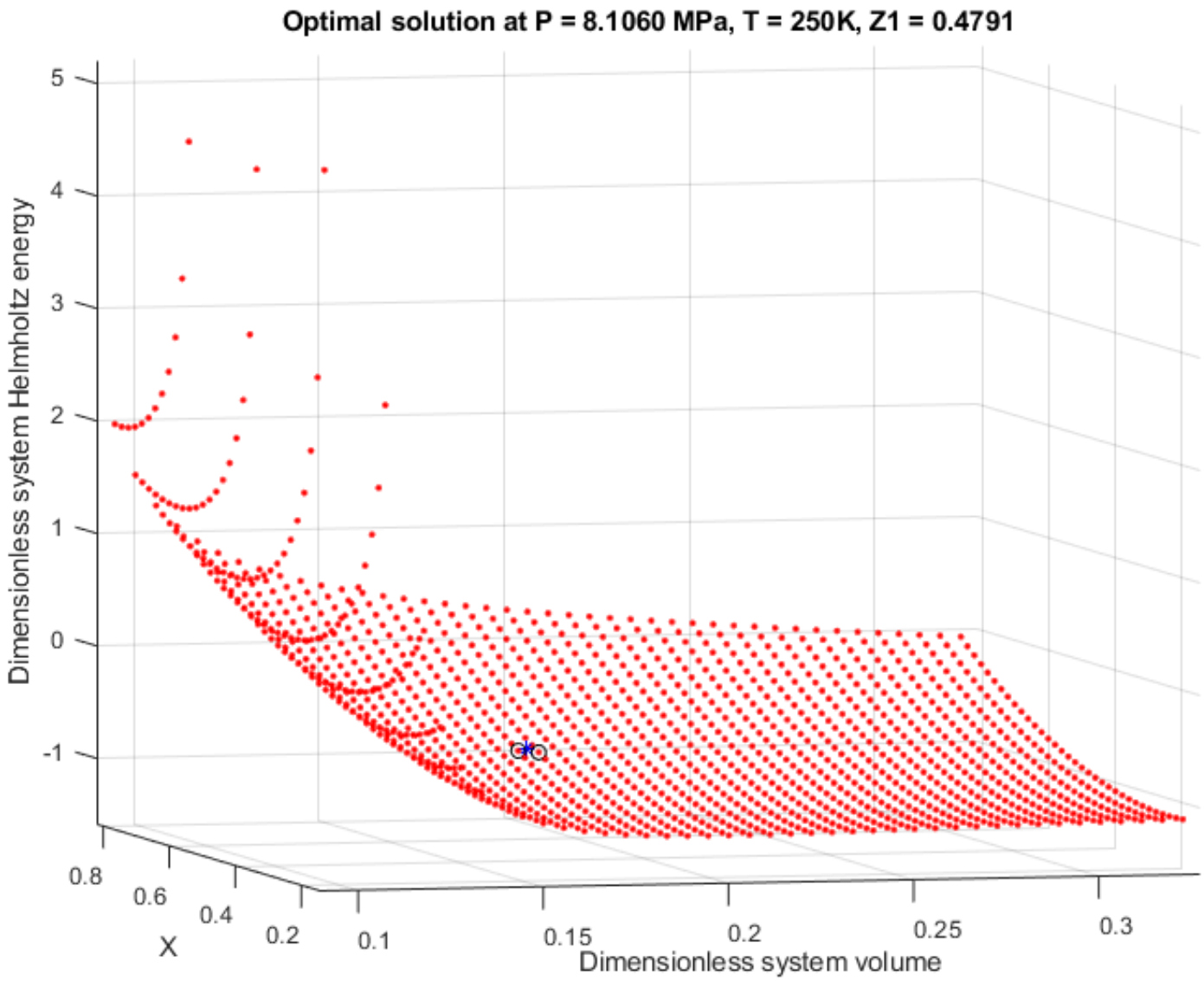

(b)

Figure 4.3. Visualization of dimensionless system Helmholtz energy in discrete volume and compositional space for binary system Methane-Ethane under different initial conditions (blue star), and corresponding optimal solution (black circles). a) Initial conditions correspond to the two-phase region: P = 4.8114 MPa, T = 250 K, Z1 = 0.4791; b) Initial conditions correspond to the critical region: P = 8.1060 MPa, T = 250 K, Z1 = 0.4791.

4.1.3 Minimization of Gibbs energy

The Gibbs energy minimization can be used to reduce the number of space dimensions of independent variables and, as a result, to decrease memory reservation during calculations. Let us consider the Gibbs energy G of a multi-component system (phase) with N_c components. With independent variables of temperature T and pressure p, it can be formally written

$$G = G\left(T, p, n_1, ...n_{N_c}\right),$$

where n_i, as above, is the number of moles of each component, $i = 1, \ldots, N_c$.

For simplicity, let us consider one mole of a multi-component multiphase system; hence, EOS (1) for a one-mole system may be rewritten as

$$pV^3 + (B_M p - T)V^2 + (A_M - 2TB_M - 3B_M^2 p)V + B_M^3 p + TB_M^2 - A_M B_M . \quad (13)$$

Choosing the real roots of (13) we can calculate the molar volumes $V_\alpha = V_\alpha\left(T, x_{i,\alpha}, p\right)$ of each phase. Substituting $V_\alpha = V_\alpha\left(T, x_{i,\alpha}, p\right)$ to the expression for Helmholtz energy of individual phase $F_\alpha = F_\alpha\left(T, x_{i,\alpha}, V_\alpha\right)$, we make a transition from independent variables of $\left(T, x_{i,\alpha}, V_\alpha\right)$ to $\left(T, x_{i,\alpha}, p\right)$.

Taking into account $G_\alpha = F_\alpha + pV_\alpha$ finally gives the expression for Gibbs energy for each individual phase

$$\begin{aligned} G_\alpha\left(T, x_{i,\alpha}, p\right) &= C(T) + \sum_{i=1}^{N_c} RT\left(\ln\left(RT\right) - 1\right) - \\ &- RT\ln\left(V_\alpha - B_{\mathrm{M}}\right) + \frac{A_{\mathrm{M}}}{B_{\mathrm{M}}\left(\xi_1 - \xi_2\right)} \ln\left(\frac{V_\alpha + \xi_2 B_{\mathrm{M}}}{V_\alpha + \xi_1 B_{\mathrm{M}}}\right) + pV_\alpha , \end{aligned} \quad (14)$$

The total Gibbs energy for a multiphase system has the form

$$G = \sum_{\alpha=1}^{N_P} G_\alpha \pi_\alpha , \quad (15)$$

where G_α is the Gibbs energy of phase α per mole, π_α is the number of moles of phase α, N_P denotes the number of phases. For one mole of a multi-component multiphase system, it can be written

$$\sum_{\alpha=1}^{N_P} \pi_\alpha = 1. \qquad (16)$$

In the case of a vapor-liquid system, the Helmholtz energy (9) is in the form $F = F_V \pi_V + F_L \pi_L$, where π_V and π_L are the mole fractions of vapor and liquid phases, respectively, $\pi_V + \pi_L = 1$.

Let us formalize the requirement for the Gibbs energy minimum under thermodynamic equilibrium conditions. One mole of a mixture is considered in which the overall mole fraction of component i is $z_i, i = 1,2,\ldots,N_c$. At a given pressure p and temperature T we search for the global minimum value of (15) for all possible combination of phases π_α and component distribution $x_{i,\alpha}$. The mole fractions of phases π_α and component fractions in phases $x_{i,\alpha}$ must satisfy (16) and the following additional conditions

$$\sum_{\alpha=1}^{N_P} x_{i,\alpha}\pi_\alpha = z_i, \qquad i = 1,2,\ldots,N_c. \qquad (17)$$

The thermodynamic equilibrium conditions can be rewritten in the form of the following linear programming problem:

$$x_{i,\alpha}, \pi_\alpha = \arg\left(\min_{\tilde{x}_{i,\alpha}, \tilde{\pi}_\alpha} \left(\sum_{\alpha=1}^{N_P} G_\alpha \tilde{\pi}_\alpha \right) \right), \qquad (18)$$

where $x_{i,\alpha}$ and π_α must satisfy the constraints (16) and (17); the values $G_\alpha = G_\alpha\left(T, x_{i,\alpha}, p\right)$ in (12) are calculated in accordance with (14).

The Gibbs energy minimization algorithm for solving the minimization problem specified by (18) with the constraints (16) and (17) is implemented in Matlab and presented in Figure 4.4. The algorithm is similar to the Helmholtz energy minimization algorithm and includes discretization of the independent variable space, determination of the values of free-energy at each point of the discretized space, and solving the constrained minimization problem

with linear programming solver (LinProg) with predetermined input data (system temperature and pressure, discretized component compositions in the range of (0, 1) and values of Gibbs energy for each grid point of the discretized compositional space). At each point $x_{i,\alpha}$ several coexisting phases (two, vapor and liquid, for hydrocarbon mixtures) with its own value of phase volume exist, and for each of these phases, the Gibbs energy should be specified and used as input data in the LinProg solver.

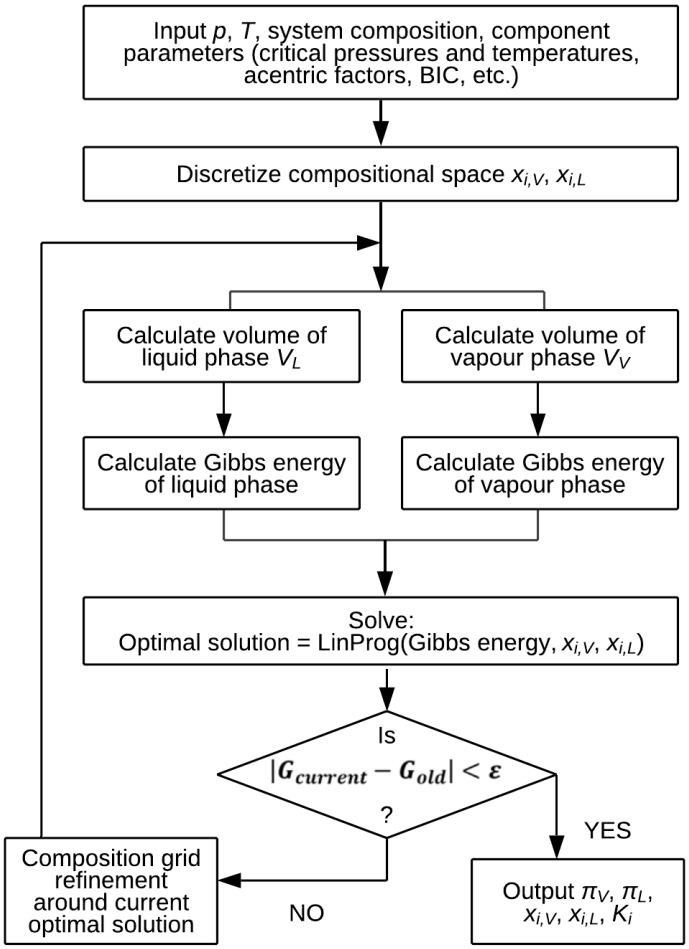

Figure 4.4. Flowchart of Gibbs energy minimization algorithm (vapor-liquid equilibrium case)

It should be mentioned that under equilibrium conditions, the system pressure coincides with the pressures of each coexisting phase. Thus, in the case of Gibbs energy $G_\alpha = G_\alpha\left(T, x_{i,\alpha}, p\right)$ minimization at given P-T-Z conditions, only the compositional space

is required to be discretized. This allows us to reduce the dimension of the discretized independent variable space in comparison to Helmholtz energy minimization and, as a result, to reduce the amount of reserved computer memory necessary for calculation.

In order to illustrate the result of the Gibbs energy minimization algorithm, let us consider the binary Methane-Ethane system at the same conditions described in Section 4.1.2, where the graphical representation of the Helmholtz energy minimization algorithm is discussed. In the case of Gibbs energy, the discretized space of independent variables is one-dimensional (1D) - composition of Methane space. The discrete values of Gibbs energy at each point of the 1D compositional space obtained for the binary Methane-Ethane system under different initial conditions (blue star), and the corresponding optimal solution (black circles), as a result of Gibbs energy minimization, are visualized in Figure 4.5. The discretized 2D-volume-compositional space used in the case of Helmholtz energy (Figure 4.3) is collapsed to 1D-compositional space (see Figure 4.5 (a), (c)). Figure 4.5 (b) and Figure 4.5 (d) show a graphical representation of the optimal solutions found as a result of the Gibbs energy minimization algorithm for the case of two coexisting phases and for the case when the system is in a critical state. It should be noted that the obtained molar fractions of resulting phases and phase compositions coincide with the results of the Helmholtz energy minimization algorithm (Section 4.1.2). Note, the system volume, which is an input parameter for the Helmholtz energy minimization algorithm, is calculated in the postprocessing of the Gibbs energy minimization algorithm according to (11).

It should be noted that the proposed algorithms (Figure 4.2 and Figure 4.4) can be implemented in CUDA on graphical processing units (GPUs). The results presented in this chapter were calculated in Matlab without any specific parallel computing technology application. It has been proven that that the implementation of high dimension linear programming algorithms on GPUs could give the performance advantages more than one order (Boyer et al., 2017).

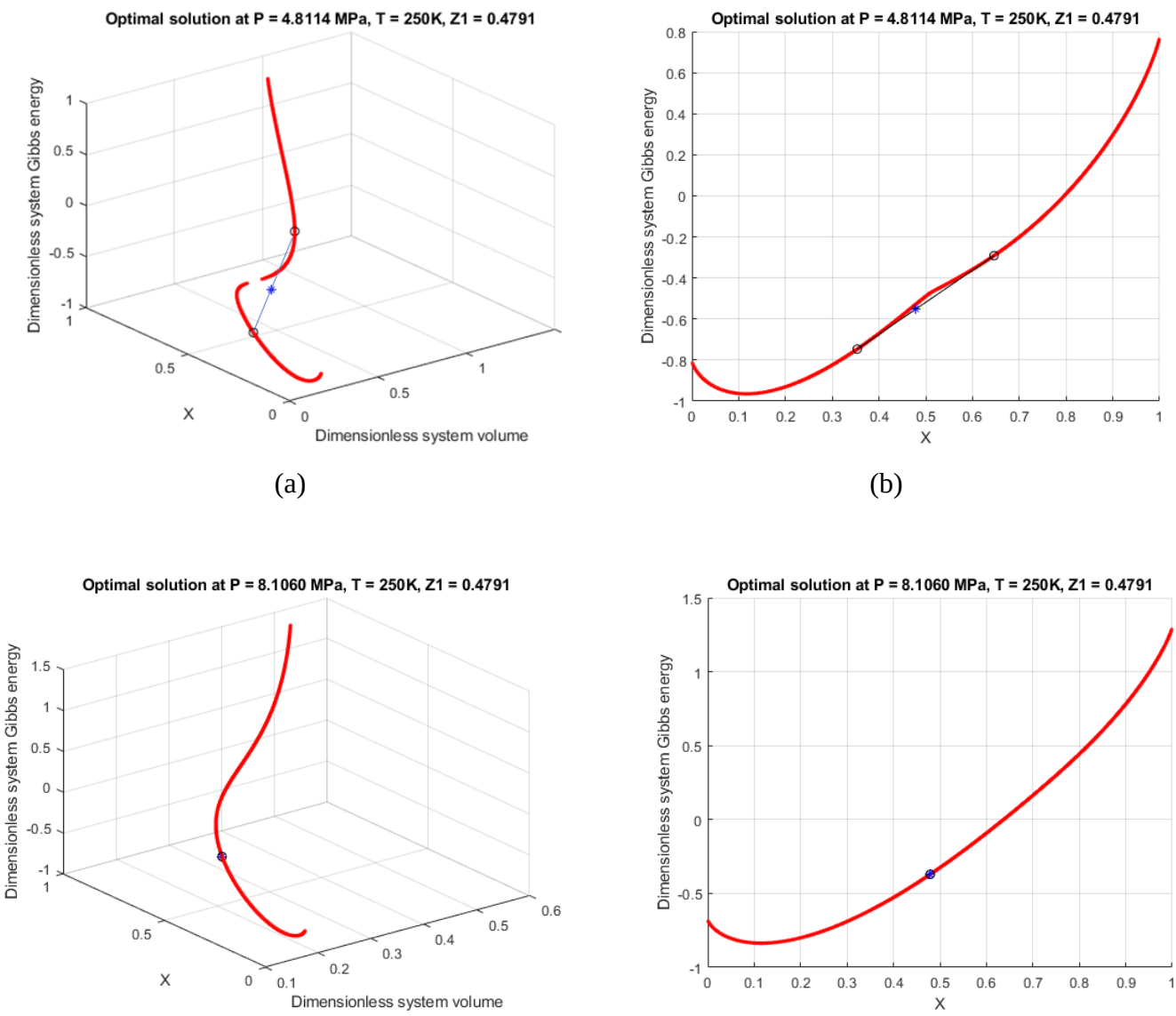

Figure 4.5. Visualization of dimensionless system Gibbs energy in discrete compositional space for binary Methane-Ethane system under different initial conditions (blue star), and corresponding optimal solution (black circles). a,b) Initial conditions correspond to the two-phase region: P = 4.8114 MPa, T = 250 K, Z1 = 0.4791; c,d) Initial conditions correspond to the critical region: P = 8.1060 MPa, T = 250 K, Z1 = 0.4791.

4.2 Results

Flash calculations and the proposed free-energy minimization technique were compared in numerical simulations. The numerical calculations provided by the Helmholtz and Gibbs minimization algorithms are identical and differ in computation time. The Gibbs minimization algorithm has an advantage in its computation time since it makes it possible to reduce the dimension of the discretized space of an independent variable in comparison to the Helmholtz energy minimization. Thus, the results presented in this Section are provided based on the minimization of Gibbs energy. To proceed, the binary mixtures are considered, the experimental parameters of which are known.

As discussed above, flash calculations result in K-values that are considered to correspond to the system vapor-liquid equilibrium. In addition to the set of K-values, mole fractions and compositions of the equilibrated phases are obtained. Thus, we can present the calculation results, for example, in the form of a pressure-composition phase diagram. Figure 4.6 (a) demonstrates the pressure-composition phase diagram for the Methane—Ethane binary mixture obtained by flash calculations (the Methane—Ethane mixture was considered at a temperature of 250 K). The component parameters (critical temperature, critical pressure, acentric factor, BIC, etc.) correspond to the tables in Appendix A in (Danesh 1998). We use PR EOS in our simulations. The color in Figure 4.6 (a) gives information on the calculated mole fraction of vapor: dark red represents the pure vapor phase without liquid; dark blue color represents the pure liquid phase without vapor. The multicolor transition from dark blue to dark red corresponds to the two-phase region and represents the evaporation process. The white circles in the diagram demonstrate experimental data, which show the boundaries of the two-phase region (Davalos et al., 1976). The calculated boundaries of the two-phase region are shown by a thin white line in Figure 4.6 (a).

Figure 4.6 (b) presents the calculated pressure-composition phase diagram obtained by the proposed Gibbs energy minimization technique. The colors and other designations in Figure 4.6 (b) are the same as in Figure 4.6 (a). By analyzing Figure 4.6 (a) and Figure 4.6(b), we can draw the following conclusions. First, it can be seen that there is good

agreement between the diagrams calculated by the two different approaches. One might not even visually recognize the difference in the diagrams in Figure 4.6 (a) and Figure 4.6 (b). Indeed, the difference is small up to the critical region. This fact is illustrated in Figure 4.7. Figure 4.7 shows the modulus of the difference in the calculated mole fractions of the vapor phase obtained by two approaches. The maximum pressure presented in Figure 4.7 is equal to 95% of the critical pressure. Thus, at such pressures, the mole fractions of the vapor calculated by the two approaches differ in no more than the second digit after the decimal point. The greatest difference is seen in the critical region. Figure 4.8 (a) shows the zoomed in area of the diagram in Figure 4.6 (a) corresponding to the critical region. Figure 4.6 (b) shows the same zoomed area taken from the diagram in Figure 4.6 (b). A difference in the diagram behavior can be seen. This result is quite expected since flash calculations may result in unreliable values for physical properties in the critical region (Danesh, 1998). Flash calculations require large numbers of iterations in the critical region – Figure 4.9 shows the actual number of iterations used in our simulations to obtain the results in Figure 4.8 (a). The maximum number of iterations is 100. This limitation is used to get the results of flash calculations in a reasonable time. In this case, the computational time required to obtain the vapor-liquid equilibrium parameters at constant composition is equal to 58.89s. The same calculations take 22.03s in the case of Gibbs energy minimization. The flash calculations computation time is mostly controlled by the time necessary to calculate the parameters of vapor-liquid equilibrium near the critical zone (see Figure 4.19). Thus, the chosen limitation for a maximum number of iterations is large enough to provide an accuracy of the calculation near the critical zone that can be compatible with the one provided by the free energy minimization algorithm. Note, the maximum number of iterations is equal to six by default in ECLIPSE 300 (ECLIPSE 2014). Thus, we see in Figure 4.9 that even with such large values of the maximum number of iterations, performing flash calculations in the critical region is problematic. However, comparing Figure 4.8 (a) and Figure 4.8 (b), to confirm or disprove that the flash calculations introduce the greatest error, we need more detailed experimental data on the parameters of the mixture in the critical region. Second, both the Gibbs energy

minimization technique and flash calculations give good agreement between calculated and experimental results. It can be seen that the calculated boundaries of two-phase regions are very close to the experimental data obtained by Davalos et al.,1976.

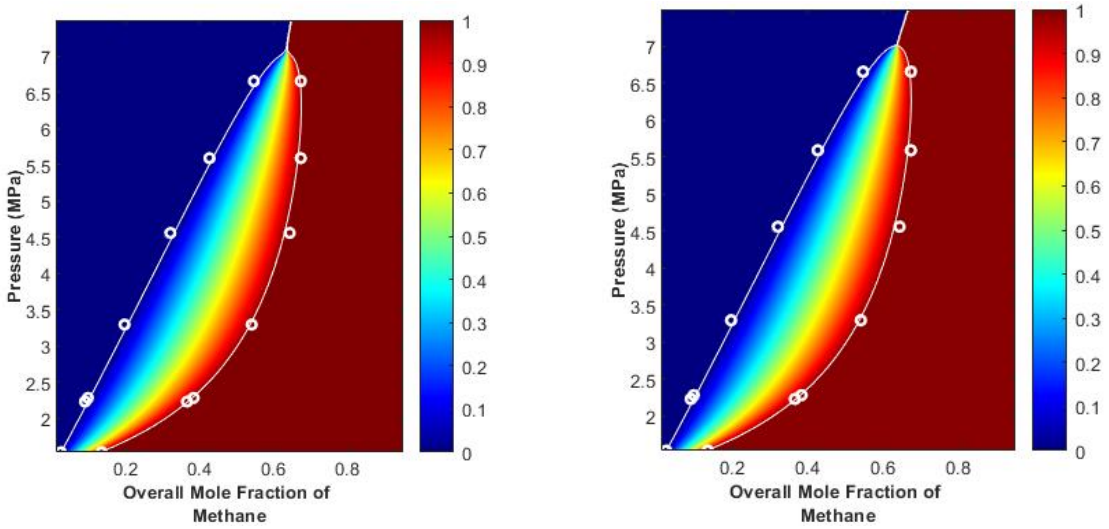

(a) (b)

Figure 4.6 Pressure-composition phase diagram for methane—ethane binary mixture at T = 250 K as a result of a) flash calculations and b) Gibbs minimization algorithm

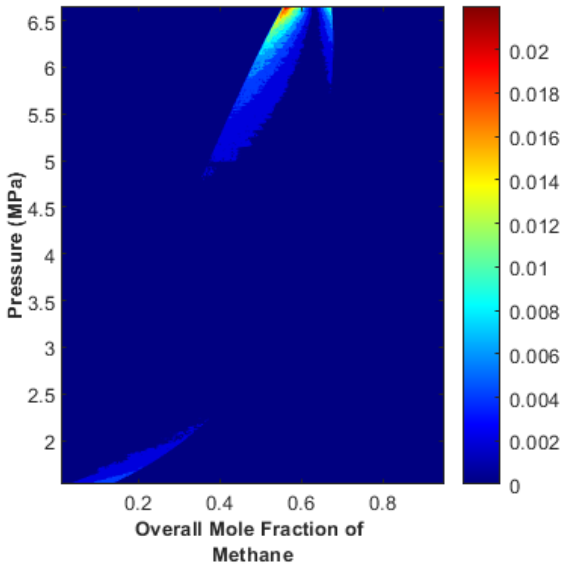

Figure 4.7 Modulus of difference in molar fractions of vapor phase calculated by flash calculations and the proposed Gibbs energy minimization technique (methane—ethane binary mixture)

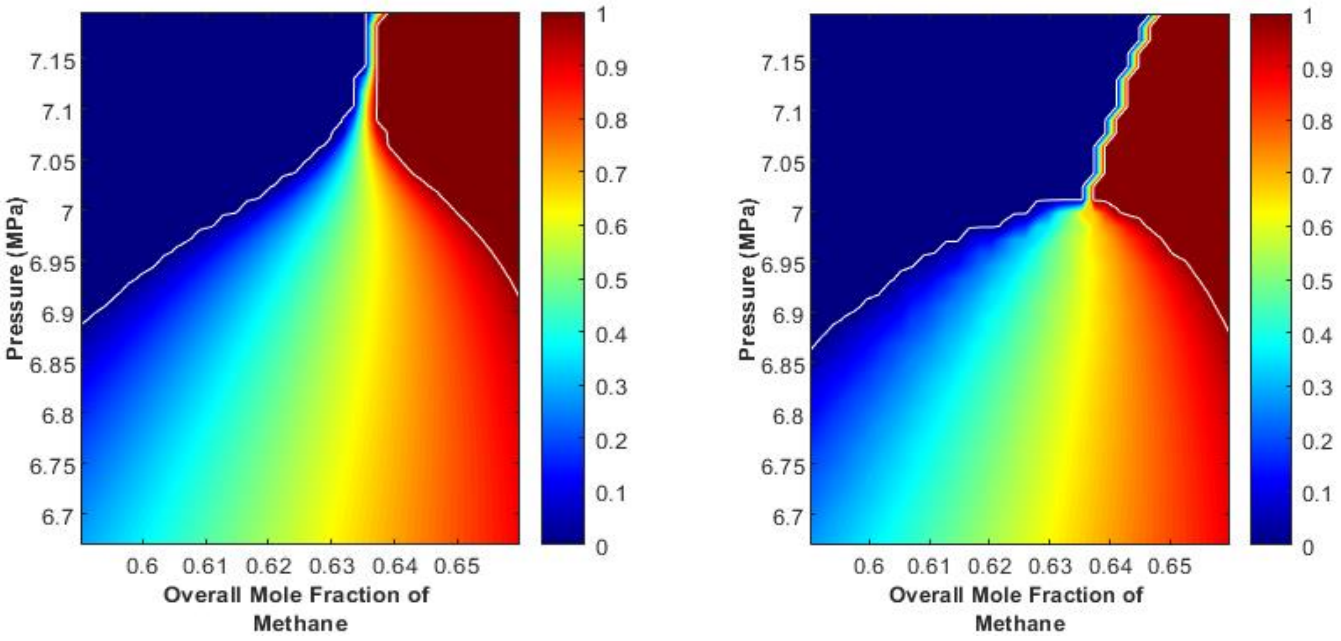

(a) (b)

Figure 4.8 Zoomed in fragment of pressure-composition phase diagram for methane—ethane binary mixture at T = 250 K as a result of a) flash calculations and b) Gibbs minimization algorithm

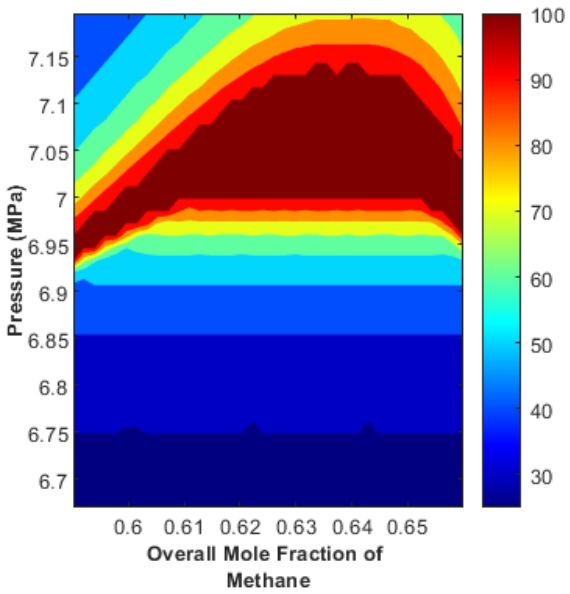

Figure 4.9 Actual number of iterations used in flash calculations (methane—ethane binary mixture)

Since K-values and phase compositions are important in reservoir simulation, these parameters are considered for the methane—ethane binary mixture. Figure 4.10 shows the obtained K-values at different pressures for this mixture: Figure 4.10 (a) presents K-values for methane; Figure 4.10 (b) presents K-values for ethane. The K-values obtained by flash calculations are shown in blue, and the K-values obtained by the Gibbs energy minimization technique is shown in red. The experimental K-values are also shown in Figure 4.10 by black circles (Davalos et al. 1976). Figure 4.11 gives information on the phase compositions in the same pressure range for the methane—ethane binary mixture. Figure 4.11 (a) presents the composition of liquid phase. Figure 4.11 (b) presents the composition of vapor phase. The experimental mole fractions of methane are shown by green circles, and the mole fractions of ethane are shown by black circles in Figure 4.11 (Davalos et al. 1976). The values obtained by flash calculations are shown in blue, and the values obtained by the Gibbs energy minimization technique are shown in red. Analyzing Figure 4.10 and Figure 4.11 shows a good correspondence between the calculated and experimental values. Thus, it can be stated that the proposed Gibbs energy minimization technique is not inferior in accuracy to flash calculations for the methane—ethane binary mixture.

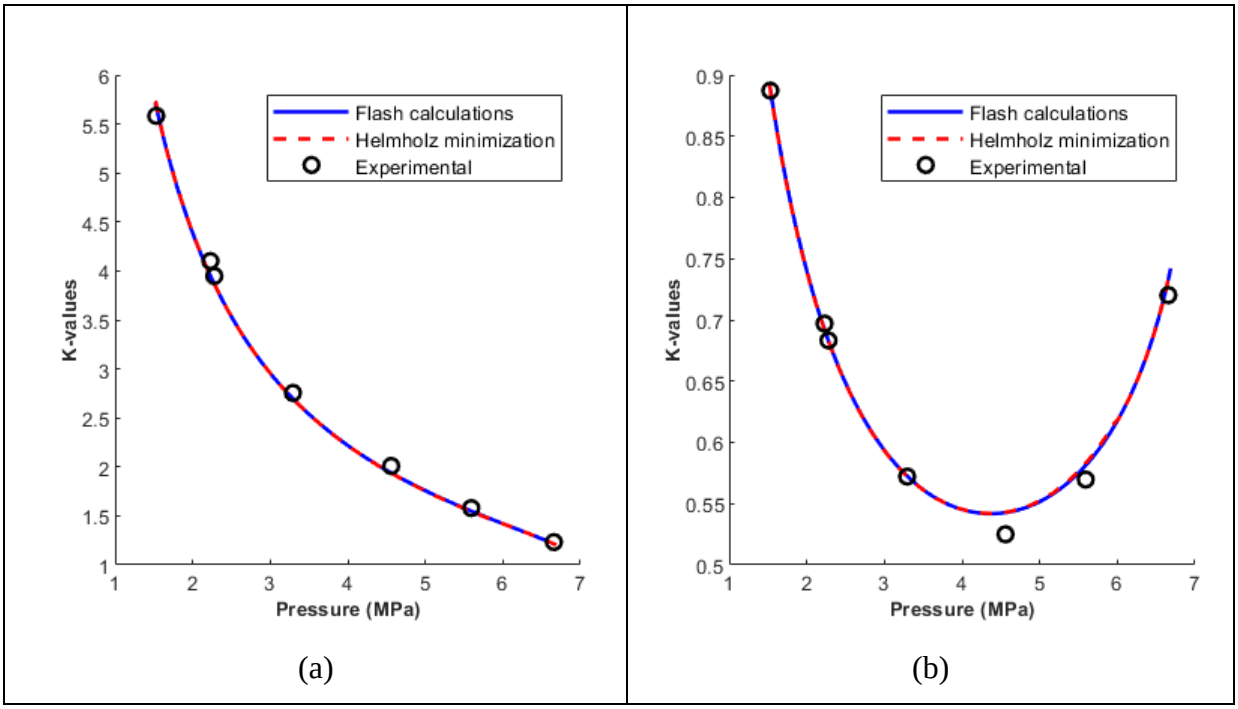

Figure 4.10 K-values at different pressures for methane—ethane binary mixture at T = 250 K for a) methane and b) ethane component

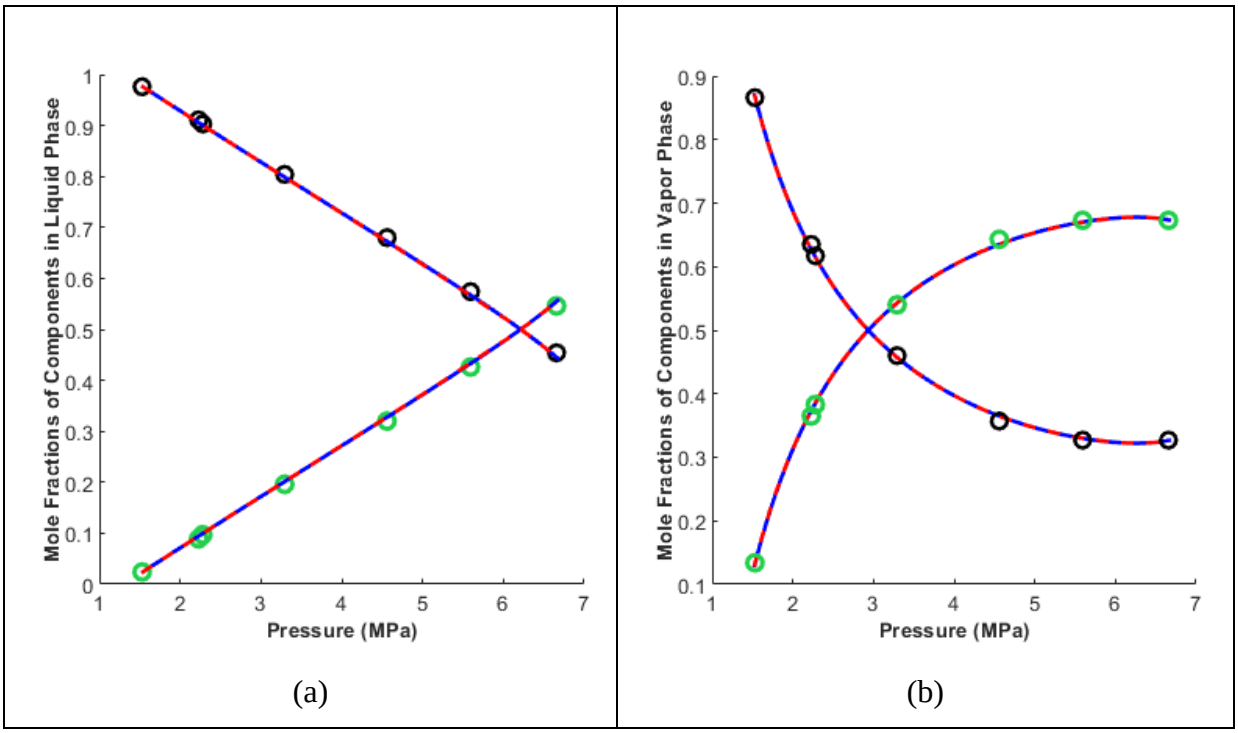

Figure 4.11 Phase compositions at different pressures for methane—ethane binary mixture at T = 250 K: a) liquid phase, b) vapor phase

Analogous calculations were performed for the methane—n-heptane binary mixture (the methane—n-heptane mixture considered at a temperature 344.3 K). The corresponding pressure-composition diagrams are shown in Appendix D. It is advisable to consider here the K-values and phase compositions for this mixture. Figure 4.12 (a) presents K-values for methane, and Figure 4.12 (b) presents K-values for n-heptane. The designations in Figure 4.12 are the same as in Figure 4.10. Figure 4.13 (a) and Figure 4.13 (b) present the phase compositions of liquid and vapor phases by analogy with Figure 4.11 (a) and Figure 4.11 (b). The experimental mole fractions of methane are shown by green circles, and mole fractions of n-heptane are shown by black circles in Figure 4.13 (Reamer et al. 1956). Values obtained by flash calculations are shown in blue, and values obtained by the Gibbs energy minimization technique are shown in red. We see that for pressures above 20 MPa the values obtained by the proposed Gibbs energy minimization technique are closer to the experimental data than the values obtained by flash calculations. In this pressure range, the methane—n-heptane mixture approaches its critical region (see also figure D.1 in Appendix D). As discussed above, flash calculations may result in inaccurate values for physical properties of phases. This effect explains the results in Figure 4.12 and Figure 4.13. Thus, we show that the proposed Gibbs energy minimization technique has advantages in describing physical properties of phases in the critical region.

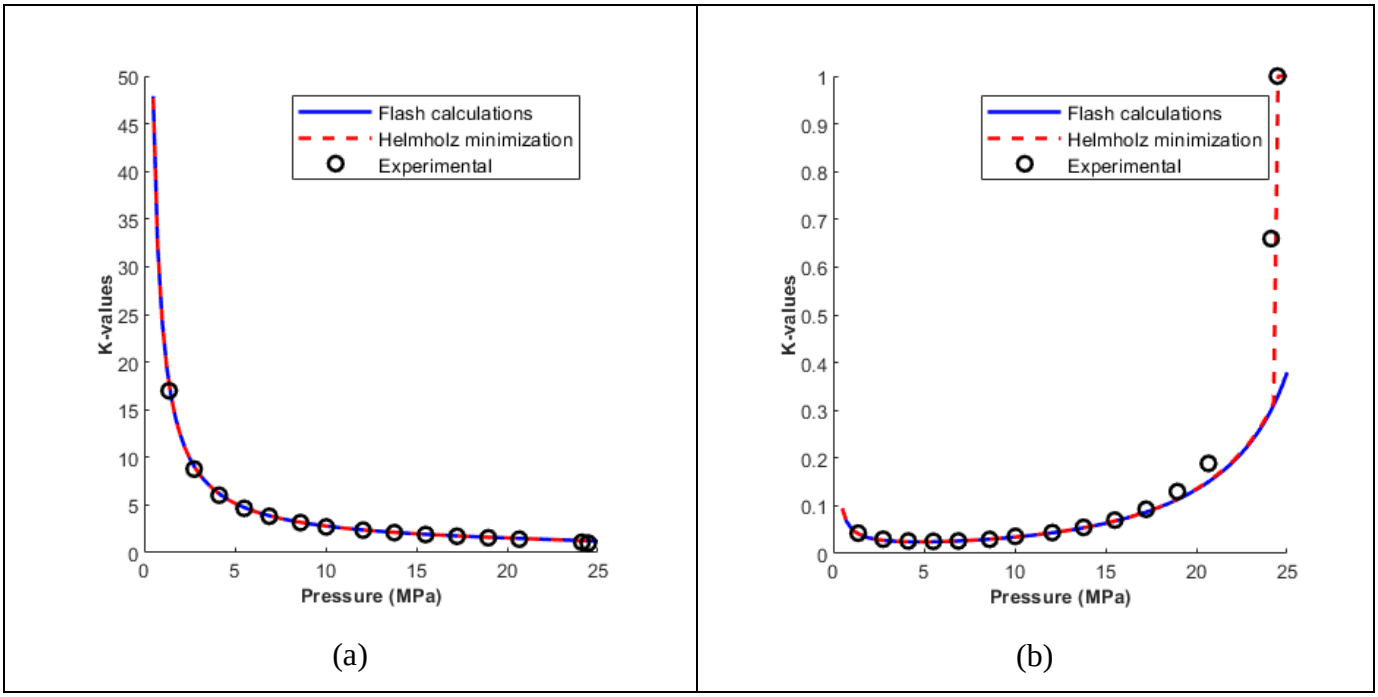

Figure 4.12 K-values at different pressures for methane—n-heptane binary mixture at T = 344.3 K for a) methane and b) n-heptane

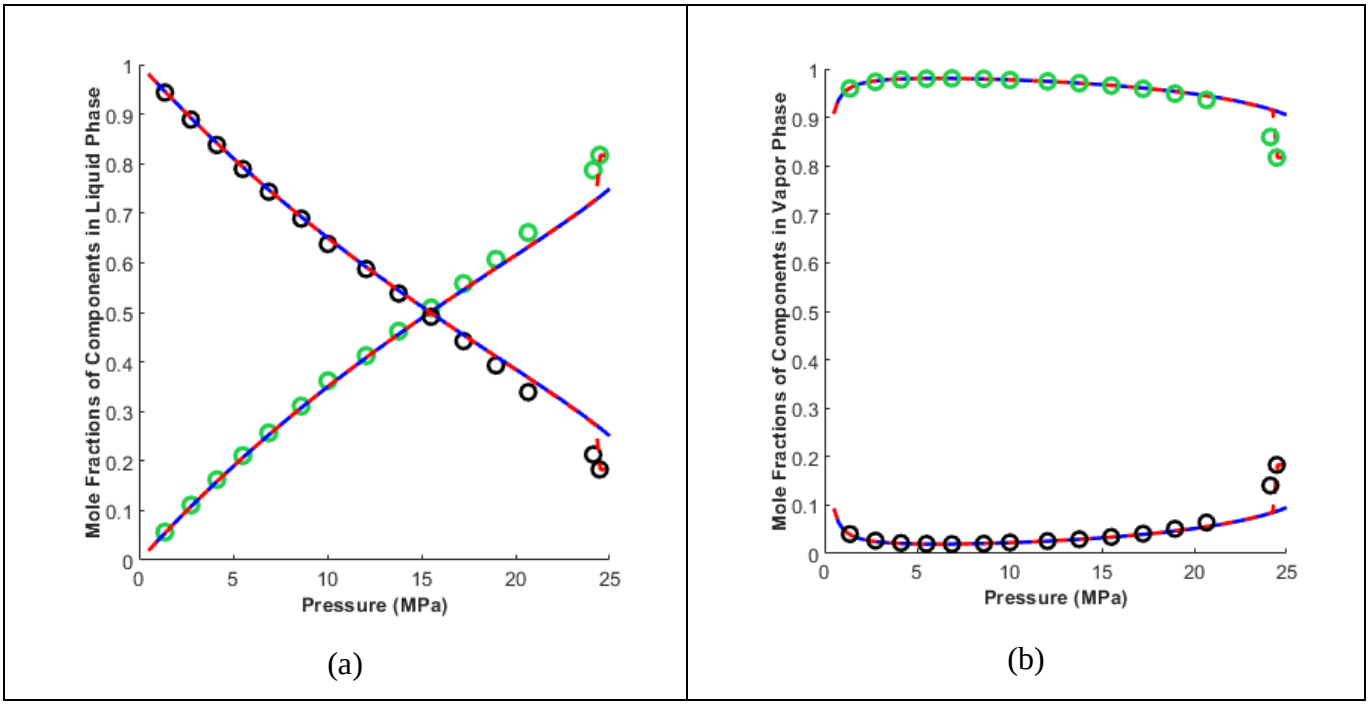

Figure 4.13 Phase compositions at different pressures for methane—n-heptane binary mixture at T = 344.3 K: a) liquid phase, b) vapor phase

In addition to the binary mixtures of hydrocarbons, we consider binary mixtures of hydrocarbons with carbon dioxide: methane—carbon dioxide and ethane—carbon dioxide binary mixtures. The corresponding pressure-composition diagrams and other results are shown in Appendix D. Overall results obtained for the binary mixtures suggest that the proposed Gibbs energy minimization technique is applicable to describe the vapor-liquid equilibrium for both pairs of hydrocarbons and binary mixtures of hydrocarbons with carbon dioxide.

In order to illustrate the applicability of the proposed Gibbs energy minimization technique for mixtures with more than two components, we consider ternary mixtures and 5-component mixture with known experimental data. Figure 4.14 shows the ternary diagram for the methane—ethane—carbon dioxide mixture (at a pressure 2.53 MPa and temperature 250 K). The rules for reading the ternary diagram in Figure 4.14 correspond to Brusilovsky 2002. The color scheme in Figure 4.14 is the same as used in Figure 4.6: the transition from dark blue to dark red corresponds to an increase in the mole fraction of vapor from zero to one. Figure 4.12 (a) presents the results obtained by flash calculations. Figure 4.12 (b) presents results obtained by the proposed Gibbs energy minimization technique. White circles in Figure 4.14 demonstrate the experimental boundaries of the two-phase region (Davalos et al. 1976). We see that the two considered methods give close results and demonstrate good correspondence to the experimental data. We present the results of analogues calculations for the methane—ethane—n-pentane ternary mixture in Appendix E.

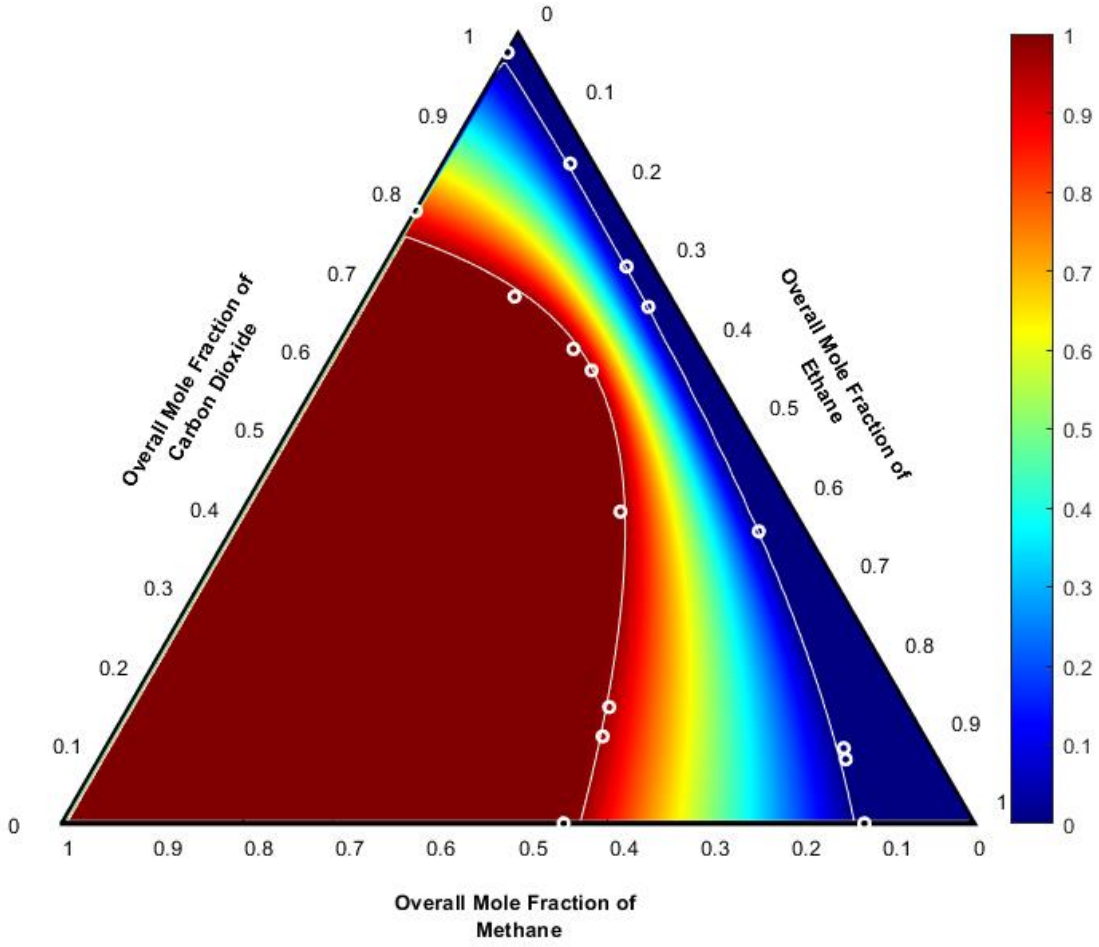
Overall Mole Fraction of Carbon Dioxide
Overall Mole Fraction of Ethane
Overall Mole Fraction of Methane
0
0.1
0.2
0.3
0.4
0.5
0.6
0.7
0.8
0.9
1

(a)

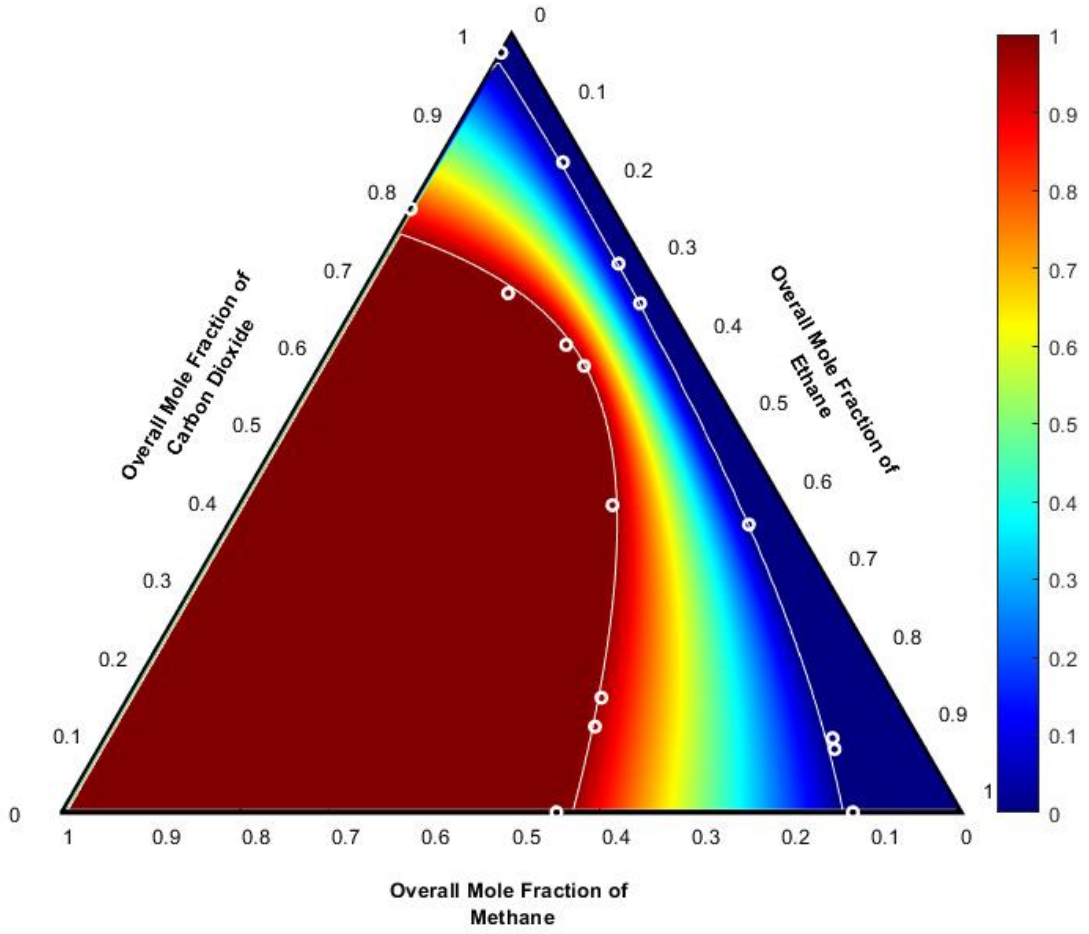

(b)

Figure 4.14 Ternary phase diagram for the methane—ethane—n-pentane ternary mixture at at P = 2.53 MPa and T = 250 K obtained by a) flash calculations and b) Gibbs energy minimization algorithm. The transition from dark blue to dark red corresponds to an increase in the mole fraction of vapor from zero to one. White circles and white lines demonstrate the experimental and calculated boundaries of the two-phase region, respectively

We consider a multicomponent mixture with five components: methane (70.57 mole%), ethane (6.69 mole%), propane (4.13 mole%), n-butane (5.08 mole%), n-pentane (13.53 mole%). The quinary mixture considered at a pressure of 9.867 MPa and temperature 311 K. Figure 4.15 presents both calculated and experimental K-values of the components. Figure 4.16 (a) shows the corresponding composition of the liquid phase, and Figure 4.16 (b) shows the composition of the vapor phase. The experimental values in Figure 4.15 and

Figure 3.16 are shown in yellow and taken from (Hanson and Brown, 2002). The K-values obtained by flash calculations are shown in blue, and the K-values obtained by the Gibbs energy minimization technique is shown in red. We see an agreement between the calculated and experimental values. Thus, we see that the proposed Gibbs energy minimization technique is applicable to predict the parameters of multicomponent mixtures with more than two components.

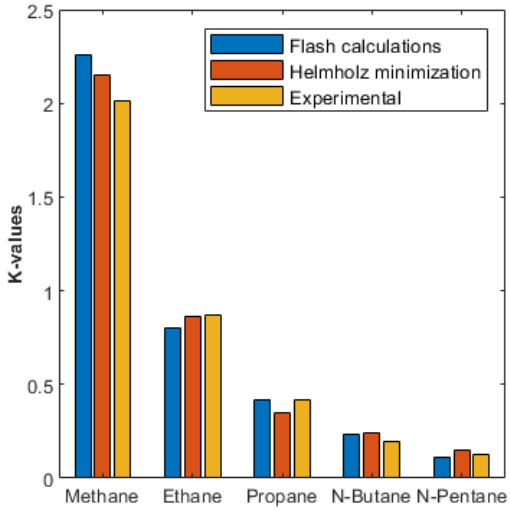

Figure 4.15 K-values for the components of the quinary mixture

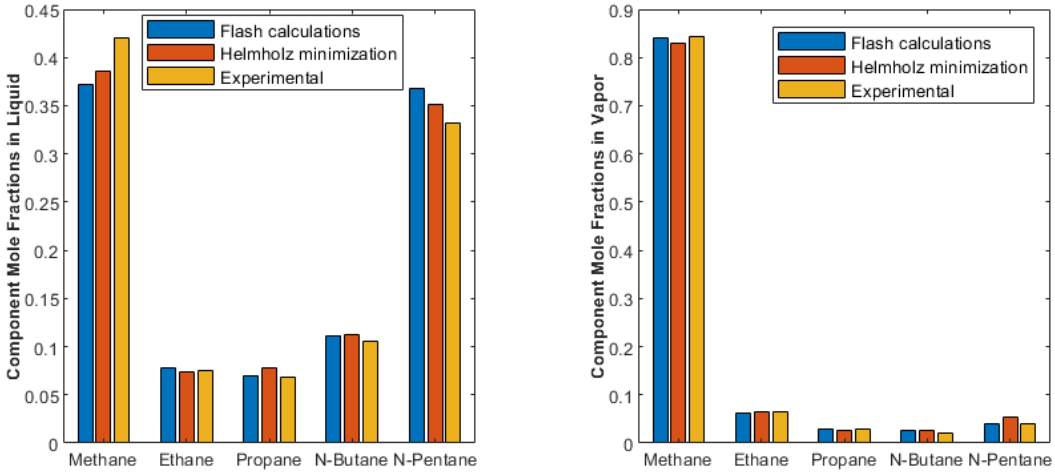

(a) (b)

Figure 4.16 Phase compositions of the quinary mixture at P = 9.867 MPa and T = 311 K in a) liquid and b) vapor phases in case of flash calculations (blue), Gibbs energy minimization algorithm (red) and experiment (orange)

Figure 4.17 shows the results calculated for the same quinary mixture at different pressures: 3.5646 MPa, 6.5224 MPa, 8.9425 MPa, 9.8664 MPa, 11.9693 MPa. In the bar chart, a column represents the fractions of each component in liquid and vapor phases in quinary mixture at different P-T conditions, the total sum of fractions equals to 1. The columns with the blue and red frames reflect results calculated by flash algorithm and Gibbs energy minimization algorithm, respectively, and show a good correspondence with experimental values (columns with green frames). In addition, the effect of hydrocarbons condensation with increasing pressure is observed in the bar chart.

In the case of a quinary mixture, the Gibbs energy minimization algorithm requires 4-dimensional compositional space to be discretized. The directions of the compositional space correspond to the range of possible compositions of hydrocarbons; the considered mixture consisted of (in this case, methane, ethane, propane, and n-butane). To reach a calculation accuracy compatible with the accuracy we observed in case of binary mixtures, or, in another words, to obtain the results close to experimental, it was necessary to use a number of grid points of order of 1000 in each direction. In the case of 4D compositional space, the total number of grid points tended to 1000^4, which resulted in computer memory problems. To avoid it, Gibbs minimization algorithm with developed compositional space refinement option was used. It allowed to reduce the necessary number of points in compositional space to 576, which corresponded to 6×6×4×4 grid points in each directions (it the direction of methane, ethane, propane, and n-butane composition, respectively). This refining algorithm included determination of an optimal solution on a coarse-grained composition, the initial guess, as a result of the first iteration, and following compositional grid refinement around an optimal solution defined in the previous iteration step. In this case, the number of compositional space refining iterations were 50, and the tolerance number to exit the iteration was chosen as 10^{-4}. The resulting total computational time was 1.6615s, which was even less than the computational time required to calculate one point in pressure-compositional diagram (see Figure 4.6).

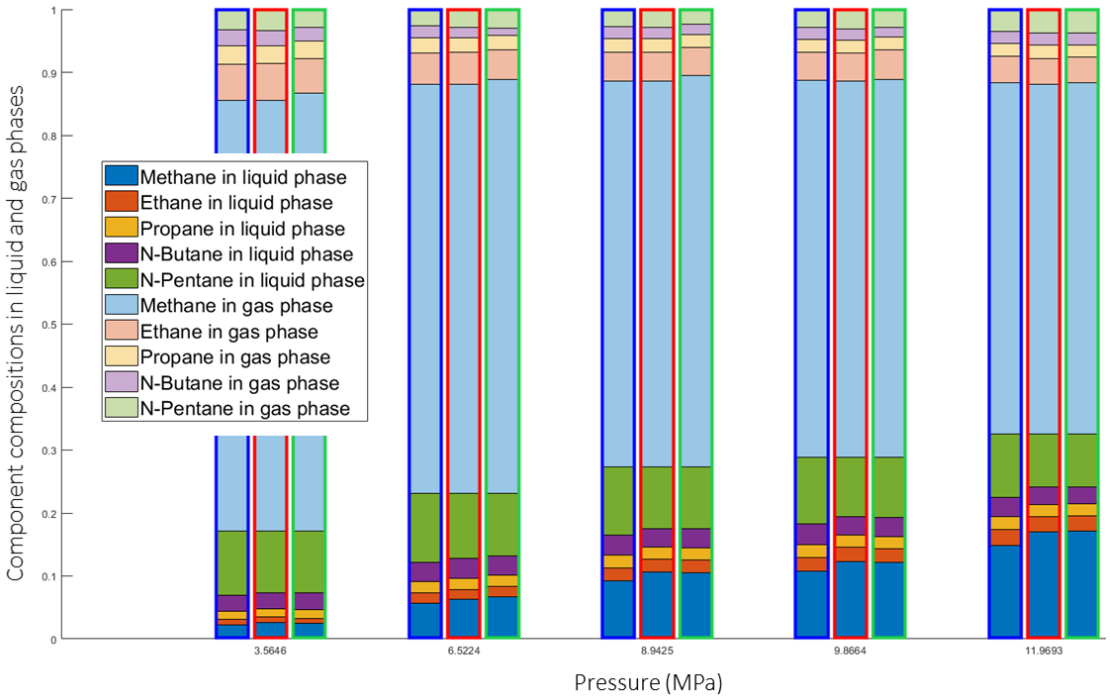

Figure 4.17 Compositions of the quinary mixture for vapor and liquid phases at T = 311 K and different pressures: 3.5646 MPa, 6.5224 MPa, 8.9425 MPa, 9.8664 MPa, 11.9693 MPa in case of flash calculations (blue frame), Gibbs energy minimization algorithm (red frame) and experiment (green frame)

The developed algorithm allows solving the phase (vapor-liquid) equilibrium problem also for more than 5-component mixtures avoiding the computational memory problem appearing due to increasing the compositional space dimension. Its performance efficiency was demonstrated on the example of phase equilibrium determination for 11-component mixture at the conditions that experimental results were known. The liquid and vapor phase compositions calculated and compared with experimental results published in RD 39-1-348-80 are presented in Figure 4.18. This mixture consists of hydrocarbons (methane, ethane, propane, i-butane, n-butane, i-pentane, n-pentane, hexane, and heptane) and non-hydrocarbons, such as nitrogen, carbon dioxide, which are compulsorily presented in reacting and propagating fluids during ISC or HPAI and influence on the phase equilibrium. The vapor and liquid compositions calculated with Gibbs energy calculation algorithm give a good correspondence with experimental values.

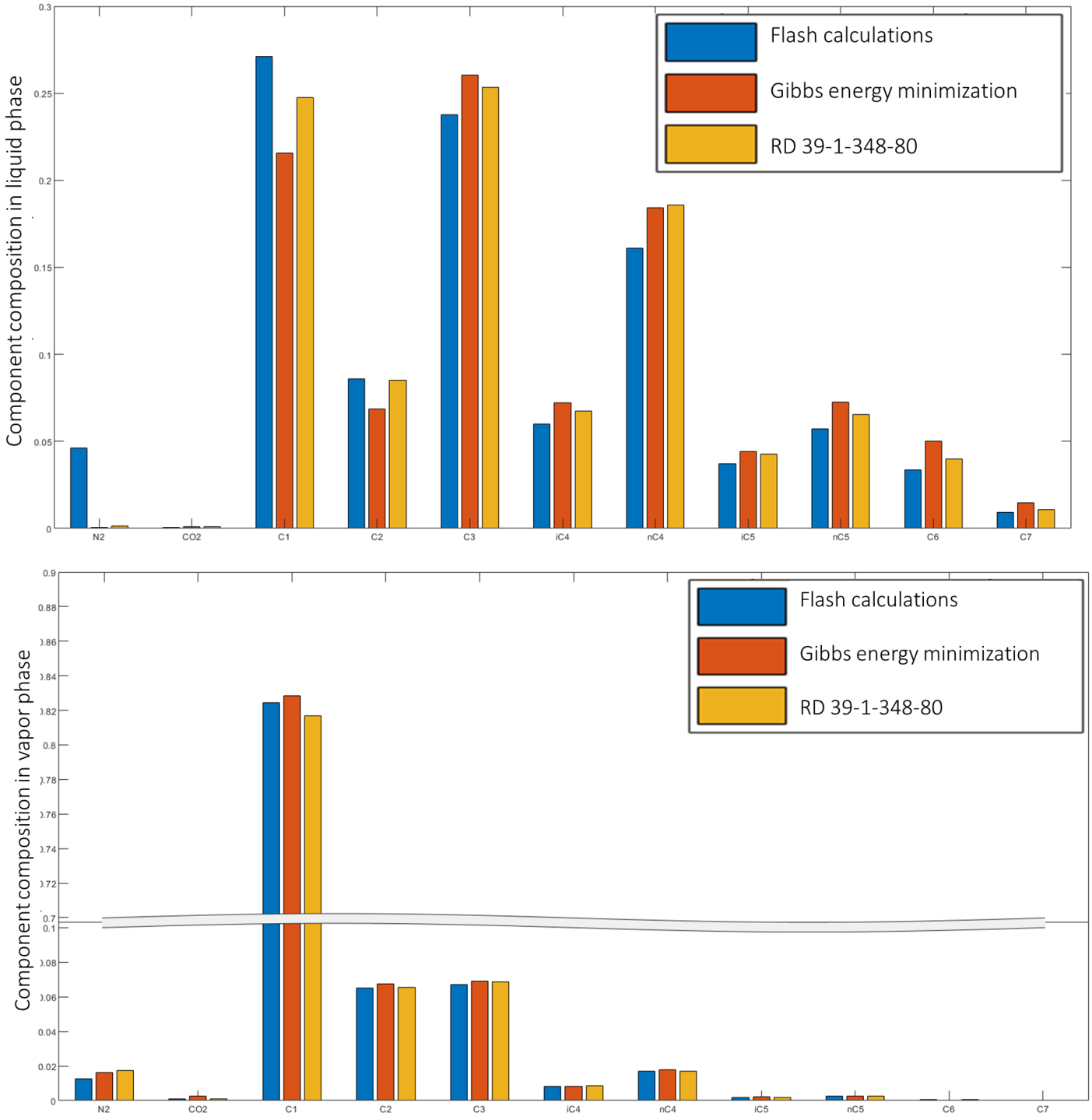

Figure 4.18 Phase compositions of the 11-component mixture: concentration of nitrogen, carbon dioxide, methane, ethane, propane, i-butane, n-butane, i-pentane, n-pentane, hexane and heptane in liquid (above) and vapor phases in case of flash calculations (blue), Gibbs energy minimization algorithm (red) and experiment (orange) (below)

Finally, it is important to discuss the computation performance aspect of the proposed Gibbs energy minimization technique. The required computational time to find the optimal solution depends on the number of grid points in discretized compositional space due to the special aspects of the algorithm shown previously. The procedure does not change, when the considered temperatures and pressures approach to the critical region. In contrast, as discussed above, if the system temperatures and pressures are close to their critical values, the required number of iterations in flash calculations increases. We illustrate this fact by the example of the methane—n-heptane binary mixture. Figure 4.19 shows the computational time required to obtain the parameters of vapor-liquid equilibrium: the red curve corresponds to the proposed Gibbs energy minimization technique; the blue curve corresponds to the flash calculations. For the considered in Figure D.1 methane—n-heptane mixture, the pressure above 24 MPa approaches the critical value. The flash calculations require 70 times longer computational time with increasing pressure. Remarkably, the required computational time by the proposed Gibbs energy minimization technique remains almost constant with increasing pressure. This result suggests that the proposed Gibbs energy minimization technique is promising for reservoir simulations, when possible variations of pressure-temperature conditions and fluids composition may result in the critical state.

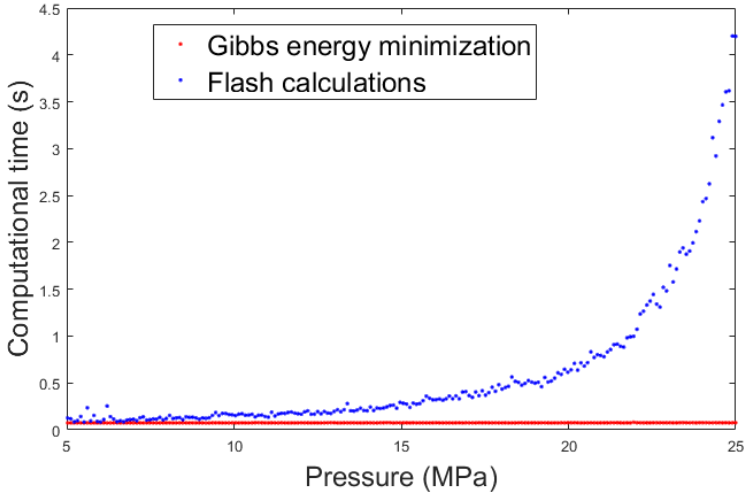

Figure 4.19 Computational time at different pressures for the methane—n-heptane binary mixture

4.3 Conclusions to chapter 4

In this chapter, the Helmholtz and Gibbs energy minimization technique was proposed to describe the phase behavior of multicomponent hydrocarbon systems. SRK and PR EOS (1) and random mixing rules (2) were considered to characterize a multicomponent mixture. The corresponding expression for the Helmholtz (8) and Gibbs (14) energies are derived. This expression is suitable for describing processes with a mass exchange between the phases. In order to determine the parameters of a multicomponent mixture in the thermodynamic equilibrium, we consider the constrained Helmholtz and Gibbs energy minimization problem. It is demonstrated that this minimization problem can be considered as a linear programming problem in the form (12), (18) with the constraints (10), (16) and (11), (17) for the case of Helmholtz and Gibbs energy, respectively, and solved numerically by the simplex method. A numerical algorithm is implemented in Matlab and adapted for any number of components and phases. It should be mentioned that the equilibrated state is found from all possible variants for specific system composition at a given pressure and temperature conditions, and prior knowledge about expecting a number of phases is not required. Along with the linear programming solver, the algorithm includes an optional iterative block – the consequent refinement of discretized compositional space near-optimal solution, which is used to avoid computational memory problems in high dimensional cases (5-component systems or more). The proposed Gibbs energy minimization techniques were validated against experimental data and flash calculations in a series of numerical simulations. A set of binary, ternary, 5, and 11-component mixtures were considered within this work. These mixtures were selected since its physical properties and experimental data were known and published in the literature (Billman et al. 1948; Davalos et al. 1976; Reamer et al. 1956; Hanson and Brown 2002; RD 39-1-348-80). First, the overall results obtained for the binary mixtures suggest that the proposed Gibbs energy minimization technique is applicable to describe the vapor-liquid equilibrium for both pairs of hydrocarbons and binary mixtures of hydrocarbons with carbon dioxide. Furthermore, predictive and computational advantages of the proposed technique were demonstrated in the region close to the critical. Second, the applicability of the proposed

algorithm for multicomponent systems is demonstrated for the system consisting of at least 11 components (methane, ethane, propane, i-butane, n-butane, i-pentane, n-pentane, hexane, heptane, nitrogen, and carbon dioxide), which is even more than usually used in HPAI or ISC simulations. Next, the detailed analysis of the simulations for ternary, 5, and 11-component mixtures indicates that flash calculations and the Gibbs energy minimization technique give equivalent results for the mole fractions of phases and phase compositions. Thus, it could be concluded that the proposed Gibbs energy minimization technique is promising for reservoir simulations, especially when possible variations of pressure-temperature conditions and fluids composition in a reservoir may result in the state close to the critical since it doesn't achieve a performance limit at any conditions of interest. In addition, the proposed algorithm can be implemented using GPUs, which will allow us to significantly accelerate the calculations for high dimension cases or, in other words, for the systems with a large number of components.

Chapter 5. Summary, conclusions, and recommendations for future research

5.1 Summary

In the first part of this work (Chapter 2, Chapter 3), we focused on the development of a general methodology and its application for modeling of HPAI and ISC as a basis for air-injection based EOR methods evaluation using capabilities of commercial thermal simulator CMG STARS. This approach consisted of comprehensive experimental and numerical studies. It allowed adapting reaction kinetic models for bitumen undergoing ISC (Samara region oil sand bitumen), medium oil in carbonate reservoir undergoing HPAI, and light oil in organic-rich source rock undergoing HPAI (Bazhenov shale formation).

3D digital models of oxidation and combustion performance laboratory tests were constructed in CMG STARS thermal hydrodynamic simulator (Section 2.1, 2.2) in order to be able to provide the history matching and validation of laboratory-scale HPAI and ISC numerical models with the experimental results. The existence of any constructional uncertainties significantly influences on the consistency of experimental results adaptation on modeling. Therefore, the used digital models of experimental setups were constructed to repeat its multilayer design and corresponding heater regimes. During the research, the importance HPAI and ISC laboratory-scale numerical models validation on RTO test results was shown by the several examples (Section 3.1.1, Section 3.2.4).

The methodology for HPAI and ISC numerical models construction was applied for three different unconventional reservoirs examples: Samara region oil sand bitumen (Section 3.1), carbonate oil field (Section 3.2), and Bazhenov shales (Section 3.3).

In Section 3.1, ISC numerical model for oil sand bitumen was proposed. The kinetic parameters for the adapted reaction scheme, describing ISC process for bitumen, were adjusted by the history matching procedure of laboratory-scale numerical model with RTO test results. The proposed model gave a good agreement with experimental results such as the location of LTR (180 to 310°C), HTR (350 to 470°C), and NTGR (310 to 350°C), the

obtained amount of oil and water, O2 uptake, CO2 generation, oil recovery factor of 0.33, and oxidation front velocity of 6.79 cm/hr. The adapted reaction scheme included thermal cracking of asphaltenes, the polymerization reaction of malthenes and asphaltenes in LTR, coke combustion in the HTR, and vapor-phase combustion reaction of light oil in HTR, which appeared in the system due to LTO reactions and asphaltenes cracking. During the RTO test, the heat generation in HTR was observed to be induced by coke burning and vapor-phase combustion.

To investigate the oxidation behavior and HPAI performance for carbonate oil field 3D numerical simulations of RTO and CT tests and its validation on the experimental results were provided (Section 3.2). Two sets of kinetic parameters were obtained for two adapted reaction schemes (the traditional reaction scheme (Table 3.11) and the modified one (Table 3.17)) by the history matching procedure. The laboratory-scale HPAI numerical model with adjusted kinetic parameters for the traditional reaction scheme showed low predictability in RTO test simulations. Along with capturing the oxidation initiation temperature and general exothermic behavior, it did not reproduce NTGR. It gave around 30% discrepancies in calculated and experimental values of produced fluids and gases after the history matching. The modified reaction scheme was proposed to increase the predictive power of the developed HPAI numerical model for carbonate oil field. The modification resulted in the incorporation of a bond-scission reaction of maltenes in LTR. The stoichiometry and initial kinetics were estimated based on the PDSC test and element analysis for the original and modified oil fractions used in the model. The laboratory-scale HPAI numerical model with adjusted kinetic parameters for the modified reaction scheme reproduced exothermic (two waves for the first five zones of the reactor) and endothermic fronts traversing the core pack during RTO test, NTGR (290°C - 350°C) and cumulative masses of produced fluids and gasses with not more than 1% deviation from experimental values. It should be mentioned that the combustion mechanism, in this case, assumes a relatively low rate of Coke combustion, which corresponds to the experimental observations. At the same time, the numerical simulations of MPCT experiment showed a good correlation with experimental results for both reaction kinetic models adapted to the

exclusion of produced carbon dioxide and consumed oxygen and the shape of the particular exothermic peaks. The discrepancies in these characteristics were significantly reduced after the history matching procedure in the case of the HPAI numerical model in which the modified reaction scheme was adapted. This result emphasizes the importance of RTO test in reaction kinetic scheme verification and construction of a feasible HPAI numerical model. The only HPAI numerical model validation on the CT test results does not guarantee its feasibility from the oxidation behavior point of view. As a result of MPCT experiment for the carbonate oil field, the oil recovery factor reached 0.89. The stable combustion front velocity was 18.1 cm/h, and the optimal airflow rate was equal to 220 $st.m^3/m^3$.

The proposed HPAI and ISC laboratory-scale numerical models for bitumen oil sands and carbonate oil field satisfactory matched the starting and ending temperatures for each oxidation regions resulting from RTO tests. However, numerically obtained temperature peaks located close to the NTGR did not replicate experimental ones well. That was because the mechanism undergoes the NTGR existence based on the vaporization of oil fractions for further combustion (Mallory et al., 2018). This fact significantly increases the importance of correct numerical simulation of phase transitions in multicomponent hydrocarbon mixtures and the investigation of the basic oxidation reaction model. There is an object for further studies since the problem of phase equilibrium is solved using the approximation of composition-independent k-values in CMG STARS. Such an approach does not sufficiently take into account the influence of oxidation processes on the structures of phase equilibria.

In Section 3.3, the investigation of oxidation processes during HPAI in oil shales by applying a complex approach, including a set of oxidation experiments and complementary numerical simulation, was demonstrated. The oxidation behavior of Bazhenov shales was studied by RTO and PDSC tests. Based on obtained data and experimental observations, the basic set of chemical reactions was proposed. It can represent oxidation behavior and chemical changes of both oil and kerogen, occurring during HPAI process in Bazhenov Formation. Moreover, the corresponding kinetic

parameters were obtained based on experimentally estimated Arrhenius parameters for LTR and HTR and adjusted during history matching procedure for laboratory-scale HPAI numerical model was developed. During validation of the numerical model with the experimental results, it was revealed that kerogen or its derivatives undergo oxidation in several temperature regions. Therefore, it should be represented by individual pseudo-components, which reflect their different physical-chemical properties. As a result, a minimum set of kerogen pseudo-components in the solid phase necessary for describing oxidation reactions in LTR and HTR and pyrolysis reaction was determined. On the one hand, when solid non-permeable components occupy pore space, this approach does not introduce kerogen into the hydrodynamic model as an organic matrix able to filter liquid and gas oil components. However, on the other hand, this one can be implemented using only the capabilities of CMG STARS commercial simulator adapted for reservoir engineers. Implementing the experimental work has made it possible to substantially reduce the uncertainties revealed in air injection modeling in oil shales.

Notwithstanding all weaknesses of developed numerical models of HPAI and ISC have appropriate predictable power, they are adapted for a commercial simulator widely used by reservoir engineers. They are ready for being upscaled and used in full-field simulations. It was demonstrated during validation of presented numerical models against 1D laboratory-scale representation of HPAI and ISC processes, provided in CT tests. In addition, several developed numerical models, as they are, have already been used as a start model for full-field simulations in order to evaluate ISC and HPAI potential for the particular oil field. (Mukhina et al., 2020, Askarova et. al, 2020). As was mentioned in Askarova et. al, 2020, to upscale the earlier developed laboratory-scale HPAI numerical model (Khakimova et al., 2020) and to provide full-field simulations using SMG STARS, areal heterogeneity, displacement effectivity, and numerical algorithm convergence difficulties had been considered.

In the second part of this study (Chapter 4), the Helmholtz and Gibbs energy minimization techniques were developed to describe the phase behavior of multicomponent hydrocarbon systems as an alternative to flash calculations. The proposed

algorithm was implemented in Matlab and allowed to solve non-linear constrained minimization problem by its reduction to linear minimization procedure with compositional space discretization in which the minimum is guaranteed (Ignizio, 1981). The algorithm was adapted for any number of phases and components. The problem with computation memory in multi-dimensional cases was solved by developing an optional iterative block within the proposed Gibbs energy minimization algorithm. It provided the consequent refinement of the discretized compositional space around the current optimal solution from the previous iteration. The Gibbs energy minimization algorithm was validated against the available experimental data (Billman et al. 1948; Davalos et al. 1976; Reamer et al. 1956; Hanson and Brown 2002) and compared with widely used flash calculations. It was revealed that the Gibbs energy minimization algorithm had a set of advantages. First, it was demonstrated on the set of examples that the parameters of hydrocarbon mixtures predicted by the proposed algorithm were closer to the corresponding experimental values than the parameters calculated using the iterative flash calculations, especially in the region close to the critical. Second, the computational complexity of the Gibbs energy minimization algorithm did not undergo a rise in the near critical region and kept constant. At the same time, the usage of a standard iterative flash calculations algorithm resulted in the increasing of the required computational time in more than an order of magnitude with approaching the critical region. The applicability of the proposed algorithm was shown for the multi-component hydrocarbon mixtures with non-hydrocarbon species included (nitrogen and carbon dioxide) with the maximal total number of components - 11, which is even more than used for air injection-based EOR simulations. Besides, the Gibbs energy minimization algorithm can be implemented using GPUs, which will allow accelerating the calculations for high dimensional cases (then the number of components in the mixture is more than 5) and decrease the computational time in more than one order of magnitude (Boyer et al., 2017).

5.2 Conclusions

1. The adaptation and history matching of ISC and HPAI performance laboratory experimental results for numerical modeling of air-injection based EOR for different types of reservoirs was provided.

- 3D digital models of oxidation and combustion performance experiments (RTO and CT) were constructed using the thermal hydrodynamic simulator CMG STARS for further validation against experimental data.
- During the validation, the adapted reaction and kinetic model to take into account kerogen oxidation behavior during HPAI in the organic-rich source rock was proposed.
- During the validation of developed laboratory-scale HPAI and ISC numerical models, the improved reaction scheme and associated kinetic parameters describing HPAI process for medium oil carbonate reservoir and ISC for bitumen was provided. The importance of correct representation of phase transitions in multicomponent hydrocarbon mixtures during HPAI and ISC was described.
- The developed HPAI and ISC numerical models were used as start models for full-field simulations to evaluating ISC and HPAI potential for the particular oil fields.

2. An alternative approach to calculating phase behavior in multicomponent multiphase hydrocarbon systems was developed.

- Direct free-energy (Gibbs and Helmholtz energy) minimization technique was implemented for multiphase multicomponent hydrocarbon mixtures. The applicability of the proposed algorithm was shown for the multi-component hydrocarbon mixtures with non-hydrocarbon species included (up to 11 components). The compositional refinement strategy for avoiding computer memory problems in the case of a large number of components was developed.
- Validation of the implemented free-energy minimization algorithm on experimental data and iterative flash calculations was provided. It was revealed that the developed algorithm gives advantages in computational time and computational accuracy near the critical region in comparison to non-linear iterative methods.

5.3 Recommendations for future research

The newly developed robust algorithm is a useful tool for further reactive transport code development, which describes multi-phase fluid flow in porous media associated with chemical reactions and its kinetics with significant temperature and volume effect and treats porosity and permeability evolution at different scales (Khakimova et al., 2019). The developed algorithm for phase equilibrium determination had been shown to be an external compositional solver. It allows calculating compositions and physical properties of the equilibrated phase, as a preliminary calculated lookup table for considered pressure-temperature-composition (of any number of components) space (Vrijmoed and Podladchikov, 2015). Since it has no restrictions on the number of considered phases in compositional space, it could be extended to include species, which could form a solid phase that can be treated as a porous medium in a multiphase problem (Malvoisin et al., 2015). Getting physical properties of solid phase, liquid, and gas phases, predicted by Gibbs/Helmholtz minimization technique, it could be possible to describe mass exchange and coupled changes for solid and fluids simulation of thermo-chemical hydrocarbon recovery processes (for organic-rich source rocks, carbonates, etc.). It should be mentioned that coupled changes in fluid-solid interaction during reactive fluid flow in porous media, based on analogous techniques, have already been demonstrated in the case of heterogeneous mineral reactions and isothermal processes (Malvoisin et al., 2015, Plumper et al, 2017, Beinlich et al., 2020). In this work, the predictive power of Gibbs/Helmholtz minimization technique was demonstrated for a set of molecular species (hydrocarbons, CO2, N2, etc.), considering as endmembers could form phases. Assuming the other level of abstraction and considering atoms (C, O, H, etc.) as phase (molecules) generating endmembers allows us to consider homogenous and heterogeneous reactions, finding the optimal combination of atoms at considered pressure-temperature-composition conditions. This approach will help to significantly reduce the number of uncertainties during thermal decomposition and oxidation kinetic parameters evaluation by history matching procedure for specific reaction schemes and pseudo-components forming. It should be mentioned that statement of applied problems (air-injection based and thermal EOR simulation) implies

sharp interfaces such as shocks and chemical reactions. Transport equations should be presented in the conservative form and solved using a finite difference approach on a staggered grid and characteristic-based Lax-Friedrichs different order schemes to treat the disintegration of discontinuities (Roe, 1986, Mallison et al, 2005). Besides, numerical models describing thermal EOR, such as HPAI or ISC, should be validated not only HPAI or ISC performance laboratory experiments but against analytical or semi-analytical solutions to ensure its correct numerical implementation. For this purpose, asymptotic solutions, developed by Zeldovich and Frank-Kamenetskii for flame (slow-wave, reaction front) propagation, which are becoming classical fundamentals in the theory of combustion (Zeldovich, & Frank-Kamenetskii, 1938, Zeldovich et al, 1985), could be considered.

Moreover, finally, the problem of upscaling in the thermal EOR simulations arises since considered subprocesses (reaction and evaporation front, anisotropy, local heterogeneity of porous media properties, etc.) occur at different time and length scales (from 1 day to 1 year; from 1 cm to 1 km) (Gutierrez et al., 2011). There are several upscaling routines published in the literature, which are developed to capture local-scale processes and to approximate the developed model for subprocesses description. (Christensen et al., 2004; De Zwart et al., 2008; Druganova et al., 2010; Marjerrison and Fassihi, 1992; Van Batenburg et al., 2011) For example, the dynamic gridding technique makes it possible to refine grid cells near sharp fronts and to coarse grid cells in the other region. (Christensen et al., 2004) Nevertheless, there is no straightforward algorithm to tune the model in the case of a high heterogeneous reservoir and to choose the proper size of refining blocks for dynamic gridding, which significantly complicates the upscaling procedure.

Instead of approximating the developed model for subprocesses description, one can accurately resolve these coupled processes, which requires a high-performance computing approach to achieve high spatial and temporal resolution requirements. In this regard, authors of the work (Alkhimenkov, Khakimova et al, 2020) developed a multi-GPU numerical implementation of the anisotropic elastodynamic equations (Biot's equations, a well-known example of a coupled system with the ability to take into account anisotropic

behavior) that relied on a conservative numerical scheme to simulate in a few seconds wave fields for model domains involving more than 1.5 billion grid cells. It is possible to achieve 90% effective memory throughput and close-to-ideal parallel efficiency (98% and 96%) on weak scaling tests on multi-GPU systems. Moreover, the effectiveness of parallel computing for "upscaling candidates" has already been shown by numerical results demonstration for resolving spontaneous channeling of porous fluids owing to decompaction weakening (Omlin et al., 2018; Räss et al., 2018; Räss et al., 2019; Duretz et al., 2019) in case of hydro and thermomechanical coupled problems.

Bibliography

Adegbesan, K.O., Donnelly, J.K., Moore, R.G., Bennion, D.W., 1987. Low-temperature oxidation kinetic parameters for in-situ combustion numerical simulation. SPE reservoir Engineering 2, 573–582.

Air Injection at Mordovo-Karmalskoye field: simulation and IOR evaluation - OnePetro [WWW Document], n.d. URL https://www.onepetro.org/conference-paper/SPE-136020-MS (accessed 10.14.20).

Alfarge, D., Wei, M., Bai, B., 2017. IOR Methods in Unconventional Reservoirs of North America: Comprehensive Review. Presented at the SPE Western Regional Meeting, Society of Petroleum Engineers. https://doi.org/10.2118/185640-MS

Alkhimenkov, Y., Khakimova, L., Raess, L., Quintal, B., Podladchikov, Y., 2020. Parallel Numerical Modeling of Poroelastic Wave Propagation Using Multiple NVIDIA Volta GPUs. Presented at the 82nd EAGE Annual Conference & Exhibition Workshop Programme, European Association of Geoscientists & Engineers, pp. 1–5. https://doi.org/10.3997/2214-4609.202011839

Aysylu, A., Alexander, C., Aleksei, S., Alexey, C., 2020. Evaluation of the subject geological area suitability for oil recovery by High-Pressure Air Injection method, in: EGU General Assembly Conference Abstracts. p. 22560.

Balushkina, N.S., Kalmykov, G.A., Khamidullin, R.A., Belokhin, V.S., Korobova, N.I., Petrakova, N.N., Bakay, A.I., 2014. Complex lithophysical typization of Bazhenov Formation rocks from core analysis and well logging, in: SPE Russian Oil and Gas Exploration & Production Technical Conference and Exhibition. Society of Petroleum Engineers.

Barenblatt, G., 1985. The Mathematical Theory of Combustion and Explosions. Springer US.

Barzin, Y., Moore, R.G., Mehta, S.A., Ursenbach, M.G., Tabasinejad, F., 2010. Impact of distillation on the combustion kinetics of high pressure air injection (HPAI), in: SPE Improved Oil Recovery Symposium. Society of Petroleum Engineers.

Beinlich, A., John, T., Vrijmoed, J.C., Tominaga, M., Magna, T., Podladchikov, Y.Y., 2020. Instantaneous rock transformations in the deep crust driven by reactive fluid flow. Nature Geoscience 13, 307–311.

Belgrave, J.D.M., Moore, R.G., Ursenbach, M.G., Bennion, D.W., 1993. A comprehensive approach to in-situ combustion modeling. SPE Advanced Technology Series 1, 98–107.

Belgrave, J.D.M., Moore, R.G., Ursenbach, M.G., Bennion, D.W., n.d. A Comprehensive Approach to In-Situ Combustion Modeling.

Belov, N., 2016. Precise approximations of phase equilibrium of multicomponent mixtures, in preparation.

Bethke, C.M., 2007. Geochemical and biogeochemical reaction modeling. Cambridge University Press.

Bhattacharya, S., Belgrave, J.D., Mallory, D.G., Moore, R.G., Ursenbach, M.G., Mehta, S.A., 2017. Investigation of thermal fingerprint in accelerating-rate calorimetry for air-injection enhanced-oil-recovery processes. SPE Journal 22, 548–561.

Bhattacharya, S., Mallory, D.G., Moore, R.G., Ursenbach, M.G., Mehta, S.A., 2016. Vapor phase combustion in Accelerating Rate Calorimetry for air-injection EOR processes, in: SPE Western Regional Meeting. Society of Petroleum Engineers.

Billman, G.W., Sage, B.H., Lacey, W.N., 1948. Phase Behavior in the Methane-ethane-n-pentane System. Transactions of the AIME 174, 13–24.

Bogachev, K., Zemtsov, S., Milyutin, S., Indrupskiy, I., Lobanova, O., 2019. Numerical Modeling of Non-Equilibrium Phase Transitions in the Isothermal Compositional Hydrocarbon Flow Simulations, in: SPE Russian Petroleum Technology Conference. Society of Petroleum Engineers.

Bogdanovich, N.N., Borisenko, S.A., Kozlova, E.V., Spasennykh, M.Y., Rudakovskaya, S.Y., 2017. Mosaic Hydrophobization of the Surface of Organic-Mineral Matrix from Rocks of Bazhenov Formation, in: SPE Russian Petroleum Technology Conference. Society of Petroleum Engineers.

Bondarenko, Tatiana, Cheremisin, A., Kozlova, E., Zvereva, I., Chislov, M., Myshenkov, M., Novakowski, V., 2017. Experimental investigation of thermal decomposition of Bazhenov formation kerogen: mechanism and application for thermal enhanced oil recovery. Journal of Petroleum Science and Engineering 150, 288–296.

Bondarenko, T., Khakimova, L., Cheremisin, A., Spasennykh, M., 2017. High-Pressure Air Injection Laboratory and Numerical Modelling in Bazhenov Source Rocks, in: SPE Russian Petroleum Technology Conference. Society of Petroleum Engineers.

Bondarenko, T.M., Popov, E.Y., Cheremisin, A.N., Kozlova, E.V., Karpov, I.A., Morozov, N.V., 2017. Laboratory modeling of high-pressure air injection in oil fields of Bazhenov formation (Russian). Oil Industry Journal 2017, 34–39.

Boyer, V., Baz, D.E., Salazar-Aguilar, M.A., 2017. GPU computing applied to linear and mixed-integer programming. Elsevier. https://doi.org/10.1016/B978-0-12-803738-6.00010-0

Braduchan, Y.V., Vyshemirskiy, V.S., 1990. Bazhenov Horizon of West Siberia.

Brusilovsky, A.I., 2002. Phase transformations in the development of oil and gas fields. M.:“Grail 575.

Burger, J.G., 1972. Chemical aspects of in-situ combustion-heat of combustion and kinetics. Society of Petroleum Engineers Journal 12, 410–422.

Chen, X., Chen, Z.J., Moore, R.G., Mehta, S.A., Ursenbach, M.G., Harding, T.G., 2014. Kinetic modeling of the in-situ combustion process for athabasca oil sands, in: SPE Heavy Oil Conference-Canada. Society of Petroleum Engineers.

Christensen, J.R., Darche, G., Dechelette, B., Ma, H., Sammon, P.H., 2004. Applications of dynamic gridding to thermal simulations, in: SPE International Thermal Operations and Heavy Oil Symposium and Western Regional Meeting. Society of Petroleum Engineers.

Chugunov, S.S., Kazak, A.V., Cheremisin, A.N., 2015. Integration of X-ray micro computed tomography and focused ion-beam scanning electron microscopy data fore pore-scale characterization of Bazhenov formation, Western Siberia. Oil Industry 10, 44–49.

Cinar, M., Hasçaki, B., Castanier, L.M., Kovscek, A.R., 2011. Predictability of crude oil in-situ combustion by the isoconversional kinetic approach. SPE Journal 16, 537–547.

Clara, C., Durandeau, M., Quenault, G., Nguyen, T.-H., 2000. Laboratory studies for light-oil air injection projects: potential application in handil field. SPE Reservoir Evaluation & Engineering 3, 239–248.

Comparison of Reduced and Conventional Two-Phase Flash Calculations - OnePetro [WWW Document], n.d. URL https://www.onepetro.org/journal-paper/SPE-163577-PA (accessed 10.14.20).

Connolly, J.A., 2005. Computation of phase equilibria by linear programming: a tool for geodynamic modeling and its application to subduction zone decarbonation. Earth and Planetary Science Letters 236, 524–541.

Connolly, J.A.D., 2017. A primer in gibbs energy minimization for geophysicists. Petrology 25, 526–534. https://doi.org/10.1134/S0869591117050034

Connolly, J.A.D., Galvez, M.E., 2018. Electrolytic fluid speciation by Gibbs energy minimization and implications for subduction zone mass transfer. Earth and Planetary Science Letters 501, 90–102. https://doi.org/10.1016/j.epsl.2018.08.024

Connolly, J.A.D., Kerrick, D.M., 1987. An algorithm and computer program for calculating composition phase diagrams. Calphad 11, 1–55.

Danesh, A., 1998. PVT and Phase Behaviour Of Petroleum Reservoir Fluids. Elsevier.

Davalos, J., Anderson, W.R., Phelps, R.E., Kidnay, A.J., 1976. Liquid-vapor equilibria at 250.00.deg.K for systems containing methane, ethane, and carbon dioxide [WWW Document]. https://doi.org/10.1021/je60068a030

De Zwart, A.H., van Batenburg, D.W., Blom, C.P.A., Tsolakidis, A., Glandt, C.A., Boerrigter, P., 2008. The Modeling Challenge of High Pressure Air Injection. Presented at the SPE Symposium on Improved Oil Recovery, Society of Petroleum Engineers. https://doi.org/10.2118/113917-MS

Deng, S., Wang, Z., Gu, Q., Meng, F., Li, J., Wang, H., 2011. Extracting hydrocarbons from Huadian oil shale by sub-critical water. Fuel Processing Technology 92, 1062–1067. https://doi.org/10.1016/j.fuproc.2011.01.001

Direct Characterization of Kerogen by X-ray and Solid-State 13C Nuclear Magnetic Resonance Methods | Energy & Fuels [WWW Document], n.d. URL https://pubs.acs.org/doi/abs/10.1021/ef060321h (accessed 10.14.20).

Druganova, E., Surguchev, L.M., Ibatullin, R.R., 2010. Air Injection at Mordovo-Karmalskoye field: simulation and IOR evaluation. Presented at the SPE Russian Oil and Gas Conference and Exhibition, Society of Petroleum Engineers. https://doi.org/10.2118/136020-MS

Duretz, T., Räss, L., Podladchikov, Y.Y., Schmalholz, S.M., 2019. Resolving thermomechanical coupling in two and three dimensions: spontaneous strain localization owing to shear heating. Geophys J Int 216, 365–379. https://doi.org/10.1093/gji/ggy434

ECLIPSE Technical Description, 2014.

E. V. Koldoba, “The method of construction of the thermal constants (K-values) of phase equilibrium in multicomponent solutions”, Matem. Mod., 30:4 (2018), 84–96 [WWW Document], n.d. URL http://www.mathnet.ru/php/archive.phtml?wshow=paper&jrnid=mm&paperid=3959&option_lang=eng (accessed 10.14.20).

Fadaei, H., Castanier, L.M., Kamp, A.M., Debenest, G., Quintard, M., Renard, G., 2011. Experimental and Numerical Analysis of In-Situ Combustion in a Fractured Core. SPE Journal 16, 358–373. https://doi.org/10.2118/141117-PA

Fan, Y., Durlofsky, L., Tchelepi, H.A., 2010. Numerical Simulation of the In-Situ Upgrading of Oil Shale. SPE Journal 15, 368–381. https://doi.org/10.2118/118958-PA

Fassihi, M.R., Brigham, W.E., Ramey, H.J.J., 1984. Reaction Kinetics of In-Situ Combustion: Part 1-Observations. Society of Petroleum Engineers Journal 24, 399–407. https://doi.org/10.2118/8907-PA

Fassihi, M.R., Moore, R.G., Mehta, S.A., Ursenbach, M.G., 2016. Safety Considerations for High-Pressure Air Injection Into Light-Oil Reservoirs and Performance of the Holt Sand Unit Project. SPE Production & Operations 31, 197–206. https://doi.org/10.2118/169168-PA

Firoozabadi, A., Pan, H., 2000. Fast and Robust Algorithm for Compositional Modeling: Part I - Stability Analysis Testing. Presented at the SPE Annual Technical Conference and Exhibition, Society of Petroleum Engineers. https://doi.org/10.2118/63083-MS

Freitag, N.P., Verkoczy, B., 2005. Low-Temperature Oxidation of Oils in Terms of SARA Fractions: Why Simple Reaction Models Don't Work. Journal of Canadian Petroleum Technology 44, 54–61. https://doi.org/10.2118/05-03-05

Gaganis, V., 2018. Rapid phase stability calculations in fluid flow simulation using simple discriminating functions. Computers & Chemical Engineering 108, 112–127. https://doi.org/10.1016/j.compchemeng.2017.09.006

Ghiorso, M.S., Sack, R.O., 1995. Chemical mass transfer in magmatic processes IV. A revised and internally consistent thermodynamic model for the interpolation and extrapolation of liquid-solid equilibria in magmatic systems at elevated temperatures and pressures. Contr. Mineral. and Petrol. 119, 197–212. https://doi.org/10.1007/BF00307281

Gmehling, J., Kleiber, M., Kolbe, B., Rarey, J., 2019. Chemical Thermodynamics for Process Simulation. John Wiley & Sons.

Gutiérrez, D., Moore, R.G., Mehta, S.A., Ursenbach, M., Bernal, A., 2019. Phase-Behavior Modeling of Oils in Terms of Saturates/Aromatics/Resins/Asphaltenes Fractions. SPE Reservoir Evaluation & Engineering 22, 1,015-1,029. https://doi.org/10.2118/189727-PA

Gutiérrez, D., Moore, R.G., Ursenbach, M.G., Mehta, S.A., 2012. The ABCs of In-Situ-Combustion Simulations: From Laboratory Experiments to Field Scale. Journal of Canadian Petroleum Technology 51, 256–267. https://doi.org/10.2118/148754-PA

Gutierrez, D., Skoreyko, F., Moore, R.G., Mehta, S.A., Ursenbach, M.G., 2009. The Challenge of Predicting Field Performance of Air Injection Projects Based on Laboratory and Numerical Modelling. Journal of Canadian Petroleum Technology 48, 23–33. https://doi.org/10.2118/09-04-23-DA

Hanson, G.H., Brown, G.G., 2002. Vapor-Liquid Equilibria in Mixtures of Volatile Paraffins [WWW Document]. https://doi.org/10.1021/ie50429a013

Henderson, J., 2013. Tight Oil Developments in Russia. Oxford Institute for Energy Studies.

Hendriks, E.M., van Bergen, A.R.D., 1992. Application of a reduction method to phase equilibria calculations. Fluid Phase Equilibria 74, 17–34. https://doi.org/10.1016/0378-3812(92)85050-I

Ignizio, J.P., 1981. Linear Programming in Single and Multiple Objective Systems. Pearson College Div, Englewood Cliffs, N.J.

Isaeva, A., Grushnikov, I., Dobrozhanskiy, V., 2018. Analysis of Vapor-Liquid Equilibrium Parameters of Multicomponent Hydrocarbon Mixtures Using Cubic Equations of State. Presented at the SPE Russian Petroleum Technology Conference, Society of Petroleum Engineers. https://doi.org/10.2118/191619-18RPTC-MS

Ismail, N.B., Klock, K.A., Hascakir, B., 2016. In-Situ Combustion Experience in Heavy Oil Carbonate. Presented at the SPE Canada Heavy Oil Technical Conference, Society of Petroleum Engineers. https://doi.org/10.2118/180724-MS

Jia, H., Ni, J., Pu, W., Yue, P., Jiang, H., Yang, J., 2014. New view on the oxidation mechanisms of crude oil through combined thermal analysis methods 1707–1714. https://doi.org/10.1007/s10973-014-4047-1

Jia, H., Sheng, J.J., 2016. Numerical modeling on air injection in a light oil reservoir : Recovery mechanism and scheme optimization. FUEL 172, 70–80. https://doi.org/10.1016/j.fuel.2015.12.063

Kapadia, P.R., Wang, J., Kallos, M.S., Gates, I.D., 2012. New thermal-reactive reservoir engineering model predicts hydrogen sulfide generation in Steam Assisted Gravity

Drainage. Journal of Petroleum Science and Engineering 94–95, 100–111. https://doi.org/10.1016/j.petrol.2012.06.030

Karpov, I.K., Chudnenko, K.V., Kulik, D.A., 1997. Modeling chemical mass transfer in geochemical processes; thermodynamic relations, conditions of equilibria and numerical algorithms. Am J Sci 297, 767–806. https://doi.org/10.2475/ajs.297.8.767

Kashinath, A., Szulczewski, M.L., Dogru, A.H., 2018. A fast algorithm for calculating isothermal phase behavior using machine learning. Fluid Phase Equilibria 465, 73–82. https://doi.org/10.1016/j.fluid.2018.02.004

Kelemen, S.R., Afeworki, M., Gorbaty, M.L., Sansone, M., Kwiatek, P.J., Walters, C.C., Freund, H., Siskin, M., Bence, A.E., Curry, D.J., Solum, M., Pugmire, R.J., Vandenbroucke, M., Leblond, M., Behar, F., 2007. Direct Characterization of Kerogen by X-ray and Solid-State 13C Nuclear Magnetic Resonance Methods. Energy Fuels 21, 1548–1561. https://doi.org/10.1021/ef060321h

Khakimov, L.A., Myasnikov, A.V., Bondarenko, T.M., Popov, E.Y., Cheremisin, A.N., Karpov, I.A., 2017. Validation of computational model of high-pressure air injection for Bazhenov formations by laboratory modelling results (Russian). Oil Industry Journal 2017, 85–89.

Khakimova, L., Askarova, A., Popov, E., Moore, R.G., Solovyev, A., Simakov, Y., Afanasiev, I., Belgrave, J., Cheremisin, A., 2020. High-pressure air injection laboratory-scale numerical models of oxidation experiments for Kirsanovskoye oil field. Journal of Petroleum Science and Engineering 188, 106796. https://doi.org/10.1016/j.petrol.2019.106796

Khakimova, L., Podladchikov, Y., Myasnikov, A., 2019. Modelling of some nonlinear processes in deforming and reacting porous saturated rocks., in: Geophysical Research Abstracts.

Khalimov, E.M., Melik-Pashayev, V.S., 1980. Exploration for Commercial Accumulations of Oil in the Bazhenov Formation 18, 253–256.

Khamidullin, R.R., Kalmykov, G.A., Korost, D.V., Balushkina, N.S., Bakay, A.I., 2012. Reservoir properties of the Bazhenov formation. Presented at the SPE Russian Oil and Gas Exploration and Production Technical Conference and Exhibition, Society of Petroleum Engineers. https://doi.org/10.2118/162094-MS

Kibodeaux, K.R., 2014. Evolution of Porosity, Permeability, and Fluid Saturations During Thermal Conversion of Oil Shale. Presented at the SPE Annual Technical Conference and Exhibition, Society of Petroleum Engineers. https://doi.org/10.2118/170733-MS

Kissinger, H.E., 1957. Reaction kinetics in differential thermal analysis. Analytical chemistry 29, 1702–1706.

Kok, M.V., Karacan, C.O., 1997. Behavior and Effect of SARA Fractions of Oil During Combustion. Presented at the International Thermal Operations and Heavy Oil Symposium, Society of Petroleum Engineers. https://doi.org/10.2118/37559-MS

Kokorev, V.I., Darishchev, V.I., Akhmadeishin, I.A., Shchekoldin, K.A., Boksernam, A.A., 2014. The Results of the Field Tests and Prospects of Termogas Development of Bazhenov Formation in OJSC RITEK. Presented at the SPE Russian Oil and Gas Exploration & Production Technical Conference and Exhibition, Society of Petroleum Engineers. https://doi.org/10.2118/171172-MS

Kristensen, M.R., Gerritsen, M.G., Thomsen, P.G., Michelsen, M.L., Stenby, E.H., 2008. Impact of Phase Behavior Modeling on In-Situ Combustion Process Performance. Presented at the SPE Symposium on Improved Oil Recovery, Society of Petroleum Engineers. https://doi.org/10.2118/113947-MS

Le-Doan, T.-V., Bostrom, N. w., Burnham, A. k., Kleinberg, R. l., Pomerantz, A. e., Allix, P., 2013. Experimental Study of Green River Oil Shale Pyrolysis, in: Unconventional Resources Technology Conference, Denver, Colorado, 12-14 August 2013, SEG Global Meeting Abstracts. Society of Exploration Geophysicists, American Association of Petroleum Geologists, Society of Petroleum Engineers, pp. 2241–2250. https://doi.org/10.1190/urtec2013-232

Li, J., Mehta, S.A., Moore, R.G., Zalewski, E., Ursenbach, M.G., Van Fraassen, K., 2006. Investigation of the Oxidation Behaviour of Pure Hydrocarbon Components and Crude Oils Utilizing PDSC Thermal Technique. Journal of Canadian Petroleum Technology 45. https://doi.org/10.2118/06-01-04

Li, Y., Johns, R.T., 2006. Rapid Flash Calculations for Compositional Simulation. SPE Reservoir Evaluation & Engineering 9, 521–529. https://doi.org/10.2118/95732-PA

Machine Learning Methods to Speed up Compositional Reservoir Simulation - OnePetro [WWW Document], n.d. URL https://www.onepetro.org/conference-paper/SPE-154505-MS (accessed 10.14.20).

Mallory, D.G., Moore, R.G., Mehta, S.A., 2018. Ramped Temperature Oxidation Testing and In Situ Combustion Projects. Energy Fuels 32, 8040–8056. https://doi.org/10.1021/acs.energyfuels.8b00760

Marjerrison, D.M., Fassihi, M.R., 1992. A Procedure for Scaling Heavy-Oil Combustion Tube Results to a Field Model. Presented at the SPE/DOE Enhanced Oil Recovery Symposium, Society of Petroleum Engineers. https://doi.org/10.2118/24175-MS

Moore, R.G., Mehta, S.A., Ursenbach, M.G., 2007. A Guide to High Pressure Air Injection (HPAI) Based Oil Recovery. https://doi.org/10.2118/75207-ms

Moore, R.G., Mehta, S.A., Ursenbach, M.G., Gutierrez, D., 2012. Potential for In Situ Combustion in Depleted Conventional Oil Reservoirs. Presented at the SPE Improved Oil Recovery Symposium, Society of Petroleum Engineers. https://doi.org/10.2118/154299-MS

Moore, R.G., Ursenbach, M.G., Laureshen, C.J., Belgrave, J.D.M., Mehta, S.A., 1999. Ramped Temperature Oxidation Analysis of Athabasca Oil Sands Bitumen. Journal of Canadian Petroleum Technology 38. https://doi.org/10.2118/99-13-40

Omlin, S., Räss, L., Podladchikov, Y.Y., 2018. Simulation of three-dimensional viscoelastic deformation coupled to porous fluid flow. Tectonophysics, Understanding geological processes through modelling - A Memorial Volume

honouring Evgenii Burov 746, 695–701. https://doi.org/10.1016/j.tecto.2017.08.012

Pu, W., Zhao, S., Hu, L., Varfolomeev, M.A., Yuan, C., Wang, L., Rodionov, N.O., 2020. Thermal effect caused by low temperature oxidation of heavy crude oil and its in-situ combustion behavior. Journal of Petroleum Science and Engineering 184, 106521. https://doi.org/10.1016/j.petrol.2019.106521

Räss, L., Duretz, T., Podladchikov, Y.Y., 2019. Resolving hydromechanical coupling in two and three dimensions: spontaneous channelling of porous fluids owing to decompaction weakening. Geophys J Int 218, 1591–1616. https://doi.org/10.1093/gji/ggz239

Räss, L., Simon, N.S.C., Podladchikov, Y., 2018. Spontaneous formation of fluid escape pipes in two-phase systems. AGU Fall Meeting Abstracts 34.

RD 39-1-348-80, n.d. Методика расчета фазовых равновесий и физических свойств фаз нефтегазоконденсатных систем.

Rodriguez, E., Ordonez, A., Comas, J.C., Trujillo Portillo, M.L., Belgrave, J.D.M., 2012. A Framework for Consolidating Air Injection Experimental Data. Presented at the SPE Latin America and Caribbean Petroleum Engineering Conference, Society of Petroleum Engineers. https://doi.org/10.2118/152048-MS

Taylor, S.M., Fryer, P.J., 1992. A numerical study of the use of the kissinger analysis of DSC thermograms to obtain reaction kinetic parameters. Thermochimica Acta 209, 111–125. https://doi.org/10.1016/0040-6031(92)80189-4

The Computation of Chemical Equilibria in Complex Systems | Industrial & Engineering Chemistry Fundamentals [WWW Document], n.d. URL https://pubs.acs.org/doi/pdf/10.1021/i160073a001 (accessed 10.14.20).

Ursenbach, M.G., Moore, R.G., Mehta, S.A., 2010. Air Injection in Heavy Oil Reservoirs - A Process Whose Time Has Come (Again). Journal of Canadian Petroleum Technology 49, 48–54. https://doi.org/10.2118/132487-PA

Van Batenburg, D.W., De Zwart, A.H., Boerrigter, P.M., Bosch, M., Vink, J.C., 2011. Application of dynamic gridding techniques to IOR/EOR processes, in: IOR 2011-

16th European Symposium on Improved Oil Recovery. European Association of Geoscientists & Engineers, p. cp–230.

Wood, B.J., Holloway, J.R., 1984. A thermodynamic model for subsolidus equilibria in the system CaO□MgO□Al2O3□SiO2. Geochimica et Cosmochimica Acta 48, 159–176. https://doi.org/10.1016/0016-7037(84)90358-2

Yang, M., Chen, Z., 2016. SPE-180728-MS An Improved Reaction Kinetics Model Of In-Situ Combustion For Pre-Steamed Oil Sands 7–9.

Yang, M., Chen, Z., Harding, T.G., 2016. An Improved Reaction Kinetics Model Of In-Situ Combustion For Pre-Steamed Oil Sands. Presented at the SPE Canada Heavy Oil Technical Conference, Society of Petroleum Engineers. https://doi.org/10.2118/180728-MS

Yang, X., Gates, I.D., 2009. Combustion Kinetics of Athabasca Bitumen from 1D Combustion Tube Experiments. Nat Resour Res 18, 193–211. https://doi.org/10.1007/s11053-009-9095-z

Yannimaras, D.V., Tiffin, D.L., 1995. Screening of Oils for In-Situ Combustion at Reservoir Conditions via Accelerating Rate Calorimetry. SPE Reservoir Engineering 10, 36–39. https://doi.org/10.2118/27791-PA

Yoshioka, Y., Sasaki, K., Takatsu, K., Sugai, Y., 2017. Screening of major chemical reactions in in-situ combustion process for bitumen production from oil sands reservoirs. International Journal of Petroleum and Petrochemical Engineering 3, 82–92. https://doi.org/10.20431/2454-7980.0304008

Yuan, C., Varfolomeev, M.A., Emelianov, D.A., Eskin, A.A., Nagrimanov, R.N., Kok, M.V., Afanasiev, I.S., Fedorchenko, G.D., Kopylova, E.V., 2018. Oxidation Behavior of Light Crude Oil and Its SARA Fractions Characterized by TG and DSC Techniques: Differences and Connections. Energy Fuels 32, 801–808. https://doi.org/10.1021/acs.energyfuels.7b02377

Zeldovich, Y.B., Barenblatt, G.I., 1959. Theorv of flame propagation. Combustion and Flame 3, 61–74. https://doi.org/10.1016/0010-2180(59)90007-0

Zhang, Z., Volkman, J.K., Greenwood, P.F., Hu, W., Qin, J., Borjigin, T., Zhai, C., Liu, W., 2014. Flash pyrolysis of kerogens from algal rich oil shales from the Eocene Huadian Formation, NE China. Organic Geochemistry 76, 167–172. https://doi.org/10.1016/j.orggeochem.2014.08.004

Zhao, S., Pu, W., Sun, B., Gu, F., Wang, L., 2019a. Comparative evaluation on the thermal behaviors and kinetics of combustion of heavy crude oil and its SARA fractions. Fuel 239, 117–125. https://doi.org/10.1016/j.fuel.2018.11.014

Zhao, S., Pu, W., Varfolomeev, M.A., Yuan, C., Rodionov, A.A., 2019b. Integrative Investigation of Low-Temperature Oxidation Characteristics and Mechanisms of Heavy Crude Oil. Ind. Eng. Chem. Res. 58, 14595–14602. https://doi.org/10.1021/acs.iecr.9b03346

Zhao, S., Pu, W., Varfolomeev, M.A., Yuan, C., Zhang, J., Han, X., Yang, Y., Peng, X., Wu, J., 2018. Comprehensive investigations into low temperature oxidation of heavy crude oil. Journal of Petroleum Science and Engineering 171, 835–842. https://doi.org/10.1016/j.petrol.2018.08.027

Zheng, H., Shi, W., Ding, D., Zhang, C., 2017. Numerical Simulation of In Situ Combustion of Oil Shale [WWW Document]. Geofluids. https://doi.org/10.1155/2017/3028974

Appendix A. Fugacity and fugacity coefficient

Flash calculations assume determining the component fugacities. Let us consider the general relations for fugacities and fugacity coefficients that connect them to the EOS. With independent variables of temperature T and volume V, we can formally write the Helmholtz energy as

$$F = F\left(T, V, n_1, \ldots n_{N_c}\right),$$

where n_i is the number of moles of each component, $i = 1, \ldots, N_c$. The combined first and second laws of thermodynamics states give the following expression for the phase Helmholtz energy

$$dF = -SdT - pdV + \sum_{i=1}^{N_c} \mu_i dn_i ,$$

where S is the system entropy, p is the pressure, μ_i is the chemical potential of component i. Hence, we can write:

$$\mu_i = \left.\left(\frac{\partial F}{\partial n_i}\right)\right|_{T,V,n_{j\neq i}}, \qquad \left.\left(\frac{\partial F}{\partial V}\right)\right|_{T,n_i} = -p .$$

The symmetry of second derivatives of the Helmholtz energy gives

$$\frac{\partial}{\partial V}\left[\left.\left(\frac{\partial F}{\partial n_i}\right)\right|_{T,V,n_{j\neq i}}\right]_{T,n_i} = \frac{\partial}{\partial n_i}\left[\left.\left(\frac{\partial F}{\partial V}\right)\right|_{T,n_i}\right]_{T,V,n_{j\neq i}} .$$

Thus, we can rewrite this equality using chemical potentials and pressure as

$$\left.\left(\frac{\partial \mu_i}{\partial V}\right)\right|_{T,n_i} = -\left.\left(\frac{\partial p}{\partial n_i}\right)\right|_{T,V,n_{j\neq i}} ,$$

where we assume the fixed temperature. We can use the last equation to express the change in the chemical potential due to the volume change:

$$d\mu_i = -\left.\left(\frac{\partial p}{\partial n_i}\right)\right|_{T,V,n_{j\neq i}} dV .$$

Let us link this expression with fugacities. Fugacities are defined by the following expression

$$\mu_i'' - \mu_i' = RT \ln\left(\frac{f_i''}{f_i'}\right) = RT\left(\ln\left(f_i''\right) - \ln\left(f_i'\right)\right),$$

where μ_i'' and μ_i' are the chemical potentials of component i corresponding to two different states of the system (phase), f_i'' and f_i' are the fugacities of component i in these system states. Hence, we can express the change in chemical potential through the change in fugacity

$$d\mu_i = RT\left(d\ln\left(f_i\right)\right).$$

Hence,

$$RT\left(d\ln\left(f_i\right)\right) = d\mu_i = -\left(\frac{\partial p}{\partial n_i}\right)\Bigg|_{T,V,n_{j\neq i}} dV\ .$$

Let us transform the last equation by adding the term $RT\left(d\ln\left(V/RT\right)\right)$ to both sides of it:

$$RT\left(d\ln\left(f_i\right)\right) + RT\left(d\ln\left(V/RT\right)\right) = -\left(\frac{\partial p}{\partial n_i}\right)\Bigg|_{T,V,n_{j\neq i}} dV + RT\left(d\ln\left(V/RT\right)\right).$$

Integrating this equation from the fixed phase volume V_0 to $V \to \infty$, we obtain

$$RT\left(\ln\left(\frac{f_i V}{RT}\right)\right)\Bigg|_{V_0}^{\infty} = \int_{V_0}^{\infty}\left(-\left(\frac{\partial p}{\partial n_i}\right)\Bigg|_{T,V,n_{j\neq i}} + \left(\frac{RT}{V}\right)\right)dV\ .$$

We assume that all gases behave ideally when $V \to \infty$ (Brusilovsky 2002; Danesh 1998). Hence, we can write $\lim_{V\to\infty}\frac{pV}{RT} = n$, $\lim_{V\to\infty}\frac{f_i}{x_i p} = 1$, and $\lim_{V\to\infty}\frac{f_i}{p} = \frac{n_i}{n}$. Taking these equations into account, we obtain

$$\left(\ln\left(\frac{f_i V}{RT}\right)\right)\Bigg|_{V_0}^{\infty} = \left(\ln\left(\frac{f_i pV}{pRT}\right)\right)\Bigg|_{V_0}^{\infty} = \ln\left(\frac{n_i}{n}\right) + \ln\left(n\right) - \ln\left(\frac{f_i pV_0}{pRT}\right).$$

Thus, we can rewrite the equation with integrals above as

$$RT\left(\ln\left(\frac{n_i RT}{pV_0}\right)-\ln\left(\frac{f_i}{p}\right)\right)=\int_{V_0}^{\infty}\left(-\left(\frac{\partial p}{\partial n_i}\right)\Bigg|_{T,V,n_{j\neq i}}+\left(\frac{RT}{V}\right)\right)dV\,.$$

Finally, we obtain the following expression for the fugacity

$$\ln\left(f_i\right)=\int_{V_0}^{\infty}\left(\frac{1}{RT}\left(\frac{\partial p}{\partial n_i}\right)\Bigg|_{T,V,n_{j\neq i}}-\left(\frac{1}{V}\right)\right)dV+\ln\left(\frac{n_i RT}{V_0}\right).$$

The fugacity coefficients are often used instead of fugacities. Fugacity coefficients are defined by the expression

$$\varphi_i=\frac{f_i}{x_i p}\,.$$

Hence, we can write for the fugacity coefficients:

$$\ln\left(\varphi_i\right)=\int_{V_0}^{\infty}\left(\frac{1}{RT}\left(\frac{\partial p}{\partial n_i}\right)\Bigg|_{T,V,n_{j\neq i}}-\left(\frac{1}{V}\right)\right)dV-\ln\left(Z\right),$$

where $Z=\dfrac{pV_0}{nRT}$ is the compressibility factor (by definition).

Appendix B. SRK and PR cases

In this study, we consider SRK and PR EOS (1). As shown in Appendix A, in order to obtain the corresponding fugacity coefficients, we can substitute (1) in the expression

$$\ln(\varphi_i) = \int_{V_0}^{\infty} \left(\frac{1}{RT} \left(\frac{\partial p}{\partial n_i} \right)\Big|_{T,V,n_{j\neq i}} - \left(\frac{1}{V} \right) \right) dV - \ln(Z).$$

Hence, we concern on the derivative of pressure at constant total volume, temperature and all mole numbers except n_i

$$\left(\frac{\partial p}{\partial n_i} \right)\Big|_{T,V,n_{j\neq i}} = \frac{RT}{V - nB_{\mathrm{M}}} + \frac{nRT\left(\frac{\partial nB_{\mathrm{M}}}{\partial n_i} \right)}{(V - nB_{\mathrm{M}})^2} - \frac{\left(\frac{\partial n^2 A_{\mathrm{M}}}{\partial n_i} \right)}{(V + \xi_1 nB_{\mathrm{M}})(V + \xi_2 nB_{\mathrm{M}})} +$$

$$+ n^2 A_{\mathrm{M}} \left(\frac{\xi_1\xi_2 \left(\frac{\partial (nB_{\mathrm{M}})^2}{\partial n_i} \right) + (\xi_1 + \xi_2) V \left(\frac{\partial nB_{\mathrm{M}}}{\partial n_i} \right)}{((V + \xi_1 nB_{\mathrm{M}})(V + \xi_2 nB_{\mathrm{M}}))^2} \right).$$

We use mixing rules in the form (2), hence, we can write

$$n^2 A_{\mathrm{M}} = \sum_{i=1}^{N_c} \sum_{j=1}^{N_c} n_i n_j A_{ij} \,, nB_{\mathrm{M}} = \sum_{i=1}^{N_c} n_i B_i \,.$$

For the derivatives we have

$$\left(\frac{\partial n^2 A_{\mathrm{M}}}{\partial n_i} \right)\Big|_{T,V,n_{j\neq i}} = 2\sum_{j=1}^{N_c} n_j A_{ij} = 2n\sum_{j=1}^{N_c} x_j A_{ij} \,, \qquad \left(\frac{\partial nB_{\mathrm{M}}}{\partial n_i} \right)\Big|_{T,V,n_{j\neq i}} = B_i \,.$$

Substituting these derivatives in the expression for the pressure derivative, we get

$$\left(\frac{\partial p}{\partial n_i} \right)\Big|_{T,V,n_{j\neq i}} = \frac{RT}{V - nB_{\mathrm{M}}} + \frac{nRT\, B_i}{(V - nB_{\mathrm{M}})^2} - \frac{2n\sum_{j=1}^{N_c} x_j A_{ij}}{(V + \xi_1 nB_{\mathrm{M}})(V + \xi_2 nB_{\mathrm{M}})} +$$

$$+ n^2 A_{\mathrm{M}} \left(\frac{2\xi_1\xi_2 nB_{\mathrm{M}} + (\xi_1 + \xi_2) V}{((V + \xi_1 nB_{\mathrm{M}})(V + \xi_2 nB_{\mathrm{M}}))^2} \right) B_i.$$

In order to obtain the fugacity coefficients, we need to integrate $\left(\frac{\partial p}{\partial n_i}\right)\Big|_{T,V,n_{j\neq i}}$ with respect to V. For simplicity, let us introduce the notation

$$\psi_1 = \frac{RT}{V - nB_{\mathrm{M}}} + \frac{nRT\,B_i}{\left(V - nB_{\mathrm{M}}\right)^2},\ \psi_2 = -\frac{2n\sum_{j=1}^{N_c} x_j A_{ij}}{\left(V + \xi_1 nB_{\mathrm{M}}\right)\left(V + \xi_2 nB_{\mathrm{M}}\right)},$$

$$\psi_3 = n^2 A_{\mathrm{M}}\left(\frac{2\xi_1\xi_2 nB_{\mathrm{M}} + \left(\xi_1 + \xi_2\right)V}{\left(\left(V + \xi_1 nB_{\mathrm{M}}\right)\left(V + \xi_2 nB_{\mathrm{M}}\right)\right)^2}\right)B_i.$$

Thus, we have $\left(\frac{\partial p}{\partial n_i}\right)\Big|_{T,V,n_{j\neq i}} = \psi_1 + \psi_2 + \psi_3$. It is reasonable to transform ψ_2 and ψ_3 in order to simplify the integration.

$$\psi_2 = -\frac{2n\sum_{j=1}^{N_c} x_j A_{ij}}{\left(V + \xi_1 nB_{\mathrm{M}}\right)\left(V + \xi_2 nB_{\mathrm{M}}\right)} = -\left(\frac{2\sum_{j=1}^{N_c} x_j A_{ij}}{B_{\mathrm{M}}\left(\xi_1 - \xi_2\right)}\right)\left(\frac{1}{V + \xi_2 nB_{\mathrm{M}}} - \frac{1}{V + \xi_1 nB_{\mathrm{M}}}\right).$$

$$\psi_3 = n^2 A_{\mathrm{M}}\left(\frac{2\xi_1\xi_2 nB_{\mathrm{M}} + \left(\xi_1 + \xi_2\right)V}{\left(\left(V + \xi_1 nB_{\mathrm{M}}\right)\left(V + \xi_2 nB_{\mathrm{M}}\right)\right)^2}\right)B_i =$$

$$= -\left(\frac{nA_{\mathrm{M}}B_i}{2B_{\mathrm{M}}}\right)\left(\left(\frac{1}{V + \xi_2 nB_{\mathrm{M}}}\right)^2 + \left(\frac{1}{V + \xi_1 nB_{\mathrm{M}}}\right)^2\right) + \left(\frac{A_{\mathrm{M}}B_i}{B_{\mathrm{M}}^2\left(\xi_1 - \xi_2\right)}\right)\left(\frac{1}{V + \xi_2 nB_{\mathrm{M}}} - \frac{1}{V + \xi_1 nB_{\mathrm{M}}}\right) +$$

$$+ n^2 A_{\mathrm{M}}B_i\left(\frac{\left(\xi_1 + \xi_2\right)\left(2V + \left(\xi_1 + \xi_2\right)nB_{\mathrm{M}}\right)}{2\left(\left(V + \xi_1 nB_{\mathrm{M}}\right)\left(V + \xi_2 nB_{\mathrm{M}}\right)\right)^2}\right).$$

Integration gives us the following expressions.

$$\int_{V_0}^{\infty}\psi_1 dV = \int_{V_0}^{\infty}\left(\frac{RT}{V - nB_{\mathrm{M}}} + \frac{nRT\,B_i}{\left(V - nB_{\mathrm{M}}\right)^2}\right)dV = RT\ln\left(V - nB_{\mathrm{M}}\right)\Big|_{V_0}^{\infty} - \left(\frac{nRT\,B_i}{V - nB_{\mathrm{M}}}\right)\Big|_{V_0}^{\infty},$$

$$\int_{V_0}^{\infty}\psi_2 dV = -\left(\frac{2\sum_{j=1}^{N_c} x_j A_{ij}}{B_{\text{M}}(\xi_1-\xi_2)}\right)\int_{V_0}^{\infty}\left(\frac{1}{V+\xi_2 nB_{\text{M}}}-\frac{1}{V+\xi_1 nB_{\text{M}}}\right)dV = -\left(\frac{2\sum_{j=1}^{N_c} x_j A_{ij}}{B_{\text{M}}(\xi_1-\xi_2)}\right)\ln\left(\frac{V+\xi_2 nB_{\text{M}}}{V+\xi_1 nB_{\text{M}}}\right)\Bigg|_{V_0}^{\infty}.$$

$$\int_{V_0}^{\infty}\psi_3 dV = -\left(\frac{nA_{\text{M}}B_i}{2B_{\text{M}}}\right)\int_{V_0}^{\infty}\left(\left(\frac{1}{V+\xi_2 nB_{\text{M}}}\right)^2+\left(\frac{1}{V+\xi_1 nB_{\text{M}}}\right)^2\right)dV +$$

$$+\left(\frac{A_{\text{M}}B_i}{B_{\text{M}}^2(\xi_1-\xi_2)}\right)\int_{V_0}^{\infty}\left(\frac{1}{V+\xi_2 nB_{\text{M}}}-\frac{1}{V+\xi_1 nB_{\text{M}}}\right)dV +$$

$$+\left(\frac{n^2 A_{\text{M}}B_i(\xi_1+\xi_2)}{2}\right)\int_{V_0}^{\infty}\left(\frac{(2V+(\xi_1+\xi_2)nB_{\text{M}})}{((V+\xi_1 nB_{\text{M}})(V+\xi_2 nB_{\text{M}}))^2}\right)dV = \left(\frac{nA_{\text{M}}B_i}{2B_{\text{M}}}\right)\left(\frac{1}{V+\xi_1 nB_{\text{M}}}+\frac{1}{V+\xi_2 nB_{\text{M}}}\right)\Bigg|_{V_0}^{\infty} +$$

$$+\left(\frac{A_{\text{M}}B_i}{B_{\text{M}}^2(\xi_1-\xi_2)}\right)\ln\left(\frac{V+\xi_2 nB_{\text{M}}}{V+\xi_1 nB_{\text{M}}}\right)\Bigg|_{V_0}^{\infty} - \left(\frac{n^2 A_{\text{M}}B_i(\xi_1+\xi_2)}{2}\right)\left(\frac{1}{(V+\xi_1 nB_{\text{M}})(V+\xi_2 nB_{\text{M}})}\right)\Bigg|_{V_0}^{\infty}.$$

Now we can substitute the obtained integrals in

$$\int_{V_0}^{\infty}\left(\frac{1}{RT}\left(\frac{\partial p}{\partial n_i}\right)\Bigg|_{T,V,n_{j\neq i}} - \left(\frac{1}{V}\right)\right)dV = \ln\left(\frac{V-nB_{\text{M}}}{V}\right)\Bigg|_{V_0}^{\infty} - \left(\frac{n\,B_i}{V-nB_{\text{M}}}\right)\Bigg|_{V_0}^{\infty} -$$

$$-\left(\frac{2\sum_{j=1}^{N_c} x_j A_{ij}}{RTB_{\text{M}}(\xi_1-\xi_2)}\right)\ln\left(\frac{V+\xi_2 nB_{\text{M}}}{V+\xi_1 nB_{\text{M}}}\right)\Bigg|_{V_0}^{\infty} + \left(\frac{nA_{\text{M}}B_i}{2RTB_{\text{M}}}\right)\left(\frac{1}{V+\xi_1 nB_{\text{M}}}+\frac{1}{V+\xi_2 nB_{\text{M}}}\right)\Bigg|_{V_0}^{\infty} +$$

$$+\left(\frac{A_{\text{M}}B_i}{RTB_{\text{M}}^2(\xi_1-\xi_2)}\right)\ln\left(\frac{V+\xi_2 nB_{\text{M}}}{V+\xi_1 nB_{\text{M}}}\right)\Bigg|_{V_0}^{\infty} - \left(\frac{n^2 A_{\text{M}}B_i(\xi_1+\xi_2)}{2RT}\right)\left(\frac{1}{(V+\xi_1 nB_{\text{M}})(V+\xi_2 nB_{\text{M}})}\right)\Bigg|_{V_0}^{\infty} =$$

$$= -\ln\left(1-\frac{nB_{\text{M}}}{V_0}\right)+\left(\frac{n\,B_i}{V_0-nB_{\text{M}}}\right)+\left(\frac{\left(2\sum_{j=1}^{N_c} x_j A_{ij}\right)-\frac{A_{\text{M}}B_i}{B_{\text{M}}}}{RTB_{\text{M}}(\xi_1-\xi_2)}\right)\ln\left(\frac{V_0+\xi_2 nB_{\text{M}}}{V_0+\xi_1 nB_{\text{M}}}\right) -$$

$$-\frac{nA_{\text{M}}B_i V_0}{RTB_{\text{M}}(V_0+\xi_1 nB_{\text{M}})(V_0+\xi_2 nB_{\text{M}})}.$$

Thus, for the fugacity coefficients we can write

$$\ln(\varphi_i) = \int_{V_0}^{\infty} \left(\frac{1}{RT} \left(\frac{\partial p}{\partial n_i} \right)\Big|_{T,V,n_{j\neq i}} - \left(\frac{1}{V} \right) \right) dV - \ln(Z) = -\ln\left(Z\left(1 - \frac{nB_{\mathrm{M}}}{V_0} \right) \right) + \left(\frac{n\,B_i}{V_0 - nB_{\mathrm{M}}} \right) +$$

$$+ \left(\frac{\left(2\sum_{j=1}^{N_c} x_j A_{ij} \right) - \frac{A_{\mathrm{M}} B_i}{B_{\mathrm{M}}}}{RTB_{\mathrm{M}}(\xi_1 - \xi_2)} \right) \ln\left(\frac{V_0 + \xi_2 nB_{\mathrm{M}}}{V_0 + \xi_1 nB_{\mathrm{M}}} \right) - \frac{nA_{\mathrm{M}} B_i V_0}{RTB_{\mathrm{M}}(V_0 + \xi_1 nB_{\mathrm{M}})(V_0 + \xi_2 nB_{\mathrm{M}})}.$$

EOS (1) gives the following relation

$$\frac{n^2 A_{\mathrm{M}}}{(V_0 + \xi_1 nB_{\mathrm{M}})(V_0 + \xi_2 nB_{\mathrm{M}})} = \frac{nRT}{V_0 - nB_{\mathrm{M}}} - p\,.$$

With the compressibility factor $Z = \frac{pV_0}{nRT}$, we can write

$$\frac{n^2 A_{\mathrm{M}}}{(V_0 + \xi_1 nB_{\mathrm{M}})(V_0 + \xi_2 nB_{\mathrm{M}})} = nRT\left(\frac{1}{V_0 - nB_{\mathrm{M}}} - \frac{Z}{V_0} \right).$$

Using this relation, we can transform the expression for the fugacity coefficients and obtain finally

$$\ln(\varphi_i) = -\ln\left(Z\left(1 - \frac{nB_{\mathrm{M}}}{V_0} \right) \right) + \left(\frac{n\,B_i}{V_0 - nB_{\mathrm{M}}} \right) + \left(\frac{\left(2\sum_{j=1}^{N_c} x_j A_{ij} \right) - \frac{A_{\mathrm{M}} B_i}{B_{\mathrm{M}}}}{RTB_{\mathrm{M}}(\xi_1 - \xi_2)} \right) \ln\left(\frac{V_0 + \xi_2 nB_{\mathrm{M}}}{V_0 + \xi_1 nB_{\mathrm{M}}} \right) -$$

$$- \frac{B_i V_0}{B_{\mathrm{M}}} \left(\frac{1}{V_0 - nB_{\mathrm{M}}} - \frac{Z}{V_0} \right) = -\ln\left(Z\left(1 - \frac{nB_{\mathrm{M}}}{V_0} \right) \right) + \frac{B_i}{B_{\mathrm{M}}}(Z - 1) +$$

$$+ \left(\frac{\left(2\sum_{j=1}^{N_c} x_j A_{ij} \right) - \frac{A_{\mathrm{M}} B_i}{B_{\mathrm{M}}}}{RTB_{\mathrm{M}}(\xi_1 - \xi_2)} \right) \ln\left(\frac{V_0 + \xi_2 nB_{\mathrm{M}}}{V_0 + \xi_1 nB_{\mathrm{M}}} \right).$$

The fugacity coefficients are usually considered with parameters A_i and B_i in the following dimensionless form: $\tilde{A}_i = \frac{pA_i}{R^2T^2}$, $\tilde{B}_i = \frac{pB_i}{RT}$. Using these dimensionless parameters and Z, we can express the fugacity coefficients as

$$\ln(\varphi_i) = -\ln\left(Z\left(1-\frac{\tilde{B}_m}{Z}\right)\right) + \frac{\tilde{B}_i}{\tilde{B}_m}(Z-1) + \left(\frac{\left(2\sum_{j=1}^{N_c} x_j \tilde{A}_{ij}\right) - \frac{\tilde{A}_m \tilde{B}_i}{\tilde{B}_m}}{\tilde{B}_m(\xi_1-\xi_2)}\right)\ln\left(\frac{Z+\xi_2\tilde{B}_m}{Z+\xi_1\tilde{B}_m}\right).$$

This form of the fugacity coefficients is the most popular form used in flash calculations (Danesh 1998; Orr 2005).

In this study, we consider the Helmholtz energy of a multicomponent system. Our derivation of its expression implies an analysis of the fugacity expression. Hence, we can go from the fugacity coefficients to the fugacities. Since by definition $\varphi_i = \frac{f_i}{x_i p}$, we have

$$\ln(f_i) = \ln(\varphi_i) + \ln(x_i p) = \ln(\varphi_i) + \ln(Z) + \ln\left(x_i \frac{nRT}{V_0}\right) =$$

$$= \ln\left(x_i \frac{nRT}{V_0}\right) + \int_{V_0}^{\infty}\left(\frac{1}{RT}\left(\frac{\partial p}{\partial n_i}\right)\Big|_{T,V,n_{j\neq i}} - \left(\frac{1}{V}\right)\right)dV.$$

Thus, in the particular case of SRK and PR EOS (1), we have

$$\ln(f_i) = \ln(n_i RT) - \ln(V_0 - nB_{\mathrm{M}}) + \left(\frac{n\,B_i}{V_0 - nB_{\mathrm{M}}}\right) +$$

$$+\left(\frac{\left(2\sum_{j=1}^{N_c} x_j A_{ij}\right) - \frac{A_{\mathrm{M}}B_i}{B_{\mathrm{M}}}}{RTB_{\mathrm{M}}(\xi_1-\xi_2)}\right)\ln\left(\frac{V_0+\xi_2 nB_{\mathrm{M}}}{V_0+\xi_1 nB_{\mathrm{M}}}\right) - \left(\frac{nA_{\mathrm{M}}B_i}{RTB_{\mathrm{M}}}\right)\frac{V_0}{(V_0+\xi_1 nB_{\mathrm{M}})(V_0+\xi_2 nB_{\mathrm{M}})}.$$

Appendix C. The derivatives of the Helmholtz energy

Let us consider the derivative of term $\left(F\left(T,n_i,V\right)-E\left(T,n_i\right)\right)$ presented in (5) with respect to n_i. We can write

$$\frac{\partial}{\partial n_i}\left(F\left(T,n_i,V\right)-E\left(T,n_i\right)\right)=-\frac{\partial}{\partial n_i}\left(nRT\ln\left(V-nB_{\mathrm{M}}\right)-\frac{nA_{\mathrm{M}}}{B_{\mathrm{M}}\left(\xi_1-\xi_2\right)}\ln\left(\frac{V+\xi_2 nB_{\mathrm{M}}}{V+\xi_1 nB_{\mathrm{M}}}\right)\right)=$$

$$=-RT\ln\left(V-nB_{\mathrm{M}}\right)+\frac{nRT\left(\frac{\partial nB_{\mathrm{M}}}{\partial n_i}\right)}{\left(V-nB_{\mathrm{M}}\right)}+\frac{\left(\frac{\partial n^2A_{\mathrm{M}}}{\partial n_i}\right)}{nB_{\mathrm{M}}\left(\xi_1-\xi_2\right)}\ln\left(\frac{V+\xi_2 nB_{\mathrm{M}}}{V+\xi_1 nB_{\mathrm{M}}}\right)-$$

$$-\frac{n^2A_{\mathrm{M}}}{\left(\xi_1-\xi_2\right)}\frac{\left(\frac{\partial nB_{\mathrm{M}}}{\partial n_i}\right)}{\left(nB_{\mathrm{M}}\right)^2}\ln\left(\frac{V+\xi_2 nB_{\mathrm{M}}}{V+\xi_1 nB_{\mathrm{M}}}\right)+\left(\frac{nA_{\mathrm{M}}}{B_{\mathrm{M}}\left(\xi_1-\xi_2\right)}\right)\left(\frac{\xi_2\left(\frac{\partial nB_{\mathrm{M}}}{\partial n_i}\right)}{V+\xi_2 nB_{\mathrm{M}}}-\frac{\xi_1\left(\frac{\partial nB_{\mathrm{M}}}{\partial n_i}\right)}{V+\xi_1 nB_{\mathrm{M}}}\right).$$

As shown in Appendix B, the derivatives of mixture parameters have the form

$$\left.\left(\frac{\partial n^2A_{\mathrm{M}}}{\partial n_i}\right)\right|_{T,V,n_{j\neq i}}=2\sum_{j=1}^{N_c}n_jA_{ij}=2n\sum_{j=1}^{N_c}x_jA_{ij},\qquad\left.\left(\frac{\partial nB_{\mathrm{M}}}{\partial n_i}\right)\right|_{T,V,n_{j\neq i}}=B_i.$$

Substituting these derivatives in the expression above, we get

$$\frac{\partial}{\partial n_i}\left(F\left(T,n_i,V\right)-E\left(T,n_i\right)\right)=-RT\ln\left(V-nB_{\mathrm{M}}\right)+\left(\frac{nRTB_i}{V-nB_{\mathrm{M}}}\right)+$$

$$+\frac{2\sum_{j=1}^{N_c}x_jA_{ij}}{B_{\mathrm{M}}\left(\xi_1-\xi_2\right)}\ln\left(\frac{V+\xi_2 nB_{\mathrm{M}}}{V+\xi_1 nB_{\mathrm{M}}}\right)-\frac{n^2A_{\mathrm{M}}}{\left(\xi_1-\xi_2\right)}\frac{B_i}{\left(nB_{\mathrm{M}}\right)^2}\ln\left(\frac{V+\xi_2 nB_{\mathrm{M}}}{V+\xi_1 nB_{\mathrm{M}}}\right)+$$

$$+\left(\frac{nA_{\mathrm{M}}}{B_{\mathrm{M}}\left(\xi_1-\xi_2\right)}\right)\left(\frac{\xi_2B_i}{V+\xi_2 nB_{\mathrm{M}}}-\frac{\xi_1B_i}{V+\xi_1 nB_{\mathrm{M}}}\right)=-RT\ln\left(V-nB_{\mathrm{M}}\right)+\left(\frac{nRTB_i}{V-nB_{\mathrm{M}}}\right)+$$

$$+\left(\frac{\left(2\sum_{j=1}^{N_c}x_jA_{ij}\right)-\frac{A_{\mathrm{M}}B_i}{B_{\mathrm{M}}}}{B_{\mathrm{M}}\left(\xi_1-\xi_2\right)}\right)\ln\left(\frac{V+\xi_2 nB_{\mathrm{M}}}{V+\xi_1 nB_{\mathrm{M}}}\right)-\left(\frac{nA_{\mathrm{M}}B_i}{B_{\mathrm{M}}}\right)\frac{V}{\left(V+\xi_1 nB_{\mathrm{M}}\right)\left(V+\xi_2 nB_{\mathrm{M}}\right)}.$$

We use this expression in order to derive an explicit expression for the Helmholtz energy of a multicomponent mixture.

Appendix D. Additional results for binary mixtures

We consider the methane—n-heptane, methane—carbon dioxide and ethane—carbon dioxide binary mixtures in addition to the methane—ethane binary mixture described in details in section Results. Figure D.1a shows the pressure-composition phase diagram for the methane—n-heptane binary mixture obtained by flash calculations (the methane—n-heptane mixture considered at a temperature 344.3 K). Figure D.1b shows the same diagram obtained by the proposed Gibbs energy minimization technique. Colors and other designations in Figure D.1 coincide with Figure 4.14. The experimental data presented in Figure D.1 correspond to (Reamer 1956).

Figure D.2 corresponds to the methane—carbon dioxide binary mixture (considered at a temperature 250 K). Figure D.2a shows the pressure-composition phase diagram obtained by flash calculations. Figure D.2b shows the same diagram obtained by the proposed Helmholtz energy minimization technique. Colors and designations coincide with Figure 4.14. The experimental data in figure D.2 correspond to (Davalos et al. 1976).

Figure D.3 corresponds to the ethane—carbon dioxide binary mixture (considered at a temperature 250 K). Figure D.3a shows the pressure-composition phase diagram obtained by flash calculations. Figure D.3b shows the same diagram obtained by the proposed Helmholtz energy minimization technique. Colors and designations coincide with Figure 4.14. The experimental data in Figure D.5 correspond to (Davalos et al. 1976).

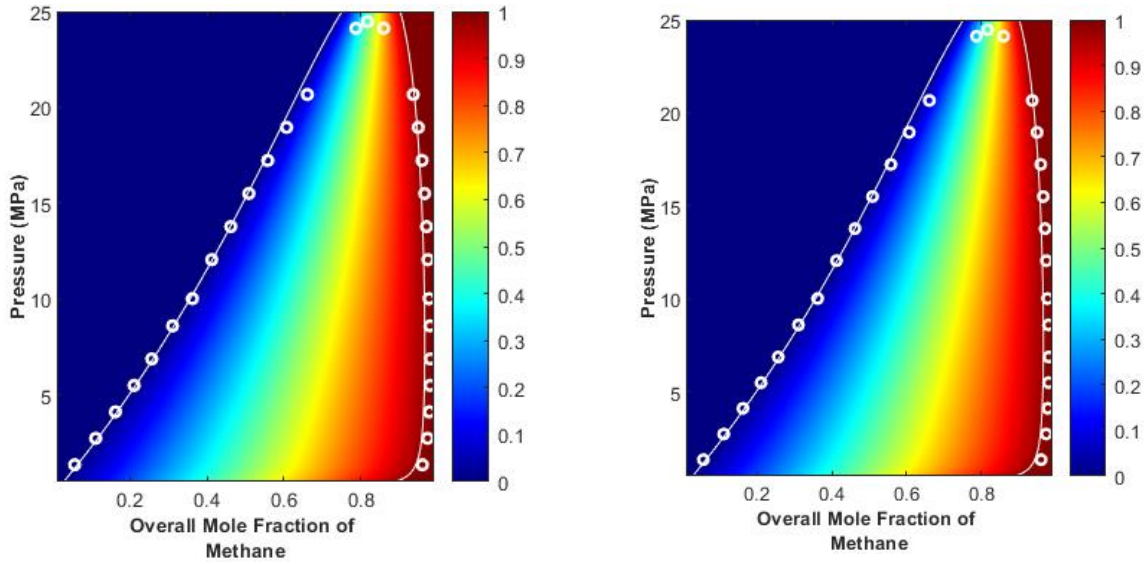

(a) (b)

Figure D.1—Pressure-composition phase diagram for the methane—n-heptane binary mixture: a) Flash calculations; b) Gibbs energy minimization algorithm

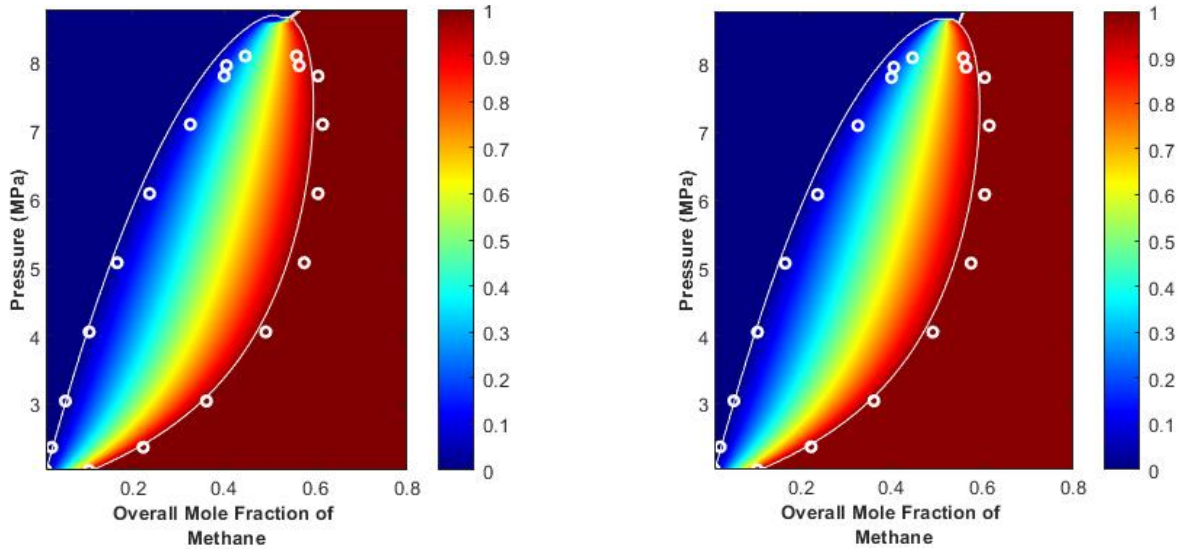

(a) (b)

Figure D.2—Pressure-composition phase diagram for the methane—carbon dioxide binary mixture: a) Flash calculations; b) Gibbs energy minimization algorithm

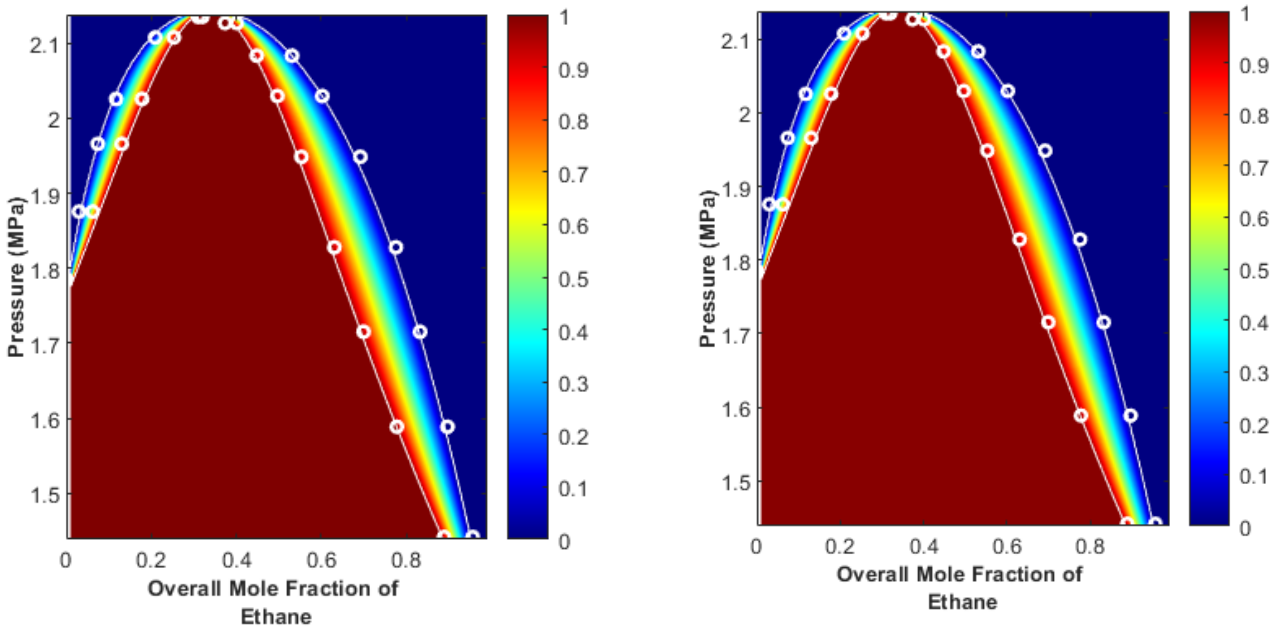

(a) (b)

Figure D.3—Pressure-composition phase diagram for the ethane—carbon dioxide binary mixture: a) Flash calculations; b) Gibbs energy minimization algorithm

Appendix E. Additional results for the methane—ethane—n-pentane ternary mixture

We consider the methane—ethane—n-pentane ternary mixture in addition to the methane—ethane—carbon dioxide mixture discussed in section Results. Figure E.1a presents the ternary diagram for the methane—ethane—n-pentane ternary mixture obtained by flash calculations. The mixture is considered at a pressure 10 MPa and temperature 310 K. Figure E.1b presents the same diagram obtained by the Gibbs energy minimization technique. The rules for reading the ternary diagram in Figure E.1 correspond to (Brusilovsky 2002). The color scheme is the same as used in Figure 4.14: the transition from dark blue to dark red corresponds to an increase in the mole fraction of vapor from zero to one. White circles in Figure E.1 demonstrate the experimental boundaries of two-phase region (Billman et al. 1948).

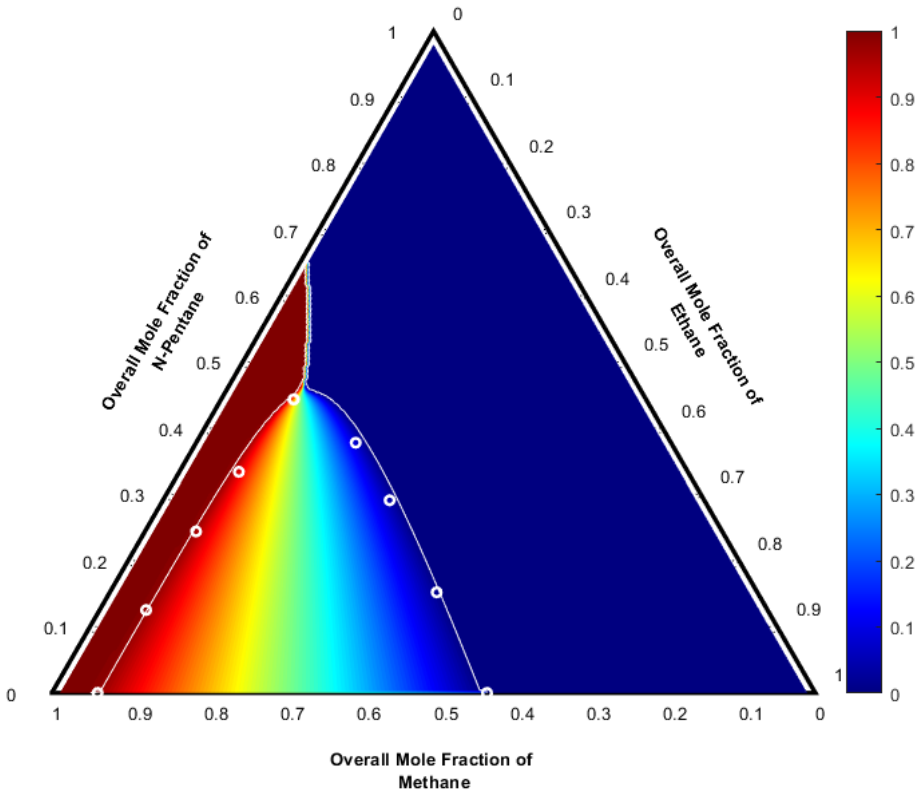

(a)

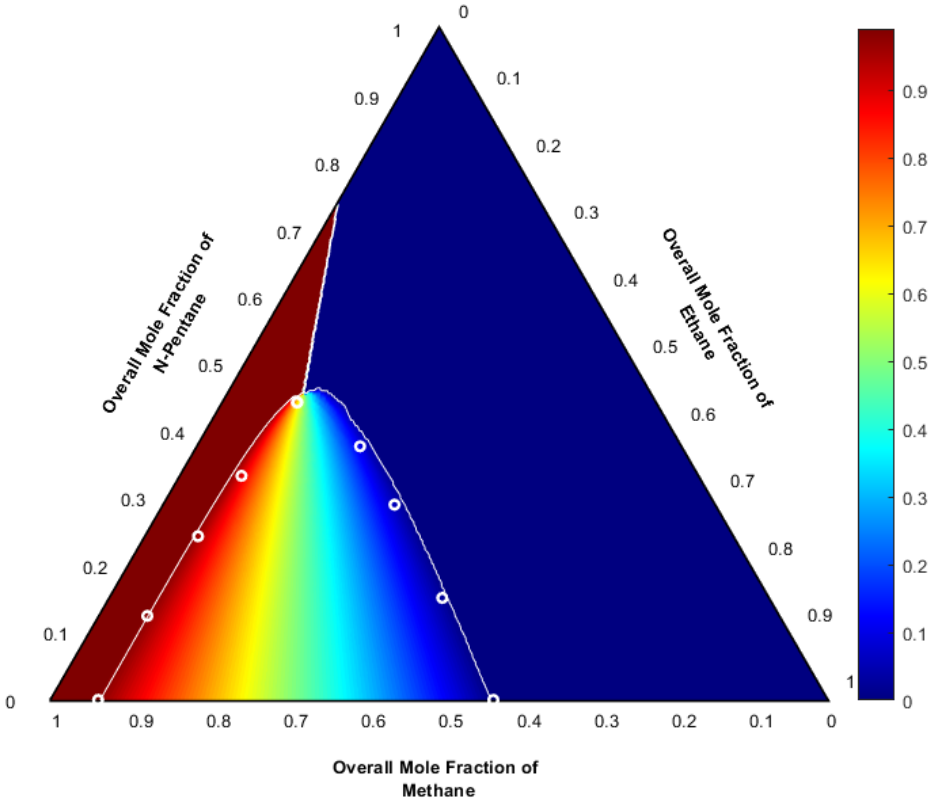

(b)

Figure E.1—Ternary phase diagram for the methane—ethane—n-pentane ternary mixture: a) Flash calculations; b) Gibbs energy minimization algorithm